Insights into Dioxygen Bond Activation and Formation by Small Biomimetic Complexes

Maksym A. Dedushko

A dissertation

submitted in partial fulfillment of the

requirements for the degree of

Doctor of Philosophy

University of Washington

2020

Reading Committee:

Julie A. Kovacs, Chair

Brandi M. Cossairt

Champak Chatterjee

Program Authorized to Offer Degree:

Chemistry

University of Washington

Abstract

Insights into Dioxygen Bond Activation and Formation by Small Biomimetic Complexes

Maksym A. Dedushko

Chair of the Supervisory Committee:
Professor Julie A. Kovacs
Department of Chemistry

Formation of an O–O bond is a crucial step in the biological oxidation of water to produce molecular O_2. Its microscopic reverse, namely the activation of an O–O bond, is an essential step in key oxidative transformations during metabolism. Both of the reactions are employed by Nature to garner energy, synthesize, and degrade biomolecules in order to sustain life. A common feature of these two seemingly opposite, yet intimately interlinked, reactions in biological systems is that they are catalyzed by first-row transition metals such as manganese, iron, and copper. Both types of reactions are proposed to proceed through several reactive intermediates. Among them, metal-(hydro)peroxo and high-valent metal-oxo are common to both an O–O bond activation and formation step. Iron-containing metalloenzymes that utilize O_2 as an oxidant perform a wide variety of biologically important chemical transformations. Cysteine-ligated iron metalloenzymes

are of particular interest due to the unique properties that thiolates impart on transition metal ions. Thiolate (RS^-) ligands form highly-covalent metal-ligand bonds, lower the activation energy barrier to O_2 binding and one-electron reduction, facilitate an O–O bond activation. This dissertation describes a *cis*-thiolate ligated $[Fe^{II}(S^{Me}N_4(tren))]^+$ complex that reacts with O_2 to afford a series of metastable intermediates such as Fe^{III}-superoxo, μ-peroxo Fe^{III} dimer, Fe^{IV}-oxo, and Fe^{III}-hydroxo at low temperature, (Chapters 2 – 3). Remarkably, addition of oxo-atom donors (OAD) to $[Fe^{II}(S^{Me}N_4(tren))]^+$ affords an identical metastable μ-peroxo Fe^{III} dimeric species, suggesting that a reversible O–O bond formation can occur, (Chapter 4). Chapter 5 describes the structure and properties of a O_2-derived thiolate-ligated, μ-peroxo-bridged Co^{III} dimer and provides a comparison with structurally analogous μ-peroxo-bridged Mn^{III} dimers. And lastly, Chapter 6 provides a detailed description of a successfully developed, versatile synthetic procedure to the Schiff-based precursors *en route* to heterobimetallic Robson-type target complexes. Moreover, a heterobimetallic $NaMn_3O_4$ cubane complex relevant to the oxygen-evolving complex (OEC) has been synthesized and crystallographically characterized.

TABLE OF CONTENTS

LIST OF FIGURES

LIST OF TABLES

LIST OF NUMBERED COMPLEXES

Chapters 2 – 4

1 $[Fe^{II}(S^{Me2}N_4(tren))]^+$

2 $[Fe^{III}(S^{Me2}N_4(tren))(O_2)]^+$

3 $[(Fe^{III}(S^{Me2}N_4(tren)))_2(\mu\text{-}O_2)]^{2+}$

4 $[Fe^{IV}(S^{Me2}N_4(tren))(O)]^+$

5 $[Fe^{III}(S^{Me2}N_4(tren))(OH)]^+$

6 $[(Fe^{III}(S^{Me2}N_4(tren)))_2(\mu\text{-}O)]^{2+}$

7-OMe $[Fe^{III}(S^{Me2}N_4(tren))(OMe)]^+$

7-MeOH $[Fe^{III}(S^{Me2}N_4(tren))(MeOH)]^{2+}$

7-MeCN $[Fe^{III}(S^{Me2}N_4(tren))(MeCN)]^{2+}$

7-N_3 $[Fe^{III}(S^{Me2}N_4(tren))(N_3)]^+$

7-OAc $[Fe^{III}(S^{Me2}N_4(tren))(OAc)]^+$

7-Cl $[Fe^{III}(S^{Me2}N_4(tren))(Cl)]^+$

8 $[Fe^{III}(S^{Me2}N_4(tren))(OOH)]^+$

Chapter 5

1 $\{[Mn^{III}(S^{Me2}(6\text{-Me-DPEN}))]_2(\textit{trans}\text{-}\mu\text{-}1,2\text{-}O_2)\}^{2+}$

2 $[Mn^{II}(S^{Me2}(6\text{-Me-DPEN}))]^+$

3 $\{[Mn^{III}(S^{Me2}(6\text{-Me-DPEN}))]_2(\mu\text{-}O)\}^{2+}$

4 $[Mn^{II}(S^{Me2}(6\text{-H-DPEN}))]^+$

5 $[Mn^{II}(S^{Me2}N_4(tren))]^+$

6 $[Mn^{II}(S^{Me2}(6\text{-MeO-DPEN}))]^+$

7 $[Mn^{II}(S^{Me2}(quinoEN))]^+$

8 $[Co^{II}(S^{Me2}N_4(tren))]^+$

9 $[Co^{III}(S^{Me2}N_4(tren))]_2(\textit{trans}\text{-}\mu\text{-}1,2\text{-}O_2)(PF_6)_2\bullet MeCN$

10 $\{[Mn^{III}(S^{Me2}N_4(quinoEN)]_2\text{-}(\mu\text{–}O_2)\}^{2+}$

11 $\{[Mn^{III}(S^{Me2}N_4(6\text{-MeO-DPEN})]_2\text{-}(\mu\text{–}O_2)\}^{2}$

12 $[Co^{III}(S^{Me2}N_4(tren))(OH)]^+$

Chapter 6

1 1-(3,5-di-t*ert*-butyl-2-hydroxyphenyl) ethanone

2-Me 2-acetyl-4,6-di-t*ert*-butylphenyl acetate

2-Ph 2-acetyl-4,6-di-t*ert*-butylphenyl benzoate

3-Me 1-(3,5-di-t*ert*-butyl-2-hydroxyphenyl)butane-1,3-dione

3-Ph 1-(3,5-di-t*ert*-butylphenyl) benzyl enol

4 $[(en)NaMn_3O_4(L_3)(OMe)]$

GLOSSARY

ACRONYMS AND ABBREVIATIONS

δ	isomer shift
$\Delta H^{\ddagger}$	activation enthalpy
ΔG	Gibbs free energy
$\Delta S^{\ddagger}$	activation entropy
e^-	electron
$E°$	standard electrode potential
ε	extinction coefficient
k_B	Boltzmann constant
μ_{eff}	effective magnetic moment
μ_B	Bohr magneton
$\perp$-mode	perpendicular mode
$\|\|$-mode	parallel mode
AB	acid-base
BDE	bond dissociation energy
bpy	2,2'-bipyridine
Ca	calcium
CDO	cysteine dioxygenase
CD_2Cl_2	deuterated methylene chloride
CD_3OD	methanol-d_4
CHD	cyclohexadiene
Cld	chlorite dismutase
CO_2	carbon dioxide
CN^-	cyanide anion
CPO	chloroperoxidase
CW	continuous wave
Cys	cysteine

DFT	density functional theory
BS-DFT	broken symmetry DFT
DHA	dihydroanthracene
DMF	dimethylformamide
EAS	electronic absorption spectrum
EPR	electron paramagnetic resonance
ET	electron transfer
EtOH	ethanol
EXAFS	extended X-ray absorption fine structure
Fe	iron
HAT	hydrogen atom transfer
HBF_4	tetrafluoroboric acid
HCl	hydrochloric acid
His	histidine
HOAc	acetic acid
HPCD	homoprotocatechuate 2,3-dioxygenase
HRP	horseradish peroxidase
H_2O	water
H_2O_2	hydrogen peroxide
H_2S	hydrogen sulfide
H_2SO_4	sulfuric acid
IBX-ester	iodoxybenzoate
IPNS	Isopenicillin *N* Synthase
J	coupling constant
KO_2	potassium superoxide
MeCN	acetonitrile
MeOH	methanol
*m*CPBA	*meta*-chloroperoxybenzoic acid
MMO	methane monooxygenase

Mn	manganese
MO	molecular orbital
NHE	normal hydrogen electrode
NIST	National Institute of Standards and Technology
N_2	dinitrogen
N4Py	*N*,*N*-bis(2-pyridyl- methyl)-*N*-bis(2-pyridyl)methylamine
OAc^-	acetate anion
O_2	dioxygen
O_2^-	superoxide
OEC	oxygen evolving complex
OH^-	hydroxide
ORTEP	Oak Ridge Thermal-Ellipsoid Program
OTf	trifluoromethanesulfonate
PhIO	iodosobenzene
pK_a	acid dissociation constant (K_a)
PPh_3	triphenylphosphine
PMe_2Ph	dimethylphenylphosphine
PS II	photosystem II
QM/MM	quantum mechanics/molecular mechanics
RC	radical coupling
Ru	ruthenium
Sr	strontium
T	calculated overlap parameter
TauD	taurine dioxygenase
TD-DFT	time-dependent density functional theory
TEMPOH	1-hydroxy-2,2,6,6-teramethyl-piperidine
THF	tetrahydrofuran
TMC	1,4,8,11-tetramethyl-1,4,-8,11-tetraaza cyclotetradecane
TMCS	1-mercaptoethyl-4,8,11-trimethyl-1,4,8,11-tetraaza cyclotetradecane

TMS	tetramethylsilane
TPA	tris(2-pyridylmethyl)amine
TPEN	N,N,N′,N′-tetrakis(2-pyridinylmethyl)-1,2-ethanediamine
tren	tris(2-aminoethyl)amine
XANES	X-ray absorption near edge structure
XFEL	X-ray free electron laser
XRD	X-ray diffraction

UNITES OF MEASURE

°C	degree(s) Celsius
amu	atomic mass unit
Å	Ångström
cm^{-1}	wavenumber(s)
G	Gauss
GHz	gigahertz
K	Kelvin
L	liter(s)
MHz	megahertz
nm	nanometer(s)
TW	terawatt (10^{12} W = 1 trillion watts)
V	volt(s)

ACKNOWLEDGEMENTS

I am most grateful to my graduate advisor Professor Julie Kovacs, whose passion for our science and depth of expertise continues to awe and inspire me. Julie is an amazing scientist and a mentor. We've spent countless hours in Julie's office discussing this science, designing experiments, and analyzing findings. She has helped me to sharpen not only my analytical thinking skills but also structure the logic of my thinking and communicating it on paper and during presentations. Julie also had the patience to allow me to learn things the hard way when I was being stubborn too. The skills I've gained in Julies lab under her mentorship are now my lifelong assets.

I am also grateful to the former group members, Dr. Benjamin Leipzig, Dr. Julian Rees and Audra Johansen, who have taught me foundational skills to succeed and build on in this group. Special thanks to my former peer group member, Dr. Maike Blakely, who went through the graduate program with me side-by-side. I would like to thank the current members of the group, Penny Poon, Dylan Rogers, Alex Downing, Maria Greiner, Julian Smith-Jones, Bennet Karel, and Paige Gannon, for their support and friendship.

The department of chemistry at the University of Washington offers a committed support to each student to learn and engage in science. I am so grateful to the many of my committee members, Professors Karen Goldberg, Ron Stenkamp, Stefan Stoll, Daniel Gamelin, Brandi, Cossairt, Champak Chatterjee, and Jerry Seidler. I have had the privilege to take their undergraduate courses as well as work for them as a teaching assistant during the graduate years. Dr. Werner Kaminsky, from the X-Ray Crystallography lab is another mentor from whom I have learned so much and look forward to learning more.

I would like to express my gratitude to my extended family for their love, support, and friendship: my loving host family Gary and Kaisa London, my kick ass fairy godparents Bob and Dana Rhodehamel, my immigration attorney Justin Moon, best friends Steve Gunn, Phung Ton, Sidney François, Olga Pyatigorets, and Xing Yee Gan. Special thanks to my wonderful boyfriend Josh Chau, who has been patient and supportive throughout my final chapter of graduate school. Lastly, I cannot thank enough my mom and dad, my grandparents, and my whole family in Ukraine who have scarified so much just to see me succeed.

DEDICATION

To my family

Chapter 1. Dioxygen Reactivity in Biology

1.1 Transition Metals in Biology and Bioinorganic Chemistry

Animal, plant, and bacterial life are sustained through complex chemical transformations carried out by enzymes. Rapid scientific progress in the fields of molecular biology, biochemistry, and genetics have enabled identification of more than a 168,000 enzyme structures up to date.[1] About a third of which are now estimated to contain transition metal ions. Nature has chosen primarily first row transition metals such as vanadium, manganese, iron, cobalt, nickel, copper, and zinc to perform a vast array of complex biological processes.[2] The biological function of metal ions ranges from stabilizing tertiary and quaternary protein structures, dioxygen binding and transport, electron transfer (ET) pathways, and promotion of catalytic reactivity.[3]

Metalloenzymes are proteins that, in general terms, contain a metal ion cofactor in the active site. Metal ions are Lewis acidic – their primary coordination environment is governed by the Lewis acid/base pair interactions with amino acid residues and substrates in the active site pocket. Metal-ligand bonds are labile, which favors changes in coordination number to allow substrate binding and release in the process of catalytic reactivity. Whereas organic molecules usually have a closed-shell electronic system, transition metal ions have partially occupied valence d-orbitals, which imparts them with unique chemical properties. The type and size of the metal ion, Lewis acidity, redox potential, spin state, and its ability to stabilize multiple oxidation steps allows for the seemingly endless and diverse array of chemical reactivity observed in biology. Even subtle changes in the coordination environment of the metal ion can modulate these physical prosperities and alter its reactivity in profound ways.

Study of metalloenzymes *in vivo*, and enzymes in general, has severe limitations. High-resolution structural information about the active site, its key metal-ligand bond lengths, presence of protons, and hydrogen bonding may be difficult to determine due to the large size of an enzyme. Multiple metal centers may be present within an enzyme, giving rise to convoluted detection signals Most metalloenzymes perform their catalytic activity at normal conditions (room temperature, atmospheric pressure, neutral pH, and in aqueous solution). At the same time, the catalytic processes of most enzymes happen on a timescale too short for many conventional measurement techniques to detect them. These biological constraints, as well as physical techniques available, make the investigation of the metal site's reaction mechanism and identity of its intermediates an arduous task.

Biomimetic chemistry offers a way to circumvent the aforementioned limitations via synthetic modeling approach. This method involves design of inorganic model complexes that mimic primary coordination environment and analogous chemical reactivity of metalloenzymes. Consequently, bioinorganic chemistry rests upon the foundations of coordination chemistry, biochemistry, and molecular spectroscopy, making it truly an interdisciplinary area of research. In addition, a bioinorganic chemist needs to possess proficiency in organic chemistry synthesis for proper design of target complexes. The aims of the field are vast, ranging from fundamental research of about the role of metals in biology, to materials synthesis, biomedical research, and industrial catalysis. At its core, bioinorganic chemistry seeks to understand the complex relationship between the geometric and electronic structure of the complex which gives rise to its function and reactivity.

1.2 Metal-Dioxygen Chemistry

Molecular dioxygen, O_2, comprises 17% of the Earth's atmosphere and plays an essential role, directly or indirectly, in almost all forms of life. In aerobic organisms, O_2 is transported from the atmosphere to cells where the oxidative power of O_2 is employed for metabolism and numerous crucial biochemical processes. Biological O_2 reactivity has been the subject of intense research by biochemists and biologists for over 200 years since Antoine Lavoisier first demonstrated the role of O_2 in combustion and respiration.

1.2.1 *Electronic Structure of Dioxygen*

Dioxygen (O_2) has a unique electronic structure, which is reflected in its properties and behavior. O_2 is the only homonuclear diatomic molecule that has a paramagnetic ground state. While simple electron-bonding description (Lewis dot structure) of two oxygen atoms is successful at predicting a double bond, it fails to rationalize its triplet ground state. It was not until 1928, and more completely in 1932, that a full description of electronic structure of O_2 was provided Robert Mulliken.[4,5] The molecular orbital (MO) description of the triplet ground state, $O_2(X^3\Sigma_g^-)$, is $(1s\sigma_g)^2(1s\sigma_u^*)^2(2s\sigma_g)^2(2s\sigma_u^*)^2(2p\sigma_g)^2(2p\pi_u)^4(2p\pi_g^*)^1(2p\pi_g^*)^1$, (Scheme 1.1). The assignment of a ground triplet state of O_2 is, in itself, a testament to the validity of MO theory. Its two lowest-energy excited electronic states, $O_2(a^1\Delta_g)$ and $O_2(b^1\Sigma_g^+)$, are singlets lying 22.53 kcal mol^{-1} and 37.51 kcal mol^{-1} above the ground state, respectively.[6]

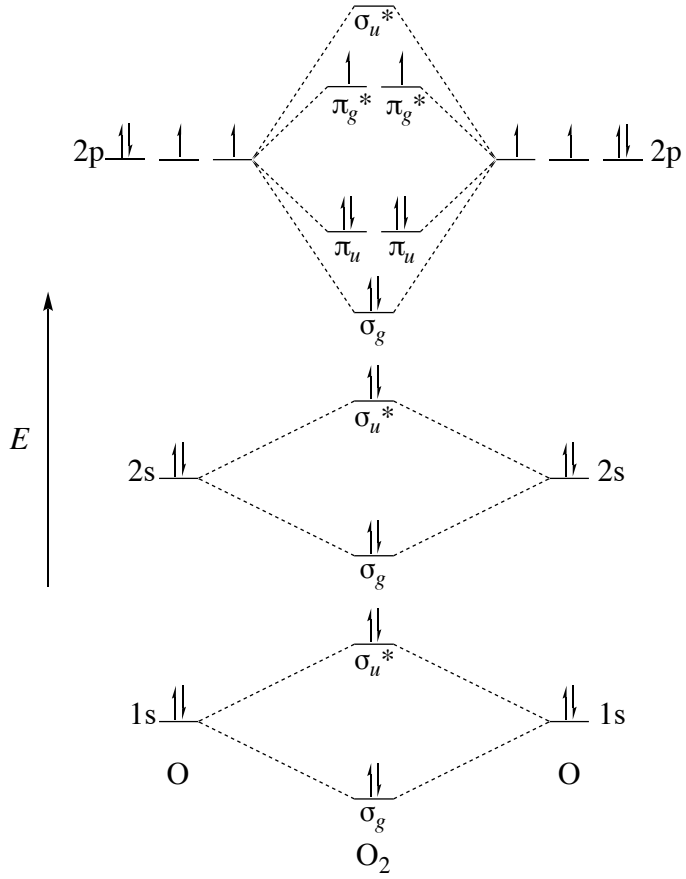

Figure 1.1. Molecular orbital (MO) diagram of dioxygen, O_2. The subscript denotes orbital inversion with respect to the point equidistant between the two nuclei (change in the sign of wavefunction, odd parity, *u* for *ungerade*; no change in the sign of wavefunction, even parity, *g* for *gerade*).

1.2.2 *Thermodynamics and Kinetics of O_2 Reactivity*

O_2-catalyzed oxidation of organic substrates is considerably thermodynamically favored. The sum of the bond dissociation energies (BDE) of C–C (83-90 kcal mol^{-1}), C–H (89-105 kcal mol^{-1}), and O–O (119 kcal mol^{-1}) bonds that are broken is less than the sum of C–O (90 kcal mol^{-1}) and O–H (110 kcal mol^{-1}) bonds that are formed. While O_2 reactivity with organic substrates is exothermic and irreversible, they are kinetically slow. Reactions of singlet-state organic reactants with a ground triplet-state O_2 to give singlet-state products are spin-forbidden. The timescale of O_2 spin inversion from the triplet ground state to its lowest singlet-state (10^{-9} to 1 second) is

considerably longer than the time at which a typical chemical reaction occurs (at a timescale of one vibration at 10^{-13} second).[7]

O_2 is the ubiquitous terminal oxidant in many biologically essential reactions. First excited singlet state $O_2(a^1\Delta_g)$ possesses reactivity that differs significantly from the $O_2(X^3\Sigma_g^-)$ triplet ground state.[6,8] Despite its greater reactivity, however, it is unlikely that the singlet O_2 is involved in enzymatic oxygen atom transfer reactions. Singlet O_2 chemistry usually leads to organic peroxides, it does not react with common biological substrates such as simple alkanes and aromatic compounds.[9] Lastly, it is improbable that oxygenase enzymes could supply sufficient energy to overcome the electronic energy barrier of 22.53 kcal mol^{-1} between the ground triplet and the excited singlet states to induce $O_2(a^1\Delta_g)$ reactivity.

Nature circumvents the sluggish kinetics of O_2 reactivity and unlocks its oxidative power by complexing it to a transition metal ion, which itself has unpaired electrons, contained within metalloenzyme's active site. The number of unpaired electrons on the overall metal complex remains constant throughout the reaction. As a result, the reaction of the metal-oxygen complex with a singlet organic substrate to give singlet-state oxidized products is now a spin-allowed process. Complexed to the metal ion, O_2 can react more readily by an ionic mechanism without overcoming the high energy barrier required to produce a singlet O_2.

1.2.3 *Reduced O_2 Chemistry*

O_2 is a four-electron oxidant which can form three successive intermediates *en route* the final product, water (H_2O), as independent entities or complexed to metal ions, (Figure 1.2). The stepwise reduction of O_2 is highly proton dependent. While the first reduction of O_2 to superoxide

(O_2^-) in aprotic solvent is endothermic (for example, in dimethylformamide (DMF), $E°$ = – 0.60 V vs. NHE), this process becomes exothermic in the presence of protons ($E°$ = + 0.12 V vs. NHE).[10]

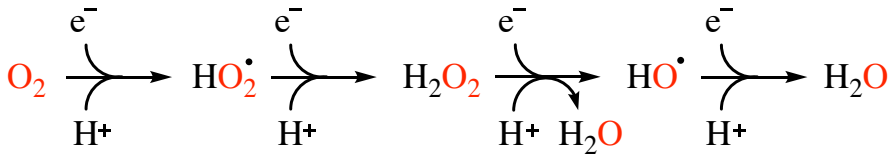

Figure 1.2. Proton-dependent four-electron reduction of O_2.

Second one-electron reduction to hydrogen peroxide (H_2O_2) is also highly exothermic in the presence of protons even at mild aqueous conditions, pH = 7.0 ($E°$ = + 0.89 V vs. NHE).[10] Favorable thermodynamics of proton-dependent one-electron reduction of O_2 can be understood in terms of charge compensation. In both steps, the O–H bond formation mitigates placement of an extra electron in the antibonding π_g* orbital. Likewise, transition metal ions can drive formal multi-electron reduction of O_2 via metal-oxygen (M–O) bond formation and stabilization through charge compensation. In biological systems, metalloenzymes in particular, protein structural constraints that favor metal-oxygen binding and fine-tuned regulation of protonation by the aqueous medium is therefore necessary.

1.3 Dioxygen Bond Activation by Iron Metalloenzymes – Cytochrome P450

Iron (Fe) is the second most abundant metal and fourth most abundant element in Earth's crust, making up 86% of its inner and outer core. Iron commonly has oxidation states of +2 "ferrous" and +3 "ferric" form as various oxide, carbonate, and sulfide ores (e.g. Fe_3O_4, Fe_2O_3, $Fe_2O_3 \cdot xH_2O$, $FeCO_3$, FeS_2).[11] Fe can access a wide range of oxidation states ranging from –2 to +6 in chemical compounds. Under physiological conditions, however, Fe^{II} and Fe^{III} is *essential to all life forms*.[11] The magnitude of the redox potential of Fe^{III}/Fe^{II} is sensitive to both the pH of the

aqueous solution and the presence of any ligands, as they modulate the electronic environment around the metal ion. Not surprisingly then, Nature has chosen Fe to perform a myriad of essential metabolic transformations because of the unique ability to finetune an extremely variable Fe^{III}/Fe^{II} redox potential through the choice of bound ligands.

1.3.1 *Historical Precedent for Biochemical O_2 Chemistry*

It was in the 1950s that an iron-containing enzyme mediated both molecular O_2 activation and oxo-atom transfer to its substrate was first demonstrated by Hayaishi *et al.*[12] Pyrocatechase of *Pseudomonas* genus catalyzes the oxidative cleavage of the catechol aromatic ring to *cis-cis*-muconic acid. It was shown that both inserted oxygen atoms were derived from molecular O_2 and not water in one of the first mechanistic studies using isotopically labeled $^{18}O_2$ and $^{18}OH_2$. Their discovery challenged the paradigm that oxygen atoms in biomolecules were exclusively derived from water via hydration reaction.

One year after Hayaishi's discovery, biosynthesis of cholesterol from the hydrocarbon squalene was shown to involve molecular O_2.[13] A series of similar experiments using isotopically labeled $^{18}O_2$ and $^{18}OH_2$ have were conclusively shown that an activated O_2 was the active oxidant and the initiating cyclization agent mediated by an enzyme termed *squalene oxidocyclase I*. The OH^- hydroxyl functional group was derived from one of the O_2 oxygen atoms, while the second oxo atom was reduced to water.[13]

And finally, in the late 1960s, prostaglandin, a hormone-like lipid involved in mediation of pain and the inflammatory response, was shown to involve O_2 in its biosynthesis. A detailed chemical mechanism for the conversion of a precursor arachidonic acid to prostaglandin was first proposed by Hamberg and Samuelsson.[14,15] Prostaglandin H Synthase is a single hemoprotein that

exhibits two enzyme activities. Cyclooxygenase incorporates endoperoxide and alkyl hydroperoxide moieties on arachidonic acid while peroxidase converts alkyl hydroperoxide to alkyl hydroxide in the presence of a reductant.[16]

As a result, molecular O_2 activation went from being a fringe biochemical process observed only in bacteria and fungi to now becoming a major theme of aerobic metabolism in higher order plants and animals. Subsequent efforts to understand and elucidate diverse molecular mechanisms of iron mediated O_2 activation has been the impetus in the development of bioinorganic chemistry.

1.3.2 *Role of Cysteine Thiolate in Fe Metalloenzymes*

Biochemical diversity observed among iron-containing metalloenzymes stems, in part, from proteins' structural differences and the active sites' primary coordination sphere. Metalloenzymes bind metal ions using amino acid residues and often incorporate cofactors or other small molecules. "2-His-1-carboxylate" facial triad is the most common binding motif in mononuclear iron oxygenases. This motif consists of two histidine (His) and one carboxylate amino acid residues arranged at the vertices of one triangular face of an octahedron, leaving the other three sites for exogenous ligand binding, solvent, or other amino acid residues.[17] While they are conglomerated into an enzyme superfamily, these enzymes have low sequence homology, suggesting that this structural motif is inherently evolutionary favored.[17–19]

Another Nature's key structural motif is iron-sulfur ligation that is found mostly in Fe-S clusters (e.g., 2S-2Fe, 3Fe-4S, 4Fe-4S),[20] heme, and non-heme iron metalloenzymes. Sulfur ($[Ne]3s^2 3p^4$) contains 4 electrons in its valence 3p orbitals available for bonding, making it a strong σ- and π-donor. Cysteine ligation imparts a set of unique, yet interrelated, physical properties.

Cysteinates form strong covalent bonds to Fe and other first row transition metals, resulting in modulation metal's reduction potential. Often coordinated *trans* to an open coordination site, cysteinates have a strong *trans* effect that influences substrate binding and release. Strong covalency of cysteines stabilizes low spin states in non-heme environments due to nephelauxetic (cloud-expanding) effect. This effect arises from the decrease in the electron-electron repulsion term afforded by the covalent character of the cysteine-metal bond.[21]

1.3.3 *Cytochrome P450*

Cytochrome P450 are a superfamily of heme ligated metalloenzymes. It is a ubiquitous enzyme with 11,500 isozymes found across numerous types of species. Cytochrome P450 originated early in the evolution as it is are found in both prokaryotic (such as bacteria and archaea) and eukaryotic domains (mammals, plants, fungi). In a broad sense, Cytochrome P450 performs two main physiological roles. Metabolism of xenobiotics is a protective function performed by the degradation of exogenous substrates or by introduction of polar groups for solubilization and excretion. Homeostasis control is the second broad role performed by Cytochrome P450 via synthesis of steroid hormones, metabolism of lipid-soluble vitamins, and oxidation of fatty acids. Cytochrome P450 is a monooxygenase whose primary role is hydroxylation of aliphatic (BDE = 96 – 105 kcal mol^{-1}) and aromatic (BDE = 113 kcal mol^{-1}) compounds.[22] The active site is constituted from three main parts: iron metal center, the porphyrin ring, and ligated cysteine amino acid residue. Iron is ligated by four nitrogens of the porphyrin in the equatorial plane. Cysteine is ligated trans to an open coordination site, (Figure 1.3). The active site is found buried within the protein matrix to prevent it from oxidizing other substrates.

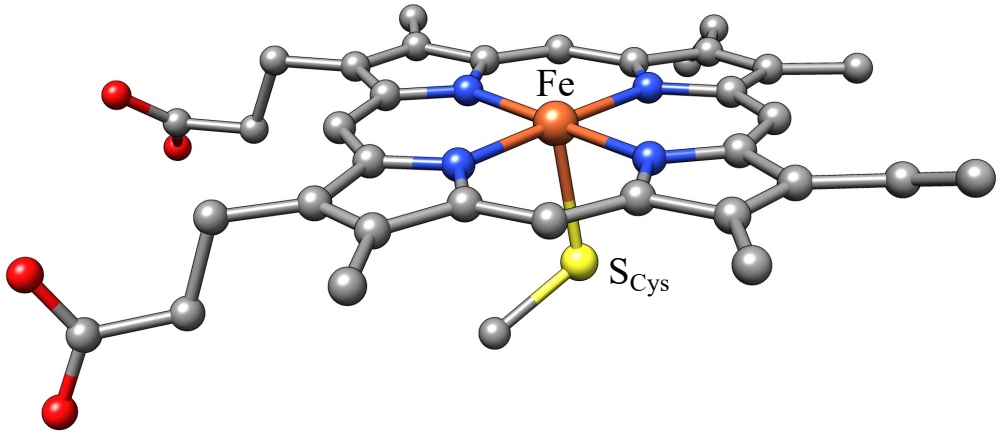

Figure 1.3.Crystal structure of Cytochrome P450 active site at the resolution of 2.8 Å from *Homo sapiens*, PDB 1W0E.[23]

All three components of the active site are covalently ligated. This produces a unique electronic structure that is at the heart of the Cytochrome P450 chemistry. Conjugated porhyrin macrocycle provides a significant spin delocalization with the iron center due to available π or π* orbitals which are close in energy to the metal's d-orbitals. Another manifestation of that is large charge transfer between the metal center, cysteine thiolate, and the porphyrin and the reduction of the formal charge. One of the elusive intermediates in the catalytic cycle (*vide infra*) of the Cytochrome P450 is high-valent iron-oxo intermediate with a formal oxidation state of Fe^{V}. Charge distribution stabilizes it by forming an d^4 Fe^{IV} species with a porphyrin bearing a π cation radical character.

Another unique feature of the active site is spin state mixing of the ground state with low-lying excited spin states of different multiplicities. Most mononuclear non-heme iron enzymes, in contrast, exhibit well defined and separated ground excited spin states. Facile spin-state transition is important to the enzyme function (*vide infra*).

Finally, porphyrin macrocycles exhibit unique electronic spectra. They consist of two π-π*charge transfer bands: a Q-band in the visible region (500 – 600 nm) and a Soret band in the UV region (408 – 450 nm).[24] They have been identified as transitions between the highest occupied $a_{1u}(\pi)$ and $a_{2u}(\pi)$ molecular orbitals and lowest unoccupied degenerate $e_g(\pi^*)$ orbitals.[25,26] They account for the facile formation of the π-cation radical porhyrin moiety during the formation of high-valent Fe-oxo intermediate.

During the catalytic cycle, Cytochrome P450 goes through seven distinct intermediate states and the iron center goes through three oxidation states (Figure 1.4). The resting state of the Cytochrome P450 has been identified as aqua bound ferric species, with relatively low reduction potential (– 330 mV) that is maintained by the anionic cysteine thiolate. Electron paramagnetic resonance (EPR) and semiempirical (INDO/ROHF) computational studies confirmed that Fe^{III}-OH_2 is in unprecedented $S = 1/2$ spin state.[27,28] The protein's conformational changes due to substrate presence triggers a spin-state transition from low-spin ($S = 1/2$) to high-spin ($S = 5/2$) state heme ferric center.[27] That results in a positive shift of redox potential to about – 200 mV.[29] Thusly, spin-state and reduction potential change of the ferric species will favor its one-electron reduction by NAD(P)H, whose redox potential is at – 320 mV.[30]

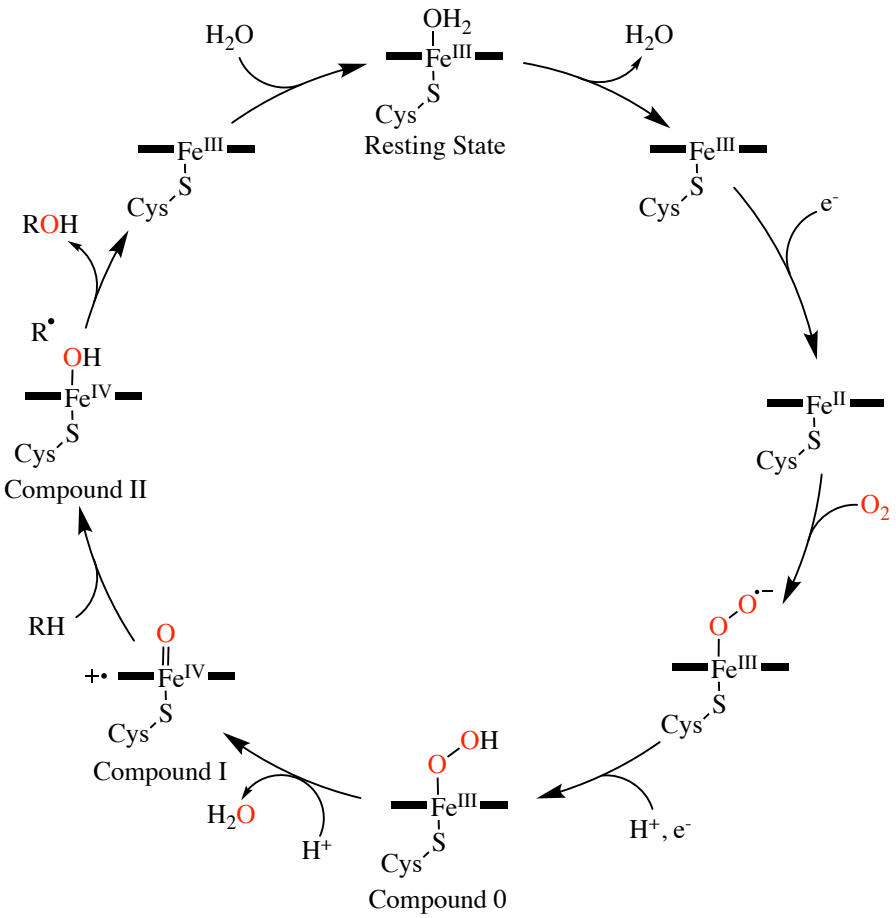

Figure 1.4. Catalytic cycle of Cytochrome P450.

Molecular O_2 readily coordinates to the reduced heme Fe^{II} center to afford either ferrous-dioxygen (Fe^{II}–O_2) or ferric-superoxo (Fe^{III}–O_2^{-}) complex. Spectroscopic and structural features of this transient intermediate provided by EPR, Mössbauer,[31] resonance Raman,[32] and X-Ray crystallographic identification are typical of ferric Fe^{III}–O_2^{-} complex.[33] Flavin induced one-electron reduction facilitates protonation of the distal oxygen to form hydroperoxo-bound ferric species, Fe^{III}–OOH, known as Compound 0. Compound 0 has a low spin $S = 1/2$ configuration, as identified by EPR.[34] Cysteine thiolate is proposed to significantly weaken the O–O bond by donating its electron density in π-overlap with Fe d-orbitals and into the antibonding σ* peroxo orbitals. This "push" effect coupled with the second protonation at the distal oxygen induces

heterolytic O–O bond cleavage to yield one molecule of water and a high-valent ferryl-oxo species termed Compound I. While its formal oxidation state is Fe^{V}, Compound I is characterized as an Fe^{IV}-oxo complex with a π-cation porphyrin radical, $((Por/S_{Cys}^{\bullet+})Fe^{IV}=O)$. Moreover, significant portion of the radical spin density resides on the cysteine thiolate itself,[35] suggesting that thiolate, together with a porphyrin, forms a powerful reducing reservoir. $((Por/S_{Cys}^{\bullet+})Fe^{IV}=O)$ compound is proposed to be the active oxidizing agent that abstracts a hydrogen atom from an aliphatic substrate. Hydrogen atom abstraction (HAT) generates Fe^{IV}–OH, also known as Compound II, at the heme center and a substrate with a carbon-centered radical. Investigations of the Compound I in Chloroperoxidase, another cysteine thiolate ligated heme-iron enzyme, have shown that the presence of the thiolate is crucial for the ability of Compound I to abstract aliphatic hydrogen atom from a substrate. Basic nature ($pK_a \geq 8.2$) of the ferryl-oxo species is attributed to the strong electron donation by the axial thiolate.[36] Finally, Compound II then hydroxylates the substrate via a rebound mechanism and returns to its resting, aqua-bound, ferric state.

1.3.4 *Biomimetic Models of Ferric-Peroxo Type and Ferryl-Oxo Intermediates*

Consensus catalytic cycle of Cytochrome P450 and its reactive intermediates came about as a result of decades of sustained research. As discussed earlier, a thorough elucidation of the nature and physical properties of these transient intermediates is challenging task due to inherent difficulties of studying biological systems *in vivo* and *in vitro*. Therefore, design and preparation of synthetic *biomimetic* complexes are instrumental to shed light on long-standing questions regarding Cytochrome P450's and many other biological processes. Biomimetic models provide key structural, electronic, spectroscopic information that can be readily correlated to metalloenzyme active site.

Synthetic porphyrin-ligated ferrous compounds were prepared as early as 1960s.[37] Reaction with O_2 resulted in generation of ferric μ-oxo-bridged dimer. The mechanism of O_2 binding and activation was investigated at low temperatures. Dinuclear μ-peroxo and high-valent Fe^{IV}=O intermediates were isolated and characterized at low temperatures.[38–40] In late 1970s, [Fe^{II}(TPP)Cl] (TPP = *mesa*-tetraphenylporphyrin) complex was prepared and shown to react with oxo-atom donors such as PhIO (iodosobenzene) and *m*CPBA (*meta*-chloroperoxybenzoic acid) to yield a high-valent Fe^{IV}=O intermediate.[41] Recent advances in porphyrin ligand design saw incorporation of steric bulk and a tethered axial ligand in [Fe^{II}(TMPIm)] (TMPIm = 5,10,15,20-tetrakis(N-methyl-4-imidazonium)porphinato dianion) complex. Xanthene derivatives around the porphyrin plane and an axial imidazole were proposed to facilitate O_2 binding at low temperature and generation of a mononuclear porphyrinoid Fe^{III}–O_2^- complex, which would go on to generate LS Fe^{III}–OO upon one-electron reduction, followed by Fe^{III}–OOH species in protic MeOH medium.[42,43]

Most of mononuclear heme and non-heme iron oxygenases are postulated to proceed through similar O_2-derived intermediates, such as those Cytochrome P450 catalytic cycle. Therefore, synthetic models for non-heme iron oxygenases are valuable systems to advance our understanding of the Cytochrome P450 cycle. A number of pentadentate synthetic models that generate ferric-peroxo intermediates have been prepared and characterized over the past few decades. The spin state and vibrational data of the peroxo moiety provide an important trend observed among these intermediates. Low-spin complexes tend to have $\nu_{Fe\text{-}O}$ stretch in the 560 – 640 cm^{-1} and $\nu_{O\text{-}O}$ stretch in the 780 – 810 cm^{-1} range, (Table 1.1). On the other hand, high-spin ferric peroxo complexes have $\nu_{Fe\text{-}O}$ stretch in the 420 – 500 cm^{-1} and $\nu_{O\text{-}O}$ stretch in the 820 – 860 cm^{-1} range. Electrons in the antibonding σ^* orbitals of high-spin ferric complexes weaken the Fe-

O bond relative to a low-spin configuration. The $\nu_{O\text{-}O}$ stretch low-spin ferric-peroxo complexes is on average 50 cm^{-1} lower than in high-spin ferric-peroxos, suggesting that low-spin ferric complexes may weaken the O–O bond. In Cytochrome P450, this trend, along with protein's environment and structural factors of the active site, may contribute to Compound 0 undergoing O–O bond cleavage.

Table 1.1. Vibrational data and spin state of metastable Fe^{III}-(hydro)peroxo intermediates in Cytochrome P450 (CYP450 Compound 0) and selected synthetic complexes.

Complex	*S*	$\nu_{Fe\text{-}O}$ (cm^{-1})	$\nu_{O\text{-}O}$ (cm^{-1})	Ref.
CYP450 Compound 0	1/2	559	799	44
TMPIm–(OO)	1/2	585	808	43
TMPIm–(OOH)	1/2	575	807	43
Py5–(OOH)	1/2	627	806	45
TPA–(OOH)	1/2	626	789	46
N4Py–(OOH)	1/2	632	790	46
TACNPy2–(OOH)	1/2	639	781	45
$S^{Me2}N_4$(tren)–(OOH)	1/2	–	784	47
N4Py–(OO)	5/2	495	827	45
EDTA–(OO)	5/2	459	816	48
Bppa–(OOH)	5/2	621	830	49
Cyclam-PrS–(OOH)	5/2	419	891	50

The final stage in O_2 activation by Cytochrome P450 is heterolytic O–O bond cleavage that yields Compound I, ($(Por/S_{Cys}^{\bullet+})Fe^{IV}$=O), (*vide supra*). High reactivity of Compound I, while the most interesting aspect of its chemistry, has precluded its direct observation and characterization for decades. It was not until 2005 when the first insights into the structure of Compound I derived from Chloroperoxidase (CPO). CPO is a heme thiolate-ligated iron oxygenase that is both structurally and catalytically similar to Cytochrome P450, making it a valuable model system.[51]

Extended X-ray absorption fine structure (EXAFS) measurements of CPO Compound I have revealed an Fe^{IV}=O bond length of 1.661 Å.[52] A decade later, successful EXAFS measurements of Cytochrome P450 Compound I established an Fe^{IV}=O bond length of 1.670 Å.[53]

Both the electron-rich thiolate and the conjugated porphyrin cofactor were assumed to be required to stabilize Fe^{IV}=O intermediate. However, recent experimental evidence supports the involvement of putative high-valent ferryl-oxo intermediates in a number of mono- and dinuclear non-heme iron oxygenases such as Isopenicillin *N* Synthase (IPNS),[54] Rieske dioxygenase,[55] methane monooxygenase (MMO),[56,57] and taurine dioxygenase (TauD).[58,59] This has encouraged synthetic chemists to search for an evidence of Fe^{IV}=O formation and involvement in oxidative reactions in non-heme iron model complexes. A major breakthrough in the field of bioinorganic chemistry came at the turn of the century when $[Fe^{II}(TPA)(NCCH_3)]^{2+}$ (TPA = tris(2-pyridylmethyl)amine) have been shown to react with H_2O_2 to form low-spin Fe^{III}–OOH intermediate, (Table 1.1).[46] Evidence suggested that the Fe^{III}–OOH intermediate underwent a heterolytic O–O bond cleavage to afford an unobserved Fe^{IV}=O responsible for stereospecific alkane hydroxylation.[60]

Since then, the bioinorganic field saw a surge of reports of structurally and spectroscopically characterized synthetic high-valent Fe^{IV}=O complexes, (Table 1.1). Several high-fidelity ligand frameworks and their derivatives capable of supporting an Fe^{IV}=O unit yielded a wealth of spectroscopic, electronic, and structural trends. Some of the more prominent systems include, but not limited to, TMC (TMC = 1,4,8,11-tetramethyl-1,4,-8,11-tetraaza cyclotetradecane), TPEN (TPEN = N,N,N′,N′-tetrakis(2-pyridinylmethyl)-1,2-ethanediamine), TPA (TPA = tris(2-pyridylmethyl)amine), TMG_3tren (TMG_3tren = 1,1,1-tris{2-[N2 -(1,1,3,3-tetramethylguanidino)]ethyl}amine), and N4Py (N4Py = *N*,*N*-bis(2-pyridyl- methyl)-*N*-bis(2-

pyridyl)methylamine). The majority of spectroscopically characterized Fe^{IV}=O complexes exhibit a weak (ε = 200 – 500 M^{-1} cm^{-1}) electronic absorption band in the near-IR (750 – 850 nm) region due to d–d transitions. Biological non-heme Fe^{IV}=O intermediates have been usually identified to be in a high S = 2 spin-state. In contrast, a predominant number of synthetic Fe^{IV}=O complexes reported have been characterized to be in the intermediate S = 1 spin-state, likely due to relatively strong-field ligands employed (tertiary amines, imines, pyridines) in a pseudo-octahedral geometry. In principle, S = 2 state may be achieved if the d_{xy} and d_{x2-y2} orbitals are sufficiently close in energy to overcome the spin-pairing energy at the d_{xy} orbital. Utilization of bulky ligands to enforce trigonal-bipyramidal geometry about the Fe center or by weakening the equatorial ligand field through steric bulk in the pseudo-octahedral geometry have been successful strategies to stabilize S = 2 ground state. Typical Fe–O bond length falls in the 1.62 – 1.70 Å range and the ν_{Fe-O} stretch usually lies in the 800 – 850 cm^{-1} region. Both metrics are interrelated and inform the extent of the Fe-O bond strength. Badger's rule, an empirical formula that relates bond distance and vibrational frequency via $r \propto 1/\nu^{2/3}$ relation, has been used to predict and validate Fe–O bond distance against its vibrational frequency.[61]

In 2005, Larry Que and coworkers reported the first spectroscopically characterized synthetic non-heme thiolate-ligated complex, $[Fe^{IV}(O)\ (TMCS)]^{+}$ (TMCS = 1-mercaptoethyl-4,8,11-trimethyl-1,4,8,11-tetraaza cyclotetradecane). Structural data obtained from EXAFS reveals an Fe–O bond length of 1.70(2) Å and an Fe–S bond length of 2.33(2) Å.[62] Thiolate incorporation into the TMC framework has a dramatic effect on the reactivity of Fe^{IV}=O unit. Unlike the analogous acetonitrile-bound $[Fe^{IV}(O)(TMC)(NCCH_3)]^{2+}$ that performs oxygen-atom transfer to PPh_3 (triphenylphosphine),[63] $[Fe^{IV}(O)\ (TMCS)]^{+}$ abstracts hydrogen atoms from

substrates like DHA (dihydroanthracene). Ligation of a π-donating thiolate ligand *trans* to an Fe^{IV}=O unit is proposed to increase its nucleophilicity and thus alter its reactivity.

Table 1.2. Structural and spectroscopic data of selected biological and synthetic heme and non-heme Fe^{IV}=O complexes.

Complex	*S*	λ_{max} (nm), ε (M^{-1} cm^{-1})	Fe–O (Å)	ν_{Fe-O} (cm^{-1})	Ref.
Biological Fe^{IV}=O intermediates					
CYP450 Compound I	1	–	1.670	–	53
CPO Compound I	1	689 (11700)	1.661	790	52,64,65
TauD	2	318 (1500)	1.62	821	58,59
Synthetic Fe^{III}-O intermediates					
$[Fe^{III}(O)(H_3buea)]^{2-}$	5/2	–	1.813(3)	671	66
Synthetic Fe^{IV}=O intermediates					
$[Fe^{IV}(O)(TMC)(NCCH_3)]^{2+}$	1	824 (400)	1.646	839	63
$[Fe^{IV}(O)(TMC)(NCS)]^{+}$	1	850 (200)	1.65	820	67
$[Fe^{IV}(O)(TMCS)]^{+}$	1	850 (250)	1.70(2)	–	62
$[Fe^{IV}(O)(15\text{-cyclam})]^{2+}$	1	750 (500)	–	841	68
$[Fe^{IV}(O)(N4Py)]^{+}$	1	695 (400)	1.639	824	69
$[Fe^{IV}(O)(TPEN)]^{+}$	1	730 (380)	–	818	70
$[Fe^{IV}(O)(TPA)(NCCH_3)]^{2+}$	1	724 (300)	1.67	–	71
$[Fe^{IV}(O)(H_2O)_5]^{2+}$	2	~ 320 (~ 500)	–	–	72
$[Fe^{IV}(O)(TMG_3tren)]^{2+}$	2	825 (260)	1.661	843	73
$[Fe^{IV}(O)(H_3buea)]^{1-}$	2	808 (280)	1.680(1)	799	66
$[Fe^{IV}(O)(tpa^{Ph})]^{1-}$	2	~ 900 (–)	1.62	850	74
Synthetic Fe^{V}=O intermediates					
$[Fe^{V}(O)(TAML)]^{1-}$	1/2	445 (5400), 630 (4200)	1.58	–	75

1.4 Dioxygen Bond Formation by Manganese Metalloenzymes – The Oxygen Evolving Complex

Manganese (Mn) is the thirteenth most abundant element in the Earth's crust and the third most abundant transition element after iron and titanium. Mn is almost exclusively found as oxides (e. g. MnO_2, Mn_3O_4, $Mn_2O_3 \cdot H_2O$, $MnSiO_3$, and $MnCO_3$). It occurs as the Mn^{II} aqua ion, $Mn(H_2O)_6^{2+}$, at a concentration of approximately 10^{-4} ppm. In minerals, Mn is most commonly found in +2 oxidation state.[76] Its inherent stability arises from the half-filled $3d^5$ high-spin (S = 5/2) electron configuration due to maximal exchange energy. The lack of ligand-field stabilization in high-spin Mn^{II} complexes results in rapid ligand exchange. As a consequence, Mn preferentially coordinates hard ligand donors such as oxygen and nitrogen. While Mn tends to stay in +2 oxidation state, ligands that favor higher oxidation states can stabilize Mn^{III}, Mn^{IV}, and Mn^{V}. The stabilizing exchange energy makes it difficult to remove fifth d-electron, making Mn^{III} complexes particularly strong oxidizing agents ($E°$ = 1.51 V, pH = 0). Mn^{IV} complexes are most commonly found with bridging or terminal oxo-ligands, or as polynuclear Mn-O clusters.[76] Although the least stable, especially under acidic conditions, Mn^{V} compounds can be synthesized as manganates ($Mn^{V}O_4^{3-}$) or synthetic models (*vide infra*). Therefore, Mn ion is capable of performing multielectron oxidation chemistry as it can access II, III, IV, and V oxidation states under physiological conditions. As a result, Nature has chosen manganese to perform what is arguably the most important reaction on Earth – photosynthetic oxidation of water and evolution of molecular dioxygen.

1.4.1 *Photosynthesis and the Oxygen-Evolving Complex Structure*

Photosynthesis is one of the most important biochemical processes that maintains the life cycle on our planet.[77–79] This process involves the catalytic oxidation of water to provide electrons for the reduction of carbon dioxide to form simple sugars and generate dioxygen as a byproduct.[79,80] The oxidation of water to molecular oxygen takes place in the protein complex photosystem II (PS II).[81] The multi-step reaction is metal-catalyzed, involving the oxo-bridged Mn cluster Mn_4CaO_5, which is referred to as the oxygen-evolving complex (OEC).[82] Water oxidation is a challenging process because the reaction is uphill thermodynamically, (ΔG = + 320 kJ mol^{-1}), (Eq. 1.1).[83] The second challenge lies in the high complexity of the reaction mechanism from a mechanistic point of view as electrons and protons (or H-atoms) must be removed from water prior to the formation of an oxygen-oxygen bond.[84]

$$2H_2O \rightarrow O_2 + 4H^+ + 4e^- \quad (1.1)$$

Both the structure of the OEC and the catalytic mechanism of water oxidation have been a subject of intense scrutiny for the past sixty years. X-ray Diffraction (XRD) have been instrumental in determining the molecular structure of OEC at the resolution of 1.9 Å in the past decade.[85] Radiation damage due to long exposure of X-rays, however, leads to Mn reduction and elongation of Mn–Mn bonds. This is evidenced by the concomitant interpretation of EXAFS and X-ray absorption near edge structure (XANES),[86,87] and quantum mechanics/molecular mechanics (QM/MM) calculation experiments.[88,89] The geometric structure of the OEC is shown in Figure 1.5. The OEC is a cuboidal Mn_4CaO_5 cluster with three Mn and a Ca^{II} ion ligated by four oxo-bridges and supported by the sidechains of the surrounding amino-acid residues. The fourth "dangling" Mn ion is connected to the cubane via *bis*-μ-oxo bridge. Despite the significant

breakthroughs, due to limitations of the preparation of the system in well-defined oxidation states and ambiguity in interpretation of experimental data, the consensus on the model of the OEC is yet to be reached.

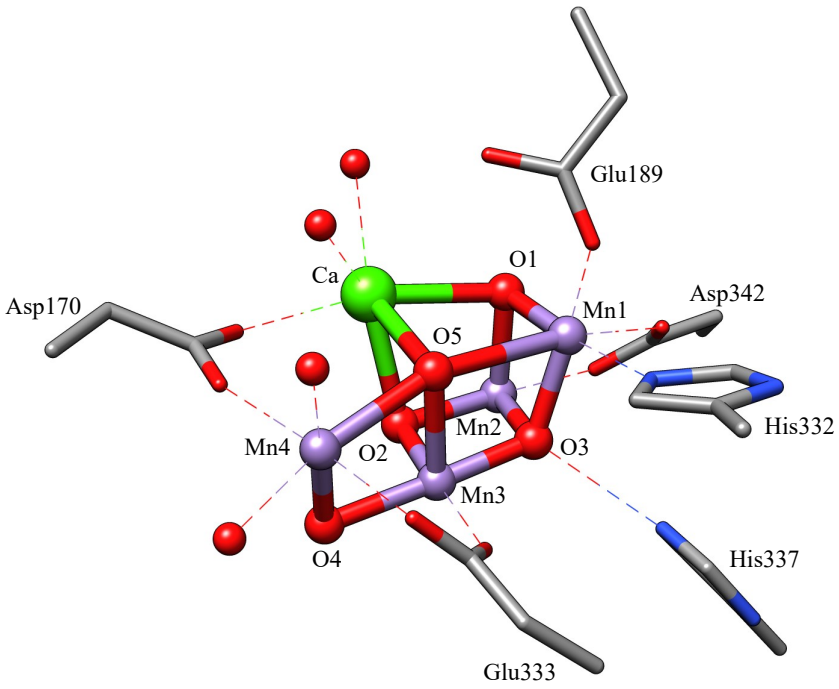

Figure 1.5. Crystal structure of active site of the OEC of photosystem II at the resolution of 1.9 Å from *Thermosynechococcus vulcanus*, PDB 3WU2.[85]

1.4.2 *The Kok Cycle*

Seminal work by Pierre Joliot and Bessel Kok have established the underlying reaction mechanism of the oxidative water splitting during the photosynthesis.[90,91] In the "Kok cycle" model, light absorption drives four-electron oxidation of water within the five sequential oxidation steps of the OEC termed S_0 through S_4. The Kok cycle is summarized in Figure 1.6 below. Single-photon driven oxidation leads the first transition from S_0 to the dark-stable S_1 state. X-ray free electron laser (XFEL) technology has been instrumental in determining the structural details of the cubane during the S_1 state. XFEL allows for data collection on a femtosecond timescale before a

sample gets damaged and modified by the incident radiation. 1.95 Å XFEL structure revealed shorter Mn–Mn bond distances than those in the 1.9 Å XRD structure. Unfortunately, structural disorder persisted in the 1.95 Å XFEL structure due to presence of a mixture of the S_0 state as well as from damaging hydroxyl radicals generated by the radiation.[92]

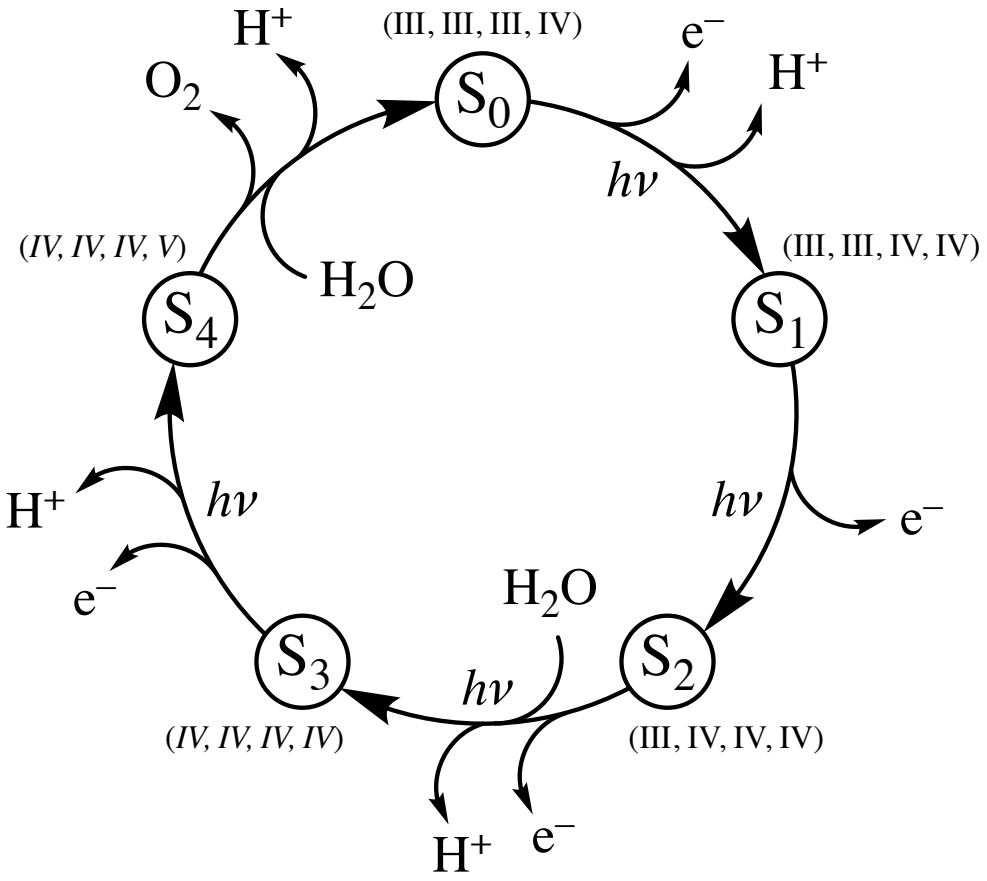

Figure 1.6. Kok cycle depicting the reaction mechanism of the light-driven water oxidation in photosystem II. Mn oxidation states at each state are indicated in the parentheses.

The $S_1 \rightarrow S_2$ transition is the only step that does not involve proton transfer. Structural changes in this step arise from one-electron oxidation process alone and are thus difficult to detect. The OEC in the S_2 state exists in two spin $S = 1/2$ and $S = 5/2$ state isomers, as confirmed by the EPR experiments.[93,94] The $S_2 \rightarrow S_3$ transition is one of the most crucial and interesting steps in the Kok cycle because S_3 is the last stable state that can be trapped and studied en route to the

unobserved S_4 state. Significant structural changes occur in this step due to binding of an additional water molecule to the cubane, resulting in its expansion. Both the "opened" conformer, in which the position of O(5) is closer to dangling Mn(4), and the "closed" conformer, where O(5) is closer to Mn(4), have been proposed in the S_3 state.[95,96] The "opened" conformed is suggested to be much more stable and is consistent with EXAFS measurements and QM/MM calculations.[97] Both the $S_3 \rightarrow S_4$ and the $S_4 \rightarrow S_0$ transition steps are poorly understood since no direct experimental observation of the S_4 state has yet been achieved. The overall $S_3 \rightarrow S_0$ transition is accompanied by the cubane compression, in spite of the change from most oxidized to most reduced state, and reversal to a structure that is more similar to an open-like S_1 and S_2 state.[98]

The nature of O–O bond formation and O_2 evolution in the elusive $S_4 \rightarrow S_0$ transition step is not well understood as it follows the rate determining step.[99] Two mechanisms for the formation of O–O have been proposed, however, based on extensive computational and biomimetic studies. These are a coupling reaction of two Mn^{IV}-oxyl radicals and nucleophilic attack of a calcium-bound water (or hydroxyl) on the electrophilic oxygen atom of high-valent $Mn^{V}\equiv O$, (Figure 1.7). Mn^{IV}-oxyl radical coupling mechanism is suggested by the computation work done by Siegbahn,[100] while nucleophilic water attack is best supported through studies of synthetic ruthenium-based water oxidation catalysts.[101]

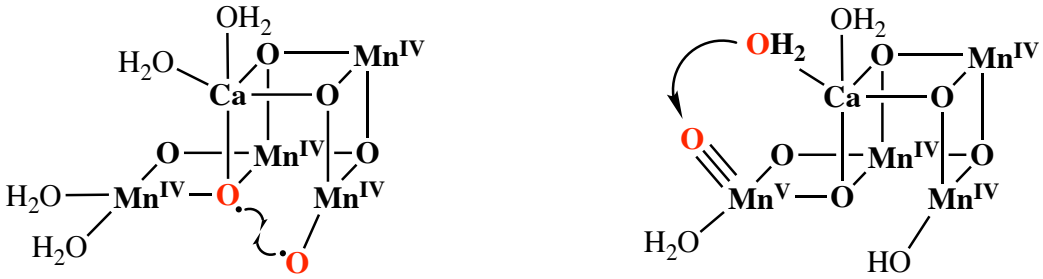

Figure 1.7. Proposed mechanisms of O–O bond formation step involving either Mn^{IV}-oxyl radical coupling (left) Ca^{II}–OH_2 nucleophilic attack on $Mn^{V}\equiv O$ (right).

Calcium ion is essential to the function of the OEC. While its exact function is not well understood, recent discoveries point its fundamental catalytic role. Lewis acidic Ca^{II} ion have been proposed to control water substrate binding and to direct nucleophilic water attack on $Mn^{V}{\equiv}O$. Polarized Mn K-edge XANES and EXAFS experiments on Ca^{II} ion depleted OEC have shown to have minimal effect on the structural integrity of the cubane.[102] Ca^{II} removal from the OEC, however, results in complete inhibition of O_2 evolution, but which can be reactivated by reconstituting Ca^{II} back. Replacement of Ca^{II} by a less Lewis acidic Sr^{II} also reactivates the catalytic function of the cubane, although resulting in a significantly decreased O_2 production.[103,104]

1.4.3 *Synthetic Models*

Synthetic modeling approach have been instrumental in interpretation of available spectroscopic data and elucidating details about the electronic structure of the OEC. Detailed structural, spectroscopic, and mechanistic characterization of synthetic Mn complexes designed to mimic structural motifs of the OEC during its various stages of the catalytic process have offer insights into the mechanism of the OEC mediated O_2 evolution. Synthetic models of the OEC can be broadly divided into *functional* and *structural* analogues. Functional analogues are molecular catalysts capable of oxidizing water to O_2 and may involve transition metals other than Mn that is employed by the OEC. Structural analogues mimic aspects of the OEC cubane itself with the goal to elucidating key geometric and electronic structural details.

In 1985, Thomas Meyer and coworkers pioneered the field of water oxidation catalysis by reporting the synthesis and characterization of the ruthenium complex capable of oxidizing water to O_2. Unlike the first-row transition metals, second row transition metals, such as ruthenium, are

larger in size, they contain spacious and diffuse 4d orbitals that lowers the electron-electron pairing energy, resulting in a low-spin configuration. The dinuclear ruthenium complex, {*cis,cis*-$[Ru^{III}(bpy)_2(H_2O)]_2(\mu\text{-}O)]^{4+}$}, (bpy = 2,2'-bipyridine), became known as the "blue dimer" because of its characteristic intense blue color ($\lambda_{max}(\varepsilon)$ = 637 nm (21,100 M^{-1} cm^{-1}); pH = 1.0).[105] Subsequent detailed mechanistic investigations laid out a proposed mechanism whereby a nucleophilic water attach on Ru_1^{V}=O is coupled by the concomitant H^+/e^- transfer to Ru_2^{V}=O.[106] In 2008, Meyer's group reported examples of mononuclear Ru catalysts, $[Ru^{II}(tpy)(bpm)(OH_2)]^{2+}$ and $[Ru^{II}(tpy)(bpz)(OH_2)]^{2+}$ (tpy = 2,2′:6′,2″-terpyridine; bpm = 2,2′-bipyrimidine; bpz = 2,2′-bipyrazine).[107] Kinetic investigations suggest that the O–O bond formation occurs via water nucleophilic attack on a highly electrophilic Ru^{V}=O intermediate to generate Ru^{III}–OOH.[107,108] Together with other successfully designed Ru complexes capable of water oxidation, these examples put forward nucleophilic water attack on Mn^{V}≡O as the possible mechanism O–O bond formation step in the OEC itself. Notwithstanding, a few examples of Ru complexes that undergo intramolecular O–O bond formation through oxyl coupling have also been reported. These include a dinuclear $\{[Ru^{II}(trpy)(H_2O)]_2(\mu\text{-bpp})\}^{3+}$ (trpy = tpy; bpp = 2,6-bis(pyridyl)pyrazolate) complex has been studied mechanistically in considerable detail,[109] and $\{[Ru^{II}(OH)(3,6\text{-}t\text{Bu}_2\text{qui})]_2(\mu\text{-btpyan})\}^{2+}$ (3,6-^{t}Bu$_2$qui = 3,6-di-*tert*-butyl-1,2-benzoquinone; btpyan = 1,8-bis(2,2′:6′,2″-terpyridyl)-anthracene) complex that contains a redox active quinone ligand.[110]

Recent efforts have been diverted to exploring the role and mechanism of first-row transition metals in O–O bond formation due to relevance of Nature's choice (the OEC) as well as affordability. Notable examples include a mononuclear $[Mn(Py_2N^tBu_2)(H_2O)_2]^{2+}$ complex, which is proposed to form a side-on η^2-peroxo bond intramolecularly via Mn^{III}-$(oxyl)_2$ radical coupling.[111] In contrast, Wonwoo Nam has reported a porphyrin-supported mononuclear

[Mn^{III}(TFMPC)] (TFMPC = 5,10,15-tris(3,5-trifluoromethylphenyl)corrolato trianion) complex capable of reversible O–O bond formation achieved through nucleophilic OH^- attack on high-valent Mn^{V}≡O corrole.[112] Cobalt-based catalysts have also been shown to be an attractive alternative, as there are examples of Kojima's catalyst such as $[Co_2(\mu\text{-}OH)_2(TPA)_2](ClO_4)_4$ that is capable of oxidizing water photocatalytically, and forming an O–O bond via oxyl-radical coupling reaction.[113] Recent work by Nocera and coworkers on a much acclaimed Co_4O_4 cubane contains a reactive high-valent Co^{IV}-oxo dimer which is involved in the O–O bond formation event via Co^{III}-oxyl coupling as well.[114] These examples demonstrate that O–O bond formation is initiated by the generation of high-valent metal-oxo intermediates. Regardless of the transition metal ion involved, both water/hydroxo nucleophilic attack on the metal-oxo or metal-oxyl radical coupling mechanisms are supported experimentally.

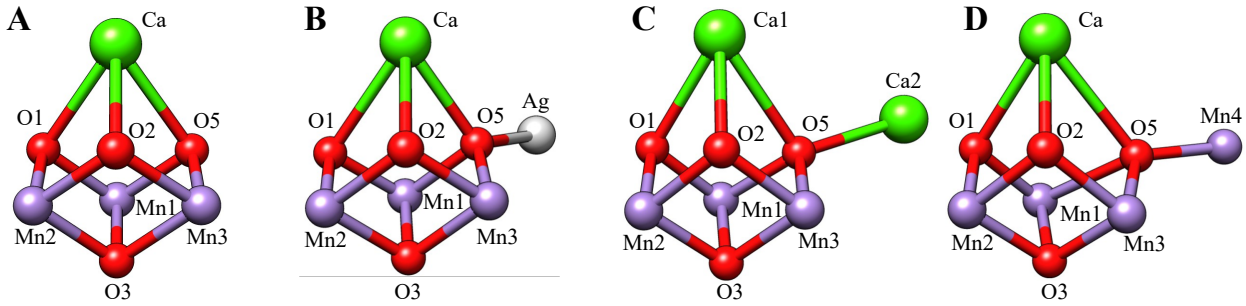

Figure 1.8. Crystal structures of synthetic complexes containing [Mn_3CaO_4] core. (**A**) [Mn_3CaO_4] core structure. (**B**) [Mn_3CaAgO_4] core structure with dangling Ag. (**C**) [$Mn_3Ca_2O_4$] core structure with dangling Ca. (**D**) [Mn_4CaO_4] core structure with dangling Mn.

A few OEC structural analogues have recently emerged in the literature as well. The first breakthrough came in 2011 when Theodor Agapie and coworkers reported the first artificial Mn_3CaO_4 cubane cluster, (Figure 1.8 A). Their synthetic strategy involved utilization of a rigid trinucleating 1,3,5-triarylbenzene spacer ligand with six pyridines and three alcohol groups (**H_3L**). Reaction of **H_3L** with three equivalents of $Mn(OAc)_2$ (OAc = acetate), followed by the treatment with two equivalents of potassium superoxide and $Ca(OTf)_2$ (OTf = trifluoromethanesulfonate), resulted in formation of a cluster with $[Mn_3CaO_4]^{6+}$ core.[115] The same group later structurally characterized an artificial Mn_3CaAgO_4 cubane with a "dangling" Ag ion as a more accurate structural model of the OEC, (Figure 1.8 B).[116] George Christou and coworkers also reported the structure with an asymmetric Mn_3CaO_4 core with an additional Ca ion attached to the cubane, (Figure 1.8 C).[117] And lastly, another milestone was achieved when Jingquan Zhao group structurally and spectroscopically characterized a synthetic Mn_3CaO_4 cubane cluster with a dangling Mn ion, making it by far the most accurate structural model of the OEC, (Figure 1.8 D).[118]

1.5 Concluding Remarks

This introductory chapter provides a brief overview of the biological inorganic chemistry of iron-catalyzed O_2 bond activation within a superfamily of Cytochrome P450 enzymes and manganese-catalyzed O–O bond formation within the OEC cubane of the PS II. These two fundamental chemical transformations are interrelated inasmuch as they are two opposing facets of the same biochemical event – making and breaking an O–O bond. What is more, transition metals are at the center of these two interlinked reactions. Indeed, their unique chemical properties,

afforded by the partially filled d-orbitals, allowed Nature to find elegant solutions of promoting H_2O oxidation in photosynthesis, and O_2 reduction in Cytochrome P450 catalysis.

The biomimetic inorganic field has made tremendous strides in understanding and elucidating how first-row transition metals promote these life-sustaining reactions. The biomimetic modeling approach will undoubtedly shed more light on the questions that still remain unanswered. While we've developed much appreciation for the role that cysteine thiolate plays in binding and promoting Fe-catalyzed O_2 activation, it is unclear how efficiently can thiolate promote this reaction *without* a conjugated porphyrin ring. The importance of the coordination of the thiolate relative to the open coordination site, whether it is *trans* or *cis*, is another question that worth exploring. As for the O–O bond formation reaction during the photosynthesis, even though significant progress in unraveling structural details of the OEC and the mechanism of biological H_2O oxidation been achieved in the past few decades, some fundamental questions remain. The elusive nature of the final step of O–O bond formation and the functional role of Ca^{II} ion are two pressing topics of research.

1.6 References

(1) Berman, H. M.; Battistuz, T.; Bhat, T. N.; Bluhm, W. F.; Bourne, P. E.; Burkhardt, K.; Feng, Z.; Gilliland, G. L.; Iype, L.; Jain, S.; Fagan, P.; Marvin, J.; Padilla, D.; Ravichandran, V.; Schneider, B.; Thanki, N.; Weissig, H.; Westbrook, J. D.; Zardecki, C. *Acta Crystallogr. Sect. D Biol. Crystallogr.* **2002**, *58* (6), 899–907.

(2) Maret, W. *Int. J. Mol. Sci.* **2016**, *17* (1), 66.

(3) Holm, R. H.; Kennepohl, P.; Solomon, E. I. *Chem. Rev.* **1996**, *96* (7), 2239–2314.

(4) Mulliken, R. S. *Nature* **1928**, *122*, 505.

(5) Mulliken, R. S. *Rev. Mod. Phys.* **1932**, *4* (1), 1–86.

(6) Foote, C. S. *Acc. Chem. Res.* **1968**, *1* (4), 104–110.

(7) Hamilton, G. A.; Hayaishi, O. In *Molecular Mechanisms of Oxygen Activation*; Academic Press: New York, 1974; pp 405–448.

(8) Clennan, E. L.; Pace, A. *Tetrahedron* **2005**, *61* (28), 6665–6691.

(9) Ogilby, P. R. *Chem. Soc. Rev.* **2010**, *39* (8), 3181.

(10) Sawyer, D. T.; Valentine, J. S. *Acc. Chem. Res.* **1981**, *14* (12), 393–400.

(11) Wiberg, E.; Wiberg, N.; Holleman, A. In *Inorganic Chemistry*; San Diego: Academic Press, 2001; pp 1430–1458.

(12) Hayaishi, O.; Katagiri, M.; Rothberg, S. *J. Am. Chem. Soc.* **1955**, *77* (20), 5450–5451.

(13) Tchen, T. T.; Bloch, K. *J. Am. Chem. Soc.* **1956**, *78* (7), 1516–1517.

(14) Hamberg, M.; Samuelsson, B. *J. Biol. Chem.* **1967**, *242* (22), 5336–5343.

(15) Hamberg, M.; Samuelsson, B. *Proc. Natl. Acad. Sci. U. S. A.* **1973**, *70* (3), 899–903.

(16) Smith, W. L.; Marnett, L. J. *Biochim. Biophys. Acta - Lipids Lipid Metab.* **1991**, *1083* (1), 1–17.

(17) Koehntop, K. D.; Emerson, J. P.; Que, L. *JBIC J. Biol. Inorg. Chem.* **2005**, *10* (2), 87–93.

(18) Bruijnincx, P. C. A.; van Koten, G.; Klein Gebbink, R. J. M. *Chem. Soc. Rev.* **2008**, *37* (12), 2716.

(19) Hegg, E. L.; Que, L. *Eur. J. Biochem.* **1997**, *250* (3), 625–629.

(20) Broderick, J. B. In *Comprehensive coordination chemistry II: from biology to nanotechnology*; Constable, E., McCleverty, J. A., Meyer, T. J., Eds.; Elsevier Pergamon: Oxford, UK; San Diego, USA, 2004; pp 739–757.

(21) Kennepohl, P.; Neese, F.; Schweltzer, D.; Jackson, H. L.; Kovacs, J. A.; Solomon, E. I.

Inorg. Chem. **2005**, *44* (6), 1826–1836.

(22) Luo, Y.-R. *Comprehensive Handbook of Chemical Bond Energies*; CRC Press, 2007.

(23) Williams, P. A. *Science* **2004**, *305* (5684), 683–686.

(24) Denisov, I. G.; Makris, T. M.; Sligar, S. G.; Schlichting, I. *Chemical Reviews*. 2005, pp 2253–2277.

(25) Hanson, L. K.; Chang, C. K.; Davis, M. S.; Fajer, J. *J. Am. Chem. Soc.* **1981**, *103* (3), 663–670.

(26) Czarnecki, K.; Proniewicz, L. M.; Fujii, H.; Kincaid, J. R. *J. Am. Chem. Soc.* **1996**, *118* (19), 4680–4685.

(27) Lipscomb, J. D. *Biochemistry* **1980**, *19* (15), 3590–3599.

(28) Loew, G.; Collins, J.; Chantranupong, L.; Waleh, A. *Int. J. Quantum Chem.* **1987**, *32* (S14), 75–83.

(29) Lawson, R. J.; Leys, D.; Sutcliffe, M. J.; Kemp, C. A.; Cheesman, M. R.; Smith, S. J.; Clarkson, J.; Smith, W. E.; Haq, I.; Perkins, J. B.; Munro, A. W. *Biochemistry* **2004**, *43* (39), 12410–12426.

(30) Fasman, G. D. *Handbook of Biochemistry and Molecular Biology*, 3rd ed.; CRC Press: Cleveland, Ohio, 1976.

(31) Sharrock, M.; Debrunner, P. G.; Schulz, C.; Lipscomb, J. D.; Marshall, V.; Gunsalus, I. C. *Biochim. Biophys. Acta - Protein Struct.* **1976**, *420* (1), 8–26.

(32) Hu, S.; Schneider, A. J.; Kincaid, J. R. *J. Am. Chem. Soc.* **1991**, *113* (13), 4815–4822.

(33) Schlichting, I.; Berendzen, J.; Chu, K.; Stock, A. M.; Maves, S. A.; Benson, D. E.; Sweet, R. M.; Ringe, D.; Petsko, G. A.; Sligar, S. G. *Science* **2000**, *287* (5458), 1615–1622.

(34) Davydov, R.; Kappl, R.; Hüttermann, J.; Peterson, J. A. *FEBS Lett.* **1991**, *295* (1–3), 113–

115.

(35) Green, M. T. *J. Am. Chem. Soc.* **1999**, *121* (34), 7939–7940.

(36) Green, M. T.; Dawson, J. H.; Gray, H. B. *Science* **2004**, *304* (5677), 1653–1656.

(37) Kao, O. H. W.; Wang, J. H. *Biochemistry* **1965**, *4* (2), 342–347.

(38) Chin, D.-H.; La Mar, G. N.; Balch, A. L. *J. Am. Chem. Soc.* **1980**, *102* (18), 5945–5947.

(39) Chin, D.-H.; La Mar, G. N.; Balch, A. L. *J. Am. Chem. Soc.* **1980**, *102* (13), 4344–4350.

(40) Balch, A. L.; Chan, Y. W.; Cheng, R. J.; La Mar, G. N.; Latos-Grazynski, L.; Renner, M. W. *J. Am. Chem. Soc.* **1984**, *106* (25), 7779–7785.

(41) Groves, J. T.; Nemo, T. E.; Myers, R. S. *J. Am. Chem. Soc.* **1979**, *101* (4), 1032–1033.

(42) Liu, J. G.; Ohta, T.; Yamaguchi, S.; Ogura, T.; Sakamoto, S.; Maeda, Y.; Naruta, Y. *Angew. Chemie - Int. Ed.* **2009**, *48* (49), 9262–9267.

(43) Liu, J. G.; Shimizu, Y.; Ohta, T.; Naruta, Y. *J. Am. Chem. Soc.* **2010**, *132* (11), 3672–3673.

(44) Denisov, I. G.; Mak, P. J.; Makris, T. M.; Sligar, S. G.; Kincaid, J. R. *J. Phys. Chem. A* **2008**, *112* (50), 13172–13179.

(45) Roelfes, G.; Vrajmasu, V.; Chen, K.; Ho, R. Y. N.; Rohde, J. U.; Zondervan, C.; La Crois, R. M.; Schudde, E. P.; Lutz, M.; Spek, A. L.; Hage, R.; Feringa, B. L.; Munck, E.; Que, L. *Inorg. Chem.* **2003**, *42* (8), 2639–2653.

(46) Ho, R. Y. N.; Roelfes, G.; Feringa, B. L.; Que, L. *J. Am. Chem. Soc.* **1999**, *121* (1), 264–265.

(47) Shearer, J.; Scarrow, R. C.; Kovacs, J. A. *J. Am. Chem. Soc.* **2002**, *124* (39), 11709–11717.

(48) Ahmad, S.; McCallum, J. D.; Shiemke, A. K.; Loehr, T. M.; Sanders-Loehr, J.; Appelman,

E. H. *Inorg. Chem.* **1988**, *27* (13), 2230–2233.

(49) Wada, A.; Ogo, S.; Nagatomo, S.; Kitagawa, T.; Watanabe, Y.; Jitsukawa, K.; Masuda, H. *Inorg. Chem.* **2002**, *41* (4), 616–618.

(50) Kitagawa, T.; Dey, A.; Lugo-Mas, P.; Benedict, J. B.; Kaminsky, W.; Solomon, E.; Kovacs, J. A. *J. Am. Chem. Soc.* **2006**, *128* (45), 14448–14449.

(51) van Rantwijk, F.; Sheldon, R. A. *Curr. Opin. Biotechnol.* **2000**, *11* (6), 554–564.

(52) Stone, K. L.; Behan, R. K.; Green, M. T. *Proc. Natl. Acad. Sci. U. S. A.* **2005**, *102* (46), 16563–16565.

(53) Krest, C. M.; Silakov, A.; Rittle, J.; Yosca, T. H.; Onderko, E. L.; Calixto, J. C.; Green, M. T. *Nat. Chem.* **2015**, *7* (9), 696–702.

(54) Roach, P. L.; Clifton, I. J.; Hensgens, C. M. H.; Shibata, N.; Schofield, C. J.; Hajdu, J.; Baldwin, J. E. *Nature* **1997**, *387* (6635), 827–830.

(55) McDonald, A. R.; Que, L. *Nat. Chem.* **2011**, *3* (10), 761–762.

(56) Shu, L. *Science* **1997**, *275* (5299), 515–518.

(57) Banerjee, R.; Proshlyakov, Y.; Lipscomb, J. D.; Proshlyakov, D. A. *Nature* **2015**, *518* (7539), 431–434.

(58) Price, J. C.; Barr, E. W.; Tirupati, B.; Bollinger, J. M.; Krebs, C. *Biochemistry* **2003**, *42* (24), 7497–7508.

(59) Riggs-Gelasco, P. J.; Price, J. C.; Guyer, R. B.; Brehm, J. H.; Barr, E. W.; Bollinger, J. M.; Krebs, C. *J. Am. Chem. Soc.* **2004**, *126* (26), 8108–8109.

(60) Chen, K.; Costas, M.; Kim, J.; Tipton, A. K.; Que, L. *J. Am. Chem. Soc.* **2002**, *124* (12), 3026–3035.

(61) Green, M. T. *J. Am. Chem. Soc.* **2006**, *128* (6), 1902–1906.

(62) Bukowski, M. R. *Science* **2005**, *310* (5750), 1000–1002.

(63) Rohde, J.-U.; In, J.-H.; Lim, M. H.; Brennessel, W. W.; Bukowski, M. R.; Stubna, A.; Münck, E.; Nam, W.; Que Jr., L. *Science* **2003**, *299* (5609), 1037–1039.

(64) Schulz, C. E.; Rutter, R.; Sage, J. T.; Debrunner, P. G.; Hager, L. P. *Biochemistry* **1984**, *23* (20), 4743–4754.

(65) Palcic, M. M.; Rutter, R.; Araiso, T.; Hager, L. P.; Dunford, H. B. *Biochem. Biophys. Res. Commun.* **1980**, *94* (4), 1123–1127.

(66) Lacy, D. C.; Gupta, R.; Stone, K. L.; Greaves, J.; Ziller, J. W.; Hendrich, M. P.; Borovik, A. S. *J. Am. Chem. Soc.* **2010**, *132* (35), 12188–12190.

(67) Jackson, T. A.; Rohde, J. U.; Mi, S. S.; Sastri, C. V.; DeHont, R.; Stubna, A.; Ohta, T.; Kitagawa, T.; Münck, E.; Nam, W.; Que, L. *J. Am. Chem. Soc.* **2008**, *130* (37), 12394–12407.

(68) Suh, Y.; Seo, M. S.; Kim, K. M.; Kim, Y. S.; Jang, H. G.; Tosha, T.; Kitagawa, T.; Kim, J.; Nam, W. *J. Inorg. Biochem.* **2006**, *100* (4), 627–633.

(69) Kaizer, J.; Klinker, E. J.; Oh, N. Y.; Rohde, J. U.; Song, W. J.; Stubna, A.; Kim, J.; Münck, E.; Nam, W.; Que, L. *J. Am. Chem. Soc.* **2004**, *126* (2), 472–473.

(70) Martinho, M.; Banse, F.; Bartoli, J.-F.; Mattioli, T. A.; Battioni, P.; Horner, O.; Bourcier, S.; Girerd, J.-J. *Inorg. Chem.* **2005**, *44* (25), 9592–9596.

(71) Lim, M. H.; Rohde, J.-U.; Stubna, A.; Bukowski, M. R.; Costas, M.; Ho, R. Y. N.; Munck, E.; Nam, W.; Que, L. *Proc. Natl. Acad. Sci. U. S. A.* **2003**, *100* (7), 3665–3670.

(72) Pestovsky, O.; Stoian, S.; Bominaar, E. L.; Shan, X.; Münck, E.; Que, L.; Bakac, A. *Angew. Chemie Int. Ed.* **2005**, *44* (42), 6871–6874.

(73) England, J.; Martinho, M.; Farquhar, E. R.; Frisch, J. R.; Bominaar, E. L.; Münck, E.;

Que, L. *Angew. Chemie Int. Ed.* **2009**, *48* (20), 3622–3626.

(74) Bigi, J. P.; Harman, W. H.; Lassalle-Kaiser, B.; Robles, D. M.; Stich, T. A.; Yano, J.; Britt, R. D.; Chang, C. J. *J. Am. Chem. Soc.* **2012**, *134* (3), 1536–1542.

(75) de Oliveira, F. T.; Chanda, A.; Banerjee, D.; Shan, X.; Mondal, S.; Que, L.; Bominaar, E. L.; Munck, E.; Collins, T. J. *Science* **2007**, *315* (5813), 835–838.

(76) Wiberg, E.; Wiberg, N.; Holleman, A. In *Inorganic Chemistry*; San Diego: Academic Press, 2001; pp 1405–1415.

(77) Leslie, M. *Science* **2009**, *323* (5919), 1286–1287.

(78) Des Marais, D. *Science* **2000**, *289* (5485), 1703–1705.

(79) Dismukes, G. C. *Science* **2001**, *292* (5516), 447–448.

(80) Cox, N.; Retegan, M.; Neese, F.; Pantazis, D. A.; Boussac, A.; Lubitz, W. *Science* **2014**, *345* (6198), 804–808.

(81) Deisenhofer, J.; Epp, O.; Miki, K.; Huber, R.; Michel, H. *Nature* **1985**, *318* (6047), 618–624.

(82) Cox, N.; Retegan, M.; Neese, F.; Pantazis, D. a.; Boussac, a.; Lubitz, W. *Science* **2014**, *345* (6198), 804–808.

(83) Armstrong, F. A. *Philos. Trans. R. Soc. B Biol. Sci.* **2008**, *363* (1494), 1263–1270.

(84) Yano, J.; Kern, J.; Sauer, K.; Latimer, M. J.; Pushkar, Y.; Biesiadka, J.; Loll, B.; Saenger, W.; Messinger, J.; Zouni, A.; Yachandra, V. K. *Science* **2006**, *314* (5800), 821–825.

(85) Umena, Y.; Kawakami, K.; Shen, J.-R.; Kamiya, N. *Nature* **2011**, *473* (7345), 55–60.

(86) Yano, J.; Kern, J.; Irrgang, K.-D.; Latimer, M. J.; Bergmann, U.; Glatzel, P.; Pushkar, Y.; Biesiadka, J.; Loll, B.; Sauer, K.; Messinger, J.; Zouni, A.; Yachandra, V. K. *Proc. Natl. Acad. Sci.* **2005**, *102* (34), 12047–12052.

(87) Grundmeier, A.; Dau, H. *Biochim. Biophys. Acta - Bioenerg.* **2012**, *1817* (1), 88–105.

(88) Pal, R.; Negre, C. F. A.; Vogt, L.; Pokhrel, R.; Ertem, M. Z.; Brudvig, G. W.; Batista, V. S. *Biochemistry* **2013**, *52* (44), 7703–7706.

(89) Luber, S.; Rivalta, I.; Umena, Y.; Kawakami, K.; Shen, J.-R.; Kamiya, N.; Brudvig, G. W.; Batista, V. S. *Biochemistry* **2011**, *50* (29), 6308–6311.

(90) Joliot, P.; Barbieri, G.; Chabaud, R. *Photochem. Photobiol.* **1969**, *10* (5), 309–329.

(91) Kok, B.; Forbush, B.; McGloin, M. *Photochem. Photobiol.* **1970**, *11* (6), 457–475.

(92) Suga, M.; Akita, F.; Hirata, K.; Ueno, G.; Murakami, H.; Nakajima, Y.; Shimizu, T.; Yamashita, K.; Yamamoto, M.; Ago, H.; Shen, J.-R. *Nature* **2015**, *517* (7532), 99–103.

(93) Dismukes, G. C.; Siderer, Y. *Proc. Natl. Acad. Sci.* **1981**, *78* (1), 274–278.

(94) Haddy, A.; Lakshmi, K. V.; Brudvig, G. W.; Frank, H. A. *Biophys. J.* **2004**, *87* (4), 2885–2896.

(95) Cox, N.; Retegan, M.; Neese, F.; Pantazis, D. A.; Boussac, A.; Lubitz, W. *Science* **2014**, *345* (6198), 804–808.

(96) Capone, M.; Bovi, D.; Narzi, D.; Guidoni, L. *Biochemistry* **2015**, *54* (42), 6439–6442.

(97) Askerka, M.; Wang, J.; Vinyard, D. J.; Brudvig, G. W.; Batista, V. S. *Biochemistry* **2016**, *55* (7), 981–984.

(98) Yano, J.; Yachandra, V. *Chem. Rev.* **2014**, *114* (8), 4175–4205.

(99) Vinyard, D. J.; Khan, S.; Brudvig, G. W. *Faraday Discuss.* **2015**, *185*, 37–50.

(100) Siegbahn, P. E. M. *Biochim. Biophys. Acta - Bioenerg.* **2013**, *1827* (8–9), 1003–1019.

(101) Romain, S.; Vigara, L.; Llobet, A. *Acc. Chem. Res.* **2009**, *42* (12), 1944–1953.

(102) Lohmiller, T.; Shelby, M. L.; Long, X.; Yachandra, V. K.; Yano, J. *J. Phys. Chem. B* **2015**, *119* (43), 13742–13754.

(103) Boussac, A.; Rutherford, A. W. *Biochemistry* **1988**, *27* (9), 3476–3483.

(104) Renger, G. *J. Photochem. Photobiol. B Biol.* **2011**, *104* (1–2), 35–43.

(105) Gilbert, J. A.; Eggleston, D. S.; Murphy, W. R.; Geselowitz, D. A.; Gersten, S. W.; Hodgson, D. J.; Meyer, T. J. *J. Am. Chem. Soc.* **1985**, *107* (13), 3855–3864.

(106) Liu, F.; Concepcion, J. J.; Jurss, J. W.; Cardolaccia, T.; Templeton, J. L.; Meyer, T. J. *Inorg. Chem.* **2008**, *47* (6), 1727–1752.

(107) Concepcion, J. J.; Jurss, J. W.; Templeton, J. L.; Meyer, T. J. *J. Am. Chem. Soc.* **2008**, *130* (49), 16462–16463.

(108) Binstead, R. A.; Chronister, C. W.; Ni, J.; Hartshorn, C. M.; Meyer, T. J. *J. Am. Chem. Soc.* **2000**, *122* (35), 8464–8473.

(109) Romain, S.; Bozoglian, F.; Sala, X.; Llobet, A. *J. Am. Chem. Soc.* **2009**, *131* (8), 2768–2769.

(110) Wada, T.; Tsuge, K.; Tanaka, K. *Angew. Chemie Int. Ed.* **2000**, *39* (8), 1479–1482.

(111) Crandell, D. W.; Xu, S.; Smith, J. M.; Baik, M.-H. *Inorg. Chem.* **2017**, *56* (8), 4435–4445.

(112) Kim, S. H.; Park, H.; Seo, M. S.; Kubo, M.; Ogura, T.; Klajn, J.; Gryko, D. T.; Valentine, J. S.; Nam, W. *J. Am. Chem. Soc.* **2010**, *132* (40), 14030–14032.

(113) Ishizuka, T.; Watanabe, A.; Kotani, H.; Hong, D.; Satonaka, K.; Wada, T.; Shiota, Y.; Yoshizawa, K.; Ohara, K.; Yamaguchi, K.; Kato, S.; Fukuzumi, S.; Kojima, T. *Inorg. Chem.* **2016**, *55* (3), 1154–1164.

(114) Brodsky, C. N.; Hadt, R. G.; Hayes, D.; Reinhart, B. J.; Li, N.; Chen, L. X.; Nocera, D. G. *Proc. Natl. Acad. Sci.* **2017**, *114* (15), 3855–3860.

Chapter 2. Mechanism of Dioxygen Binding by a Non-Heme Thiolate-Ligated Iron Complex

2.1 Introduction

Key biochemical reactions are driven by metal mediated O_2 oxidation.[1–3] Generally, these reactions involve a highly controlled process of O_2 binding, followed by a number of sequential one-electron reduction steps which eventually leads to an O–O bond activation.[2,4] During the process, a number of key transient metal-O_2 intermediates are formed and have been a major focus of research within the bioinorganic community. Owing to their extremely reactive and transient nature, however, much of our understanding about the key reactive intermediates comes from small-molecule research instead. However, only a small number of these examples are derived from O_2,[5–9] and even less of them have been shown to proceed through successive and spectroscopically distinct intermediates.[9] A subset of heme (e.g., cytochrome P450, CPO)[4,10,11] and non-heme (e.g., IPNS, CDO)[2,12,13] iron-containing metalloenzymes also contain cysteine thiolate ligated to the metal center. Covalently coordinated thiolate sulfur not only modulates the reactivity of the iron center,[14–16] but is itself susceptible to O_2 oxidation.[17,18] Therefore, investigating how a thiolate-ligated Fe binds and activates O_2 in small-molecule system, while preserving its own structural integrity, is essential to our understanding how thiolate-ligated metalloenzymes function.

Previously in our group, thiolate-ligated complex $[Fe^{II}(S^{Me2}N_4(tren))]^+$ (**1**) has been shown to generate a metastable ferric-hydroperoxo intermediate, $[Fe^{III}(S^{Me2}N_4(tren))(OOH)]^+$ (**8**), upon reaction with superoxide (O_2^-) (in the form of potassium superoxide (KO_2) solubilized with excess 18-crown-6) in MeOH/THF (1:9) at –90 °C, (Figure 2.1). Spectroscopic characterization revealed

that **8** is a low spin $S = 1/2$ ferric complex and exhibits an intense sulfur-to-metal charge transfer band at $\lambda_{max}(\varepsilon)$ = 452 nm (2780 M^{-1} cm^{-1}). EXAFS measurements resolved the presence of a proximal oxygen atom at a distance of 1.86(3) Å and a distal oxygen atom at a distance of 2.79(6) Å from the metal ion. Vibrational data supported the assignment of an end-on peroxo with a Fermi doublet at $\nu_{O\text{-}O}$ = 788 and 781 cm^{-1} that collapses upon the addition of deuterium oxide (D_2O), suggesting that protons are necessary in forming this intermediate.[19] Detailed kinetic studies established that external proton source (such as MeOH, EtOH, or NH_4^+) is required to convert O_2^- to HO_2, which then reacts with and concomitantly oxidizes **1** to generate **8.**[20,21]

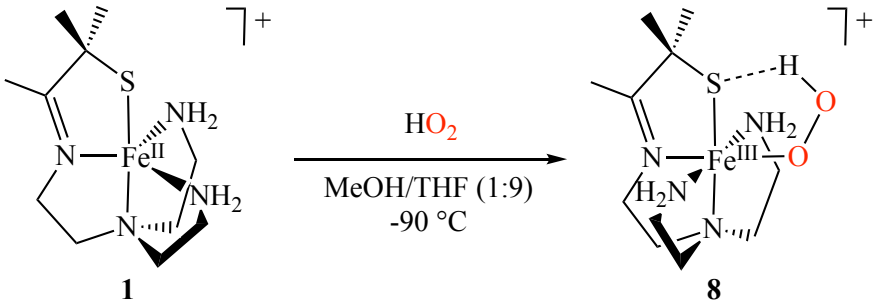

Figure 2.1. Reaction of $[Fe^{II}(S^{Me2}N_4(tren))]^+$ (**1**) with superoxide (O_2^-) results in proton-dependent formation of metastable ferric-hydroperoxo $[Fe^{III}(S^{Me2}N_4(tren))(OOH)]^+$ (**8**) intermediate in MeOH/THF (1:9) at –90 °C.

Our group has also reported that thiolate-ligated complex **1** reacts instantly O_2 at ambient temperature to form a μ-oxo-bridged diiron complex, $[(Fe^{III}(S^{Me2}N_4(tren)))_2(\mu\text{-}O)]^{2+}$ (**6**), (Figure 2.2).[22] Dimeric **6** forms in a variety of solvents, both protic and aprotic. It is brick-red in color and is characterized by an intense sulfur-to-metal charge transfer band in the 480-500 nm region, depending on the solvent. Namely, **6** exhibits a $\lambda_{max}(\varepsilon)$ = 483 nm (5,290 M^{-1} cm^{-1}) in MeCN, a $\lambda_{max}(\varepsilon)$ = 500 nm (5,500 M^{-1} cm^{-1}) in MeOH, and a $\lambda_{max}(\varepsilon)$ = 480 nm (~ 5,300 M^{-1} cm^{-1}) in THF. Dimeric **6** has been structurally characterized by X-ray crystallography and its magnetic properties have been investigated by SQUID and paramagnetic NMR methods.[22,23] Generally, μ-oxo iron

dimers are stable and chemically inert, representing a "thermodynamic pit" of in ferric chemistry.[24] Reactivity studies, on the other hand, have shown that the μ-oxo bridge of **6** can be reversibly cleaved. The μ-oxo bridge can cleaved by either weak (HOAc, NH_4PF_6, LutHCl) or strong (HCl, HBF_4) proton donors.[22,23]

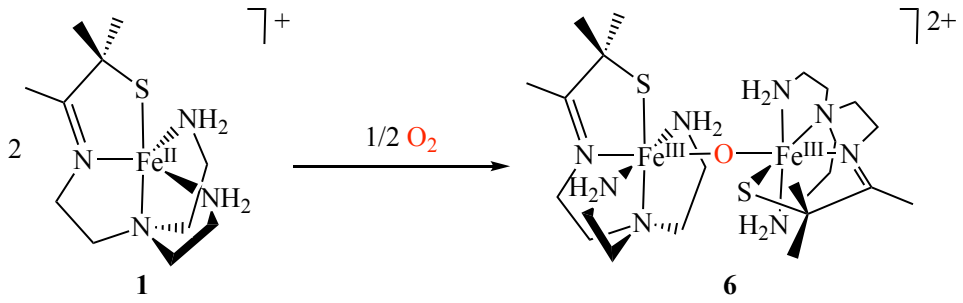

Figure 2.2. Reaction of **1** with O_2 at room temperature results in formation of μ-oxo-bridged diiron complex, $[(Fe^{III}(S^{Me2}N_4(tren)))_2(\mu\text{-}O)]^{2+}$ (**6**).[22]

The ability of **1** to react with O_2 to form a μ-oxo dimer indicates that this thiolate-ligated ferrous complex is capable of binding O_2 and activating the O–O bond. The current understanding of iron-mediated O_2 binding and O–O bond activation, which could lead to μ-oxo dimer formation, comes from both biomimetic and enzymatic iron heme and non-heme systems reported in the literature.[25–27] However, the role of thiolate ligands in non-heme iron chemistry has yet to be explored in detail. Figure 2.3 summarizes generalized mechanistic pathways of iron mediated O_2 activation. Initial coordination of O_2 to Fe^{II} leads to one-electron reduction of O_2 via an inner-sphere mechanism to afford an Fe^{III}–O_2^- (ferric-superoxo) intermediate. The Fe^{III}–O_2^- can then undergo a second one-electron reduction via hydrogen atom transfer (HAT) to form an Fe^{III}–OOH (ferric-hydroperoxo). The Fe^{III}–OOH can then undergo protonation at the proximal oxygen to release hydrogen peroxide (H_2O_2), analogous to the mechanism of SOR, as well as and **1** with HO_2, (*vide supra*).[19] Protonation of the distal oxygen of the Fe^{III}–OOH, on the other hand, leads to heterolytic O–O bond cleavage to release one equivalent of H_2O and generate a high-valent Fe^{V}=O

(perferryl-oxo), followed by one-electron reduction to afford high-valent Fe^{IV}=O (ferryl-oxo), in accord with cytochrome P450 chemistry.[28] The oxo of the latter has been shown to be highly basic, despite its high-valent oxidation state, due to the electron donating thiolate, and is thus protonated under physiological conditions to form a ferryl hydroxo species.[29]

In synthetic heme and non-heme iron chemistry, the afforded ferric-superoxo, Fe^{III}-O_2^{-}, may instead react with one equivalent of Fe^{II} starting material to form a $Fe_2^{III}(\mu\text{-}O_2^{2-})$ (diferric μ-peroxo) in aprotic solvents.[26,27,30] The crucial next step involving homolytic O–O bond cleavage would result in the formation of two equivalents of high-valent Fe^{IV}=O (ferryl-oxo) species. The highly reactive Fe^{IV}=O intermediate may react with the Fe^{II} starting complex to form a thermodynamically stable μ-oxo dimer product.[30] However, depending on the complex under investigation and the environment (solvent, substrates present, temperature), an Fe^{IV}=O may abstract a hydrogen atom to afford an Fe^{III}–OH (ferric-hydroxo). Finally, condensation of two equivalents of Fe^{III}-OH would lead to μ-oxo dimer product and the release of one molecule of H_2O.

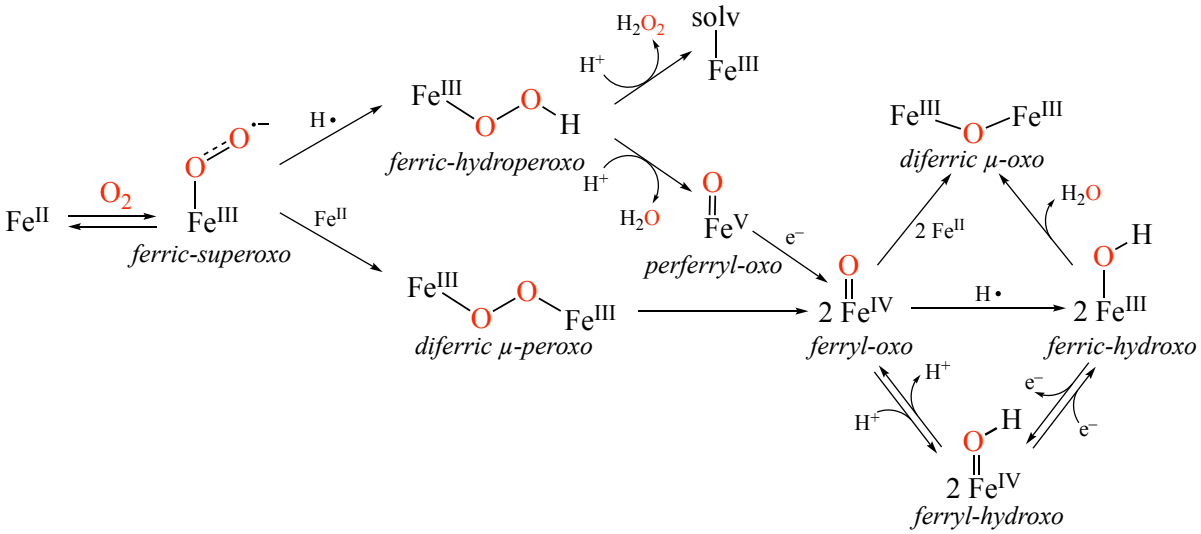

Figure 2.3. Mechanistic pathways of biological and biomimetic iron mediated O_2 activation.

This chapter provides a more in-depth analysis and discussion of the initial stage of reactivity between the thiolate-ligated complex $[Fe^{II}(S^{Me2}N_4(tren))]^+$ (**1**) and O_2 at low temperatures. The studies described herein have resulted in observation of the first metastable intermediate formed upon the addition of O_2 to **1** in cryogenic conditions, namely a ferric-superoxo species, followed by conversion to the second metastable intermediate, a μ-peroxo dimer. These two intermediates have been characterized by the electronic absorption spectroscopy, X-band EPR spectroscopy, low temperature ^{1}H NMR spectroscopy, reactivity and computational studies. Kinetic data for the formation of the second observed intermediate, μ-peroxo dimer, was obtained using rapid-scanned stopped-flow spectrophotometry, which has allowed for a mechanistic proposal for the O_2 reaction with **1** to be made.

2.2 Experimental

General Methods. All manipulations were performed using standard Schlenk techniques or under an N_2 atmosphere in a glovebox. Reagents and solvents were purchased from chemical vendors, were of highest available purity, and were used without further purification unless otherwise specified. $CDCl_3$ was purchased from Cambridge Isotope Labs and used as received. Tetrahydrofuran (THF) and diethyl ether (Et_2O) were purchased from Sigma-Aldrich and purified using a solvent purification column housed in a custom stainless-steel cabinet and dispensed by a stainless steel Schlenk-line (GlassContour). Methanol (MeOH) and methanol-d_4 (CD_3OD) were distilled over magnesium turnings and sublimed iodine, and rigorously degassed prior to use. CD_3OD was purchased from Cambridge Isotope Labs.

^{1}H NMR spectra were obtained on a Bruker AV300, AV301, or AV500 spectrometers. Chemical shifts are listed in parts per million and were reported relative to TMS by referencing

the residual solvent. Magnetic moments (solution state) were obtained using the Evans method as modified for superconducting solenoids.[31,32] Temperatures were obtained using Van Geet's method.[33] UV/Vis spectra were recorded on a Varian Cary 60 spectrophotometer equipped with a fiber optic cable connected to a "dip" ATR probe (C-technologies). A custom-built two neck solution sample holder equipped with a threaded glass connector was sized specifically to fit the "dip" probe. Electrospray-ionization mass spectra were obtained on a Bruker Esquire Liquid Chromatograph-Ion Trap mass spectrometer. Gas chromatography-mass spectrometry (GC/MS) data were obtained using a 6890 gas chromatograph equipped with a 7683 autosampler and interfaced with a 5973 mass spectrometer. FT-IR spectra were recorded on a Perkin-Elmer Frontier FT-IR spectrometer as nujol mulls on NaCl salt plates. X-ray crystallography data were recorded on a Bruker APEX II single crystal X-ray diffractometer with Mo Kα radiation.

Synthesis of $[Fe^{II}(S^{Me2}N_4(tren))](PF_6)$ (1). 3-mercapto-3-methyl-2-butanone (0.260 g, 2.2 mmol), was dissolved in 10 mL MeOH. To that, NaOMe (0.108 g, 2.0 mmol) was added and the mixture was stirring for 10 min, followed by the addition of *tris*(2-amonoethyl)amine (TREN) (0.234 g, 2.2 mmol). After stirring for an additional 20 min, the solution was cooled to –40 °C for an hour. In a separate vial, $FeCl_2$ (0.456 g, 2.0 mmol) was dissolved in MeOH (5 mL) and cooled to –40 °C for an hour as well. The ferrous solution was then added dropwise into the cooled solution containing thiolate and TREN ligand. The solution turned dark green immediately, was let stirring at room temperature for an hour, followed by addition of $NaPF_6$ (0.334 g, 2.0 mmol). The reaction solution was stirred at room temperature overnight and then filtered through a bed of celite. MeOH was evacuated and the resulting dark-green precipitate was redissolved in MeCN (10 mL). The solution was filtered through a bed of celite again, MeCN concentrated down to 3

mL. The concentrate was layered with Et_2O (17 mL) to crush out the complex over two nights at –40 °C. To attain highest purity, the resulting dark brown-red solid was redissolved in MeOH (3 mL), filtered through a fine frit, and recrystallized under layered Et_2O over two nights at –40°C. Final light-green solid (0.6 g, 70% yield) is 96% pure using quantitative UV/Vis of $[(Fe^{III}(S^{Me2}N_4(tren)))_2(\mu\text{-}O)](PF_6)_2$ (**6**) in MeCN with λ_{max} (ε): 480 nm (5270 M^{-1} cm^{-1}, 20 °C).

Formation of $[Fe^{III}(S^{Me2}N_4(tren))(O_2)](PF_6)$ (2) via the Addition of 1 to O_2-Saturated MeOH/EtOH (1:1) Solution. A 2.0 mM solution of **1** was prepared in MeOH/EtOH (1:1) mixture under an inert atmosphere in a glovebox. Saturated solution of O_2 was prepared by bubbling dry O_2 gas for 15 minutes into a septum-capped MeOH/EtOH (1:1) mixture in a round-bottom flask at 25 °C. O_2-saturated MeOH/EtOH (1:1) mixture (4 mL) was then added to a modified Schlenk cuvette (1 cm path-length) and cooled to –130 °C using liquid nitrogen (LN_2) Unisoku USP-203-B cryostat attached to Cary bio-50 UV−vis spectrophotometer where low-temperature electronic absorption spectra were obtained. Using a gastight syringe, solution of **1** (200 μL, 4.0 x 10^{-4} mmol) was injected into the O_2-saturated MeOH/EtOH (1:1) slurry while recording spectra at 3 seconds intervals.

Formation of $[(Fe^{III}(S^{Me2}N_4(tren)))_2(\mu\text{-}O_2)](PF_6)_2$ (3) via the Addition of O_2 to 1. A 0.378 mM solution of **1** was prepared in MeOH under an inert atmosphere in a glovebox. The resulting solution was transferred via gastight syringe to a custom-made two-neck vial equipped with septum cap and threaded dip-probe feed-through adaptor that had been previously purged with argon gas through a septum cap for at least 20 minutes. The solution was cooled in an acetone/dry ice bath to –73 °C. Argon stream was removed from the vial and a stream of O_2 gas was bubbled

through the solution over the course of 2 minutes, resulting in the formation of metastable **3**. The same procedure was used to prepare 0.4 mM samples of **3** in EPR tubes for EPR spectroscopy and 10 mM samples in NMR tubes for ^{1}H NMR spectroscopy. Electronic absorption of **3** in MeOH with λ_{max} (ε): 465 nm (3,000 M^{-1} cm^{-1}, –73 °C), EPR (MeOH/EtOH glass (9:1), 8.0 K): silent in $\perp$ and || mode.

Kinetic Measurements. All of the solutions were prepared under anerobic conditions ([O_2] < 0.5 ppm) in a glovebox and placed in Hamilton gastight® syringes equipped with three-way valves. Time-resolved spectra (350−820 nm) were acquired at low temperatures using a TgK Scientific (U.K.) CSF-61DX2 Multi-Mixing CryoStopped-Flow Instrument equipped with a tungsten visible light source. The stopped-flow instrument is equipped with PEEK tubing fitted inside stainless-steel plumbing, a 1.00 cm^3 quartz mixing cell, and an anaerobic kit purged with an inert gas. The temperature in the mixing cell was maintained to ± 0.1 °C, and the mixing time was 2-3 ms. All flow lines of the instrument were extensively washed with degassed, anhydrous MeOH before charging the driving syringes with solutions containing the reactants. The reactions were studied by rapid scanning spectrophotometry under pseudo-first order conditions with excess oxygen. Saturated solutions of O_2 were prepared by bubbling dry O_2 gas for 15 min into gastight syringes containing dry MeOH at 25 °C. The solubility of O_2 as 8.6 mM in MeOH at 25 °C. The O_2 concentration was assumed not to change upon cooling, given that the system is closed, and the solutions were not in contact with the gas phase (small variations in the solvent density were not taken into account). Dilutions of the O_2-saturated solvent were performed anaerobically to obtain the desired [O_2]. All concentrations reported in stopped-flow experiments refer to the “after mixing” conditions. Experiments were performed in single-mixing mode, with a 1:1 (v/v) mixing ratio. A series of three or four measurements gave an acceptable standard deviation (within 10%).

Rates reported for the oxygen dependence are the average of at least three different trials. The O_2 concentration was assumed not to change. Data analysis was performed with Kinetic Studio software from TgK Scientific. Data was fit at a single wavelength (465 nm) using the following equation:

$$A_t = A_\infty - (A_\infty - A_0)e^{-k_{obs}t} \quad (1)$$

An example of data fitting to the single-wavelength kinetic trace and its residuals describing the goodness of fit is shown in Figure 2.4.

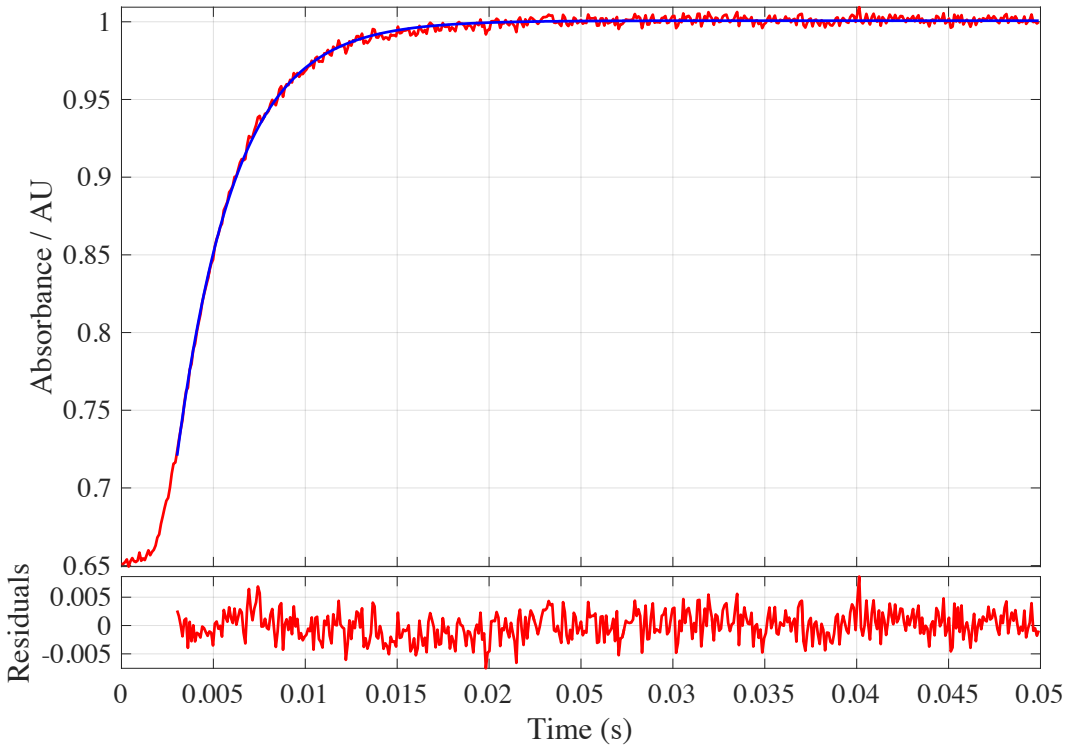

Figure 2.4. Kinetic trace at λ = 465 nm acquired at –50 °C with [**1**] = 0.2 mM and [O_2] = 4.3 mM. The experimental trace is shown in red; fit to the equation (1) shown in blue; residuals (in red) are appended at the bottom of the graph.

Hydrogen Peroxide Detection Using a Potassium Permanganate Assay. A concentrated methanolic solution of **1** (0.2 mL, 5.5 mM) was prepared under an inert atmosphere in a glovebox. After cooling the solution to –73 °C in a dry ice/acetone cold bath for 10 min, dry O_2 was gently bubbled into a solution for another 10 min while stirring. O_2 bubbling promoted a rapid color change of the solution to dark orange, indicating a formation of peroxo-bridged **3**. A single drop of concentrated H_2SO_4 was then added to the dark orange solution of **3**, causing a rapid color change to purple (λ_{max} = 565 nm, solvent bound $[Fe^{III}(S^{Me2}N_4(tren))(MeOH)]^{2+}$ (**7-MeOH**)).[20] The purple solution was then filtered through a small silica plug, collected, and added in a single aliquot to a stirring aqueous solution of $KMnO_4$ (6 mL, 1.23 x 10^{-4} M). The decrease in $KMnO_4$ absorption band was monitored spectroscopically in one-minute intervals until no further change was detected. The amount of hydrogen peroxide present was calculated based on the decrease in absorbance at λ_{max} (ε) = 550 nm (2455 M^{-1} cm^{-1}, 293 K) according to the following reaction:

$$2\ KMnO_4 + 5H_2O_2 + 6H^+ \rightarrow 2Mn^{2+} + 5O_2 + 8H_2O + 2K^+$$

Hydrogen Peroxide Detection Using a Catalase Assay. Both the *reaction* 50 mL three-neck flask with concentrated methanolic solution of **1** (5 mL, 20 mM) and the *indicator* 50 mL three-neck flask with concentrated acetonitrile solution of **1** (10 mL, 10 mM) were prepared under inert conditions in a glovebox. The two flasks were connected by a glass joint with a stopcock to isolate both mixtures, (Figure 2.5). The indicator flask was set under static vacuum at room temperature, while the reaction flask was cooled to –73 °C in a cold well inside the glovebox.

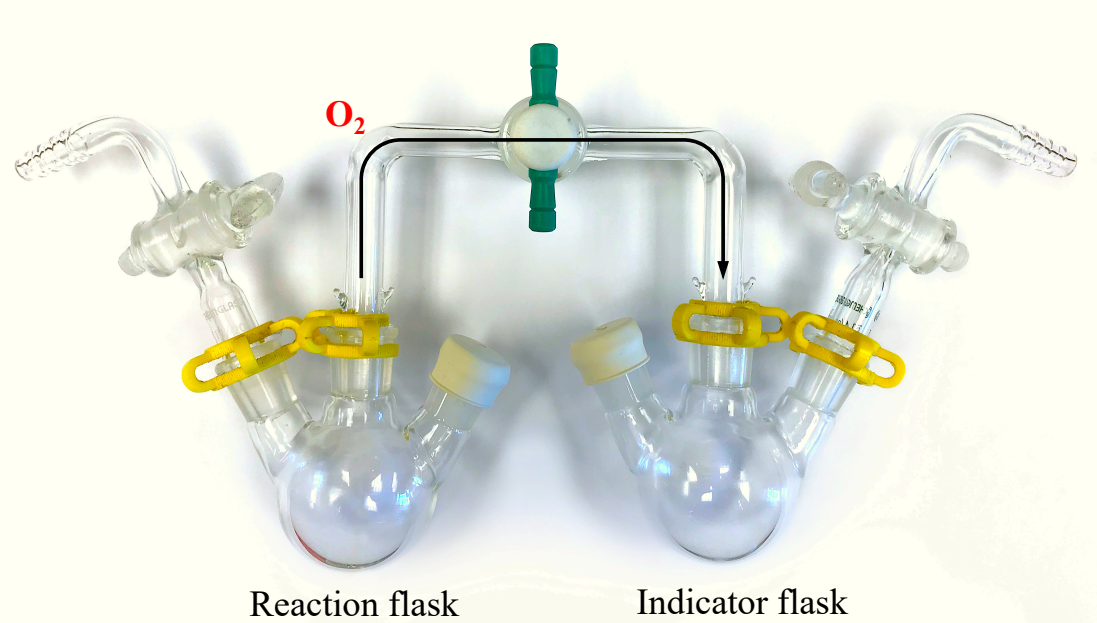

Figure 2.5. Experimental set up for catalase produced O_2 detection in the glovebox. The reaction flask (right) contains concentrated methanolic solution of **1** (5 mL, 20 mM). The indicator flask contains concentrated acetonitrile solution of **1** (15 mL, 10 mM) under static vacuum.

Then, saturated-O_2 methanolic solution (2.8 mL, 1.2 equiv, 0.12 mmol) was injected using a gastight syringe into the reaction flask while stirring. O_2 injection promoted a rapid color change of the solution to dark orange, indicating a formation of peroxo-bridged **3**. After stirring for 10 minutes, any excess of O_2 was removed by evacuation for an additional 10 minutes and refilled with N_2 gas. Then, pre-degassed, concentrated H_2SO_4 (10 μL, 1.8 equiv, 0.18 mmol,) was injected into the reaction flask, causing a rapid color change from dark orange to purple (λ_{max} = 565 nm, solvent bound **7-MeOH**).[20] Finally, a solution of catalase (5 mL, 0.02 g, 2000 units) in phosphate buffer (50 mM, pH = 7) was prepared aerobically in a glovebox and injected into the reaction flask using a gastight syringe. O_2 was generated, in the form of vigorous bubbling, according to the catalase reaction with hydrogen peroxide:

$$2H_2O_2 \rightarrow 2H_2O + O_2$$

Then, the stopcock to the indicator flask was opened. The released O_2 reacted with **1** in the indicator flask at room temperature to form brick-red μ-oxo dimer **6**. After 20 minutes, the methanolic solution of dimeric **6** was drawn with a gastight syringe and injected to a custom-made two-neck vial equipped with septum cap and threaded dip-probe feed-through adaptor that had been previously purged with argon gas (20 minutes) through a septum cap. The amount of catalase-generated O_2 was calculated based on the absorbance of **6** at λ_{max} (ε) = 500 nm (5500 M^{-1} cm^{-1})[22] according to the following reaction:

$$2\ [Fe^{II}(S^{Me2}N_4(tren))]^+ + \tfrac{1}{2}\ O_2 \rightarrow [(Fe^{III}(S^{Me2}N_4(tren))_2(\mu\text{-}O)]^{2+}$$

Hydrogen Peroxide Detection by GC/MS. A concentrated methanolic solution of **1** (3 mL, 100 mM) was prepared under inert atmosphere in a glovebox. After the solution was cooled to –73 °C in a dry ice/acetone cold bath for 10 min, dry O_2 was gently bubbled into a solution for another 10 min while stirring. O_2 bubbling promoted a rapid color change of the solution to dark orange, indicating a formation of peroxo-bridged **3**. Methanolic solution of H_2SO_4 (0.5 eq., 50 μL, 0.15 mmol) was injected into the dark-orange solution, causing a rapid color change to purple (λ_{max} = 565 nm, solvent bound **7-MeOH**).[20] The resulting solution mixture was filtered through a small silica plug. The methanolic filtrate (1.0 μL) was manually injected into a GC MS with modified parameters, followed by the second injection of pure methanol (1.0 μL) 2 min into the run. Second injection was used to subtract solvent and gas background. GC injection split ratio was set to 10.0:1.0, gas saver to 20.0 mL/min after 2.0 min. Starting temperature: 40 °C, run temperature: 90 °C; total run time: 5.0 min. MS scanning parameters were set 10 – 60 amu.

Computational Details. All calculations were performed using the ORCA v.4.1.1 quantum chemistry package developed by Neese and coworkers,[34] and employed the def2-TZVP basis set

and the def2/J auxiliary basis set for Coulomb fitting, the atom-pairwise dispersion correction of Grimme (D3BJ).[35] Tight convergence criteria, together with Grid5 (GridX5) and FinalGrid6 (FinalGridX6) integration grid size, were required for self-consistent field (SCF) solutions. Geometry optimization were performed using B3LYP hybrid functional, with the resolution of identity (RI) chain-of-spheres (RIJCOSX) approximation,[36,37] and initiated from the crystallographic coordinates when available. Analytical frequency calculations were performed on all optimized structures to determine whether the obtained stationary points correspond to local minima.

Previously reported[38] crystallographically determined structure of azide-bound $[Fe^{III}(S^{Me2}N_4(tren))(N_3)]^+$ (**7-N$_3$**) was used as a starting point for the calculated ferric-superoxo $[Fe^{III}(S^{Me2}N_4(tren))(O_2)]^+$ (**2**) intermediate. Specifically, the distal azide nitrogen N(6) atom was removed, and the proximal N(4) and middle N(5) atoms were replaced with oxygen atoms. The Fe^{III} metal center was assumed to be in the $S = 1/2$ state. A low spin-state was shown previously to be stabilized with thiolate-ligated Fe^{III} complexes due to the thiolate's nephelauxetic effect.[14,39,40] Based on optimized bond lengths reported for the arylthiolate-ligated $[Fe^{III}(LN_3S(O_2))]$,[17] $r_{Fe–O}$ and $r_{O–O}$ were set to 2.089 Å and 1.290 Å, respectively, as a starting point.

Calculations for the ferric-superoxo complex, $[Fe^{III}(S^{Me2}N_4(tren))(O_2)]^+$ (**2**), employed the broken-symmetry formalism to model coupled paramagnetic sites. An SCF calculation was first performed for the high spin (HS) state of the iron-superoxo complex, $Fe^{III}(S = 1/2, \uparrow)$-$O_2^{\bullet-}$ ($S = 1/2, \uparrow$). Next, a broken symmetry state was set up with the spin-flip chosen at the iron center (final total $m_s = 0$) and another SCF calculation was ran to calculate energy of the "broken symmetry" (BS), $Fe^{III}(S = 1/2, \downarrow)$-$O_2^{\bullet-}$ ($S = 1/2, \uparrow$), state. Finally, the energies of both HS and BS states were used to

estimate the coupling constant, J, (associated with the phenomenological Hamiltonian $\hat{H} = -2J_{12}\hat{S}_1\hat{S}_2$) using the equation $J = -(E_{HS} - E_{BS})(\langle S^2\rangle_{HS} - \langle S^2\rangle_{BS})$, which is valid over the entire coupling strength regime. E_{HS} and E_{BS} are the energies of the high-spin (HS), and the broken-symmetry (BS) states, respectively, and $\langle S^2\rangle$ are the expectation values of the squared spin operator for the HS and BS states.[41] The coupling constant $J^{calc} = -180$ cm^{-1} was obtained for putative ferric-superoxo **2**.

Hybrid time-dependent DFT (TD-DFT) calculations employed the RIJCOSX and the Tamm-Dancoff approximations (TDA).[42,43] Excited states from TD-DFT calculations were analyzed using Natural Transition orbitals (NTOs) and by visualizing their difference densities between the ground and excited states. Canonical molecular orbital isosurfaces and natural transition orbitals in the TD-DFT were visualized at an isovalue of 0.03 a_0^3 using UCSF Chimera software.[44]

2.3 Results and Discussion

2.3.1 *Evidence for Putative Ferric-Superoxo, $[Fe^{III}(S^{Me2}N_4(tren))(O_2)]^+$ (**2**), Formation*

As discussed earlier, the reaction between **1** and O_2 at ambient conditions results in formation of a μ-oxo dimer **6** in both protic and aprotic solvents. In aprotic solvents, dimeric **6** is the only observed product across the available temperature range from room temperature (20 °C) to near solvent's freezing point. The formation of **6** was observed in MeCN at –40 °C, THF at –90 °C, DCM at –90 °C, Me-THF at –120 °C, and even THF/Me-THF (1:1) mixture at –135 °C. In protic MeOH solvent, μ-oxo dimeric **6** is also the final product in the reaction between **1** and O_2. At low temperatures, on the other hand, two intensely colored metastable intermediates are

observed via electronic absorption spectroscopy *en route* to **6**. In MeOH, the first metastable intermediate is stabilized starting from –35 °C to –115 °C range. The same intermediate is also observed in EtOH protic solvent at temperatures as low as –114 °C. Experimental evidence described herein indicates that it is likely a peroxo-type intermediate ($Fe_2^{III}(\mu\text{-}O_2^{2-})$), a *second* step in iron-O_2 chemistry, as outlined in scheme 2.3. Characterization of these intermediates are discussed in great detail in the following sections. The *initial* step in iron-O_2 chemistry involves O_2 binding to the iron center to form ferric-superoxo intermediate.

Our group recently reported a well-characterized metastable bis-thiolate-ligated ferric-superoxo $[Fe^{III}(S_2^{Me2}N_3(Pr,Pr))(O_2)]$, derived from the reaction of O_2 with the starting ferrous complex $[Fe^{II}(S_2^{Me2}N_3(Pr,Pr))]$ in THF or DCM at –73 °C.[45] This diamagnetic ferric-superoxo intermediate consists of a low-spin ($S = 1/2$) Fe^{III} metal center strongly ($J^{calc} = -450\ cm^{-1}$) coupled to an $S = 1/2$ superoxo radical. It was also shown that the same ferric-superoxo intermediate could be generated from oxidized $[Fe^{III}(S_2^{Me2}N_3(Pr,Pr))]^+$ and KO_2 in THF at –73 °C. However, in this system, no reaction is observed upon the addition of KO_2, solubilized in 18-crown-6, to oxidized $[Fe^{III}(S^{Me2}N_4(tren))(MeCN)]^{2+}$ (**7-MeCN**) in MeCN at –40 °C.[46] The reaction was performed with stoichiometric as well as excess amount of KO_2 and over prolonged reaction times. At room temperature, **7-MeCN** has been shown to undergo slow nitrile exchange with the bulk solvent, ($k_{ex}^{298K} = 1.25(1) \times 10^1\ s^{-1}$).[47] Therefore, the lack of reactivity of **7-MeCN** with excess KO_2 is also likely the result of the relatively slow ligand exchange. This is, in part, a consequence of acetonitrile being a π-acceptor ligand which stabilizes the low-spin $S = 1/2$ ground state of **7-MeCN** ($g_\perp = 2.17$, $g_\parallel = 2.00$).[46,47]

A more reactive oxidized derivative of **1**, $[Fe^{III}(S^{Me2}N_4(tren))(THF)]^{2+}$ (**7-THF**), can be prepared by oxidizing the BPh_4^- salt of **1** with $[Cp_2Fe](BPh_4)$ in THF. The stoichiometric addition

of KO_2 (solubilized with excess 18-crown-6) to **7-THF** at –73 °C affords the orange λ_{max} = 465 nm intermediate **3** with concomitant release of ~0.5 equivalents of O_2. This suggests that the orange intermediate **3** requires two iron equivalents per O_2^- consumed.[48] Coordinating anionic ligands (OAc^-, CN^-, Cl^-) have been shown to inhibit the superoxide reaction with **7-THF**, as well as O_2 evolution.[38,48] This implies that **7-THF** mediated O_2^- oxidation to O_2 occurs via a *mechanism that involves O_2^-coordination to the Fe^{III} metal center followed by inner-sphere electron transfer.* Therefore, a superoxo-bound ferric complex **2**, $[Fe^{III}(S^{Me2}N_4(tren))(O_2)]^+$, is likely the intermediate that forms prior to O_2 release, (Figure 2.6). The reverse of this reaction, namely O_2 reaction with **1**, should also proceed via ferric-superoxo **2** formation *en route* to μ-oxo dimeric **6**, (*vide supra*). However, **2** appears inaccessible to spectroscopic detection, in the range of the aforementioned experimental conditions, due to its extremely fleeting nature.

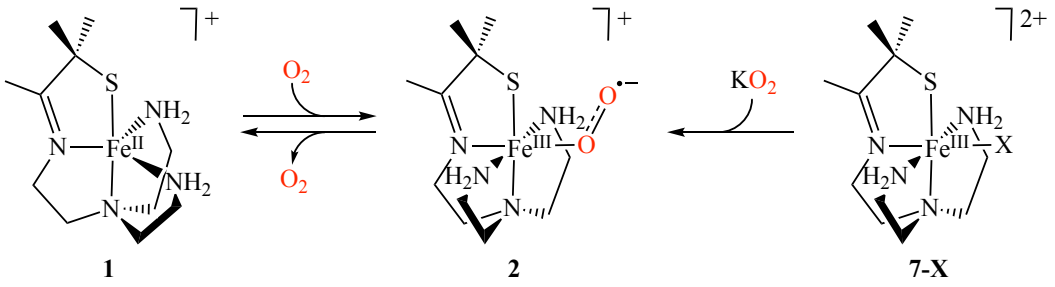

Figure 2.6. Superoxo-bound ferric intermediate **2** is accessible via the initial O_2 binding and oxidation of **1** or via the O_2^- substitution of the solvent-bound ferric **7-X** complex (X = solvent).

In an attempt to observe transient ferric-superoxo intermediate **2**, the reactivity between **1** and O_2 was explored by cryogenic UV/Vis spectroscopy. Since O_2 and **1** bind reversibly, the equilibrium may be shifted to the right to favor the formation of ferric-superoxo **2** by using excess O_2 (~100-fold excess). At that stage, the reaction may be arrested or slowed down from either going backwards or forward onto the next step (orange intermediate **3**) by immobilizing the reactants in a frozen solvent matrix. This was achieved by adding **1** to a saturated O_2 viscous

MeOH/EtOH (1:1) mixture near its freezing point (–130 °C). Here, the [O_2] is estimated to be ~ 8.6 mM based on a saturated O_2 solution of MeOH at room temperature.[49]

Addition of **1** (200 μL, 4.0 x 10^{-4} mmol) to a saturated O_2 solution (4 mL, ~ 3.4 x 10^{-2} mmol) of MeOH/EtOH at –130 °C reproducibly resulted in the formation of an intermediate characterized by the growth a broad band at λ_{max} = 690 nm over the course of 2.5 minutes, (Figure 2.7). Some of the orange species **3** grows in as well, suggesting that its formation is favored even under these conditions. The absorption band of **3** at λ_{max} = 465 nm is asymmetrically broadened and is likely a convolution of two additional peaks centered around 400 and 530 nm, which may belong to the same species with the a clearly resolved low-energy band at λ_{max} = 690 nm.

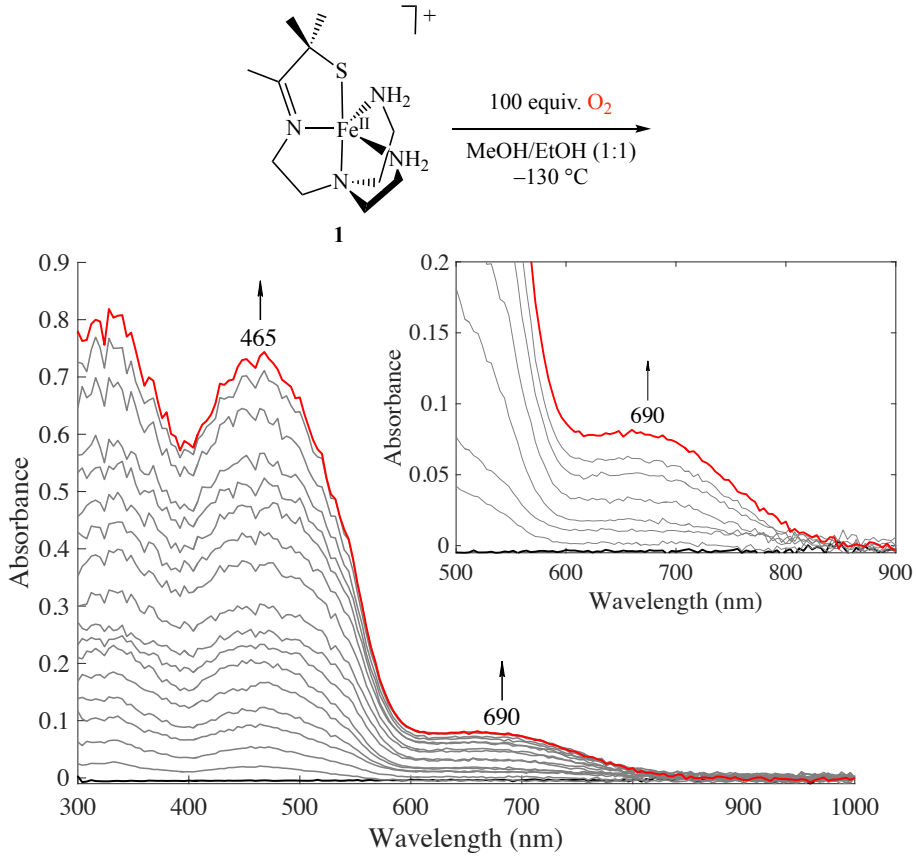

Figure 2.7. Cryogenic electronic absorption spectrum of the addition of **1** (4.0 x 10^{-4} mmol) to a saturated O_2 (~ 3.4 x 10^{-2} mmol) solution of MeOH/EtOH (1:1) at –130 °C shows growth of a mixture of intermediates **2** (λ_{max} = 690 nm) and **3** (λ_{max} = 465 nm). Inset of 500-900 nm region is shown for clarity.

Gaussian fitting using FityK software[50] was performed in order to confirm the presence of multiple absorption bands observed in the cryogenic electronic absorption spectrum in figure 2.1. The data in the visible region can be successfully fit with as a peak at 465 nm, characteristic of peroxo-type intermediate **3** (green). As a control, separate curve-fitting of the fully converted peroxo intermediate **3** confirmed that a single Gaussian curve centered at 465 nm is required to model its absorption band (data not shown). Therefore, the other four peaks (purple) in the visible region that are centered at 401, 530, 610, and 690 nm are putatively assigned to superoxo-bound **2**, (Figure 2.8). Two more Gaussian curves (light grey) were used to simulate the absorbance in the higher energy region above 400 nm in order to correctly predict (blue dashed line) the overall experimental spectrum.

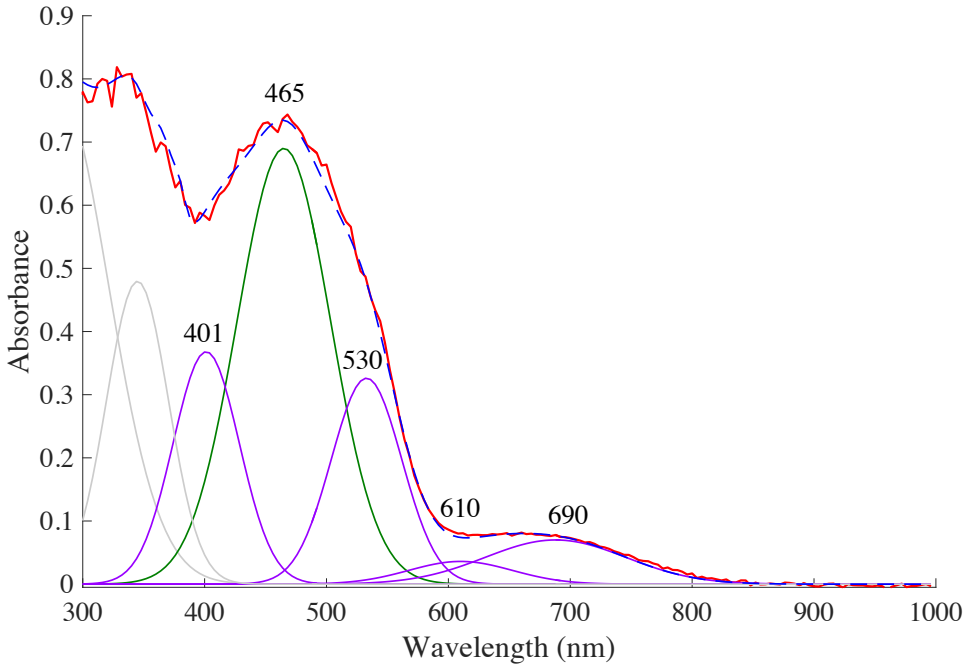

Figure 2.8. Gaussian fitting using Fityk software[50] of the cryogenic electronic absorption spectrum of the addition of **1** (4.0 x 10^{-4} mmol) to a saturated O_2 (~ 3.4 x 10^{-2} mmol) solution of MeOH/EtOH (1:1) at –130 °C. Experimental data is depicted in red (——), sum of the Gaussian fits to simulate experimental data is depicted in blue (-----), Gaussian fits of peaks at 401, 530, 610, and 690 nm characteristic of the intermediate **2** are in purple (——), Gaussian fit of a peak at 465 nm characteristic of the intermediate **3** is in green (——), and higher energy bands are depicted in light grey (——).

A slight temperature increase of the reaction mixture to –115 °C causes the disappearance of the band at 690 nm and sharpening of the band at 465 nm, (Figure 2.9). This is likely due to the decrease of solvent mixture viscosity, which improves mixing and the translational motion of the complex in solution. Sharpening of the 465 nm peak is consistent with the spectral convolution observed prior to warming. Moreover, simultaneous disappearance of the 690 nm band and the convoluted peaks around 400 and 530 nm suggests that they associated with the same intermediate. No further spectral changes are observed when the reaction mixture is cooled back to –130 °C. This implies that the intermediate **2** is consumed irreversibly and replaced by a peroxo-type species **3**. These results are consistent with the formation of a metastable ferric-superoxo species that forms via the initial binding of O_2 to **1**.

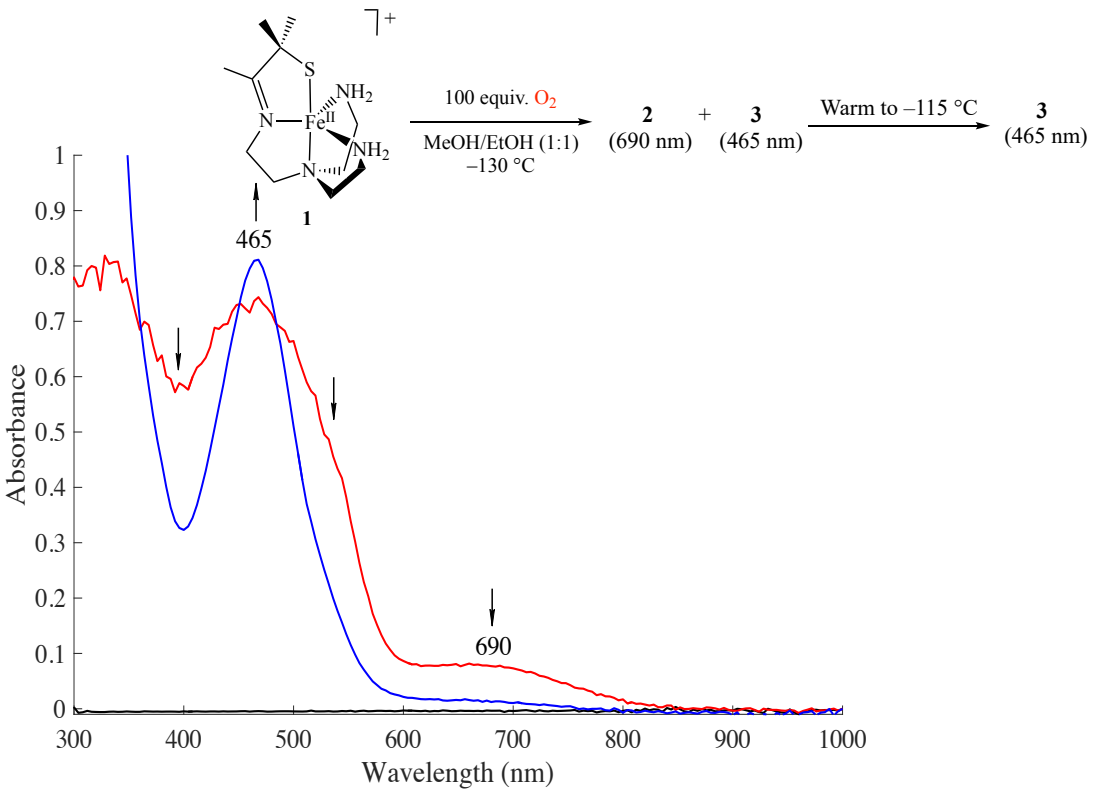

Figure 2.9. Cryogenic electronic absorption spectrum of the intermediate **2** (λ_{max} = 690 nm) at –130 °C (red scan). Warming up to –115 °C results in irreversible conversion to **3** at λ_{max} = 465 nm (blue scan).

The assignment of the cryogenically generated O_2 intermediate as a ferric-superoxo complex is supported by computational studies. In the absence of a crystal structure of **2**, crystallographic coordinates of the previously characterized[38] low-spin (S = 1/2) azide-bound $[Fe^{III}(S^{Me2}N_4(tren))(N_3)]^+$ (**7-N$_3$**) complex were used as a starting point, with the N_3^- replaced by a O_2^- ligand. The superoxo-bound Fe^{III} metal center was assumed to be in the S = 1/2 state, given the diamagnetic nature of previously reported $[Fe^{III}(S_2^{Me2}N_3(Pr,Pr))(O_2)]$,[45] as well as our group's prior work showing that thiolates stabilize low-spin ferric complexes through the nephelauxetic effect.[14,39,40] Extended broken symmetry density functional theory (BS-DFT) calculations were performed with the B3LYP* hybrid functional and the Def2-TZVP polarized triple-ζ-valence basis set. The amount of Hartree-Fock exchange in B3LYP functional was increased from 20% to 25%. The optimized structure of ferric-superoxo **2** contains an O_2^- moiety *cis* to the thiolate sulfur, (Figure 2.10). Calculated O–O (1.306 Å) and Fe–O (1.943 Å) bond lengths are typical of ferric-superoxo complexes.[17,51–54] The Fe–S (2.177 Å) and an average Fe–N_{ave} (2.02 Å) metal-ligand distances are consistent with a low-spin ferric center. Strong hydrogen-bonding (1.8-2.3 Å) between the O_2^- moiety and the neighboring primary amine protons appears to stabilize the superoxo in the equatorial plane perpendicular to the thiolate, (Figure 2.10, right).

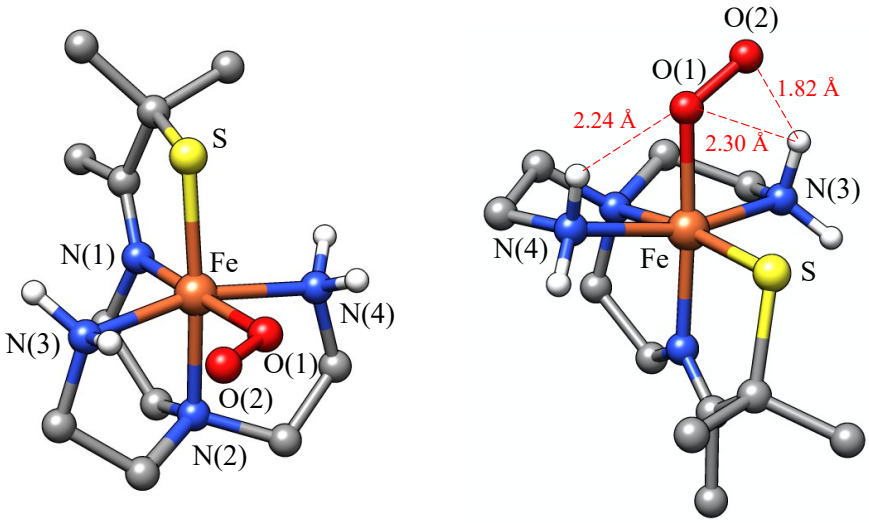

Figure 2.10. BS-DFT (B3LYP/Def2-TZVP) geometry optimized structure of putative $[Fe^{III}(S^{Me2}N_4(tren)(O_2))]^+$ (**2**) (left) together with its sideview (right) depicting strong hydrogen bonding between the superoxo (O_2^-) moiety and the hydrogen atoms of the neighboring amine arms.

Analysis of the electronic structure of **2** reveals two singly occupied frontier molecular orbitals that contain two unpaired electrons of opposite spin, (Figure 2.11). The overlap parameter $T = 0.17$ and the calculated coupling constant $J^{calc} = -180$ cm^{-1} indicate that the two unpaired electrons couple antiferromagnetically. Ferric-superoxo complex **2** is expected to be diamagnetic ($S = 0$), and therefore EPR silent. The spin up electron is located in the superoxo π*(O–O) orbital and the spin down electron in an antibonding π*(Fe(d_{yz}) – S(p_y)) orbital. This is in contrast to our recently reported bis-thiolate-ligated ferric-superoxo $[Fe^{III}(S_2^{Me2}N_3(Pr,Pr))(O_2)]$ complex (*vide supra*),[45] which exhibits a coupling constant ($J^{calc} = -450$ cm^{-1}) between the spin-up electron on the superoxo π*(O–O) orbital a spin-down electron in a non-bonding d_{xy} orbital that is twice as strong as that of **2**.

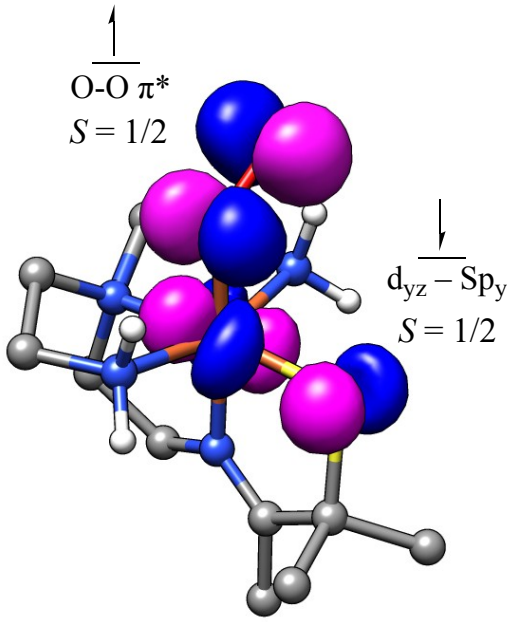

Figure 2.11. Singly occupied molecular orbitals (SOMO) of **2** contain strongly coupled electrons of opposite spin, with the spin-up electron of the superoxo π*(O–O) orbital coupling to the spin-down electron in an antibonding π*(Fe(d_{yz}) – S(p_y)) orbital.

The time-dependent DFT (TD-DFT) calculated electronic absorption spectrum of **2** nicely replicates the low-energy band observed experimentally (λ_{max} = 690 nm (Figure 2.7), $\lambda_{max,\ calc}$ = 692 nm (Figure 2.12)). Moreover, the calculated CT bands at $\lambda_{max,\ calc}$ = 410, 430, 542, and 615 nm are consistent with the presence of additional absorption peaks that were convoluted by the CT band of **3** (λ_{max} = 465 nm) present in solution, (Figure 2.7). The calculated spectrum shows that superoxo π*(O–O) → d_{x2-y2} (Fe) and d_{xy} (Fe) → π*(O–O) charge transfer transitions contribute to the higher energy bands, while a thiolate RS^- → Fe–O_2^- charge transfer transition contributes to the lower energy bands. Both the experimental and calculated electronic absorption spectra of **2** share common features with the recently reported [$Fe^{III}(S_2{}^{Me2}N_3(Pr,Pr))(O_2)$] and its β-hydrogen derivative [$Fe^{III}(S_2{}^{\beta H2}N3(Pr,Pr))(O_2)$],[55] supporting its assignment as a ferric-superoxo species. Lastly, all three ferric-superoxo complexes appear to be characterized by multiple absorption bands of successively decreasing intensity in the 400, 500, and 700 nm regions. These rich spectral

features seem to define thiolate-ligated ferric-superoxo complexes as a result of simultaneous charge-transfer transitions occurring between the π-donating thiolate, the ferric center and the superoxo moiety that act as both donor and acceptor orbitals.

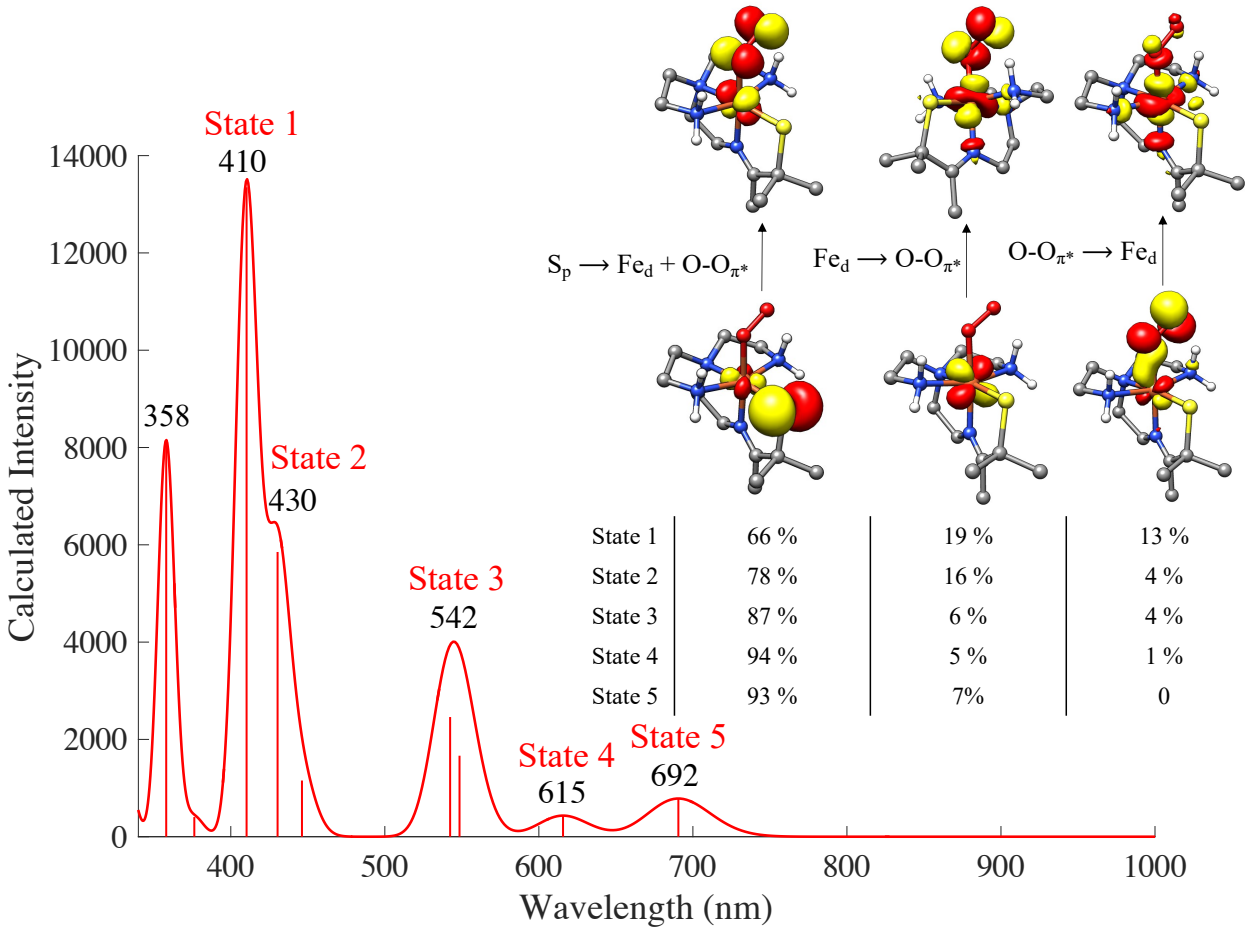

Figure 2.12. TD-DFT calculated electronic absorption spectrum of ferric-superoxo complex $[Fe^{III}(S^{Me2}N_4(tren))(O_2)]^+$ (**2**) including natural transition orbitals (NTO) describing the charge transfer (CT) transitions.

Previously reported $[Fe^{III}(S_2{}^{Me2}N_3(Pr,Pr))(O_2)]$ has been shown to abstract a hydrogen atom from THF solvent (BDE(C–H) = 92 kcal mol^{-1})[56] at –73 °C over the course of ~40 minutes.[45] Evidence to support $[Fe^{III}(S_2{}^{Me2}N_3(Pr,Pr))(O_2)]$-promoted hydrogen atom transfer (HAT) is provided by an observed deuterium isotope effect of $k_H/k_D = 4.8$, comparable to that of IPNS (k_H/k_D = 5.2),[57] *en route* to ferric-hydroperoxo, $[Fe^{III}(S_2{}^{Me2}N_3(Pr,Pr))(OOH)]$. The observed reactivity of

bis-thiolate ligated [$Fe^{III}(S_2{}^{Me2}N_3(Pr,Pr))(O_2)$] was interpreted to arise from π-back donation to the superoxo by the electron-rich alkyl-thiolate ligands. This increases the basicity of the distal oxygen, thus making hydrogen atom abstraction more favorable. In contrast, mono thiolate-ligated **2** converts to peroxo **3** instantaneously at temperatures as low as –115 °C. Moreover, no deuterium isotope effect is observed when this reaction is carried out in CD_3OD, and k_H/k_D = 1.0, for the formation of **3** at –73 °C, (see Chapter 3). This indicates that a fast electron transfer event takes place, rather than hydrogen atom transfer. The calculated geometric structure of **2**, (Figure 2.10), may provide a clue regarding this difference in reactivity. Unlike [$Fe^{III}(S_2{}^{Me2}N_3(Pr,Pr))(O_2)$] and its β-hydrogen derivative [$Fe^{III}(S_2{}^{\beta H2}N_3(Pr,Pr))(O_2)$], the superoxo moiety of **2** is supported and stabilized by strong hydrogen bonding with the neighboring primary amine protons. Hydrogen bonding between the distal superoxo oxygen to N(3)–H, which is calculated to be 1.80 Å away, and that of the proximal superoxo oxygen to both N(3)–H and N(4)–H. This may provide enough electrostatic attraction to the lower distal oxygen's basicity to the point where H-atom abstraction is no longer favored. Consistent with this, Mulliken charge analysis, which is used to calculate relative electron densities. The calculated Mulliken charge of O_{dist} (– 0.26) in **2** is less negative than that of [$Fe^{III}(S_2{}^{Me2}N_3(Pr,Pr))(O_2)$], (– 0.30). Similarly, O_{prox} of **2** bears less electron density (– 0.15) relative to O_{prox} on [$Fe^{III}(S_2{}^{Me2}N_3(Pr,Pr))(O_2)$], (– 0.18). Distal oxygen of **2** is unlikely to abstract amine hydrogen atoms due to its relatively lower basicity and prohibitively large BDE of primary amines, (BDE(N–H) = 101 kcal mol^{-1}).[56,58] Taken together, the unique structural and electronic properties of the *cis*-thiolate ligated ferric-superoxo **2** render it unsuitable for HAT reactivity, in contrast to that observed with the related bis-thiolate ligated superoxo intermediate, [$Fe^{III}(S_2{}^{Me2}N_3(Pr,Pr))(O_2)$]. At the same time, its rapid conversion to peroxo-type **3** at cryogenic conditions points towards an inner-sphere electron transfer event.

2.3.2 *Characterization of a Dimeric μ-Peroxo, $[(Fe^{III}(S^{Me2}N_4(tren)))_2(\mu\text{-}O_2)]^{2+}$ (**3**), Intermediate*

As discussed in previous section, putative ferric-superoxo, **2**, converts to a second metastable intermediate **3** at the temperatures above –115 °C in MeOH/EtOH (1:1) solvent mixture. Ranging from moderately low temperatures (–40 °C) to the near freezing point of EtOH (–114 °C) and MeOH (–96 °C), orange **3** is the only initial intermediate observed upon the addition of O_2 to **1**. Orange intermediate **3** is characterized by an intense ligand-to-metal charge-transfer (LMCT) band at $\lambda_{max}(\varepsilon)$ = 465 nm (~ 3,000 M^{-1} cm^{-1}), (Figure 2.13). The intense LMCT band of **3** likely corresponds to a sulfur-to-metal charge transfer transition, which would be consistent with one-electron oxidation to Fe^{III}. Moreover, the CT band position and intensity of **3** is very similar, albeit slightly red-shifted, to our previously reported ferric-hydroperoxo $[Fe^{III}(S^{Me2}N_4(tren))(OOH)]^+$ (**8**) species. Intermediate **8** was observed in the reaction between **1** and O_2^- in MeOH and characterized by a LMCT band at λ_{max} = 452 nm (2,780 M^{-1} cm^{-1}). Given the striking spectral similarity to ferric-hydroperoxo **8**, orange species **3** is likely a dinuclear μ-peroxo ($Fe_2^{III}(\mu\text{–}O_2^{2-})$), or a mononuclear hydroperoxo (Fe^{III}–OOH). However, while these two intermediates appear almost identical at a glance, their behavior and reactivity are drastically different.

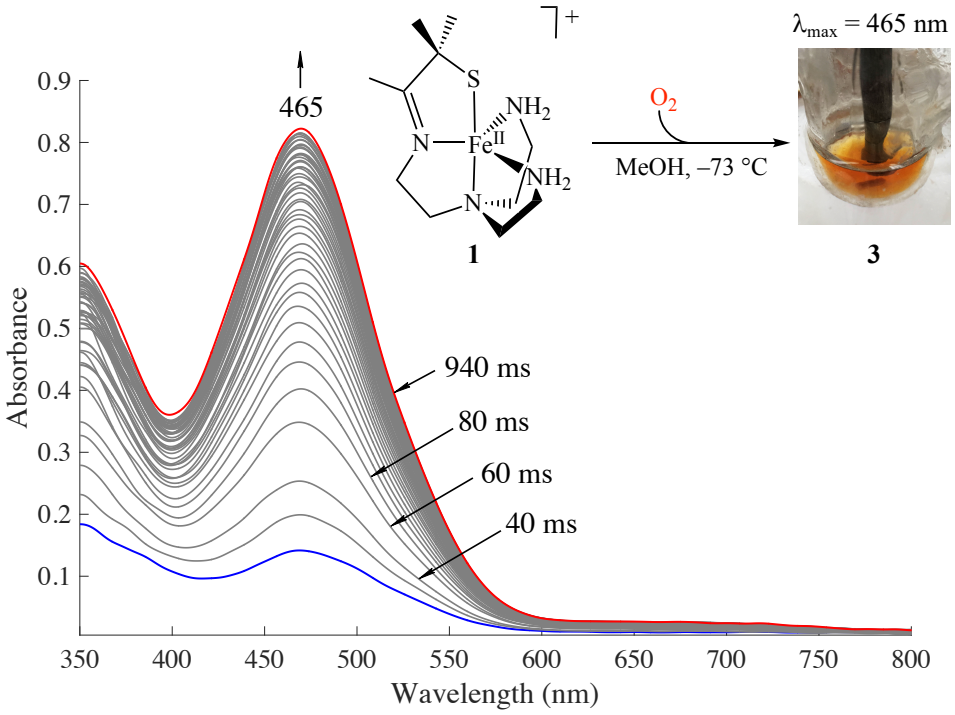

Figure 2.13. Electronic absorption spectrum showing that addition of excess O_2 (4.3 mM) to $[Fe^{II}(S^{Me2}N_4(tren))]^+$ (**1**) in MeOH at –73 °C results in a rapid (under 1 second) formation of an orange intermediate **3** at $\lambda_{max}(\varepsilon)$ = 465 nm (3,000 M^{-1} cm^{-1}).

Previously characterized ferric-hydroperoxo $[Fe^{III}(S^{Me2}N_4(tren))(OOH)]^+$ (**8**) is a transient intermediate that is unstable at low temperatures. Even at –90 °C, **8** cleanly converts to methoxide-bound **7-OMe** (λ_{max} = 511 nm) in about 10 minutes.[19] This is consistent with a mechanism of MeOH-induced protonation of the proximal oxygen of the Fe^{III}–OOH moiety, H_2O_2 release, and OMe^- ligand substitution. In contrast, orange intermediate **3** is stable at –80 °C for up to 90 days. Moreover, warming the orange intermediate **3** from –73 °C to room temperature results in red-shift from λ_{max} at 465 nm to that of 500 nm, (Figure 2.14), consistent with μ-oxo dimeric **6** formation instead of conversion to $[Fe^{III}(S^{Me2}N_4(tren))(OMe)]^+$ (**7-OMe**), as was seen with **8**. Assignment of μ-oxo dimeric **6** as the final product was supported by spiking it with authentically synthesized (in MeCN) and isolated **6** and obtaining its X-ray crystallographic structure. Cooling

the reaction mixture back to –73 °C shows no spectral changes, indicating that conversion to μ-oxo dimeric **6** is irreversible.

In aprotic solvents, the orange intermediate **3** is not observed even at –120 °C (Me-THF), and the reaction between **1** and O_2 results in direct conversion to μ-oxo dimeric **6**. Low-temperature formation of the orange intermediate **3** appears protic-solvent dependent. However, based on the conversion of **3** to μ-oxo dimeric **6** instead of methoxide-bound **7-OMe**, this indicates that protonation and H_2O_2 release is not taking place. Indeed, no H_2O_2 was detected by performing catalase assay on the room-temperature stable product derived from orange intermediate **3**. This would be consistent with orange intermediate **3** being a μ-peroxo dimer, $[(Fe^{III}(S^{Me2}N_4(tren)))_2(\mu\text{-}O_2)]^{2+}$, as opposed to previously characterized hydroperoxo-bound $[Fe^{III}(S^{Me2}N_4(tren))(OOH)]^{+}$ (**8**). It may be the case that protic solvent is necessary to stabilize μ-peroxo dimeric **3** via hydrogen bonding to the peroxo moiety and/or thiolate sulfur.

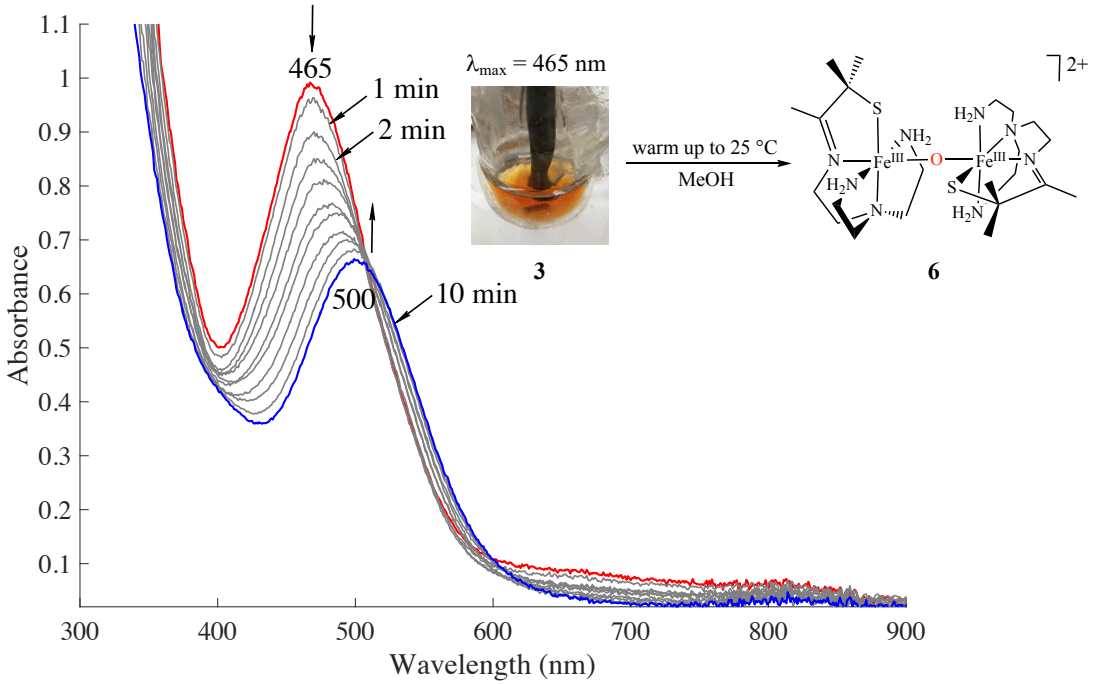

Figure 2.14. Electronic absorption spectrum showing that the orange intermediate **3** (λ_{max}= 465 nm) converts to μ-oxo dimeric $[(Fe^{III}(S^{Me2}N_4(tren)))_2(\mu\text{-}O)]^{2+}$ (**6**) (λ_{max}= 500 nm) in MeOH.

2.3.3 *Magnetic Characterization of μ-Peroxo **3** Intermediate*

EPR measurements were performed in order to gain more insight into the electronic structure of the orange intermediate **3**. CW X-band EPR (⊥-mode) spectroscopy, which probes half-integer spin systems, shows a featureless spectrum of the starting ferrous complex **1**, (Figure 2.15, top). Ferrous complex **1** is a high-spin (S = 2) system and is expected to have no signal in ⊥-mode.[23,59] The O_2-generated orange intermediate **3** also shows no signal in the ⊥-mode in the range from 4.2 to 120 K, (Figure 2.15, bottom). This result is in contrast to the previously reported low-spin (S = 1/2) ferric-hydroperoxo **8** intermediate which was characterized by an axial signal ($g_\perp$ = 2.14, $g_\parallel$ = 1.97) at 120 K in MeOH/THF (1:9) glass.[19] These experiments suggest that the orange intermediate **3** is *not a mononuclear system with a half-integer spin*, ($S \neq 1/2$, 3/2, or 5/2). Moreover, this is the first substantive evidence that the O_2-generated orange intermediate **3** is not a low-spin ferric-hydroperoxo **8**, which was previously characterized. Additional EPR measurements, in collaboration with Professor David Britt at the University of California, Davis, corroborated that the orange species **3** was EPR silent in both the ⊥- and ||-modes over the temperature range from 4.2 to 120 K, thus excluding **3** from being an integer spin system as well ($S \neq 1$, 2). As a result, EPR measurements suggest that the orange intermediate **3** is an overall diamagnetic system, S = 0.

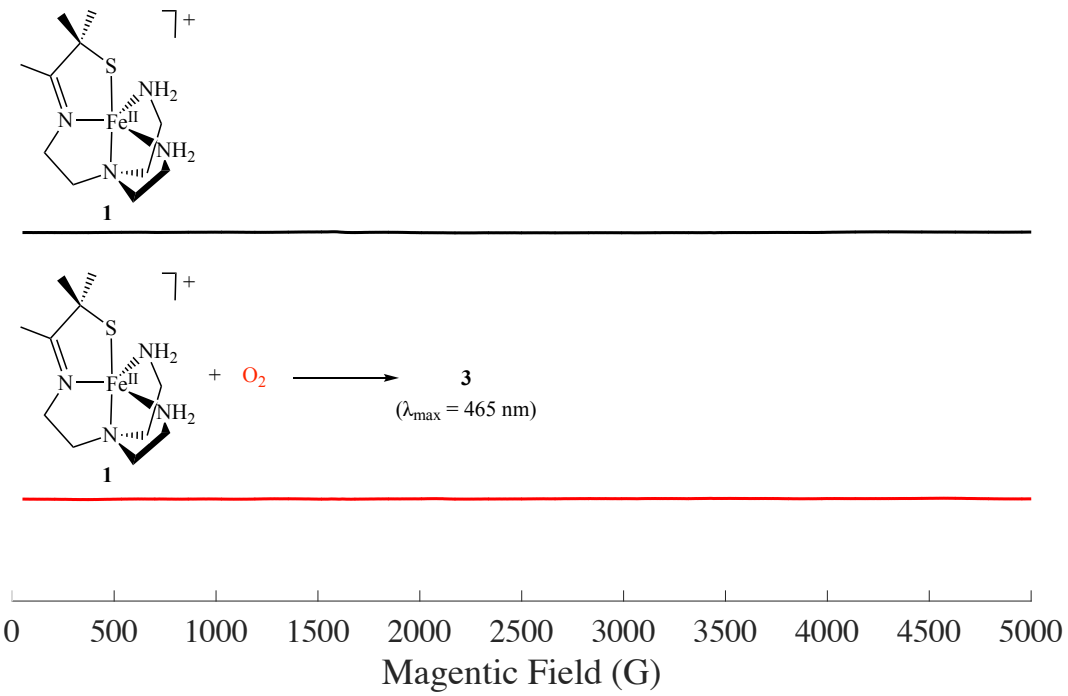

Figure 2.15. 9.65 GHz CW X-band EPR spectrum (⊥-mode) of the starting ferrous compound **1** (top) and the O_2-generated orange intermediate **3** (bottom) at 4.2 K in MeOH/EtOH (9:1) glass.

Next, the same set of species, namely ferrous **1** and its O_2-derived orange intermediate **3**, were studied with low temperature paramagnetic ^{1}H NMR spectroscopy. Measurements were taken in the +150 to –150 ppm range. The ^{1}H NMR spectrum of the parent compound **1** (10 mM) in CD_3OD at 193 K shows a single clearly resolved paramagnetically shifted peak at 117 ppm, (Figure 2.16, top). Moreover, the calculated magnetic moment of **1** is $\mu_{eff} = 4.64\ \mu_B$ in CD_3OD at 193 K, consistent with a $S = 2$ spin-state. Next, dry O_2 gas was bubbled into the NMR tube of **1** at –73 °C, resulting in formation of **3**, and the ^{1}H NMR spectrum was taken again. The paramagnetically shifted peak of **1** at 117 ppm collapsed upon the formation of **3**, (Figure 2.16, middle). However, the orange intermediate **3** shows a sharp peak 8.97 ppm and at least two broadened peaks in 18 – 25 ppm region associated with solvent-exchangeable N–H protons, suggesting that the local ferric centers are paramagnetic at 193 K. The calculated magnetic moment

of **3** is μ_{eff} = 1.96 μ_B per iron, consistent with a S = 1/2 spin-state. Low temperature ^{1}H NMR spectrum of **3** is also distinct from its room temperature final product, μ-oxo dimeric **6**, (Figure 2.16, bottom).

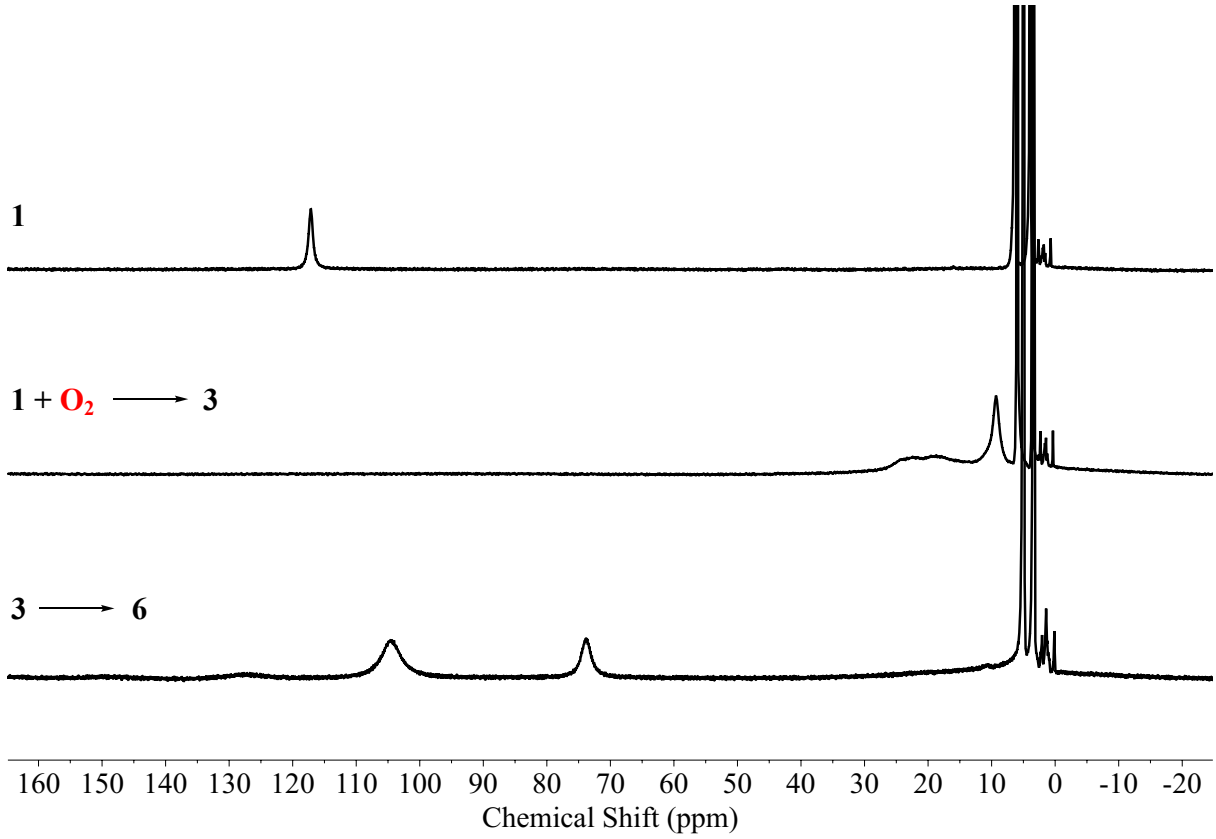

Figure 2.16. The paramagnetically shifted signal in the ^{1}H NMR spectra (500 MHz) of **1** (top) collapses to a new set of paramagnetically shifted signals upon the addition of O_2 and formation of the orange intermediate **3** (middle). The orange intermediate **3** is distinct from its room-temperature final product, μ-oxo dimeric **6** (bottom). Spectra were taken in CD_3OD at 193 K.

EPR measurements suggest that the orange intermediate **3** is likely diamagnetic (S = 0) in the temperature range from 4.2 to 120 K. This would be consistent with either ferric-superoxo species where the low-spin ferric ion couples antiferromagnetically to the superoxo ligand in the manner of Fe^{III}(S = 1/2, ↓)–$O_2^{\cdot-}$ (S = 1/2, ↑) or a dinuclear μ-peroxo species where both low-spin ferric ions couple via the peroxo ligand in the manner of Fe^{III}(S = 1/2, ↓)–O_2^{2-}–Fe^{III}(S = 1/2, ↑). The ferric-superoxo intermediate has been observed prior to formation of **3** in cryogenic conditions

and can, therefore, be ruled out. The diamagnetic coupling is indicative of the lower bound of the coupling constant *J*, associated with the phenomenological Hamiltonian $\hat{H} = -2J_{12}\hat{S}_1\hat{S}_2$, which is greater than the thermal energy k_BT for T below or equal to 120 K. The upper bound of the coupling constant *J* is calculated at 193 K, where the orange intermediate **3** shows distinct paramagnetically shifted signals in the ^{1}H NMR spectrum. The spin coupling constant of **3** can therefore be approximated to fall in the range of $-42\ cm^{-1} < J < -67\ cm^{-1}$. This *J*-value range indicates that the putative μ-peroxo **3** exhibits a somewhat stronger antiferromagnetic coupling than the μ-oxo dimeric **6**, ($J = -28\ cm^{-1}$).[22] However, it would fall in the lower range of other synthetic and biological primarily N-, O-ligated diferric-peroxo systems ($-33\ cm^{-1} < J < -140\ cm^{-1}$).[60–64] Smaller coupling observed in the μ-peroxo dimeric **3** and the μ-oxo dimeric **6** suggests that the thiolate-sulfur weakens this coupling in both systems.

2.3.4 *Kinetic Measurements of μ-Peroxo **3** Formation*

As noted above, the electronic absorption spectrum of the O_2-derived orange intermediate **3** is very similar to that of the previously characterized HO_2-derived ferric-hydroperoxo **8**. If the O_2-derived intermediate **3** were also a ferric-hydroperoxo species, the initial ferric-superoxo intermediate **2** would need to undergo one electron reduction and protonation by MeOH solvent or abstract a hydrogen atom from MeOH solvent. In the former case, 0.5 equiv. of **1** could serve as a sacrificial electron donor, which would afford 0.5 equiv. of $[Fe^{III}(S^{Me2}N_4(tren))(OOH)]^+$ (**8**) and 0.5 equiv. of $[Fe^{III}(S^{Me2}N_4(tren))(OMe)]^+$ (**7-OMe**). This mechanism can be ruled out because the reaction between **1** and O_2 affords full conversion to μ-oxo dimeric **6** in MeOH at room temperature. Moreover, there is no indication of formation of the solvent-bound **7-OMe** species at $\lambda_{max} = 511$ nm at either room or low temperatures. Alternatively, the preceding ferric-superoxo **2**

could potentially convert to a ferric-hydroperoxo species by abstracting a hydrogen atom from MeOH.

In other to test this hypothesis, electronic absorption spectroscopy was used to monitor the reaction between **1** and O_2 using a cryogenic stopped-flow instrument in MeOH and CD_3OD. The growth of the absorption band at 465 nm was monitored under pseudo first order conditions with excess O_2. Saturated O_2 solutions were prepared by bubbling dry O_2 gas into a small round-bottom flask containing dry MeOH for 15 min at 25 °C. The solubility of MeOH was taken as 8.6 mM in MeOH at 25 °C.[49] The dilutions of the O_2-saturated solvent were performed aerobically to obtain the desired O_2 concentration. The reaction between **1** (0.3 mM) and O_2 (4.3 mM) was recorded at the single wavelength (465 nm) at –50 °C. The kinetic trace for the change in absorbance at λ_{max} = 465 nm was fit to a single exponential of equation (1).

$$A_t = A_\infty - (A_\infty - A_0)e^{-k_{obs}t} \quad (1)$$

The observed rate of formation of **3** is identical in both MeOH (k_H = 267(3) s^{-1}) and in CD_3OD (k_D = 266(3) s^{-1}), indicating that there is no kinetic isotope effect (k_H/k_D = 1.0), (Figure 2.17). *Formation of the orange intermediate **3** does not appear to involve either protonation or hydrogen atom abstraction from the solvent and is consistent with **3** being a μ-peroxo dimer.*

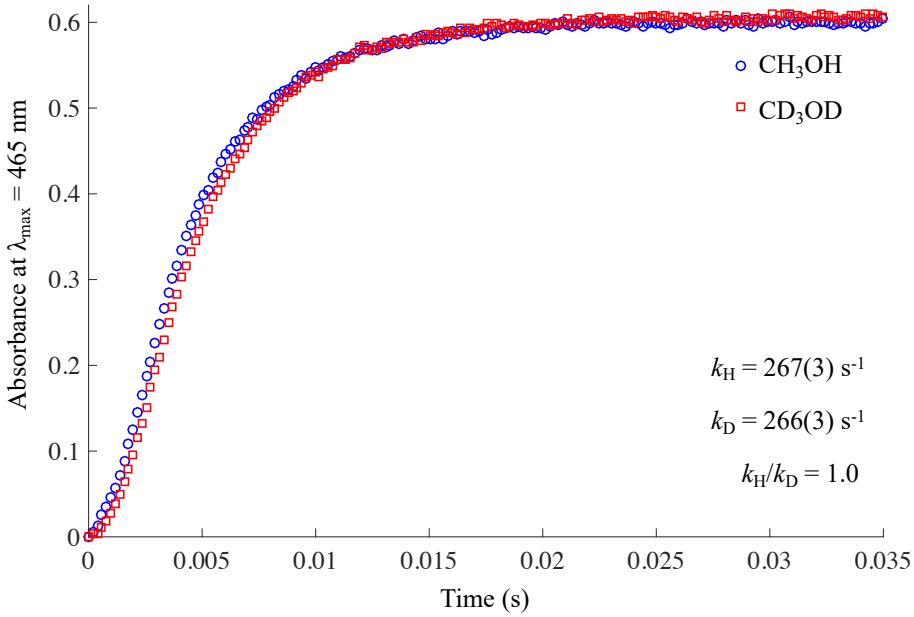

Figure 2.17. Kinetic traces at λ_{max} = 465 nm showing the formation of the orange intermediate **3** in MeOH (blue) and CD_3OD (red) obtained upon mixing solutions of (**1**) (0.3 mM) and O_2 (4.3 mM) at –50 °C.

To further elucidate the mechanism by which the peroxo-dimeric **3** forms, its dependence with respect to starting ferrous complex **1** and O_2 was explored separately. The reaction order with respect to iron was determined by varying the concentration of **1** over the range [**1**] = 0.05 mM to 0.3 mM in MeOH while maintaining a constant amount of excess O_2 at 4.3 mM. The formation of **3** was monitored by time-dependent absorbance changes at 465 nm. All kinetic traces from these set of experiments were fit with equation (1) to afford pseudo first-order rate constant, k_{obs}. The observed rate constant for the formation of μ-peroxo **3** (k_{obs}) was shown to increase linearly with increasing [**1**] in excess O_2, (Figure 2.18), consistent with an overall second-order dependence on [**1**].

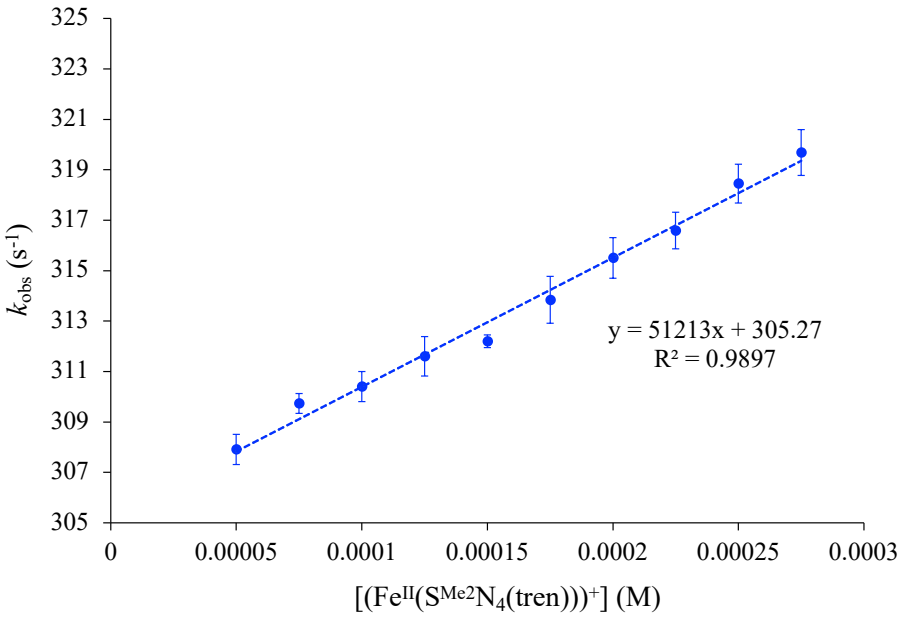

Figure 2.18. Plot of the observed rate constants (k_{obs}) for the formation of μ-peroxo dimeric **3** versus [**1**] (M) concentration at –40 °C in MeOH. [O_2] after mixing = 4.3 mM.

The reaction order with respect to O_2 was determined by varying the concentration of O_2 over the range [O_2] = 2.15 mM to 4.3 mM in MeOH. The observed rate constant, k_{obs}, also increases linearly with increasing [O_2], (Figure 2.19, left), consistent with first order dependence on O_2. Activation parameters for the formation of μ-peroxo **3** ($\Delta S^{\ddagger}$ = –102.3 J mol^{-1} K^{-1}; $\Delta H^{\ddagger}$ = 11.06 kJ mol^{-1}) were obtained from the Eyring plot, (Figure 2.19, right). The negative entropy of activation, $\Delta S^{\ddagger}$, is consistent with an associative process involving O_2 binding.

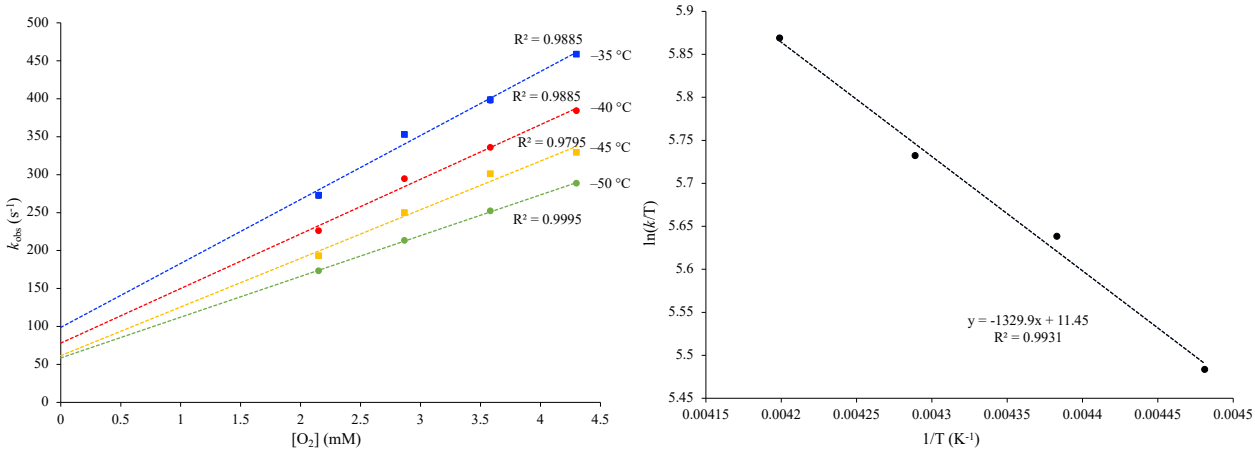

Figure 2.19. (Left) Plots of the observed rate constants (k_{obs}) for the formation of μ-peroxo intermediate **3** versus O_2 concentration over the temperature range –50 °C to –10°C in the reaction between **1** (0.2 mM) and O_2 in MeOH. (Right) Eyring plot (–50 °C to –10 °C) for O_2 binding to **1** to form μ-peroxo dimeric intermediate **3** in MeOH, from which activation parameters ($\Delta S^{\ddagger}$ = –102.3 J mol^{-1} K^{-1}; $\Delta H^{\ddagger}$ = 11.06 kJ mol^{-1}) were derived.

The general kinetic scheme is shown in Figure 2.20. The formation of the ferric-superoxo **2** is assumed to be a reversible step (equation (2)) based on the O_2 evolution studies described in section 2.3.1 above. The next step of the ferric-superoxo **2** reacting with the starting complex **1** to afford the μ-peroxo dimer **3** is assumed to be an irreversible step. No changes in the electronic absorption spectra of the μ-peroxo dimeric **3** were observed when the methanolic solution **3** was purged with a stream of argon for one hour or the O_2 actively pumped off from at –73 °C. Likewise, addition of the limited amount of O_2 (0.6, 0.3, and 0.1 equiv.) resulted in stoichiometric formation of **3** without further changes over the course of 2 hours. The overall rate of formation of the μ-peroxo dimeric **3** will depend on the relative magnitudes of rate constant (k_{-1}) of the dissociation of ferric-superoxo back to **1** and O_2 on one hand, and the rate constant (k_2) of the ferric-superoxo binding to another equiv. of **1** to afford μ-peroxo dimer **3**. Both scenarios are described below.

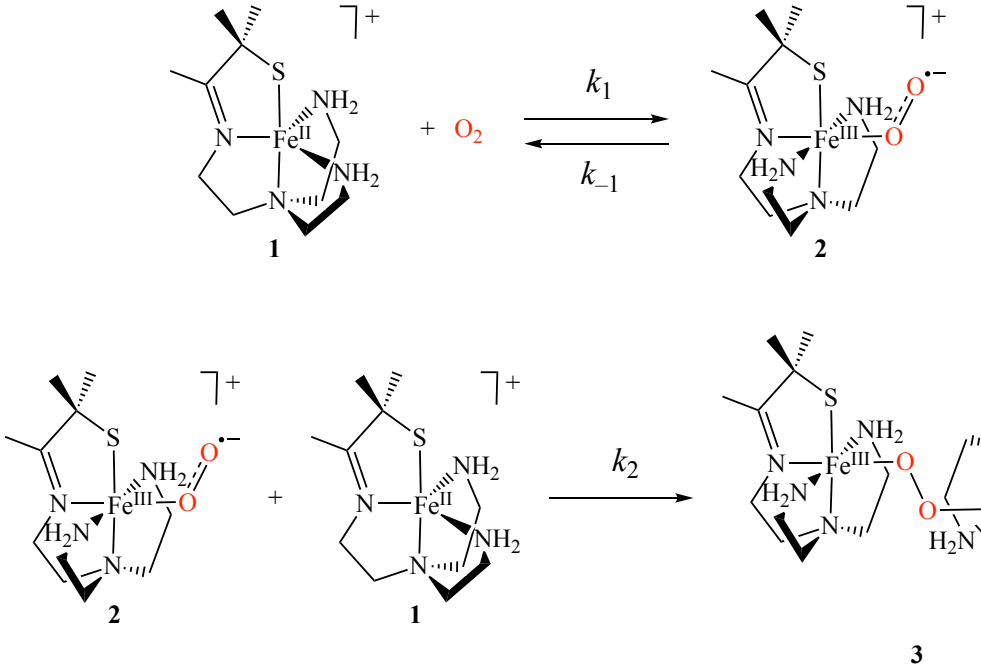

(2)

(3)

Figure 2.20. General kinetic scheme for the formation of μ-peroxo bridged **3** from **1** and O_2.

Scenario (i): $k_{-1} >> k_2$

In this scenario, the rate constant for (k_{-1}) the O_2 dissociation from ferric superoxo **2** is assumed to be much larger than the rate constant for the conversion of ferric-superoxo **2** to μ-peroxo dimeric **3** (k_2). The overall rate expression can be thus written and simplified as,

$$\text{rate} = \frac{k_2 k_1 [Fe^{II}]^2 [O_2]}{k_{-1} + k_2 [Fe^{II}]} = \frac{k_2 k_1 [Fe^{II}]^2 [O_2]}{k_{-1}} \qquad (4)$$

Where the rate is second order with respect to $[Fe^{II}]$,

$$\text{rate} = k_{obs} [Fe^{II}]^2 \qquad (5)$$

Under pseudo first order conditions with respect to O_2, observed rate constant (k_{obs}) is then equal to

$$k_{obs} = k_2 \frac{k_1}{k_{-1}} [O_2] \qquad (6)$$

Scenario (ii): $k_{-1} << k_2$

In the second scenario, the rate constant for (k_{-1}) the O_2 dissociation from ferric superoxo **2** is assumed to be much smaller than the rate constant for the conversion of ferric-superoxo **2** to μ-peroxo dimeric **3** (k_2). The overall rate expression can be thus written and simplified as,

$$\text{rate} = \frac{k_2 k_1[Fe^{II}]^2[O_2]}{k_{-1} + k_2[Fe^{II}]} = \frac{k_2 k_1[Fe^{II}]^2[O_2]}{k_2[Fe^{II}]} = k_1[Fe^{II}][O_2] \qquad (7)$$

Where the rate is first order with respect to $[Fe^{II}]$,

$$\text{rate} = k_{obs}[Fe^{II}] \qquad (8)$$

Observed rate constant (k_{obs}) is then equal to the rate of formation of ferric-superoxo **2** under pseudo first order conditions with respect to O_2,

$$k_{obs} = k_1[O_2] \qquad (9)$$

Based on the experimental data, the formation of the μ-peroxo bridged **3** exhibits a first-order dependence on O_2 under pseudo-first order conditions with excess O_2, (Figure 2.19, left) and second-order dependence on the starting ferrous complex **1**, (Figure 2.18), with rate = $k_{tot}[O_2][Fe^{II}]^2$, where k_{tot} is the experimentally determined rate constant that encompasses individual rates from equation (6). The results are consistent with the reversible formation of ferric-superoxo **2**, which was evidenced by the O_2 evolution and anionic ligand inhibition studies (*vide supra*). The rate of ferric-superoxo **2** and starting complex **1** binding is larger than the reverse step of the ferric-superoxo dissociation. The orange μ-peroxo intermediate **3** forms irreversibly. Finally, while μ-peroxo dimeric **3** has been observed to form only in a protic solvent such as MeOH, it does not appear to play a direct role in its formation as a proton or hydrogen atom donor. MeOH solvent may perhaps stabilize the μ-peroxo dimeric **3** via hydrogen bonding to the peroxo moiety and/or thiolate sulfurs.

2.3.5 *Theoretical Characterization of a μ-Peroxo Bound **3***

The assignment of the orange species **3** at λ_{max} = 465 nm as a μ-peroxo bound $[(Fe^{III}(S^{Me2}N_4(tren)))_2(\mu\text{-}O_2)]^{2+}$ ferric complex is supported by computational studies. Extended broken symmetry density functional theory (BS-DFT) calculations were performed with the B3LYP* hybrid functional and the Def2-TZVP polarized triple-ζ-valence basis set. The amount of Hartree-Fock exchange in B3LYP functional was increased from 20% to 25%. The optimized structure of a μ-peroxo **3** contains an O_2^{2-} moiety *cis* to the thiolate sulfur. The energy minimized structure obtained from this calculation was found to contain equivalent bond lengths for each half of the dimer with an O–O bond length of 1.430 Å, Fe–O bond lengths of 1.827 Å, Fe–S bond lengths of 2.256 Å, Fe···Fe distance of 4.39 Å, and Fe–O–O angle of 114.3°, (Figure 2.21). Strong hydrogen-bonding (1.92 - 2.39 Å) between the O_2^{2-} moiety and the neighboring primary amine protons stabilizes the peroxo in the equatorial plane perpendicular to the thiolate. The overlap parameter T = 0.08 and the calculated coupling constant J^{calc} = –57 cm^{-1} indicate that the two unpaired electrons are weakly antiferromagnetically coupled. Importantly, the calculated coupling constant of $J^{calc} = -57\ cm^{-1}$ falls in the range of $-42\ cm^{-1} < J < -67\ cm^{-1}$ determined experimentally from LT EPR and ^{1}H NMR measurements. The geometry optimized structure of **3** was further used for TD-DFT calculations. The TD-DFT calculated electronic absorption spectrum of a μ-peroxo 3 reproduces the main CT band in the visible region well. Specifically, the experimental absorption band at λ_{max} = 465 nm is simulated at $\lambda_{max,\ calc}$ = 462 nm. The calculated UV/Vis spectrum was found to contain an intense peroxo (O–Oπ^*) to Fe (dz^2) charge transfer, (Figure 2.22).

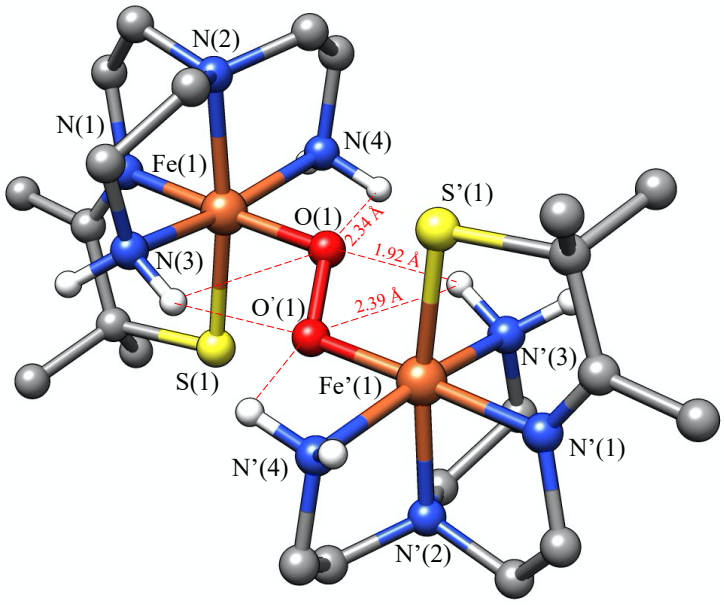

Figure 2.21. BS-DFT optimized geometry of a low-spin μ-peroxo bound $[(Fe^{III}(S^{Me2}N_4(tren)))_2(\mu\text{-}O_2)]^{2+}$. Selected calculated bond lengths and angles for (**3**): Fe–N(1), 1.974 Å; Fe–N(2), 2.060 Å; Fe–N(3), 2.036 Å; Fe–N(4), 2.046 Å; Fe–S(1), 2.256 Å; Fe–O(1), 1.827 Å; O(1)–O'(1), 1.430 Å; Fe–O(1)–O(1), 114.3°.

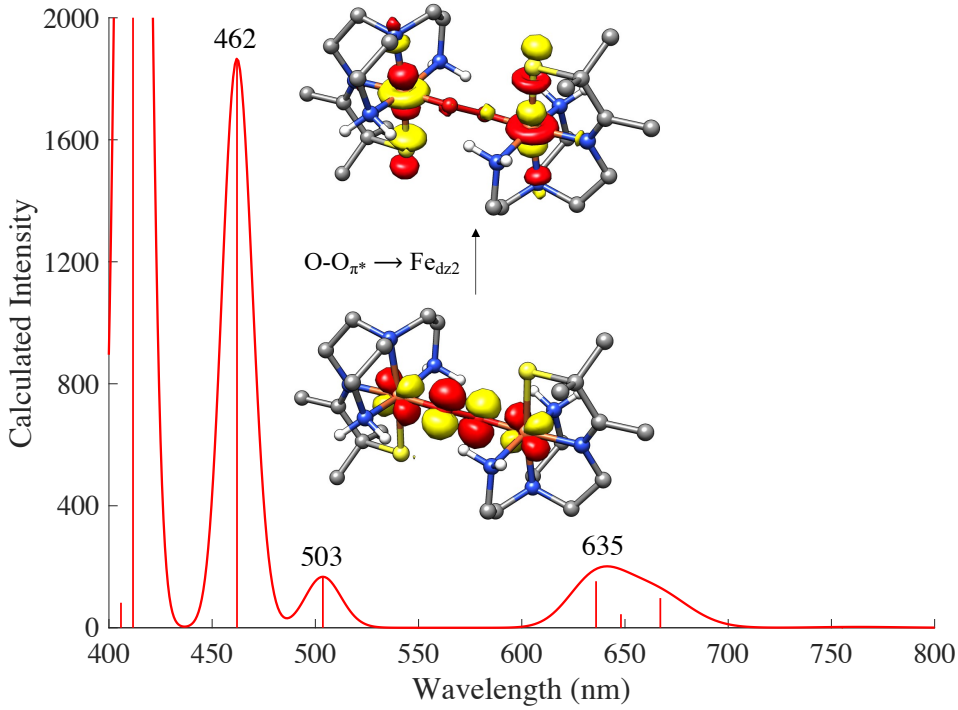

Figure 2.22. TD-DFT calculated electronic absorption spectrum of a μ-peroxo bound $[(Fe^{III}(S^{Me2}N_4(tren)))_2(\mu\text{-}O_2)]^{2+}$ (**3**) including natural transition orbitals (NTO) describing the charge transfer (CT) transitions.

2.3.6 *Reactivity of μ-Peroxo **3** Intermediate*

Reactivity with reduced $[Fe^{II}(S^{Me2}N_4(tren))]^+$ (1)

Kinetic measurements are consistent with **3** being a μ-peroxo dimer. Magnetic measurements have also indicated that the orange intermediate **3** is in a diamagnetic (S = 0) state with a fairly weak antiferromagnetic coupling ($-42\ cm^{-1} < J < -67\ cm^{-1}$). Although an intermediate, putatively assigned as ferric-superoxo **2**, which forms prior to **3** has been observed, it would also be in a diamagnetic state (S = 0). Likewise, high-valent Fe^{IV}=O intermediate, which could form as a result of O–O bond homolysis in **3,** may also be in a diamagnetic state (S = 0). (see Chapter 3). However, if the orange intermediate **3** was in fact a ferric-superoxo, it could potentially react with **1** to afford a true μ-peroxo dimer. On the other hand, if **3** were a high-valent Fe^{IV}=O, it could potentially react with **1** to afford μ-oxo dimeric **6** with (λ_{max}= 500 nm). Thus, the reaction between the orange intermediate **3** and the starting ferrous complex **1** was monitored by the UV/Vis spectroscopy in MeOH at –73 °C in order to ascertain if the orange intermediate **3** would be susceptible to one-electron reduction from another equivalent of ferrous **1**.

First, the orange intermediate **3** was formed by bubbling O_2 was through a precooled solution of **1** (5 mL, 0.4 mM) for 15 minutes. Then, the methanolic solution of **3** was purged with a stream of argon gas for one hour to remove any unreacted O_2 from the reaction mixture. Finally, 1 equiv. of **1** (5 mL, 0.4 mM) was added to the reaction cell containing a purged solution of **3** using a gas-tight syringe. No spectral changes, indicative of a μ-oxo **6** or of another intermediate, other than dilution and a decrease in absorbance by a half ($A_{initial}$ = 1.4 to A_{final} = 0.7 at λ_{max}= 465 nm) were observed, (Figure 2.21, A). O_2 was then bubbled again to see if the added solution of **1** remained unreacted in the cell. Indeed, the absorbance at 465 nm returned to A = 1.4, indicating

that the orange intermediate **3** is unreactive towards a reduced starting complex **1,** (Figure 2.21, B).

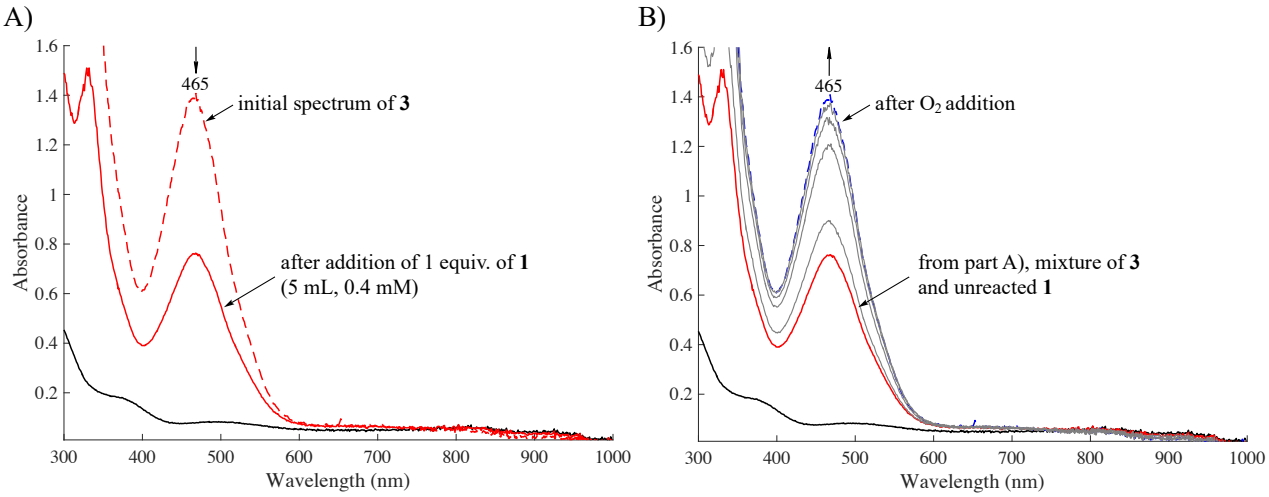

Figure 2.23. Electronic absorption spectra showing A) addition of 1 equiv. of **1** (5 mL, 0.4 mM) to **3** (5 mL, 0.4 mM) after a one-hour argon purge showing no spectral changes other than dilution of the chromophore by half. B) reopening the reaction mixture back to O_2 resulted in conversion of the unreacted **1** to afford **3**. Experiments were carried out in MeOH at –73 °C.

Acid/base chemistry

In order to examine the role of protons in formation and structural stability of the putative μ-peroxo dimeric **3**, its reactivity with various bases and acids were monitored by the UV/Vis spectroscopy in MeOH at –73 °C. Addition of non-coordinating (Et_3N, pK_a =10.8) or coordinating (NaOH, pK_a = 13.8; NaOMe, pK_a = 15.5) bases to O_2-derived peroxo **3** in stoichiometric and excess (100 equiv.) amount resulted in no apparent spectral changes when over the course of 2 hours. Likewise, addition of the same bases prior to O_2 addition to **1** showed no apparent inhibition in the rate and amount of formation of **3**. These results suggest that the formation of the intermediate **3** is proton-independent, consistent with a putative assignment of **3** as μ-peroxo dimer, $[(Fe^{III}(S^{Me2}N_4(tren)))_2(\mu\text{-}O_2)]^{2+}$. In contrast, formation of the $[Fe^{III}(S^{Me2}N_4(tren))(OOH)]^+$ (**8**) in THF at –78 °C was shown to be strongly correlated with proton donor pK_a of various acids, while inhibited in the presence of methoxide base.[21] On the other hand, intermediate **3** instantaneously

(less than 1 minute) reacts with a number of acids (HCl, H_2SO_4, HBF_4, and HOAc) in stoichiometric amount to cleanly convert to a previously characterized solvent-bound $[(Fe^{III}(S^{Me2}N_4(tren)))_2(MeOH)]^{2+}$ (**7-MeOH**) (λ_{max}= 565 nm) in MeOH at –73 °C, (Figure 2.22).[20] Addition of an excess amount of acid at low temperature results in loss of spectral features and bleaching out of the reaction mixture. This is indicative of protonation of the thiolate sulfur and subsequent decomposition of the iron complex.

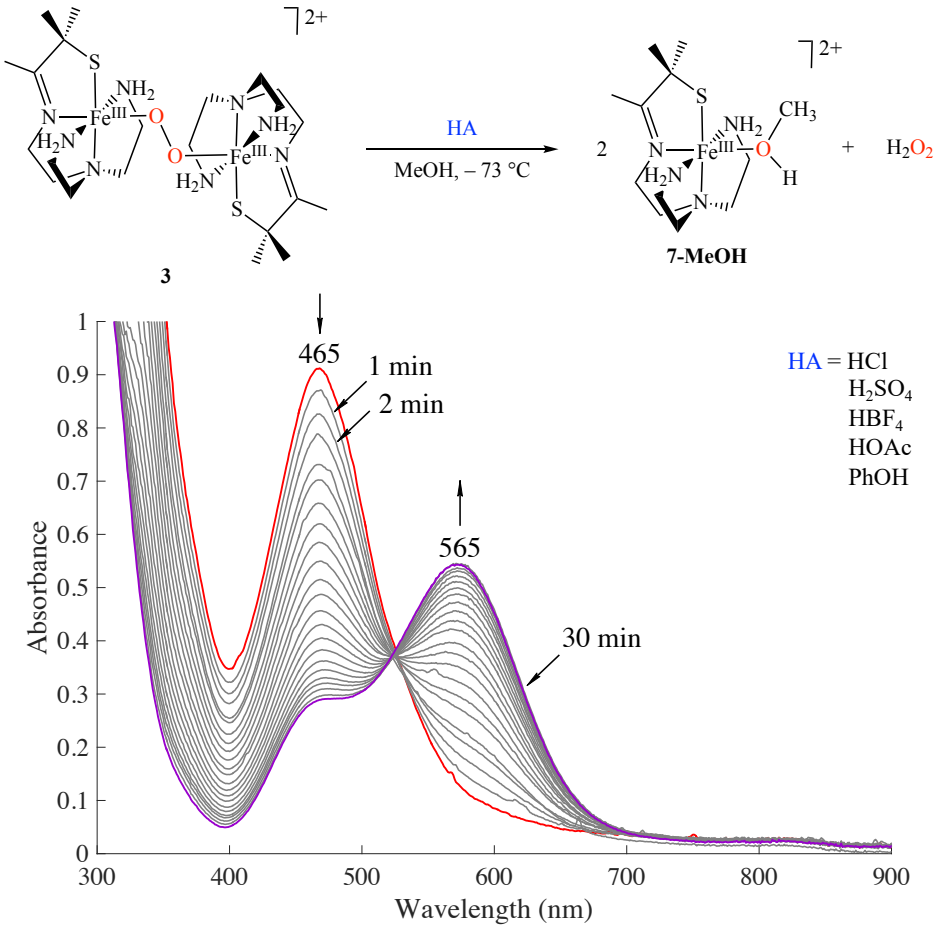

Figure 2.24. Electronic absorption spectrum showing a reaction between μ-peroxo **3** (λ_{max}= 465 nm) and various acids (HA = HCl, H_2SO_4, HBF_4, HOAc, PhOH) results in conversion to solvent-bound $[(Fe^{III}(S^{Me2}N_4(tren)))_2(MeOH)]^{2+}$ (**7-MeOH**) (λ_{max}= 565 nm) in MeOH at –73 °C.

HAT chemistry

Reactivity of the putative μ-peroxo dimeric **3** was also explored with HAT as well as oxygen atom transfer (OAT) reagents. In the presence of either stoichiometric or excess (100 equiv.) amount of hydrogen atom donors such as DHA (BDE(C–H) = 78 kcal mol^{-1}),[65,66] 1,4-cyclohexadiene (CHD) (BDE(C–H) = 76 kcal mol^{-1}),[66] and 1-hydroxy-2,2,6,6-teramethyl-piperidine (TEMPOH) (BDE(O–H) = 69 kcal mol^{-1}),[65,67] and, no decrease in absorbance or other spectral changes were observed in MeOH at –73 °C when monitored by UV/Vis over the course of 2 as well as 24 hours. Intermediate **3** appears to be unreactive towards hydrogen atom transfer reagents. Reactivity of **3** was also explored with 2,4-di-*tert*-butylphenol, which can act either as a hydrogen atom donor due to its relatively weak O–H bond (BDE(O–H) ~ 80 kcal mol^{-1})[65,67] or as a proton source (pK_a = 10.87).[67] 2,4-di-*tert*-butylphenol acts as an acid toward **3** and protonates it to form solvent-bound **7-MeOH**. As monitored by UV/Vis spectroscopy, addition of 1 equiv. of 2,4-di-*tert*-butylphenol at –73 °C in MeOH resulted in clean conversion to solvent-bound **7-MeOH** (λ_{max}= 565 nm) over the course of 30 minutes. Complex **3** reacted with phenol in an analogous manner to that with strong acids (e.g. H_2SO_4, HCl, and HBF_4), albeit at a much slower rate. If 2,4-di-*tert*-butylphenol acted a hydrogen atom donor, the resultant phenoxy radical would readily dimerize to form dimeric product, (3,3',5,5'-tetra-*tert*-butyl-2,2'-dihydroxybiphenyl).[68] However, no phenolic dimer was observed by GC/MS chromatography in this reaction relative to control.

Oxygen atom transfer (OAT) chemistry

Reaction between the μ-peroxo dimeric **3** and OAD reagents such as triphenylphosphine (PPh_3), dimethylphenylphosphine (PMe_2Ph), and thioanisole (PhSMe) was carried out in order to determine if the putative peroxo complex is capable of transferring oxygen atoms. In the presence

of either stoichiometric or excess (100 equiv.) amount of either phosphine, no spectral changes were observed in MeOH at –73 °C when monitored by UV/Vis over the course of 2 hours as well as 24 hours. Moreover, no phosphine oxide product ($Ph_3P=O$ or $Me_2PhP=O$) or methylphenyl sulfoxide (MePhS=O) was detected by GC/MS chromatography relative to control.

2.3.7 *Hydrogen Peroxide Detection*

The orange intermediate **3** is best described as a μ-peroxo bridged dimer, $[(Fe^{III}(S^{Me2}N_4(tren)))_2(\mu\text{-}O_2)]^{2+}$, based on its magnetic and kinetic characterization. Its reactivity with typical HAT and OAT reagents is also consistent with it being a dinuclear complex. Moreover, the dinuclear μ-peroxo **3** reacts readily with various acids to afford 2 equiv. of solvent bound **7-MeOH** (λ_{max}= 565 nm) and 1 equiv. of H_2O_2 in MeOH at –73 °C, (Figure 2.22). A few types of H_2O_2 detection assays were employed in order to detect and attempt to determine the stoichiometry of H_2O_2 released relative to starting complex **1** consumed.

H_2O_2, released as a result of acid addition to O_2-generated solution of **3**, was detected using $KMnO_4$ detection assay. Here, the orange intermediate **3** was generated by bubbling dry O_2 gas to a precooled methanolic solution of **1** (5.5 mM). A few drops of concentrated H_2SO_4 immediately afforded a solvent-bound **7-MeOH**. After the reaction mixture was passed through a plug of silica, the resulting filtered methanolic solution (0.2 mL) was added to the aqueous solution of $KMnO_4$ (6 mL, 1.23 x 10^{-4} M), (Figure 2.23). The amount of $KMnO_4$ consumed was calculated based on the change of absorbance at λ_{max} (ε) = 550 nm (2455 M^{-1} cm^{-1}, 293 K) according to the reaction shown in equation (10). According to the stoichiometry $KMnO_4$ consumed, 0.48 ± 0.01 equiv. H_2O_2 was produced per 1 equiv. of **1** utilized, consistent with a 2:1 ratio of **1** and O_2 used to

generate the orange intermediate **3**. In the control experiments, no $KMnO_4$ was consumed in the presence of H_2SO_4 only or in the presence of μ-oxo dimeric **6**.

$$2\ KMnO_4 + 5H_2O_2 + 6H^+ \rightarrow 2Mn^{2+} + 5O_2 + 8H_2O + 2K^+ \quad (10)$$

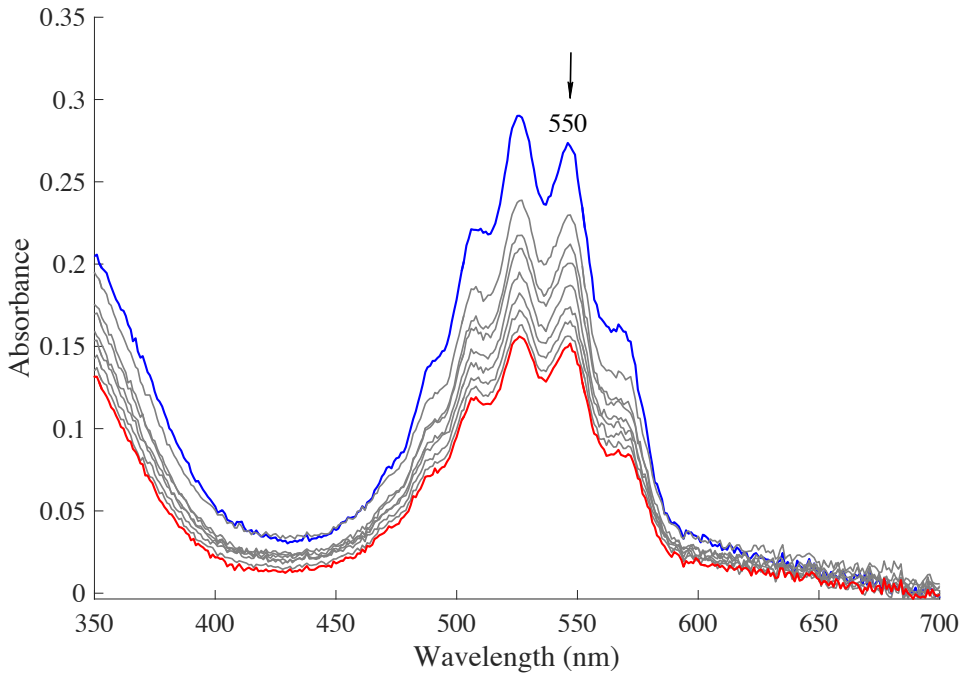

Figure 2.25. Electronic absorption spectrum showing the change in absorption of $KMnO_4$ (6 mL, 1.23 x 10^{-4} M aqueous solution, blue spectrum) which occurs upon the addition of H_2O_2 (red spectrum) that is released in the reaction between concentrated H_2SO_4 (2 drops) and **3** (0.2 mL, 5.5 mM in MeOH).

H_2O_2 released from the orange intermediate **3** was also detected using catalase assay. Addition of the aqueous solution of catalase (0.02 g, 2000 units, 5 mL) to the acidified solution of **3** (5 mL, 20 mM) afforded vigorous bubbling as a result of O_2 evolution according to the reaction shown in equation (11).

$$2H_2O_2 \rightarrow 2H_2O + O_2 \quad (11)$$

Spectroscopic detection and stoichiometric determination of O_2 released as a result of H_2O_2 consumption was attempted by allowing the released O_2 to react with an indicator in a two-bulb

closed system designed for the experiment, (see Figure 2.1 in experimental section). The MeCN solution of **1** (10 mL, 10 mM) was used as an indicator because it reacts with O_2 in ppm quantities to cleanly afford μ-oxo dimeric **6** (λ_{max} = 480 nm). Based the stoichiometry of O_2 released by the catalase reaction, around 0.23 ± 0.7 equiv. of H_2O_2 was detected per equiv. of **1** consumed in the reaction flask. On the other hand, no O_2 evolution was detected in the control experiments where the μ-oxo dimeric **6** was acidified at –73 °C. The enzymatic function of catalase is optimal near room temperature. Therefore, the acidic solution of **7-MeOH** and H_2O_2 needs to be warmed up for the catalase to react and evolve O_2. Unfortunately, **7-MeOH** itself is susceptible to H_2O_2 attack and decomposition at temperatures close to 0 °C and above, as evidenced by the gradual bleaching of the solution at room temperature. The low amount of H_2O_2 detected is likely the result of some H_2O_2 being consumed in the competing reaction.

Finally, H_2O_2 was detected using a modified GC/MS procedure that was developed for this work. The mass spectrum of cations produced by electron impact ionization for H_2O_2 (1.0 μL, 3.26 M) in H_2O/MeOH (1:3) solution is shown in Figure 2.24. The final spectrum was generated by subtracting the background spectrum (atmospheric gases, MeOH, and H_2O) from the signal spectrum. The base peak at 34 amu was set to 100. Relative intensities of the fragment cations are also tabulated, (Table 2.1), and are in close agreement with the values obtained by S. N. Foner and R. L. Hudson.[69]

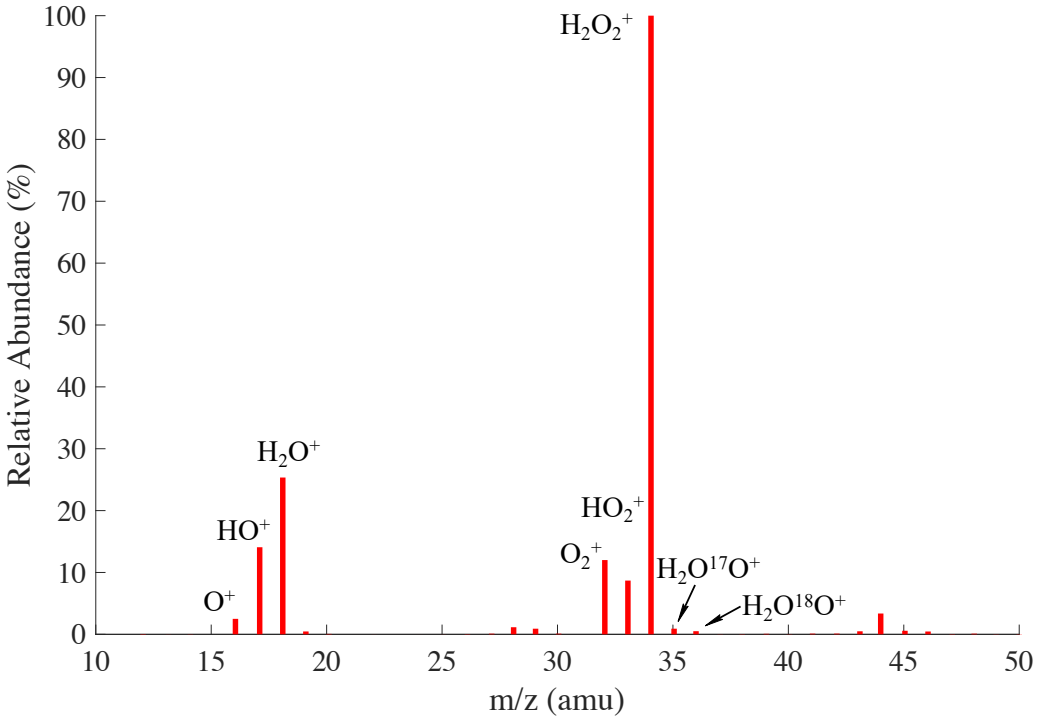

Figure 2.26. The mass spectrum of cations produced by electron impact ionization for H_2O_2 (1.0 μL, 3.26 M) in H_2O/MeOH (1:3) solution. Background spectrum was subtracted from the signal spectrum to produce a spectrum due to the H_2O_2 target molecule only, and the base peak *i.e. m/z* = 34 amu was normalized to 100.

To our best knowledge, there is no data available for the fragmentation of H_2O_2 in the National Institute of Standards and Technology (NIST) database to date.[70] Instead, H_2O_2 mass spectrum is identified as hydrogen sulfide (H_2S), which also bears the same atomic weight as H_2O_2 (*m/z* = 34). Therefore, the mass spectra of H_2S, provided by the NIST database, and the mass spectra experimentally determined H_2O_2 were distinguished between each other based on the relative abundance of their fragmented cations. In short, fragmentation ions of H_2O_2 at *m/z* = 33 (HO_2^+) and 32 (HO_2^+) are much less abundant, 8.7 % and 12.0 %, respectively, than those of H_2S (42.3 % for H_2S^+ and 44.8 % for HS^+). H_2S has no fragmentation cations below m/z = 32. Moreover, the naturally occurring isotopic form of $H_2{}^{36}S$, at *m/z* = 36, is almost ten times more abundant than $H_2O^{18}O^+$.

Table 2.1. The experimentally determined mass spectrum of H_2O_2 compared to the mass spectrum of H_2S obtained from the NIST database.[70]

Mass (amu)	Ion	Relative abundance (%)	Ion	Relative abundance (%)
36	$H_2O^{18}O^+$	0.51	$H_2{}^{36}S^+$	4.4
35	$H_2O^{17}O^+$	0.91	$H_2{}^{35}S^+$	0.8
34	$H_2O_2^+$	100.0	H_2S^+	100.0
33	HO_2^+	8.7	HS^+	42.3
32	O_2^+	12.0	S^+	44.8
18	H_2O^+	25.3	…	…
17	HO^+	14.1	…	…
16	O^+	2.5	…	…
2	H_2^+	…	…	…
1	H^+	…	…	…

The GC/MS detection limit of the H_2O_2 base peak at *m/z* = 34 by was found to be at 50 mM, which requires a 100 mM solution of starting complex **1,** assuming a 2:1 ratio for **1** and O_2. Otherwise, the preparation procedure of H_2O_2 released from the orange intermediate **3** is the same as outlined for the $KMnO_4$ detection assay. The base peak for $H_2{}^{16}O_2$ at *m/z* = 34, released from the $^{16}O_2$-generated orange intermediate **3**, was detected by the GC/MS, (Figure 2.25, A). Moreover, the base peak $H_2{}^{18}O_2$ at *m/z* = 38 was also detected from the orange intermediate **3** prepared from the isotopically labeled $^{18}O_2$, (Figure 2.25, B). Some $H_2{}^{16}O_2$ was also detected as a result of $^{16}O_2$ contamination. Background spectrum, also accounting for the natural abundance of $CH_3{}^{18}O^+H$ at *m/z* = 34 at 0.244(32) %,[70] was subtracted from the signal spectrum and the sum of

base peaks *i.e. m/z* = 34 amu (for $H_2{}^{16}O_2$) and 38 amu (for $H_2{}^{18}O_2$) was normalized to 100.

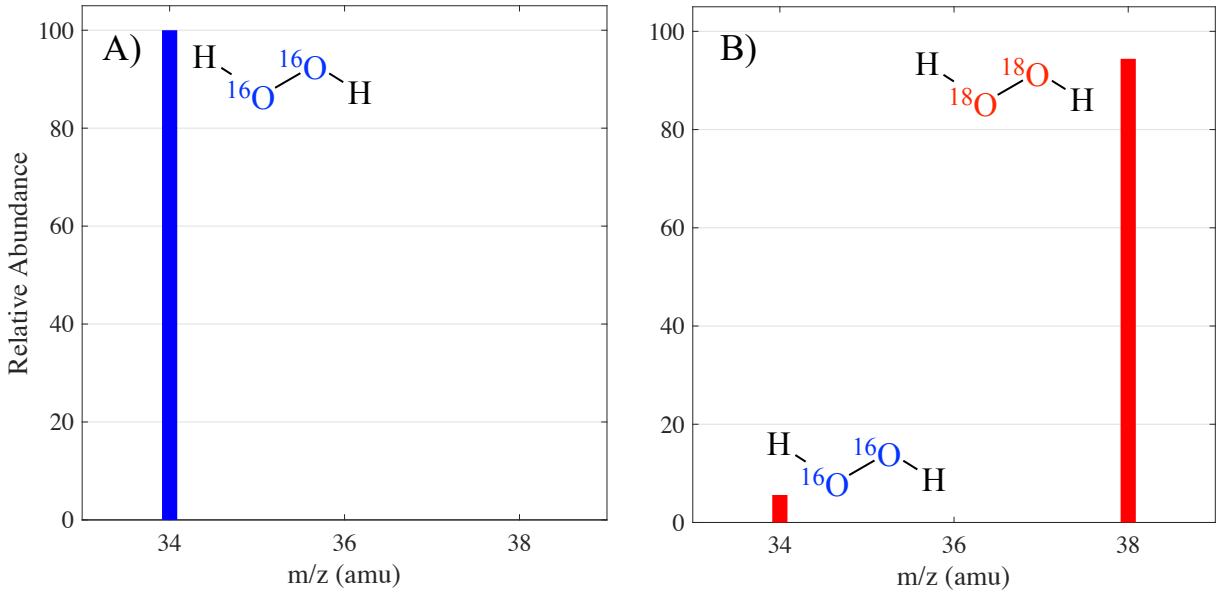

Figure 2.27. Mass spectra of cations produced by electron impact ionization for H_2O_2 generated from the addition of concentrated H_2SO_4 (1 drop) to the orange intermediate **3** formed from an addition of **A**) $^{16}O_2$ and **B**) $^{18}O_2$ to **1** (3 mL, 100 mM) in MeOH at –73 °C. Background spectrum was subtracted from the signal spectrum and the sum of base peaks *i.e. m/z* = 34 amu (for $H_2{}^{16}O_2$) and 38 amu (for $H_2{}^{18}O_2$) was normalized to 100.

2.3.8 *Binding of O_2 to **1** in Crystallo*

The orange intermediate **3** is stable in MeOH at temperatures below –80 °C for weeks. Unfortunately, ongoing attempts to crystallize the μ-peroxo intermediate *in situ* have been unsuccessful so far, regardless of the counterion (PF_6^-, SbF_6^-, BF_4^-, and BPh_4^-) employed. Therefore, recent attempts have been focused on trapping a crystallographically characterizing O_2-derived intermediates *in crystallo*. This technique has been successfully applied to characterizing and studying three different intermediates in the O_2 activation and insertion reactions of an estradiol dioxygenase, an non-heme iron enzyme which catalyzes degradation of aromatic compounds in bacteria.[71] In this study, single crystals of homoprotocatechuate 2,3-dioxygenase (HPCD) were allowed to react with a slow-binding substrate 4-nitrocatechol in the presence of a

low concentration of O_2 before cryofreezing. As a result, a side-on Fe^{II}–O_2, an Fe^{II}–alkylperoxo, and an Fe^{II}–product intermediates were trapped in different subunits of a single crystal.[71]

In this preliminary work, a single of transparent crystal of $[(Fe^{II}(S^{Me2}N_4(tren))](BPh_4)$ (**1·BPh$_4$**), measuring 0.26 x 0.24 x 0.23 mm^3, was used to collect the X-ray diffraction data as a starting point. The small crystal was then left in a septum capped 20 mL vial, purged with a gentle stream of dry O_2 for 10 minutes, and left undisturbed for two days at room temperature. After two days, the crystal turned dark red, and the X-ray diffraction measurements were taken again, revealing that around 10 % of the crystal structure has changed. The solution obtained for the modified crystal contains mostly starting ferrous complex **1·BPh$_4$** and a dimeric structure bridged by O_2 molecule, (Figure 2.26). The O–O bond length is found at 1.468 Å, consistent with two-electron reduction to peroxo (O_2^{2-}). Interestingly, this complex has a very short Fe–O bond length at 1.574 Å and an long Fe–S bond length at 2.362 Å, which is very similar to the bond length found in a crystal structure of high-valent $[Fe^{IV}(S^{Me2}N_4(tren))(O)]^+$ (**4**) (Fe–S, 2.365 Å; Fe–O, 1.602 Å), (see Chapter 3). The obtained solution may therefore be a combination of μ-peroxo dimer **3** and a high-valent ferryl-oxo **4** found in a single crystal. While at this stage, these preliminary results cannot be taken for granted, *in crystallo* reactivity studies and structural characterization show a promising route to exploring iron-dioxygen chemistry and is currently developed further.

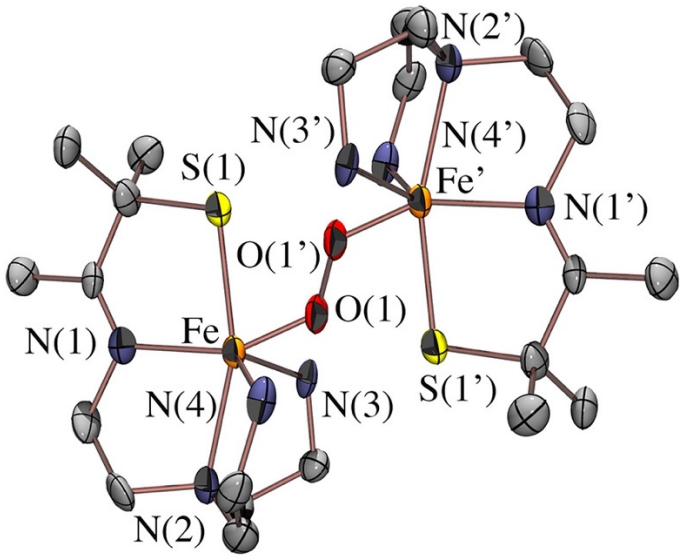

Figure 2.28. Crystal structure of the O_2-derived species trapped during *in crystallo* reaction of **1·BPh₄** with O_2, best described as $[(Fe^{III}(S^{Me2}N_4(tren)))_2(\mu\text{-}O_2)]^{2+}$ (**3**). All hydrogen atoms, counterions, and solvents of crystallization have been removed for clarity. Selected bond lengths for **3**: Fe–N(1), 2.048 Å; Fe–N(2), 2.263 Å; Fe–N(3), 2.147 Å; Fe–N(4), 2.120 Å; Fe–S(1), 2.362 Å; Fe–O(1), 1.574 Å; O(1)–O(1'), 1.468 Å.

2.4 Conclusions

This chapter describes the initial stage of O_2 binding in thiolate-ligated iron-dioxygen chemistry and characterization of two metastable intermediates. First step of O_2 binding to a thiolate-ligated complex $[Fe^{II}(S^{Me2}N_4(tren))]^+$ (**1**) affords a ferric-superoxo intermediate, $[Fe^{III}(S^{Me2}N_4(tren)(O_2))]^+$ (**2**). Ferric-superoxo **2** has been observed by cryogenic UV/Vis spectroscopy and its assignment has been supported by the DFT and TD-DFT calculations. Similar to our recently characterized bis-thiolate-ligated ferric-superoxo $[Fe^{III}(S_2{}^{Me2}N_3(Pr,Pr)(O_2)]$,[45] **2** is characterized by multiple absorption bands in the visible region, which are reproduced well computationally. Ferric-superoxo **2** is best described as a low-spin (S = 1/2) ferric complex antiferromagnetically coupled to the superoxide radical.

Unlike a bis-thiolate-ligated $[Fe^{III}(S_2{}^{Me2}N_3(Pr,Pr)(O_2)]$ that is capable of abstracting H atoms from strong C–H bonds,[45] ferric-superoxo **2** reacts with another equivalent of ferrous **1** to

afford a second metastable intermediate, best described as a dinuclear μ-peroxo, $[(Fe^{III}(S^{Me2}N_4(tren)))_2(\mu\text{-}O_2)]^{2+}$ (**3**). The dinuclear μ-peroxo **3** has been characterized as dimer with two low-spin ($S = 1/2$) ferric ions that couple antiferromagnetically ($-42\ cm^{-1} < J < -67\ cm^{-1}$) via an O–O peroxo bridge. **3** is stable at low temperature (–73 °C) in the presence of bases, HAT, and OAT reagents. However, μ-peroxo **3** reacts readily with acids to release around 0.5 equiv. H_2O_2 per iron, as seen by multiple H_2O_2 detection assays. H_2O_2 has been also detected by GC/MS method developed specifically for this work. Kinetic investigations suggest that the formation of the μ-peroxo bridged **3** is a second-order process overall with a first-order dependence on O_2 and first-order dependence on the starting ferrous complex **1**. Finally, preliminary *in crystallo* reactivity of **1·BPh$_4$** with O_2 reveal a dimeric structure with a peroxo O–O bridge, which may be consistent with a combination of μ-peroxo dimeric **3** and a high-valent Fe^{IV}=O **4**, which would form as a result of O–O bond activation and is a subject of the next chapter.

2.5 References

(1) Kovaleva, E. G.; Lipscomb, J. D. *Nat. Chem. Biol.* **2008**, *4* (3), 186–193.

(2) Costas, M.; Mehn, M. P.; Jensen, M. P.; Que, L. *Chem. Rev.* **2004**, *104* (2), 939–986.

(3) Abu-Omar, M. M.; Loaiza, A.; Hontzeas, N. *Chem. Rev.* **2005**, *105* (6), 2227–2252.

(4) Poulos, T. L. *Chem. Rev.* **2014**, *114* (7), 3919–3962.

(5) Kim, S. O.; Sastri, C. V.; Seo, M. S.; Kim, J.; Nam, W. *J. Am. Chem. Soc.* **2005**, *127* (12), 4178–4179.

(6) Chin, D.-H.; La Mar, G. N.; Balch, A. L. *J. Am. Chem. Soc.* **1980**, *102* (18), 5945–5947.

(7) Jiang, Y.; Telser, J.; Goldberg, D. P. *Chem. Commun.* **2009**, No. 44, 6828–6830.

(8) Thibon, A.; England, J.; Martinho, M.; Young, V. G.; Frisch, J. R.; Guillot, R.; Girerd, J.

J.; M??nck, E.; Que, L.; Banse, F. *Angew. Chemie - Int. Ed.* **2008**, *47* (37), 7064–7067.

(9) Gordon, J. B.; Vilbert, A. C.; DiMucci, I. M.; MacMillan, S. N.; Lancaster, K. M.; Moënne-Loccoz, P.; Goldberg, D. P. *J. Am. Chem. Soc.* **2019**, *141* (44), 17533–17547.

(10) Sono, M.; Roach, M. P.; Coulter, E. D.; Dawson, J. H. *Chem. Rev.* **1996**, *96* (7), 2841–2888.

(11) Meunier, B.; de Visser, S. P.; Shaik, S. *Chem. Rev.* **2004**, *104* (9), 3947–3980.

(12) Roach, P. L.; Clifton, I. J.; Hensgens, C. M. H.; Shibata, N.; Schofield, C. J.; Hajdu, J.; Baldwin, J. E. *Nature* **1997**, *387* (6635), 827–830.

(13) Orville, A. M.; Chen, V. J.; Kriauciunas, A.; Harpel, M. R.; Fox, B. G.; Munck, E.; Lipscomb, J. D. *Biochemistry* **1992**, *31* (19), 4602–4612.

(14) Kennepohl, P.; Neese, F.; Schweltzer, D.; Jackson, H. L.; Kovacs, J. A.; Solomon, E. I. *Inorg. Chem.* **2005**, *44* (6), 1826–1836.

(15) Kovacs, J. A.; Brines, L. M. *Acc. Chem. Res.* **2007**, *40* (7), 501–509.

(16) Brown, C. D.; Neidig, M. L.; Neibergall, M. B.; Lipscomb, J. D.; Solomon, E. I. *J. Am. Chem. Soc.* **2007**, *129* (23), 7427–7438.

(17) Kumar, D.; Sastry, G. N.; Goldberg, D. P.; De Visser, S. P. *J. Phys. Chem. A* **2012**, *116* (1), 582–591.

(18) Villar-Acevedo, G.; Lugo-Mas, P.; Blakely, M. N.; Rees, J. A.; Ganas, A. S.; Hanada, E. M.; Kaminsky, W.; Kovacs, J. A. *J. Am. Chem. Soc.* **2017**, *139* (1), 119–129.

(19) Shearer, J.; Scarrow, R. C.; Kovacs, J. A. *J. Am. Chem. Soc.* **2002**, *124* (39), 11709–11717.

(20) Theisen, R. M.; Kovacs, J. A. *Inorg. Chem.* **2005**, *44* (5), 1169–1171.

(21) Nam, E.; Alokolaro, P. E.; Swartz, R. D.; Gleaves, M. C.; Pikul, J.; Kovacs, J. A. *Inorg.*

Chem. **2011**, *50* (5), 1592–1602.

(22) Theisen, R. M.; Shearer, J.; Kaminsky, W.; Kovacs, J. A. *Inorg. Chem.* **2004**, *43* (24), 7682–7690.

(23) Theisen, R. M. Synthetic Models and Reactivity of Sulfur-Ligated Iron Metalloenzymes, University of Washington, 2005.

(24) Kurtz, D. M. *Chem. Rev.* **1990**, *90* (4), 585–606.

(25) Sahu, S.; Goldberg, D. P. *J. Am. Chem. Soc.* **2016**, *138* (36), 11410–11428.

(26) Ray, K.; Felix, F.; Wang, B.; Nam, W. *J. Am. Chem. Soc.* **2014**, *136*, 13942–13958.

(27) Balch, A. L.; Chan, Y. W.; Cheng, R. J.; La Mar, G. N.; Latos-Grazynski, L.; Renner, M. W. *J. Am. Chem. Soc.* **1984**, *106* (25), 7779–7785.

(28) Denisov, I. G.; Makris, T. M.; Sligar, S. G.; Schlichting, I. *Chem. Rev.* **2005**, *105* (6), 2253–2277.

(29) Green, M. T.; Dawson, J. H.; Gray, H. B. *Science* **2004**, *304* (5677), 1653–1656.

(30) Momenteau, M.; Reed, C. a. *Chem. Rev.* **1994**, *94*, 659–698.

(31) Evans, D. F. *J. Chem. Soc.* **1959**, 2003.

(32) Live, D. H.; Chan, S. I. *Anal. Chem.* **1970**, *42* (7), 791–792.

(33) Van Geet, A. L. *Anal. Chem.* **1968**, *40* (14), 2227–2229.

(34) Neese, F. *Interdiscipl. Rev. Comput. Mol. Sci.* **2012**, *2*, 73–78.

(35) Grimme, S.; Ehrlich, S.; Goerigk, L. *J. Comput. Chem.* **2011**, *32*, 1456–1465.

(36) Adamo, C.; Barone, V. *J. Chem. Phys.* **1999**, *110*, 6158–6170.

(37) Neese, F.; Wennmohs, F.; Hansen, A.; Becker, U. *Chem. Phys.* **2009**, *356* (1–3), 98–109.

(38) Shearer, J.; Fitch, S. B.; Kaminsky, W.; Benedict, J.; Scarrow, R. C.; Kovacs, J. a. *Proc. Natl. Acad. Sci. U. S. A.* **2003**, *100* (7), 3671–3676.

(39) Ellison, J. J.; Nienstedt, A.; Shoner, S. C.; Barnhart, D.; Cowen, J. A.; Kovacs, J. A. *J. Am. Chem. Soc.* **1998**, *120* (23), 5691–5700.

(40) Villar-Acevedo, G.; Lugo-Mas, P.; Blakely, M. N.; Rees, J. A.; Ganas, A. S.; Hanada, E. M.; Kaminsky, W.; Kovacs, J. A. *J. Am. Chem. Soc.* **2017**, *139* (1), 119–129.

(41) Soda, T.; Kitagawa, Y.; Onishi, T.; Takano, Y.; Shigeta, Y.; Nagao, H.; Yoshioka, Y.; Yamaguchi, K. *Chem. Phys. Lett.* **2000**, *319* (3–4), 223–230.

(42) Hirata, S.; Head-gordon, M. **1999**, No. December, 291–299.

(43) Neese, F.; Olbrich, G. **2002**, *362* (August), 170–178.

(44) Pettersen, E. F.; Goddard, T. D.; Huang, C. C.; Couch, G. S.; Greenblatt, D. M.; Meng, E. C.; Ferrin, T. E. *J. Comput. Chem.* **2004**, *25*, 1605–1612.

(45) Blakely, M. N.; Dedushko, M. A.; Yan Poon, P. C.; Villar-Acevedo, G.; Kovacs, J. A. *J. Am. Chem. Soc.* **2019**, *141* (5), 1867–1870.

(46) Shearer, J.; Nehring, J.; Lovell, S.; Kaminsky, W.; Kovacs, J. A. *Inorg. Chem.* **2001**, *40* (22), 5483–5484.

(47) Shearer, J.; Jackson, H. L.; Schweitzer, D.; Rittenberg, D. K.; Leavy, T. M.; Kaminsky, W.; Scarrow, R. C.; Kovacs, J. A. *J. Am. Chem. Soc.* **2002**, *124* (38), 11417–11428.

(48) Pikul, J. Modeling Superoxide Reductase and Superoxide Dismutase Reactivity, University of Washington, 2011.

(49) Battino, R.; Clever, H. L.; Young, C. L. In *Oxygen and Ozone*; Elsevier, 1981; Vol. 7, pp xiii–xviii.

(50) Wojdyr, M. *J. Appl. Crystallogr.* **2010**, *43* (5), 1126–1128.

(51) Ohta, T.; Liu, J.-G.; Nagaraju, P.; Ogura, T.; Naruta, Y. *Chem. Commun.* **2015**, *51* (62), 12407–12410.

(52) Fischer, A. A.; Lindeman, S. V.; Fiedler, A. T. *Chem. Commun.* **2018**, *54* (80), 11344–11347.

(53) Hong, S.; Sutherlin, K. D.; Park, J.; Kwon, E.; Siegler, M. a; Solomon, E. I.; Nam, W. *Nat. Commun.* **2014**, *5*, 5440.

(54) Oddon, F.; Chiba, Y.; Nakazawa, J.; Ohta, T.; Ogura, T.; Hikichi, S. *Angew. Chemie - Int. Ed.* **2015**, *54* (25), 7336–7339.

(55) Greiner, M. *Unpublished Results*.

(56) Luo, Y.-R. *Comprehensive Handbook of Chemical Bond Energies*; CRC Press, 2007.

(57) Baldwin, J. E.; Abraham, E. *Nat. Prod. Rep.* **1988**, *5* (2), 129.

(58) Lalevée, J.; Allonas, X.; Fouassier, J.-P. *J. Am. Chem. Soc.* **2002**, *124* (32), 9613–9621.

(59) Brines, L. M.; Shearer, J.; Fender, J. K.; Schweitzer, D.; Shoner, S. C.; Barnhart, D.; Kaminsky, W.; Lovell, S.; Kovacs, J. A.; Uni, V.; Chem, D. P. J. A. **2007**, *46* (22), 8569–8574.

(60) Makris, T. M.; Vu, V. V.; Meier, K. K.; Komor, A. J.; Rivard, B. S.; Münck, E.; Que, L.; Lipscomb, J. D. *J. Am. Chem. Soc.* **2015**, *137* (4), 1608–1617.

(61) Zheng, H.; Zang, Y.; Dong, Y.; Young, V. G.; Que, L. *J. Am. Chem. Soc.* **1999**, *121* (10), 2226–2235.

(62) Dong, Y.; Menage, S.; Brennan, B. A.; Elgren, T. E.; Jang, H. G.; Pearce, L. L.; Que, L. *J. Am. Chem. Soc.* **1993**, *115* (5), 1851–1859.

(63) Kitajima, N.; Tamura, N.; Amagai, H.; Fukui, H.; Moro-oka, Y.; Mizutani, Y.; Kitagawa, T.; Mathur, R.; Heerwegh, K. *J. Am. Chem. Soc.* **1994**, *116* (20), 9071–9085.

(64) Cranswick, M. A.; Meier, K. K.; Shan, X.; Stubna, A.; Kaizer, J.; Mehn, M. P.; Münck, E.; Que, L. *Inorg. Chem.* **2012**, *51* (19), 10417–10426.

(65) Warren, J. J.; Mayer, J. M. *Proc. Natl. Acad. Sci.* **2010**, *107* (12), 5282–5287.

(66) Xue, X. S.; Ji, P.; Zhou, B.; Cheng, J. P. *Chem. Rev.* **2017**, *117* (13), 8622–8648.

(67) Warren, J. J.; Tronic, T. a.; Mayer, J. M.; Bond, S. V. G. *Chem. Rev.* **2010**, *110* (12), 6961–7001.

(68) Tsuchida, E.; Yamamoto, K. In *Bioinorganic Catalysis*; Reedijk, J., Ed.; Marcel Dekker, Inc.: New York, 1993; pp 29–87.

(69) Foner, S. N.; Hudson, R. L. *J. Chem. Phys.* **1962**, *36* (10), 2676–2680.

(70) Tanko, J. M. *CRC Handbook of Chemistry and Physics: A Ready-Reference of Chemical and Physical Data*, 85th ed.; David R. Lide, Ed.; CRC Press LLC: Boca Raton, FL., 2004; Vol. 127.

(71) Kovaleva, E. G.; Lipscomb, J. D. *Science* **2007**, *316* (5823), 453–457.

Chapter 3. Activation of an O–O Bond by a Non-Heme Thiolate-Ligated Iron Complex

3.1 Introduction

Biological heme and non-heme iron enzymes comprise an important group of O_2-activating enzymes that are involved in many important oxidative transformations.[1–5] The mechanistic details of O_2 activation by enzymes and biomimetic model complexes has been studies extensively over the past few decades. As a result, high-valent Fe^{IV}=O intermediates have been proposed to form as a result of Fe-mediated O–O bond cleavage and have been hypothesized to be the active oxidizing species in enzymatic and biomimetic reactions. The best known examples of biological high-valent Fe^{IV}=O intermediates are those that were observed in cysteine-thiolate ligated heme enzymes such as CPO[6] and Cytochrome P450.[7] Recent experimental evidence also supports the involvement of high-valent Fe^{IV}=O species in a number of mono- and dinuclear non-heme iron enzymes such as IPNS,[8] Rieske dioxygenase,[9] MMO,[10,11] and TauD.[12,13] The bioinorganic community has sought to gain more insight into the electronic structure and function of these reactive intermediates. To that end, more than 60 synthetic high-valent Fe^{IV}=O complexes have been reported to date.[14–26]

Depending on the enzyme or synthetic complex in question, the fate of its high-valent Fe^{IV}=O intermediate varies. In biology, the Fe^{IV}=O reactive species can either perform an oxygen atom transfer reaction (for example in CDO)[27,28] or abstract a hydrogen atom from a substrate (for example in Cytochrome P450[7,29], IPNS[8], or MMO[10,11]). In the latter case, the afforded ferryl- and ferric-hydroxo (Fe^{III}–OH) intermediates proceed to hydroxylate a substrate via a rebound mechanism.[7,8,11,29] Therefore, ferric-hydroxo species also comprise an important class of reactive

intermediates derived from O_2 activation. While not observed spectroscopically, an Fe^{III}–OH intermediate was postulated to form as a result of hydrogen atom abstraction by a synthetic thiolate-ligated $[Fe^{IV}(O)(TMCS)]^{+}$.[22] More recently, several examples of structurally and spectroscopically characterized O_2-derived Fe^{III}–OH intermediates in synthetic complexes have been reported.[30–35] However, in most of the examples, the sequential O_2-derived intermediates that lead to the formation of these Fe^{III}–OH species were not observed.

This chapter describes experimental and theoretical evidence for the mechanism of an O–O bond activation in the reaction between the thiolate-ligated complex $[Fe^{II}(S^{Me2}N_4(tren))]^{+}$ (**1**) and O_2 at low temperatures. Specifically, theoretical calculations described herein provide groundwork to our understanding of the complex electronic structure of the high-valent ferryl-oxo intermediate, which has been previously crystallographically characterized. Next, spectroscopic and computational studies provide evidence for the ferric-hydroxo intermediate formed via hydrogen atom abstraction from solvent. Next, the chapter provides a description of the major pathway to the final μ-oxo dimer **6** product and minor pathways to afford a solvent-bound **7-OMe**, which has been crystallographically characterized.

3.2 Experimental

General Methods. All manipulations were performed using standard Schlenk techniques or under an N_2 atmosphere in a glovebox. Reagents and solvents were purchased from chemical vendors, were of highest available purity, and were used without further purification unless otherwise specified. $CDCl_3$ was purchased from Cambridge Isotope Labs and used as received. Tetrahydrofuran (THF) and diethyl ether (Et_2O) were purchased from Sigma-Aldrich and purified using a solvent purification column housed in a custom stainless-steel cabinet and dispensed by a

stainless steel Schlenk-line (GlassContour). Methanol (MeOH) and methanol-d_4 (CD_3OD) were distilled over magnesium turnings and sublimed iodine, and rigorously degassed prior to use. CD_3OD was purchased from Cambridge Isotope Labs.

^1H NMR spectra were obtained on a Bruker AV300, AV301, or AV500 spectrometers. Chemical shifts are listed in parts per million and were reported relative to TMS by referencing the residual solvent. Magnetic moments (solution state) were obtained using the Evans method as modified for superconducting solenoids.[36,37] Temperatures were obtained using Van Geet's method.[38] UV/Vis spectra were recorded on a Varian Cary 60 spectrophotometer equipped with a fiber optic cable connected to a "dip" ATR probe (C-technologies). A custom-built two neck solution sample holder equipped with a threaded glass connector was sized specifically to fit the "dip" probe. Electrospray-ionization mass spectra were obtained on a Bruker Esquire Liquid Chromatograph-Ion Trap mass spectrometer. Gas chromatography-mass spectrometry (GC/MS) data were obtained using a 6890 gas chromatograph equipped with a 7683 autosampler and interfaced with a 5973 mass spectrometer. FT-IR spectra were recorded on a Perkin-Elmer Frontier FT-IR spectrometer as nujol mulls on NaCl salt plates. X-ray crystallography data were recorded on a Bruker APEX II single crystal X-ray diffractometer with Mo Kα radiation.

Synthesis of $[Fe^{II}(S^{Me2}N_4(tren))](PF_6)$ (1). 3-mercapto-3-methyl-2-butanone (0.260 g, 2.2 mmol), was dissolved in 10 mL MeOH. To that, NaOMe (0.108 g, 2.0 mmol) was added and the mixture was stirring for 10 min, followed by the addition of *tris*(2-amonoethyl)amine (TREN) (0.234 g, 2.2 mmol). After stirring for an additional 20 min, the solution was cooled to –40 °C for an hour. In a separate vial, $FeCl_2$ (0.456 g, 2.0 mmol) was dissolved in MeOH (5 mL) and cooled to –40 °C for an hour as well. The ferrous solution was then added dropwise into the cooled

solution containing thiolate and TREN ligand. The solution turned dark green immediately, was let stirring at room temperature for an hour, followed by addition of $NaPF_6$ (0.334 g, 2.0 mmol). The reaction solution was stirred at room temperature overnight and then filtered through a bed of celite. MeOH was evacuated and the resulting dark-green precipitate was redissolved in MeCN (10 mL). The solution was filtered through a bed of celite again, MeCN concentrated down to 3 mL. The concentrate was layered with Et_2O (17 mL) to crush out the complex over two nights at –40 °C. To attain highest purity, the resulting dark brown-red solid was redissolved in MeOH (3 mL), filtered through a fine frit, and recrystallized under layered Et_2O over two nights at –40°C. Final light-green solid (0.6 g, 70% yield) is 96% pure using quantitative UV/Vis of $[(Fe^{III}(S^{Me2}N_4(tren)))_2(\mu\text{-}O)](PF_6)_2$ (**6**) in MeCN with λ_{max} (ε): 480 nm (5270 M^{-1} cm^{-1}, 20 °C).

Synthesis of $[Fe^{III}(S^{Me2}N_4(tren)(MeCN))](BPh_4)_2$·MeCN (7-MeCN). 3-mercapto-3-methyl-2-butanone (0.260 g, 2.2 mmol), was dissolved in 10 mL MeOH. To that, NaOMe (0.108 g, 2.0 mmol) was added and the mixture was stirring for 10 min, followed by the addition of *tris*(2-amonoethyl)amine (TREN) (0.234 g, 2.2 mmol). After stirring for an additional 20 min, the solution was cooled to –40 °C for an hour. In a separate vial, $FeCl_3$ (324 mg, 2.00 mmol) was dissolved in MeOH (10 mL) and cooled to –40 °C for an hour as well. In a third vial, $NaBPh_4$ (685 mg, 2.00 mmol) was dissolved in 7.5 mL MeCN and cooled at – 40 °C. In an hour, $FeCl_3$ was added dropwise to the cold ligand solution while stirring. The solution turned dark purple immediately. The solution of $NaBPh_4$ was added and the solution turned deep blue. The undissolved salts were removed by filtering through the bed of Celite, the solution was evacuated to ~ 3 mL and layered over with Et_2O. Crystals of **7-MeCN** were formed over a few days at –40 °C. Electronic absorption of $[Fe^{III}(S^{Me2}N_4(tren)(MeCN))](BPh_4)_2$·MeCN (**7-MeCN**) in MeCN

with λ_{max} (ε): 580 nm (1975 M^{-1} cm^{-1}, 20 °C), EPR (MeCN/Toluene glass (1:1), 117 K): $g_{\perp}$ = 2.17, $g_{\parallel}$ = 2.00.

Synthesis of [Fe^{III}($S^{Me2}N_4$(tren)(OMe))](PF_6) (7-OMe). In a glovebox, **1** (0.093 g, 0.209 mmol) was washed to remove residual MeCN cocrystallization solvent by dissolving in and removing MeOH (3 mL) three times and redissolved in MeOH (3 mL). In a separate vial, ferrocenium hexafluorophosphate (Cp_2FePF_6) (0.069 g, 0.209 mmol) was dissolved in MeOH (3 mL). Both vials were cooled to –40 °C for 30 minutes. Then, the Cp_2Fe^+ solution was added to the cold solution of **1**, causing an immediate color change to burgundy, indicating the formation of **7-OMe**. After the removal of MeOH, **7-OMe** was washed repeatedly with cold Et_2O (40 mL total) until no ferrocene (Cp_2Fe) remained. Isolated product (0.999 g, 100% yield) was stored at –40 °C. Electronic absorption of **7-OMe** in MeOH with λ_{max} (ε): 511 nm (1765 M^{-1} cm^{-1}, –40 °C), EPR (MeOH/EtOH glass (9:1), 8.0 K): $g_{\perp}$ = 4.10, $g_{\parallel}$ = 3.53.

Formation of [Fe^{III}($S^{Me2}N_4$(tren))(OH)](PF_6) (5) via the Addition of O_2 to 1. A 0.378 mM solution of **1** was prepared in MeOH under an inert atmosphere in a glovebox. The resulting solution was transferred via gastight syringe to a custom-made two-neck vial equipped with septum cap and threaded dip-probe feed-through adaptor that had been previously purged with argon gas through a septum cap for at least 20 minutes. The solution was cooled in an acetone/dry ice bath to –73 °C. Argon stream was removed from the vial and a stream of O_2 gas was bubbled through the solution over the course of 2 minutes, resulting in the formation of peroxo-bridged **3**. After that, **3** was brought up to –40 °C by quickly switching to acetonitrile/dry ice bath. Over the course of 30 minutes, the orange peroxo-bridged **3** cleanly converted to magenta colored **5.** The

same procedure was used to prepare 0.4 mM samples of **5** in EPR tubes for EPR spectroscopy and 10 mM samples in NMR tubes for ^{1}H NMR spectroscopy. Electronic absorption of **5** in MeOH with λ_{max} (ε): 540 nm (1750 M^{-1} cm^{-1}, –40 °C), EPR (MeOH/EtOH glass (9:1), 117 K): $g_{\perp} = 2.24$, $g_{\parallel} = 1.96$.

Alternative Formation of [$Fe^{III}(S^{Me2}N_4$(tren))(OH)](PF$_6$) (5) via the Addition of Bu_4NOH to [$Fe^{III}(S^{Me2}N_4$(tren))(OMe)]$^+$ (7-OMe) or [$Fe^{III}(S^{Me2}N_4$(tren))(MeCN)]$^+$ (7-MeCN). A 0.378 mM solution of **7-OMe** was prepared in MeOH under an inert atmosphere in a glovebox. The resulting solution was transferred via gastight syringe to a custom-made two-neck vial equipped with septum cap and threaded dip-probe feed-through adaptor that had been previously purged with argon gas through a septum cap for at least 20 minutes. The solution was cooled in an acetonitrile/dry ice bath to –40 °C. To that, methanolic solution of Bu_4NOH (100 μL, 10.0 equiv., 1.89 x 10^{-2} mmol) was injected using a gaslight syringe. The reaction was monitored by UV/Vis over the course of seven days, resulting in full conversion to magenta **5** with λ_{max} at 540 nm. Similar procedure was performed with the addition of Bu_4NOH (100 μL, 1.0 equiv., 1.89 x 10^{-3} mmol) to **7-MeCN** (0.378 mM) in MeCN at –40 °C, resulting in rapid (less than 1 minute) conversion to magenta **5** with λ_{max} at 540 nm.

X-ray Crystallographic Structure Determination. A red piece, [$Fe^{III}(S^{Me2}N_4$(tren))(OMe)]$^+$ (**2-OMe**), measuring 0.08 x 0.08 x 0.08 mm^3 was mounted on a loop with oil. Data was collected at –173 °C on a Bruker APEX II single crystal X-ray diffractometer, Mo-radiation. Crystal-to-detector distance was 40 mm and exposure time was 30 seconds per frame for all sets. The scan width was 0.5°. Data collection was 99.8% complete to 25° in θ. A total of 4637 merged reflections

were collected covering the indices, -13<=h<=13, -10<=k<=10, -15<=l<=15. 4340 reflections were symmetry independent and the R_{int} = 0.0473 indicated that the data was excellent. Indexing and unit cell refinement indicated a primitive monoclinic lattice. The space group was found to be P 2_1 (No. 4). The structure solved in space groups P 2_1 and P 2_1/m. The R_1 in the centrosymmetric space group was considerably worse than for the chiral one. In addition, the disorder model in P 2_1 sees the atoms on both sides of a pseudo-mirror plane at very different site occupancies (0.87:0.13), whereas a true mirror would have both sides at 0.5 site occupancy. The pseudo mirror symmetry was simply a result of 1:1 enantiomorphic twinning. The disordered methoxy group interacts with the disordered PF_6^- which exhibits the exact same disorder site occupancies.

Data was integrated and scaled using SAINT, SADABS within the APEX2 software package by Bruker.[39] Solution by direct methods (SHELXT[40] or SIR97[41]) produced a complete heavy atom phasing model consistent with the proposed structure. The structure was completed by difference Fourier synthesis with SHELXL.[42,43] Scattering factors are from Waasmair and Kirfel.[44] Hydrogen atoms were placed in geometrically idealized positions and constrained to ride on their parent atoms with C---H distances in the range 0.95-1.00 Angstrom. Isotropic thermal parameters U_{eq} were fixed such that they were 1.2 U_{eq} of their parent atom Ueq for CH's and 1.5 U_{eq} of their parent atom U_{eq} in case of methyl groups. All non-hydrogen atoms were refined anisotropically by full-matrix least-squares. Final solutions were plotted using ORTEP and POV-Ray programs.[45,46]

Table 3.1. Crystal data, intensity collections [a] and structure refinement parameters for $[Fe^{III}(S^{Me2}N_4(tren))(OMe)]^+$ (**7-OMe**).

	7-OMe
Formula	$C_{13}H_{32}F_6FeN_4O_2PS$
Molecular Weight (g mol^{-1})	509.30
Temperature (K)	100(2)
Crystal System	Monoclinic
Space Group	P 2_1
a, (Å)	10.4236(9)
b, (Å)	8.6965(7)
c, (Å)	12.0629
α, (°)	90
β, (°)	104.350(5)
γ, (°)	90
V (Å^3)	1059.37
Z	2
R_1	0.0562[b]
R_w	0.1097[c]
GOF	1.015

[a] Mo Ko(α,-) (λ = 0.71070 Å) radiation; graphite monochromator; -90 °C. [b] $R = \Sigma ||F_o| - |F_c|| / \Sigma |F_o|$. [c] $R_w = [\Sigma w(|F_o| - |F_c|)^2/\Sigma wF_o^2$, where $w^{-1} = [\sigma^2_{count} + (0.05\ F^2)^2]/4F^2$.

Computational Details. All calculations were performed using the ORCA v.4.1.1 quantum chemistry package developed by Neese and coworkers,[47] and employed the def2-TZVP basis set and the def2/J auxiliary basis set for Coulomb fitting, the atom-pairwise dispersion correction of Grimme (D3BJ).[48] Tight convergence criteria, together with Grid5 (GridX5) and FinalGrid6 (FinalGridX6) integration grid size, were required for self-consistent field (SCF) solutions. Geometry optimization were performed using B3LYP hybrid functional, with the resolution of identity (RI) chain-of-spheres (RIJCOSX) approximation,[49,50] and initiated from the

crystallographic coordinates when available. Analytical frequency calculations were performed on all optimized structures to determine whether the obtained stationary points correspond to local minima. Extended hybrid DFT calculations employed a modified B3LYP* functional where the amount of Hartree-Fock exchange was varied manually from 0% to 40 % in 5% increments.

3.3 Results and Discussion

3.3.1 *Structural Characterization of a cis Thiolate-Ligated $[Fe^{IV}(O)(S^{Me2}N_4(tren))]^+$ (4)*

The ability of the mono-thiolate ligated $[Fe^{II}(S^{Me2}N_4(tren))]^+$ (**1**) to bind and reduce O_2 resulted in the observation of the two metastable intermediates at low temperatures, namely a superoxo-bound $[Fe^{III}(S^{Me2}N_4(tren))(O_2)]^+$ (**2**) and a μ-peroxo dimeric $[(Fe^{III}(S^{Me2}N_4(tren)))_2(\mu\text{-}O_2)]^{2+}$ (**3**). We have also shown that the final product of the reactivity between **1** and O_2, either at room temperature[51] or by warming up the μ-peroxo intermediate **3** to room temperature, results in formation of a μ-oxo dimer **6,** bridged by a single oxygen atom. These results suggest that the mono-thiolate ligated **1** is capable of activating an O–O bond via a homolytic bond cleavage en route to forming a final μ-oxo product. If the μ-peroxo dimeric **3** undergoes an O–O bond cleavage, then it would afford two equiv. of high-valent $[Fe^{IV}(O)(S^{Me2}N_4(tren))]^+$ (**4**) species, (Figure 3.1).

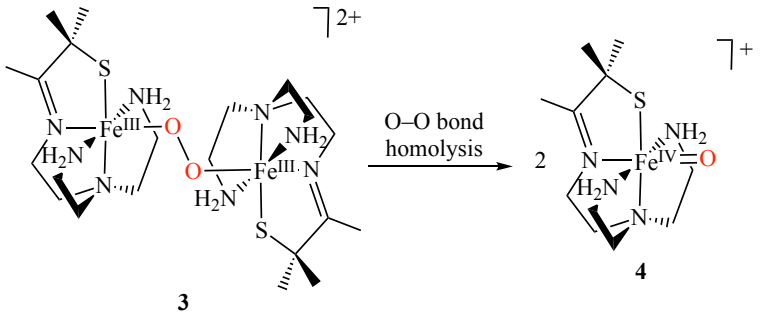

3 4

Figure 3.1. An O–O bond homolysis in μ-peroxo dimeric $[(Fe^{III}(S^{Me2}N_4(tren)))_2(\mu\text{-}O_2)]^{2+}$ (**3**) would result in formation of two equiv. of high-valent $[Fe^{IV}(O)(S^{Me2}N_4(tren))]^+$ (**4**).

When O_2 (from air) was briefly introduced into a saturated, pale yellow/green solution of $[Fe^{II}(S^{Me2}N_4(tren))](PF_6)$ (**1**)[52] in MeOH at –80 °C, maintaining the temperature at –80 °C for several days, then single crystals of a new intense green species **4** formed. As shown in the ORTEP diagram of Figure 3.2, $[Fe^{IV}(O)(S^{Me2}N_4(tren))]^+$ (**4**) contains an oxo atom O(1) coordinated to the metal *cis* to a thiolate sulfur S(1) and *trans* to the imine nitrogen N(1). The oxo atom O(1) strongly interacts with the Fe center, which is reflected in the Fe moving 0.39 Å above the S(1)-N(3)-N(2)-N(4) plane, and an elongation of the Fe–N(1) bond (2.237(9) Å) *trans* to the oxo O(1). The green species **4** was cocrystalized with one PF_6^- counterion, indicating that the overall charge of **4** is +1. Coordination of one thiolate (RS^-) and one oxygen atom in the formal O^{2-} oxidation state would indicate that the Fe center is formally in the +4 oxidation state.

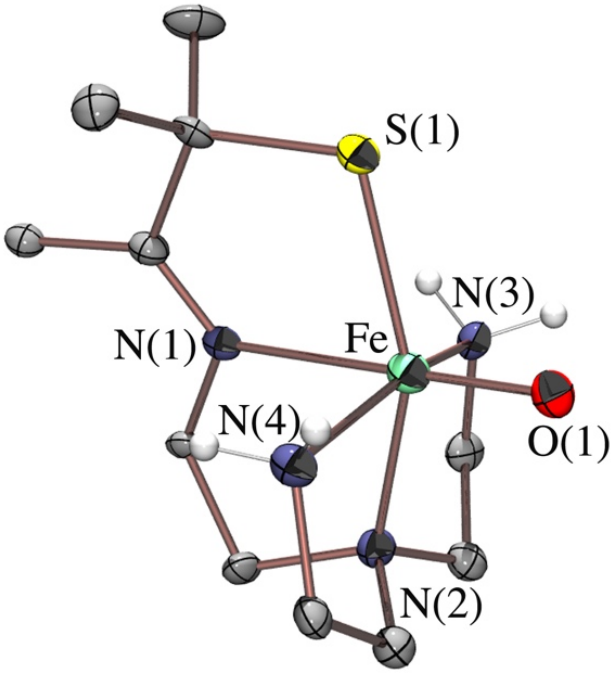

Figure 3.2. ORTEP diagram of $[Fe^{IV}(O)(S^{Me2}N_4(tren))]^+$ (**4**) displaying 50% probability ellipsoids and atom-labeling scheme. All hydrogen atoms, counterions, and solvents of crystallization have been removed for clarity. Selected bond lengths for **4**: Fe–N(1), 2.237(9) Å; Fe–N(2), 2.116(9) Å; Fe–N(3), 2.16(3) Å; Fe–N(4), 2.09(3) Å; Fe–S(1), 2.361(3) Å; Fe–O(1), 1.603(7) Å.

The crystallographically determined Fe–O(1) bond length of 1.603(7) Å (Table 3.2) is consistent with the high oxidation state at the metal center. Interestingly, the Fe–O(1) bond is shorter than any other synthetic Fe^{IV}=O complexes reported to date (range: 1.62 – 1.70 Å; Table 1.2),[16–26] as well as P450 Compound I (1.670 Å),[7] CPO Compound I (1.661 Å),[6,53,54] and TauD (1.62 Å).[12,13] This bond is significantly shorter than in lower-valent complex $[Fe^{III}(O)(H_3buea)]^{2-}$ (1.813(3) Å),[19] but is 0.02 Å longer than that of $[Fe^{V}(O)(TAML)]^{1-}$ (1.58 Å).[55] The Fe-O(1) bond length is significantly shorter than in reported examples of synthetic Fe^{III}–F complexes, with some synthesized from a PF_6^- counterion, by about 0.2 Å, (range: 1.841 – 1.91 Å).[56–59] However, as a control, the O^{2-} atom was also replaced with an F^- atom during the refinement of the X-ray structure. The F^- atom's thermal ellipsoid increased by 65% (from 0.023(2) $Å^2$ to 0.038(2) $Å^2$), indicating a poor fit, thus ruling out that **4** is a fluoro-bound complex. The Fe–S(1) bond of 2.361(3) Å is unusually long. The Fe–S(1) of **4** is longer than that of the Fe^{III} variations of this complex (**7-OMe**, **7-MeCN**, **7-N_3**, **6**) and the starting Fe^{II} complex **1**, (Table 3.2). On the other hand, it is similar in length to that of the only other reported synthetic thiolate-ligated Fe^{IV}=O $[Fe^{IV}(O)(TMCS)]^+$ (2.33(2) Å)[22] and P450 Compound I (^{Cys}S–Fe^{IV}=O = 2.391 Å), but shorter than CPO Compound I (^{Cys}S–Fe^{IV}=O = 2.481 Å).[7] The structural parameters of $[Fe^{IV}(O)(TMCS)]^+$ were obtained from EXAFS, as opposed to X-ray crystallography, with the thiolate positioned *trans* to the oxo.[22] Therefore, $[Fe^{IV}(O)(S^{Me2}N_4(tren))]^+$ (**4**) is the only crystallographically characterized example of a thiolate-ligated Fe^{IV}=O, and the first example of a *cis*-thiolate ligated Fe^{IV}=O.

Table 3.2. Comparison of selected bond distances (Å), angles (deg), and spin states for $[Fe^{II}(S^{Me2}N_4(tren))]^+$ (**1**),[52] $[Fe^{IV}(O)(S^{Me2}N_4(tren))]^+$ (**4**), μ-oxo bridged $[(Fe^{III}(S^{Me2}N_4(tren)))_2(\mu\text{-}O)]^{2+}$ (**6**),[51] $[Fe^{III}(S^{Me2}N_4(tren))(OMe)]^+$ (**7-OMe**), $[Fe^{III}(S^{Me2}N_4(tren))(MeCN)]^{2+}$ (**7-MeCN**),[52] $[Fe^{III}(S^{Me2}N_4(tren))(OMe)]^+$ (**7-N_3**).[60]

	1 $S = 2$	**4**	**6** $S = 3/2$	**7-OMe** $S = 3/2$	**7-MeCN** $S = 1/2$	**7-N_3** $S = 1/2$
Fe-S(1)	2.3281(9)	2.361(3)	2.317(4)	2.3138(18)	2.146(1)	2.176(2)
Fe-N(1)	2.091(3)	2.237(9)	2.19(1)	2.169(6)	1.911(2)	1.917(6)
Fe-N(2)	2.268(3)	2.116(9)	2.24(1)	2.231(6)	2.026(2)	2.002(6)
Fe-N(3)	2.131(3)	2.16(3)[a]	2.21(1)	2.149(9)	2.001(2)	2.011(5)
Fe-N(4)	2.117(3)	2.09(3)	2.17(1)	2.148(9)	2.018(2)	2.002(5)
Fe-O(1)	N/A	1.603(7)	1.807(8)	1.885(6)	N/A	N/A
N(1)-Fe-N(3)	124.95(1)	82.9(8)	89.1(4)	92.1(4)	95.43(8)	90.8(2)
N(3)-Fe-N(4)	115.2(1)	157.1(3)	153.2(4)	150.4(2)	163.79(7)	165.6(2)
S(1)-Fe-N(2)	163.02(7)	156.0(3)	154.5(4)	157.66(16)	171.96(6)	172.1(2)
S(1)-Fe-N(1)	84.02(8)	78.0(2)	80.4(3)	80.27(17)	86.59(6)	86.8(2)
S(1)-Fe-O(1)	N/A	102.5(3)	99.6(3)	97.5(3)	N/A	N/A
O(1)-Fe-N(1)	N/A	177.75(8)	178.6(4)	177.7(4)	N/A	N/A
O(1)-Fe-N(4)	N/A	98.3(9)	103.2(4)	85.6(4)	N/A	N/A
O(1)-Fe-N(2)	N/A	101.6(4)	102.9(4)	104.8(3)	N/A	N/A
O(1)-Fe-N(3)	N/A	94.9(8)	92.3(4)	88.8(4)	N/A	N/A

[a]Disorder about a crystallographic mirror plane that relates N(3) and N(4) increases the error associated with these bond lengths in structure **4**.

The thiolate and the oxo ligands are both strong π-donors and the *trans* influence of the thiolate in $[Fe^{IV}(O)(TMCS)]^+$ complex was thought to contribute to the lengthening of both the Fe–S and the Fe–O bonds.[61] This is consistent with the unusually short Fe–O bond in *cis*-thiolate ligated **4**, but not with its long Fe–S bond. The unusually long and short Fe–S and Fe–O bonds, respectively, can be rationalized if the characteristic bonding properties of the thiolate and the oxo ligands are taken into account. The thiolate and the oxo ligands form highly covalent σ and π bonds

and, as a result, compete for the Fe's σ- and π-symmetry d-orbitals in **4**. The oxo ligand is more electronegative than the thiolate and will likely dominate both bonding and anti-bonding interactions. This is consistent with the short Fe–O bond, along the z-axis, and the pull of the Fe metal out of the xy-plane (S(1)-N(3)-N(2)-N(4) plane). The short Fe–O bond suggests that the σ-(d_{z2}) and π-symmetry (d_{xz}, d_{yz}) d-orbitals are empty. The long Fe–S bond indicates that the d_{x2-y2} orbital pointing toward the thiolate sulfur is filled. Since both the oxo and the thiolate ligands are strong π-donors, this scenario is possible in a d^4 ion where the π-symmetry (d_{xz}, d_{yz}) d-orbitals are more destabilized than and lie above the σ-symmetry d_{x2-y2} orbital, (Figure 3.3). Moreover, the simultaneous π-overlap of the d_{xz} orbital with both the thiolate and the oxo would lift the degeneracy of the d_{xz} and d_{yz} orbitals, which favors the $S = 1$ spin state in most reported Fe^{IV}=O compounds.[14] The $S = 2$ spin state may be achieved in trigonal geometry where the d_{xy} and d_{x2-y2} orbitals become degenerate as well. The unique combination of the strong thiolate and oxo π-donors *cis* to each other in a pseudo-octahedral geometry lifts the degeneracy of the metal's d-orbitals, which may give rise to an $S = 0$ spin state.

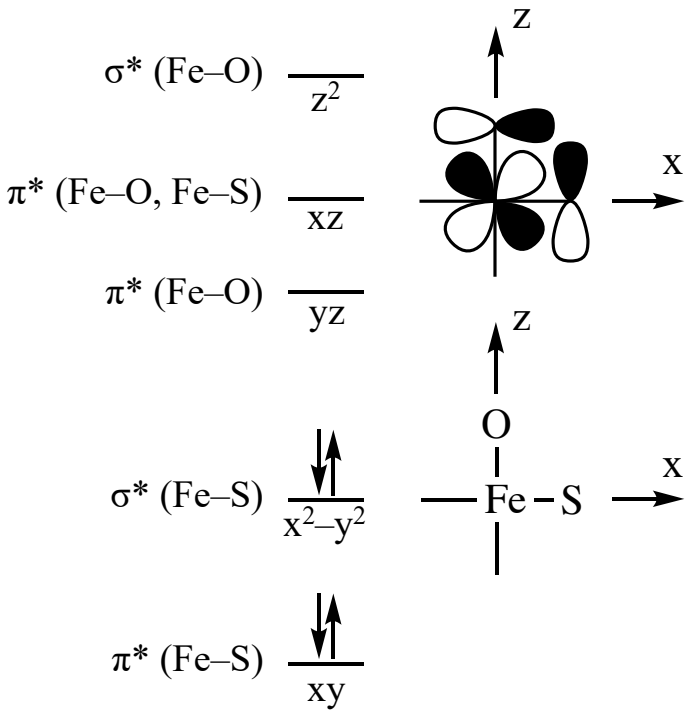

Figure 3.3. A proposed d-orbital splitting diagram of $[Fe^{IV}(O)(S^{Me2}N_4(tren))]^+$ (**4**) which is consistent with the short Fe–O bond as a result of strong antibonding interaction of the metal's d_{z2}, d_{xz}, d_{yz} orbitals with the oxo's p-orbitals and the long Fe–S bond as result of populated d_{xy} and d_{x2-y2} orbitals.

3.3.2 *Theoretical Characterization of a cis Thiolate-Ligated $[Fe^{IV}(O)(S^{Me2}N_4(tren))]^+$ (4)*

In order to gain more insight into the electronic nature of the *cis*-thiolate ligated Fe^{IV}=O $[Fe^{IV}(O)(S^{Me2}N_4(tren))]^+$ (**4**) complex, computational studies were performed at various theory levels. Crystallographic parameters of **4** were used as a starting point for all calculations and geometry optimizations were performed for $S = 0$, 1, and 2 states. Def2-TZVP polarized triple-ζ-valence basis set was used in every calculation. Pure and hybrid DFT calculations using various functionals (*e.g.*, BP86, B3LYP, PBE0, TPSSh) all fail to accurately model the geometric structure of **4**. Specifically, every calculation overestimates the Fe–O bond length and drastically underestimates the Fe–S bond length. Examples of calculated bond lengths from geometry optimizations using PBE0 and TPSSh functionals are shown in Table 3.3.

Table 3.3. Comparison of selected bond distances between the crystallographically-characterized **4** and its geometry optimizations for $S = 0$, 1, and 2 spin states.

	4	PBE0/Def2-TZVP			TPSSh/Def2-TZVP		
		$S = 0$	$S = 1$	$S = 2$	$S = 0$	$S = 1$	$S = 2$
Fe-O(1)	1.603(7)	1.634	1.633	1.634	1.631	1.624	1.642
Fe-S(1)	2.361(3)	2.258	2.256	2.221	2.225	2.225	2.194
Fe-N(1)	2.237(9)	2.014	2.013	2.203	2.105	2.115	2.020
Fe-N(2)	2.116(9)	2.009	2.017	2.174	2.207	2.251	2.168
Fe-N(3)	2.16(3)	2.006	2.007	2.233	2.291	2.234	2.253
Fe-N(4)	2.09(3)	2.005	2.005	2.235	2.038	2.045	2.255

Given the unsatisfactory results of standard hybrid DFT calculations, theoretical modeling **4** was explored through the extended hybrid DFT technique. Extended hybrid DFT calculations entail manual modification of the amount of Hartree-Fock (HF) exchange in a given functional. For this study, the structure of **4** was reoptimized using a modified B3LYP* functional by manually changing the amount of HF exchange from 0 % to 40 % in 5 % increments. Systematic variation of the amount of HF, or exact, exchange energy was performed in order to survey how the geometry of **4** responds to the increasing contribution of the electron-electron interactions. The unusual geometric structure of **4**, described above, points out to a complex electronic structure where the thiolate and the oxo compete and strongly influence the ordering of the metal's d-orbitals.

Successful geometry optimizations of **4** were performed for $S = 0$, 1, and 2 spin-states. The Fe–O and Fe–S bond length variation as a function of HF exchange is shown in Figure 3.4. The accuracy of computational modeling of **4** though the extended DFT technique improves with the increasing amount of HF exchange for every spin-state, albeit at a varied amount. Geometry optimizations of **4** in the $S = 2$ spin state are least accurate, with the longest Fe–O bond length that levels off around 1.628 Å with higher HF exchange mixing. This is reasonable because in the high-

spin $S = 2$ state the four unpaired electrons will occupy t_{2g} and e_g* orbitals, which would lead to the Fe–O bond elongation. Calculations of the $S = 1$ spin state shows the most accurate modeling of the Fe–O bond, reaching the crystallographically determined bond at 1.603 Å at 35% HF exchange mixing. Calculations for the $S = 0$ spin state provide the Fe–O bond length at 1.616 Å but a much better modeling for the Fe–S bond, which reaches 2.265 Å at 40% HF exchange mixing. While these calculations still underestimate the Fe–S bond length, they are an improvement to the traditional pure and hybrid DFT calculations on **4** we have to date. The geometric structure of **4** is decently modeled for both the $S = 0$ and $S = 1$ spin states at the higher HF exchange mixing. This may indicate that the electronic structure of **4** could be described as a combination of the $S = 0$ spin state and an accessible, low-lying, $S = 1$ state.

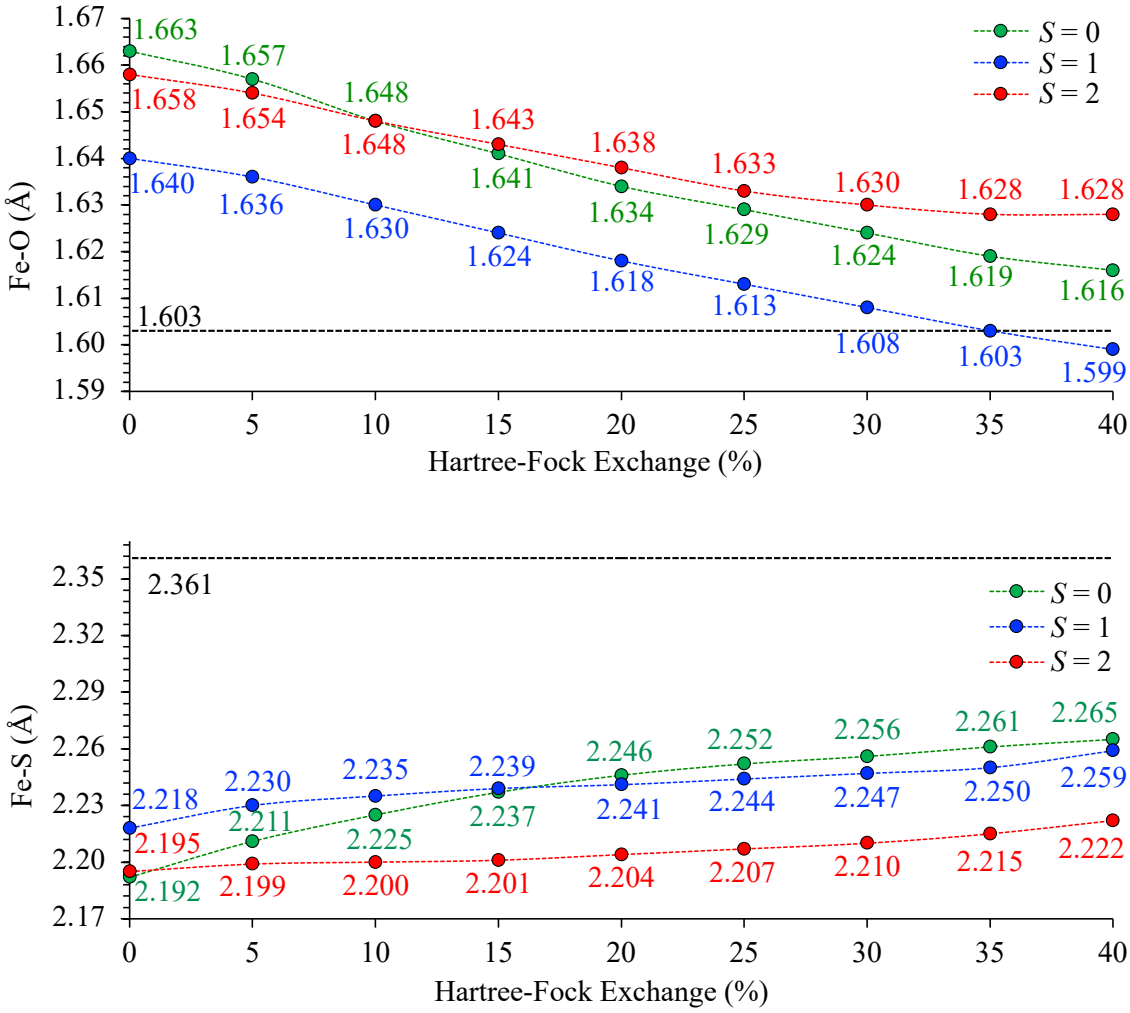

Figure 3.4. The Fe–O and the Fe–S bond lengths derived from geometry optimizations using the extended hybrid DFT using a modified B3LYP* functional. The amount of Hartree-Fock exchange was manually changed from 0% to 40% in 5% increments.

3.3.3 *Characterization of a Ferric-Hydroxo, $[Fe^{III}(S^{Me2}N_4(tren))(OH)]^+$ (**5**), Intermediate*

As discussed in Chapter 2, the μ-peroxo dimer **3** is stable for hours in MeOH at –73 °C. Upon warming from –73 °C to room temperature, **3** fully converts in less than 10 minutes to an EPR silent (at 117 K $\perp$-mode) μ-oxo dimer **6** at λ_{max}= 500 nm, (Figure 2.9; Chapter 2). However, when **3** is warmed to –40 °C, as opposed to room temperature, it converts to a new magenta species, characterized by an absorption band at λ_{max}= 540 nm, over the course of 30 minutes, (Figure 3.5).

At –80 °C, **3** remains stable for weeks and eventually converts to the same magenta species at λ_{max}= 540 nm. The long reaction time, coupled with the need for warming, implies that this conversion reaction has to overcome a high activation energy barrier, which may be indicative of an O–O bond cleavage and/or hydrogen atom abstraction process.

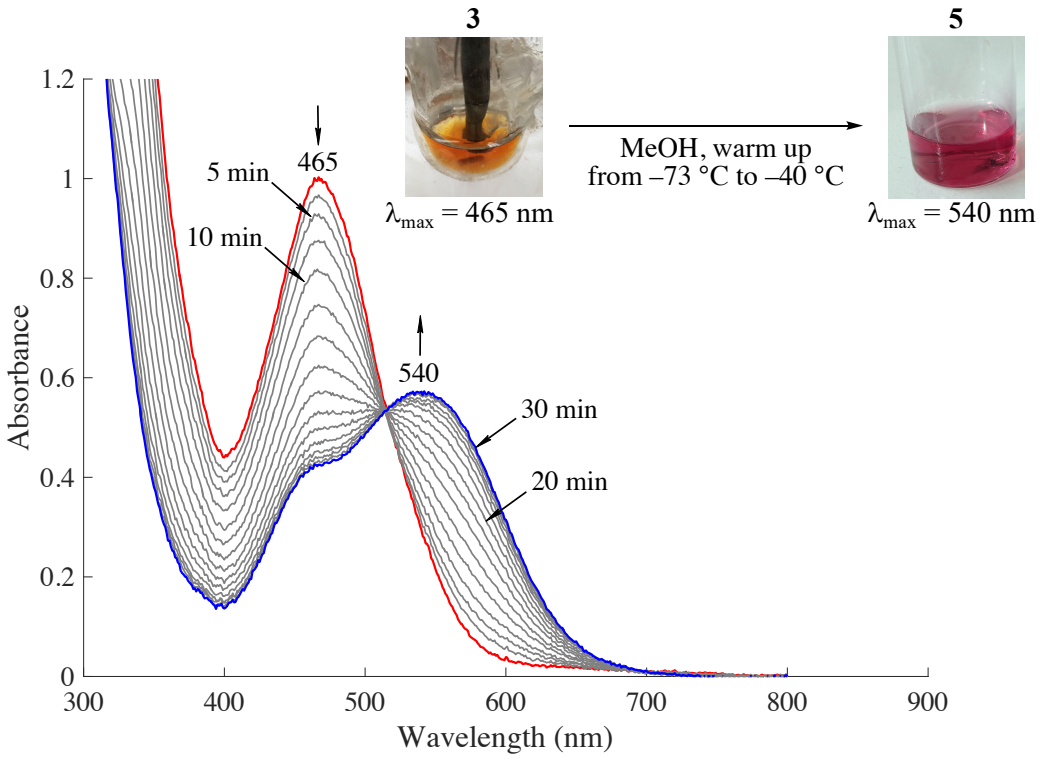

Figure 3.5.Electronic absorption spectrum of the conversion of the orange intermediate **3** (λ_{max} = 465 nm) to a new metastable magenta intermediate **5** (λ_{max} = 540 nm) over the course of 30 minutes in MeOH as a result of warming the reaction solution from –73 °C to –40 °C.

Although a single crystal of high-valent ferryl-oxo **4** has been isolated and crystallographically characterized n from the low temperature reaction of **1** and O_2 in MeOH, it has been described as intensely green. The absorption band of the new magenta species at λ_{max}= 540 nm in MeOH solvent, however, falls in the usual spectral range of previously identified thiolate-ligated ferric derivatives of **1** such as **7-OMe** (λ_{max} = 511 nm),[65] **7-MeOH** (λ_{max} = 565 nm),[66] $[Fe^{III}(S^{Me2}N_4(tren))(OAc)]^+$ (**7-OAc**) (λ_{max} = 537 nm),[51] and $[Fe^{III}(S^{Me2}N_4(tren))(Cl)]^+$ (**7-**

Cl) (λ_{max} = 544 nm).[67] To test if the new O_2-derived magenta intermediate λ_{max}= 540 nm is a ferric complex, conversion from **3** to 540 nm species was monitored simultaneously by the UV/Vis and EPR. Gradual conversion of an EPR silent **3** to magenta species at 540 nm is accompanied by the concomitant growth of an axial EPR signal ($g_{\perp}$ = 2.24, $g_{\parallel}$ = 1.97), consistent this new species being a low spin S = 1/2 ferric complex, (Figure 3.6).

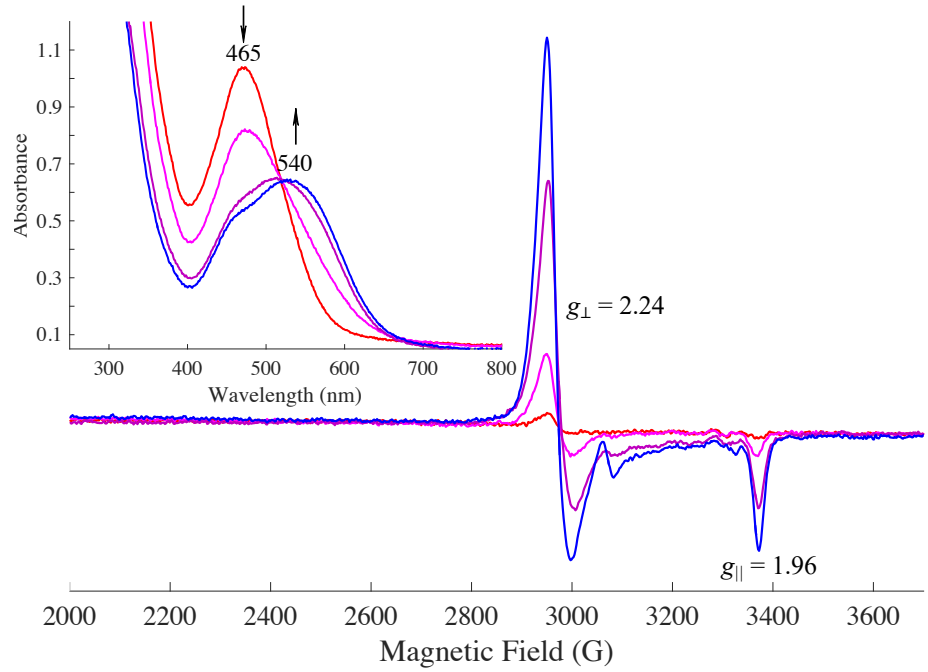

Figure 3.6. 9.28 GHz CW X-band EPR (⊥-mode) and the electronic absorption spectra (top-right inset) of the aliquots of the conversion of μ-peroxo **3** (λ_{max} = 465 nm) to a new metastable species **5** (λ_{max} = 540 nm). The conversion monitored by EPR indicates that the intermediate **5** is a low spin (S = 1/2) ferric complex with $g_{\perp}$ = 2.24 and $g_{\parallel}$ = 1.97. EPR measurements were taken at 117 K in MeOH/EtOH (9:1) glass.

Moreover, conversion of **3** to the new low-spin ferric species at 540 nm exhibits a large kinetic isotope effect in deuterated (CD_3OD) solvent. The observed rate constant for the conversion **3** to 540 nm species is $k_{obs,\,(H)}$ = 1.6 x 10^{-2} min^{-1} in CH_3OH, while in CD_3OD, the observed rate constant is $k_{obs,\,(D)}$ = 4.0 x 10^{-3} min^{-1}, resulting in the observed deuterium isotope effect of k_H/k_D = 4.0, (Figure 3.7). Preliminary studies of the conversion of **3** to the magenta species

at 540 nm in the presence of a sacrificial hydrogen atom donor (200 equiv. of TEMPOH, BDE(O–H) = 69 kcal mol^{-1})[68,69] in MeOH resulted in the observed kinetic isotope effect of k_H/k_D = 5.0. Conversion studies in the presence of a sacrificial hydrogen donor such as TEMPOH, CHD, *etc*, need to be revisited since they were done with a different batch of **1** that exhibited different rate constants ($k_{obs,\,(H)}$ = 3.8 x 10^{-3} min^{-1} and $k_{obs,\,(TEMPOH)}$ = 1.9 x 10^{-2} min^{-1}).

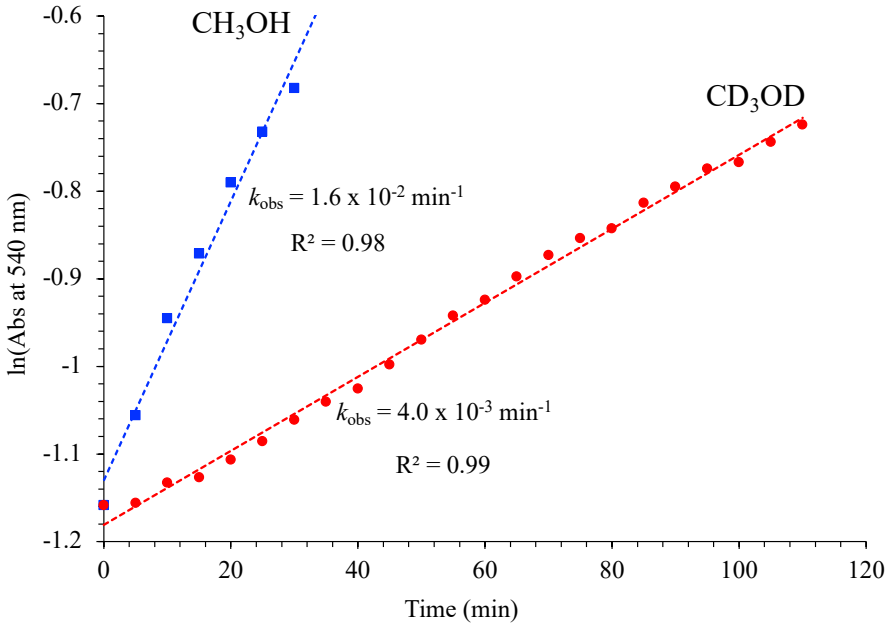

Figure 3.7. Pseudo-first order kinetic plots associated with the conversion of **3** (λ_{max} = 465 nm) to **5** (λ_{max} = 540 nm) in CH_3OH (blue) and CD_3OD (red).

In summary, the O_2-derived μ-peroxo intermediate **3** undergoes an O–O bond cleavage to generate spectroscopically unobserved, but crystallographically characterized, $[Fe^{IV}(O)(S^{Me2}N_4(tren))]^+$ (**4**), which in turn abstracts a hydrogen atom from solvent to afford a new low-spin ferric intermediate at λ_{max} = 540 nm, best described as a hydroxo-bound $[Fe^{III}(S^{Me2}N_4(tren))(OH)]^+$ (**5**). The proposed mechanism of an O–O bond activation by a thiolate-ligated **1** from μ-peroxo to ferric-hydroxo is outlined in Figure 3.8.

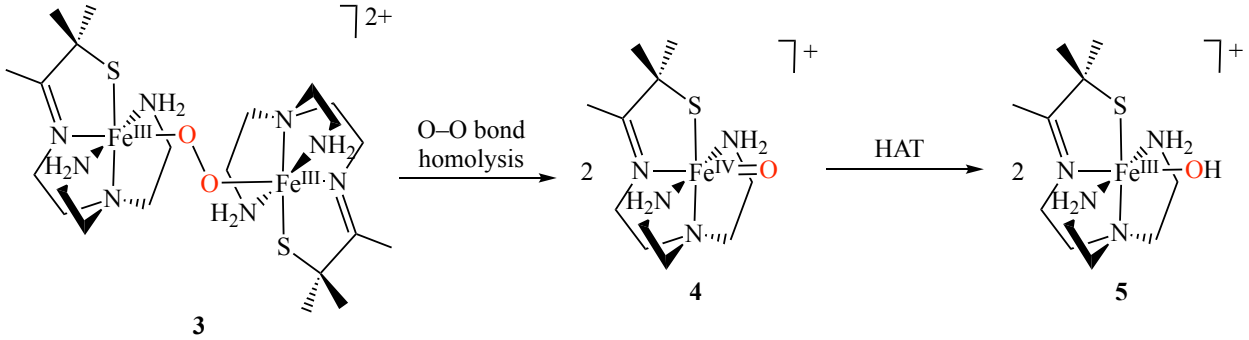

Figure 3.8. Proposed mechanism of formation of a hydroxo-bound $[Fe^{III}(S^{Me2}N_4(tren))(OH)]^+$ (**5**) (λ_{max}= 540 nm) via hydrogen atom abstraction by $[Fe^{IV}(O)(S^{Me2}N_4(tren))]^+$ (**4**) as a result of O–O bond cleavage of $[(Fe^{III}(S^{Me2}N_4(tren)))_2(\mu\text{-}O_2)]^{2+}$ (**3**).

3.3.4 *Independent Generation of a Ferric-Hydroxo **5** via Ligand Substitution*

To further confirm that the new species **5** at λ_{max}= 540 nm is a hydroxo-bound ferric complex, it was generated by solvent ligand substitution with hydroxide anion. When monitored by UV/Vis, addition of an excess (12 equiv.) of Bu_4NOH to methoxide-bound ferric complex **7-OMe** (λ_{max} = 511 nm)[65] results in the gradual shift of the 511 nm band to 540 nm over the course of six days in MeOH at –73 °C, (Figure 3.9). **7-OMe** is an intermediate S = 3/2 spin complex and appears EPR silent at 117 K in ⊥-mode. When monitored by EPR, the red-shift from **7-OMe** to 540 nm is accompanied by the growth of a low spin signal, with g-values ($g_\perp$ = 2.24, $g_\parallel$ = 1.97) identical to those seen for the O_2-derived **5** at λ_{max}= 540 nm, (Figure 3.10). Although hydroxide is a stronger field ligand than methoxide and is expected to bind more readily, the reaction takes up to six days when monitored by UV/Vis and EPR. The slow rate of ligand exchange, from methoxide to hydroxo, likely results from the extensive hydrogen bonding between the MeOH solvent and **7-OMe** as well as free OH^- ligand in solution that is competing for the iron's binding site.

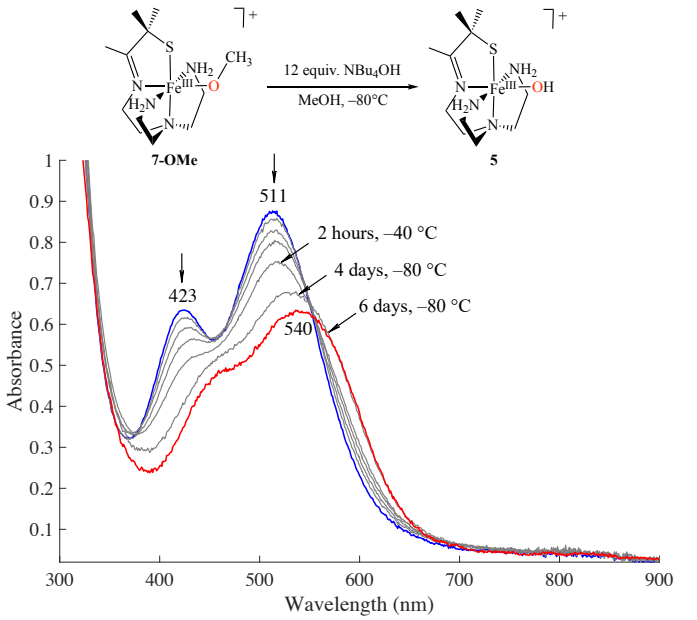

Figure 3.9. Electronic absorption spectrum of the conversion of the solvent bound $[Fe^{III}(S^{Me2}N_4(tren))(OMe)]^+$ (**7-OMe**) (λ_{max} = 511 nm), as a result of addition of excess (12 equiv.) NBu_4OH, to a hydroxo-bound $[Fe^{III}(S^{Me2}N_4(tren))(OH)]^+$ (**5**) (λ_{max} = 540 nm) in MeOH at –80 °C over the course of six days.

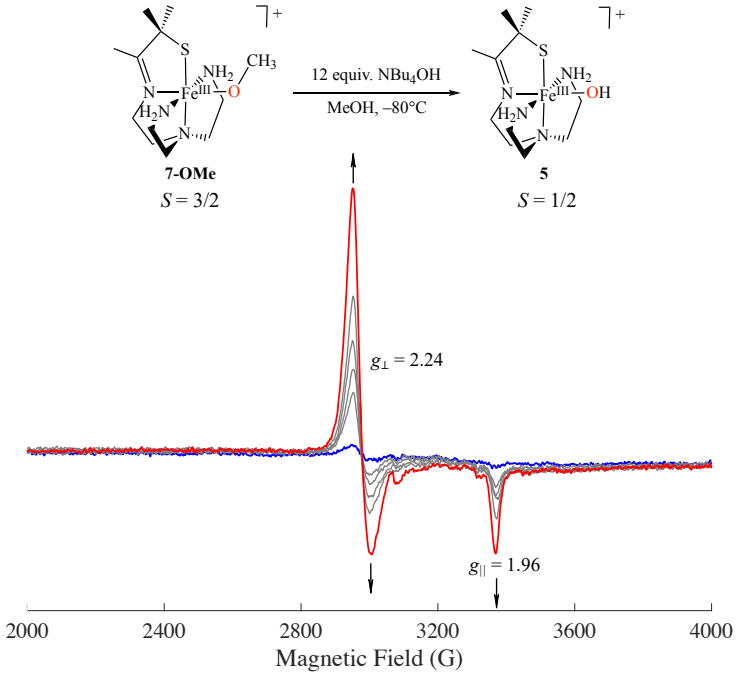

Figure 3.10. 9.28 GHz CW X-band EPR (⊥-mode) showing growth of a hydroxo-bound $[Fe^{III}(S^{Me2}N_4(tren))(OH)]^+$ (**5**) with a low spin (S = 1/2) axial signal ($g_\perp$ = 2.24, $g_\parallel$ = 1.97) as a result of addition of excess (12 equiv.) of NBu_4OH to the solvent bound $[Fe^{III}(S^{Me2}N_4(tren))(OMe)]^+$ (**7-OMe**) complex with an intermediate (S = 3/2) spin state. EPR measurements were taken at 117 K in MeOH/EtOH (9:1) glass.

To test if MeOH solvent was slowing down the ligand substitution, the proposed hydroxo-bound **5** was also generated by reacting Bu_4NOH with acetonitrile-bound **7-MeCN**, in 1:1 MeCN/toluene solvent at –40 °C. Unlike intermediate spin **7-OMe**, **7-MeCN** is a low spin $S = 1/2$ ($g_\perp = 2.17$, $g_\parallel = 2.00$), and is characterized by an intense CT transition at $\lambda_{max}(\varepsilon) = 585$ nm (1975 M^{-1} cm^{-1}).[52] When monitored by UV/Vis, the 585 nm peak of **7-MeCN** readily converted to 540 nm within 3 minutes upon the addition of only one equivalent of Bu_4NOH, (Figure 3.11). When the same reaction was monitored by EPR, a second axial signal identical to that of O_2-derived **5** appeared, indicating that **7-MeCN** and hydroxo-bound ferric complex **5** are in equilibrium (Figure 3.12). On the other hand, addition of an excess (10 equiv.) of Bu_4NOH resulted in the instantaneous growth of a band at 480 nm (5290 M^{-1} cm^{-1}) instead, indicating formation of the μ-oxo dimer **6** as a result of condensation reaction between the two ferric-hydroxo **5** intermediates**,** consistent with previously reported studies on the reversible μ-oxo dimer **6** formation.[51]

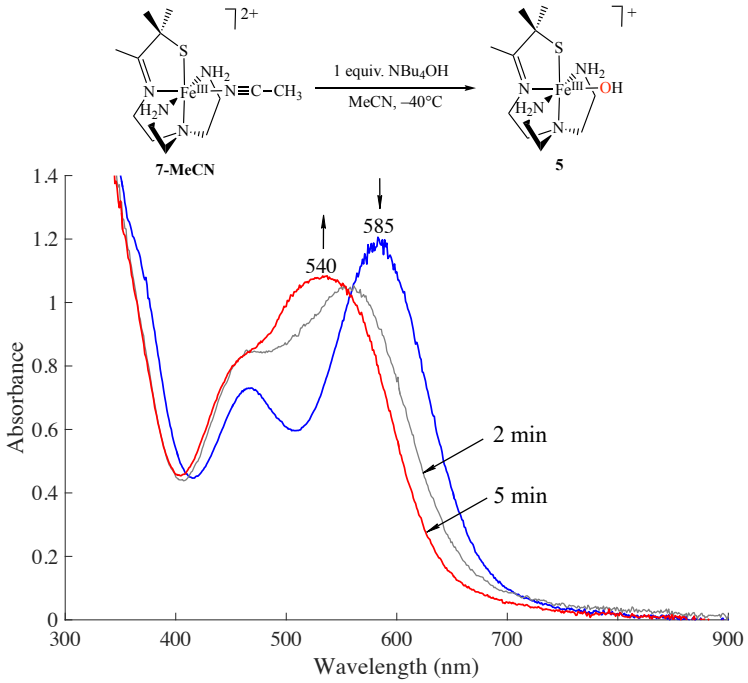

Figure 3.11. Electronic absorption spectrum of the conversion of the solvent bound $[Fe^{III}(S^{Me2}N_4(tren))(MeCN)]^{2+}$ (**7-MeCN**) (λ_{max}= 585 nm), as a result of addition of 1 equiv. NBu_4OH, to a hydroxo-bound $[Fe^{III}(S^{Me2}N_4(tren))(OH)]^{+}$ (**5**) (λ_{max}= 540 nm) in MeCN at –40 °C over the course of 5 minutes.

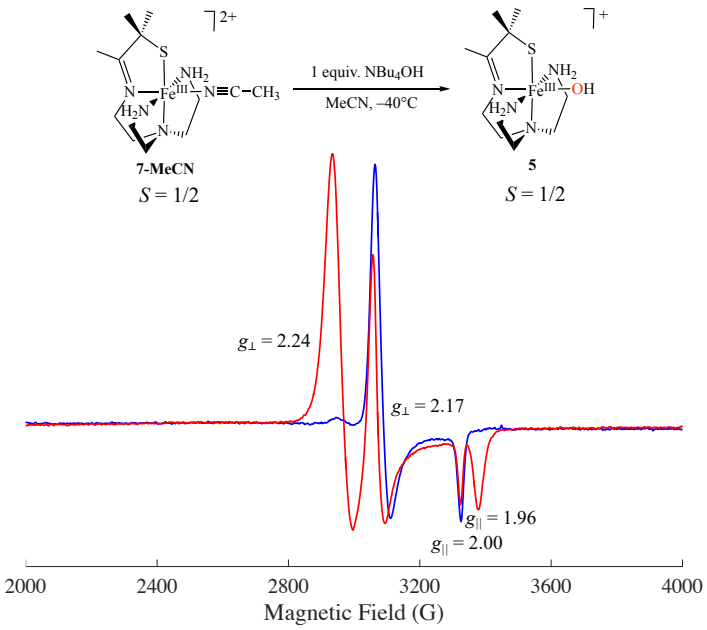

Figure 3.12. 9.28 GHz CW X-band EPR (⊥-mode) showing growth of a hydroxo-bound $[Fe^{III}(S^{Me2}N_4(tren))(OH)]^+$ (**5**) with a low spin (S = 1/2) axial signal ($g_\perp$ = 2.24, $g_\parallel$ = 1.97) as a result of addition of 1 equiv. of NBu_4OH to the low spin (S = 1/2) acetonitrile bound $[Fe^{III}(S^{Me2}N_4(tren))(MeCN)]^{2+}$ (**7-MeCN**) complex, ($g_\perp$ = 2.17, $g_\parallel$ = 2.00). EPR measurements were taken at 117 K in MeCN/Toluene (1:1) glass.

3.3.5 *Theoretical Calculation of a Hydroxo-Bound $[Fe^{III}(S^{Me2}N_4(tren))(OH)]^+$ (**5**)*

The assignment of the magenta species **5** at λ_{max} = 540 nm as a hydroxo-bound ferric complex is supported by computational studies. In the absence of a crystal structure of **5**, crystallographic coordinates of the previously characterized[60] low-spin (S = 1/2) azide-bound $[Fe^{III}(S^{Me2}N_4(tren)(N_3))]^+$ (**7-N_3**) complex were used as a starting point, with the N_3^- replaced by a OH^- ligand. DFT calculations were performed with the B3LYP* hybrid functional and the Def2-TZVP polarized triple-ζ-valence basis set. The amount of Hartree-Fock exchange in B3LYP functional was decreased to 15%. The optimized structure of ferric-hydroxo **5** contains an OH^- moiety *cis* to the thiolate sulfur, (Figure 3.13). The calculated Fe–O(1) (1.891 Å) and O(1)–H(1) (0.963 Å) bond lengths are typical for other ferric-hydroxo species (Fe–O bond length range: 1.84

– 1.93 Å).[31–33,70,71] The Fe–S(1) (2.203 Å) and an average Fe–N_{ave} (2.02 Å) metal-ligand distances are consistent with a low-spin ferric center with the $[S^{Me2}N_4(tren)]^-$ ligand system.[52,60,72]

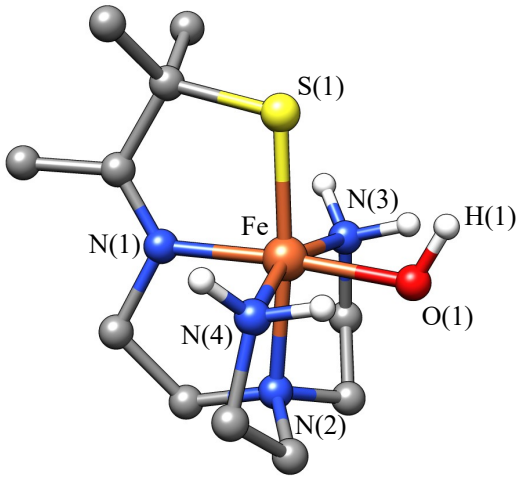

Figure 3.13. DFT optimized geometry of low-spin hydroxo-bound $[Fe^{III}(S^{Me2}N_4(tren))(OH)]^+$ (**5**). Selected calculated bond lengths and angles for **5**: Fe–N(1), 1.959 Å; Fe–N(2), 2.066 Å; Fe–N(3), 2.041 Å; Fe–N(4), 2.027 Å; Fe–S(1), 2.203 Å; Fe–O(1), 1.891 Å; O(1)–H(1), 0.963 Å; Fe–O(1)–O(1), 114.4°.

The TD-DFT calculated electronic absorption spectrum of hydroxo-bound **5** reproduces the two main CT bands in the visible region well, (Figure 3.14). Specifically, the experimental absorption band at λ_{max} = 540 nm is simulated at $\lambda_{max, calc}$ = 520 nm and shoulder at λ_{max} = 465 nm is correlated to $\lambda_{max, calc}$ = 470 nm. The calculated spectrum shows that the lower energy band at $\lambda_{max, calc}$ = 520 nm is predominantly $S_\pi \rightarrow Fe_d$ in character, while the higher energy band at $\lambda_{max, calc}$ = 520 nm is dominated by the $S_\sigma \rightarrow Fe_d$ charge transfer transition. These results are consistent with spectroscopic and computational studies of the low-spin bis-thiolate ferric complexes $[Fe^{III}(S_2^{Me2}N_3(Pr,Pr)(N_3)]$ and $[Fe^{III}(S_2^{Me2}N_3(Pr,Pr)]^+$ previously reported in collaboration with Edward Solomon.[73] Moreover, both absorption bands include a partial contribution from the hydroxo ligand in the form of $O_\pi \rightarrow Fe_d$ charge transfer transition. DFT calculations of the EPR *g*-values have also been performed at the B3LYP functional level. As seen in Figure 3.15, DFT

calculated *g*-values at $g_{\perp\,(calc)} = 2.18$ and $g_{\parallel\,(calc)} = 2.04$ are in agreement with the experimental *g*-values ($g_{\perp} = 2.24$ and $g_{\parallel} = 1.96$). Most importantly, DFT calculated EPR accurately predicts axial symmetry of the *g*-spread, with $g_x \approx g_y$. The differences are expected partly due to off-diagonal non-zero elements in the calculated *g*-matrix. B3LYP functional-based EPR calculations are considered to be the most accurate for transition metal complexes.[74,75] However, significant systematic deviations of the calculated EPR *g*-values still remain and have not yet been resolved.[75]

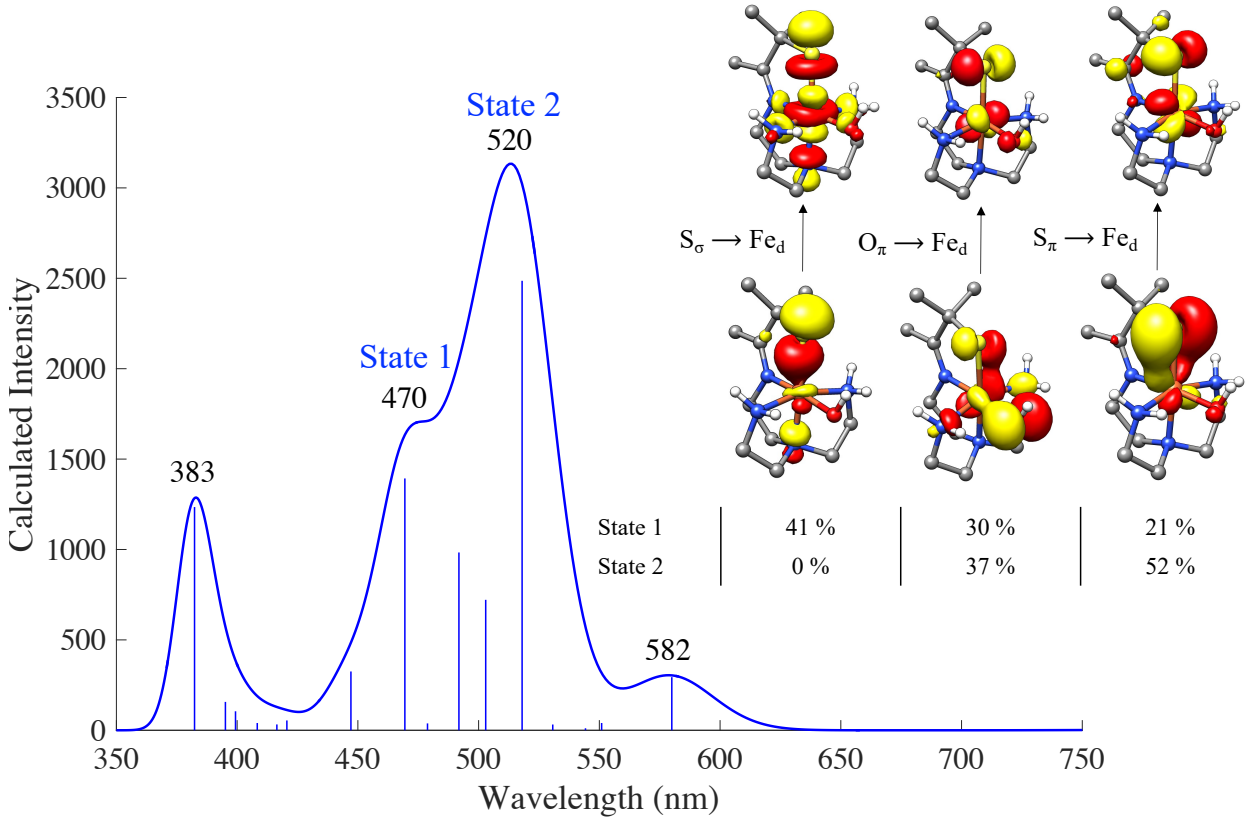

Figure 3.14. TD-DFT calculated electronic absorption spectrum of hydroxo-bound complex $[Fe^{III}(S^{Me2}N_4(tren))(OH)]^+$ (**5**) including natural transition orbitals (NTO) describing the charge transfer (CT) transitions.

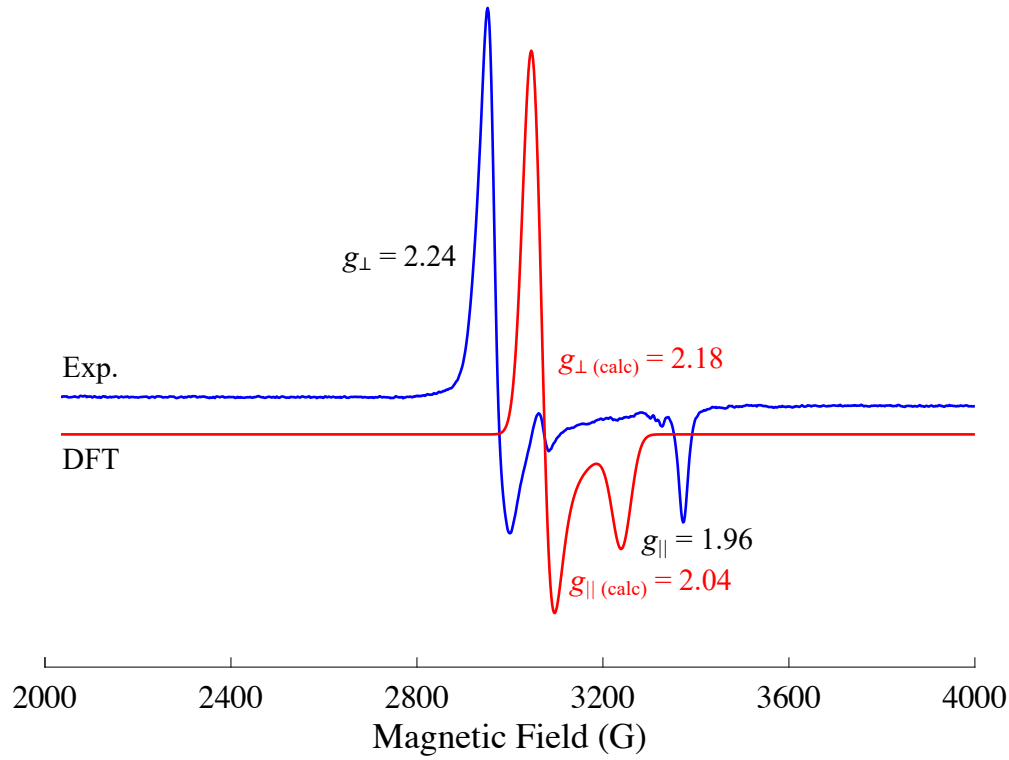

Figure 3.15. Comparison of experimental (blue) and DFT calculated (red) EPR spectra of $[Fe^{III}(S^{Me2}N_4(tren))(OH)]^+$ (**5**).

3.3.6 *Conversion of a Ferric-Hydroxo $[Fe^{III}(S^{Me2}N_4(tren))(OH)]^+$ (**5**) to the μ-Oxo Bridged $[(Fe^{III}(S^{Me2}N_4(tren)))_2(\mu\text{-}O)]^{2+}$ (**6**)*

The O_2-derived hydroxo-bound **5** is stable at –40 °C in MeOH for hours. Cooling down the solution of **5** from –40 °C back to –73 °C causes no spectral changes when monitored by UV/Vis, indicating that formation of **5** is irreversible. However, when the reaction mixture is warmed from –40 °C to room temperature, the absorption band at 540 nm of hydroxo-bound **5** converts to a band λ_{max}= 500 nm, (Figure 3.16). When the same reaction is monitored by the EPR, the characteristic low spin (S = 1/2) axial signal ($g_{\perp}$ = 2.24, $g_{||}$ = 1.97) of **5** disappears. These results are consistent with conversion of **5** to μ-oxo bridged **6** (EPR silent at 117 K) via a condensation reaction. Although previously reported crystallographically characterized μ-oxo dimer **6** was obtained in

the reaction between **1** and O_2 in aprotic MeCN solvent,[51] crystallization attempts of low temperature intermediates in the reaction between **1** and O_2 in MeOH have also resulted in crystallographic characterization of **6**.

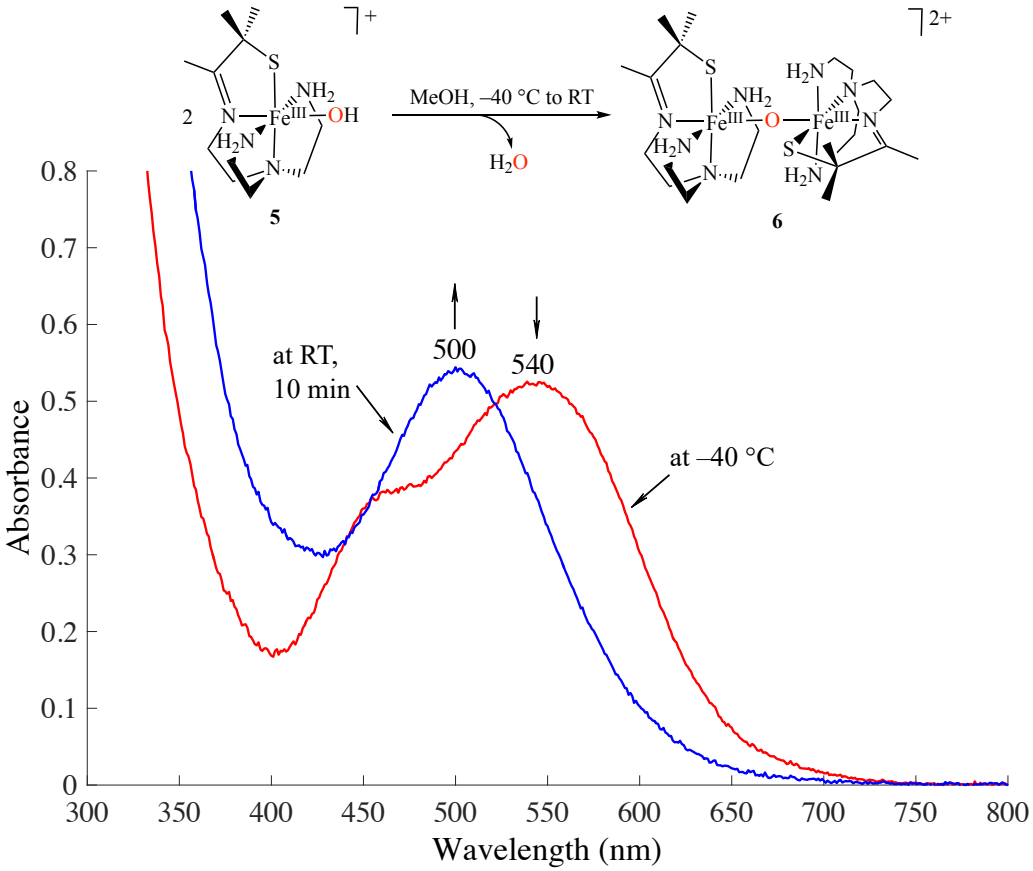

Figure 3.16. Electronic absorption spectrum of the conversion of the hydroxo-bound $[Fe^{III}(S^{Me2}N_4(tren))(OH)]^+$ (**5**) (λ_{max}= 540 nm) to μ-oxo bridged $[(Fe^{III}(S^{Me2}N_4(tren)))_2(\mu\text{-}O)]^{2+}$ (**6**) (λ_{max}= 500 nm) upon warming the reaction mixture from –40 °C to room temperature.

Formation of the final product **6** appears to follow the major pathway in the reactivity between **1** and O_2 in protic MeOH solvent. However, in one of the crystallization attempts of low temperature intermediates between **1** and O_2, a single red-purple crystal of methoxide-bound $[Fe^{III}(S^{Me2}N_4(tren))(OMe)]^+$ (**7-OMe**) complex, suitable for X-ray diffraction, was isolated in MeOH –80 °C. As shown in the ORTEP diagram, (Figure 3.17), the Fe–O(1) bond length of

1.885(6) Å and the Fe–S(1) bond length of 2.3138(18) Å are in close agreement to the EXAFS structural data previously obtained for **7-OMe** (Fe–O(1) = 1.94(10) Å, Fe–S(1) = 2.31(7) Å).[65]

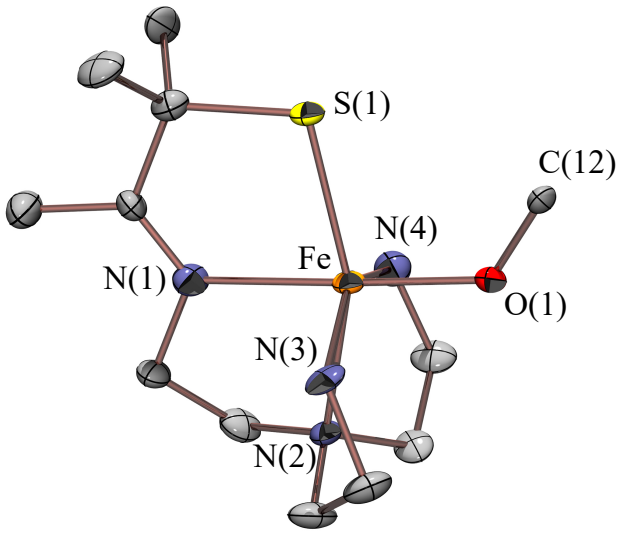

Figure 3.17. ORTEP diagram of $[Fe^{III}(S^{Me2}N_4(tren))(OMe)]^+$ (**7-OMe**) displaying 50% probability ellipsoids and atom-labeling scheme. All hydrogen atoms, counterions, and solvents of crystallization have been removed for clarity. Selected bond lengths for **7-OMe**: Fe–N(1), 2.169(6) Å; Fe–N(2), 2.231(6) Å; Fe–N(3), 2.149(9) Å; Fe–N(4), 2.148(9) Å; Fe–S(1), 2.3138(18) Å; Fe–O(1), 1.885(6) Å.

This observation indicates that there may be minor pathways that lead to the formation of **7-Me**. Specifically, it is conceivable that MeOH may protonate the hydroxo moiety of **5**, release 1 equiv. of H_2O, followed by the substitution of OMe^- ligand at the ferric site, (Figure 3.18, A). Alternatively, MeOH could potentially protonate the oxo bridge in the μ-oxo dimer **6** which would lead to the μ-oxo bridge cleavage to afford 1 equiv. of hydroxo-bound **5** and 1 equiv. of methoxide bound **7-OMe**, (Figure 3.18, B). Previously reported reactivity studies have shown that the μ-oxo bridge of **6** can be reversibly cleaved at low temperatures by either weak (HOAc, NH_4PF_6, LutHCl) or strong (HCl, HBF_4) proton donors.[51,67] MeOH is a weak proton donor (pK_a = 15.5) which also appears to be able to reversibly cleave the μ-oxo bridge of **6** at low temperature as well.

Minor pathway **A)**

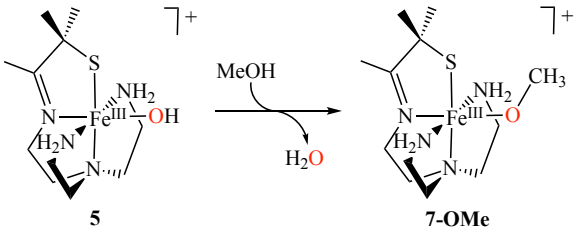

Minor pathway **B)**

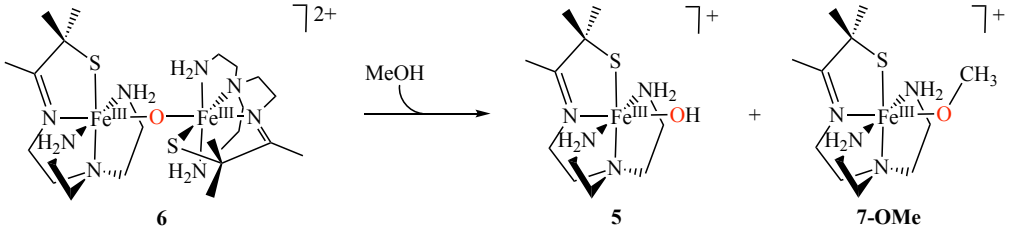

Figure 3.18. Proposed minor pathway A) of conversion $[Fe^{III}(S^{Me2}N_4(tren))(OH)]^+$ (**5**) to $[Fe^{III}(S^{Me2}N_4(tren))(OMe)]^+$ (**7-OMe**) via solvent protonation and release of 1 equiv. of H_2O; and pathway B) of solvent-induced cleavage of the μ-oxo bridged $[(Fe^{III}(S^{Me2}N_4(tren)))_2(\mu\text{-}O)]^{2+}$ (**6**) to hydroxo-bound **5** and methoxide-bound **7-OMe**.

3.4 Conclusions

This chapter describes the mechanism of an O–O bond activation by a thiolate-ligated complex $[Fe^{II}(S^{Me2}N_4(tren))]^+$ (**1**). The only crystallographically characterized example of a thiolate-ligated Fe^{IV}=O, $[Fe^{IV}(O)(S^{Me2}N_4(tren))]^+$ (**4**), and the first example of a *cis*-thiolate ligated Fe^{IV}=O is presented here. The intermediate **4** is hypothesized to have formed as a result of a homolytic O–O bond cleavage in μ-peroxo dimeric **3**. Extensive computational studies on **4** provide a groundwork towards an understanding of its unusual electronic structure that is evident in a short Fe–O(1) bond and a long Fe–S(1) bond lengths. Kinetic and spectroscopic data suggests that the high-valent Fe^{IV}=O intermediate **4** abstracts a hydrogen atom from solvent to afford a metastable hydroxo-bound $[Fe^{III}(S^{Me2}N_4(tren))(OH)]^+$ (**5**). Ferric-hydroxo **5** was characterized by UV/Vis, DFT, and was shown to be generated independently via ligand substitution of **7-OMe** and

7-MeCN. When warmed to room temperature, hydroxo-bound **5** undergoes a condensation reaction to afford the final μ-dimer **6** product. Crystallization of **7-OMe** at –80 °C from **1** and O_2 suggests that minor pathways from **5** or **6** to methoxide-bound **7-OMe** are also present.

3.5 References

(1) Costas, M.; Mehn, M. P.; Jensen, M. P.; Que, L. *Chem. Rev.* **2004**, *104* (2), 939–986.

(2) Feig, A. L.; Lippard, S. J. *Chem. Rev.* **1994**, *94* (3), 759–805.

(3) Niederhoffer, E. C.; Timmons, J. H.; Martell, A. E. *Chem. Rev.* **1984**, *84* (2), 137–203.

(4) Kovaleva, E. G.; Lipscomb, J. D. *Nat. Chem. Biol.* **2008**, *4* (3), 186–193.

(5) Poulos, T. L. *Chem. Rev.* **2014**, *114* (7), 3919–3962.

(6) Stone, K. L.; Behan, R. K.; Green, M. T. *Proc. Natl. Acad. Sci. U. S. A.* **2005**, *102* (46), 16563–16565.

(7) Krest, C. M.; Silakov, A.; Rittle, J.; Yosca, T. H.; Onderko, E. L.; Calixto, J. C.; Green, M. T. *Nat. Chem.* **2015**, *7* (9), 696–702.

(8) Roach, P. L.; Clifton, I. J.; Hensgens, C. M. H.; Shibata, N.; Schofield, C. J.; Hajdu, J.; Baldwin, J. E. *Nature* **1997**, *387* (6635), 827–830.

(9) McDonald, A. R.; Que, L. *Nat. Chem.* **2011**, *3* (10), 761–762.

(10) Shu, L. *Science* **1997**, *275* (5299), 515–518.

(11) Banerjee, R.; Proshlyakov, Y.; Lipscomb, J. D.; Proshlyakov, D. A. *Nature* **2015**, *518* (7539), 431–434.

(12) Price, J. C.; Barr, E. W.; Tirupati, B.; Bollinger, J. M.; Krebs, C. *Biochemistry* **2003**, *42* (24), 7497–7508.

(13) Riggs-Gelasco, P. J.; Price, J. C.; Guyer, R. B.; Brehm, J. H.; Barr, E. W.; Bollinger, J.

M.; Krebs, C. *J. Am. Chem. Soc.* **2004**, *126* (26), 8108–8109.

(14) Puri, M.; Que, L. *Acc. Chem. Res.* **2015**, *48* (8), 2443–2452.

(15) Chen, K.; Costas, M.; Kim, J.; Tipton, A. K.; Que, L. *J. Am. Chem. Soc.* **2002**, *124* (12), 3026–3035.

(16) Pestovsky, O.; Stoian, S.; Bominaar, E. L.; Shan, X.; Münck, E.; Que, L.; Bakac, A. *Angew. Chemie Int. Ed.* **2005**, *44* (42), 6871–6874.

(17) England, J.; Martinho, M.; Farquhar, E. R.; Frisch, J. R.; Bominaar, E. L.; Münck, E.; Que, L. *Angew. Chemie Int. Ed.* **2009**, *48* (20), 3622–3626.

(18) Bigi, J. P.; Harman, W. H.; Lassalle-Kaiser, B.; Robles, D. M.; Stich, T. A.; Yano, J.; Britt, R. D.; Chang, C. J. *J. Am. Chem. Soc.* **2012**, *134* (3), 1536–1542.

(19) Lacy, D. C.; Gupta, R.; Stone, K. L.; Greaves, J.; Ziller, J. W.; Hendrich, M. P.; Borovik, A. S. *J. Am. Chem. Soc.* **2010**, *132* (35), 12188–12190.

(20) Rohde, J.-U.; In, J.-H.; Lim, M. H.; Brennessel, W. W.; Bukowski, M. R.; Stubna, A.; Münck, E.; Nam, W.; Que Jr., L. *Science* **2003**, *299* (5609), 1037–1039.

(21) Jackson, T. A.; Rohde, J. U.; Mi, S. S.; Sastri, C. V.; DeHont, R.; Stubna, A.; Ohta, T.; Kitagawa, T.; Münck, E.; Nam, W.; Que, L. *J. Am. Chem. Soc.* **2008**, *130* (37), 12394–12407.

(22) Bukowski, M. R. *Science* **2005**, *310* (5750), 1000–1002.

(23) Suh, Y.; Seo, M. S.; Kim, K. M.; Kim, Y. S.; Jang, H. G.; Tosha, T.; Kitagawa, T.; Kim, J.; Nam, W. *J. Inorg. Biochem.* **2006**, *100* (4), 627–633.

(24) Kaizer, J.; Klinker, E. J.; Oh, N. Y.; Rohde, J. U.; Song, W. J.; Stubna, A.; Kim, J.; Münck, E.; Nam, W.; Que, L. *J. Am. Chem. Soc.* **2004**, *126* (2), 472–473.

(25) Martinho, M.; Banse, F.; Bartoli, J.-F.; Mattioli, T. A.; Battioni, P.; Horner, O.; Bourcier,

S.; Girerd, J.-J. *Inorg. Chem.* **2005**, *44* (25), 9592–9596.

(26) Lim, M. H.; Rohde, J.-U.; Stubna, A.; Bukowski, M. R.; Costas, M.; Ho, R. Y. N.; Munck, E.; Nam, W.; Que, L. *Proc. Natl. Acad. Sci. U. S. A.* **2003**, *100* (7), 3665–3670.

(27) Kumar, D.; Thiel, W.; De Visser, S. P. *J. Am. Chem. Soc.* **2011**, *133* (11), 3869–3882.

(28) Kumar, D.; Sastry, G. N.; Goldberg, D. P.; de Visser, S. P. *J. Phys. Chem. A* **2012**, *116* (1), 582–591.

(29) Green, M. T.; Dawson, J. H.; Gray, H. B. *Science* **2004**, *304* (5677), 1653–1656.

(30) Gordon, J. B.; Vilbert, A. C.; DiMucci, I. M.; MacMillan, S. N.; Lancaster, K. M.; Moënne-Loccoz, P.; Goldberg, D. P. *J. Am. Chem. Soc.* **2019**, *141* (44), 17533–17547.

(31) Gordon, Z.; Miller, T. J.; Leahy, C. A.; Matson, E. M.; Burgess, M.; Drummond, M. J.; Popescu, C. V.; Smith, C. M.; Lord, R. L.; Rodríguez-López, J.; Fout, A. R. *Inorg. Chem.* **2019**, *58* (23), 15801–15811.

(32) Yadav, V.; Gordon, J. B.; Siegler, M. A.; Goldberg, D. P. *J. Am. Chem. Soc.* **2019**, *141* (26), 10148–10153.

(33) Park, Y. J.; Cook, S. A.; Sickerman, N. S.; Sano, Y.; Ziller, J. W.; Borovik, A. S. *Chem. Sci.* **2013**, *4* (2), 717–726.

(34) Çelenligil-Çetin, R.; Paraskevopoulou, P.; Dinda, R.; Staples, R. J.; Sinn, E.; Rath, N. P.; Stavropoulos, P. *Inorg. Chem.* **2008**, *47* (3), 1165–1172.

(35) Mukherjee, J.; Lucas, R. L.; Zart, M. K.; Powell, D. R.; Day, V. W.; Borovik, A. S. *Inorg. Chem.* **2008**, *47* (13), 5780–5786.

(36) Evans, D. F. *J. Chem. Soc.* **1959**, 2003.

(37) Live, D. H.; Chan, S. I. *Anal. Chem.* **1970**, *42* (7), 791–792.

(38) Van Geet, A. L. *Anal. Chem.* **1968**, *40* (14), 2227–2229.

(39) Bruker. APEX2 (Version 2.1-4), SAINT (Version 7.34A), SADABS (Version 2007/4). BrukerAXS Inc: Madison 2007.

(40) Altomare, A.; Cascarano, G.; Giacovazzo, C.; Guagliardi, A.; Burla, M. C.; Polidori, G.; Camalli, M. *J. Appl. Crystallogr.* **1994**, *27* (3), 435.

(41) Altomare, A.; Burla, M. C.; Camalli, M.; Cascarano, G. L.; Giacovazzo, C.; Guagliardi, A.; Moliterni, A. G. G.; Polidori, G.; Spagna, R. *J. Appl. Crystallogr.* **1999**, *32* (1), 115–119.

(42) Sheldrick, G. M. SHELXL-97, Program for the Refinement of Crystal Structures, University of Göttingen, Germany 1997.

(43) Sheldrick, G. M. *Acta Crystallogr. Sect. C Struct. Chem.* **2015**, *71* (1), 3–8.

(44) Waasmaier, D.; Kirfel, A. *Acta Crystallogr. Sect. A Found. Crystallogr.* **1995**, *51* (3), 416–431.

(45) Burnett, M. N.; Johnson, C. K. ORTEP-III: Oak Ridge Thermal Ellipsoid Plot Program for Crystal Structure Illustration. Oak Ridge National Laboratory Report ORNL-6895, 1996.

(46) Persistence of Vision Raytracer. Persistence of Vision Pty. Ltd.: Williamstown, Victoria, Australia, 2004.

(47) Neese, F. *Interdiscipl. Rev. Comput. Mol. Sci.* **2012**, *2*, 73–78.

(48) Grimme, S.; Ehrlich, S.; Goerigk, L. *J. Comput. Chem.* **2011**, *32*, 1456–1465.

(49) Adamo, C.; Barone, V. *J. Chem. Phys.* **1999**, *110*, 6158–6170.

(50) Neese, F.; Wennmohs, F.; Hansen, A.; Becker, U. *Chem. Phys.* **2009**, *356* (1–3), 98–109.

(51) Theisen, R. M.; Shearer, J.; Kaminsky, W.; Kovacs, J. A. *Inorg. Chem.* **2004**, *43* (24), 7682–7690.

(52) Shearer, J.; Nehring, J.; Lovell, S.; Kaminsky, W.; Kovacs, J. A. *Inorg. Chem.* **2001**, *40* (22), 5483–5484.

(53) Schulz, C. E.; Rutter, R.; Sage, J. T.; Debrunner, P. G.; Hager, L. P. *Biochemistry* **1984**, *23* (20), 4743–4754.

(54) Palcic, M. M.; Rutter, R.; Araiso, T.; Hager, L. P.; Dunford, H. B. *Biochem. Biophys. Res. Commun.* **1980**, *94* (4), 1123–1127.

(55) de Oliveira, F. T.; Chanda, A.; Banerjee, D.; Shan, X.; Mondal, S.; Que, L.; Bominaar, E. L.; Munck, E.; Collins, T. J. *Science* **2007**, *315* (5813), 835–838.

(56) Berry, J. F.; Bill, E.; García-Serres, R.; Neese, F.; Weyhermüller, T.; Wieghardt, K. *Inorg. Chem.* **2006**, *45* (5), 2027–2037.

(57) Xue, G.; Geng, C.; Ye, S.; Fiedler, A. T.; Neese, F.; Que, L. *Inorg. Chem.* **2013**, *52* (7), 3976–3984.

(58) Berry, J. F.; Bill, E.; Bothe, E.; Neese, F.; Wieghardt, K. *J. Am. Chem. Soc.* **2006**, *128* (41), 13515–13528.

(59) Bino, A.; Ardon, M.; Lee, D.; Spingler, B.; Lippard, S. J. *J. Am. Chem. Soc.* **2002**, *124* (17), 4578–4579.

(60) Shearer, J.; Fitch, S. B.; Kaminsky, W.; Benedict, J.; Scarrow, R. C.; Kovacs, J. a. *Proc. Natl. Acad. Sci. U. S. A.* **2003**, *100* (7), 3671–3676.

(61) Bukowski, M. R. *Science* **2005**, *310* (5750), 1000–1002.

(62) Shearer, J.; Scarrow, R. C.; Kovacs, J. A. *J. Am. Chem. Soc.* **2002**, *124* (39), 11709–11717.

(63) Theisen, R. M.; Kovacs, J. A. *Inorg. Chem.* **2005**, *44* (5), 1169–1171.

(64) Theisen, R. M. Synthetic Models and Reactivity of Sulfur-Ligated Iron Metalloenzymes,

University of Washington, 2005.

(65) Warren, J. J.; Mayer, J. M. *Proc. Natl. Acad. Sci.* **2010**, *107* (12), 5282–5287.

(66) Warren, J. J.; Tronic, T. a.; Mayer, J. M.; Bond, S. V. G. *Chem. Rev.* **2010**, *110* (12), 6961–7001.

(67) Drummond, M. J.; Ford, C. L.; Gray, D. L.; Popescu, C. V.; Fout, A. R. *J. Am. Chem. Soc.* **2019**, *141* (16), 6639–6650.

(68) Neves, A.; Lanznaster, M.; Bortoluzzi, A. J.; Peralta, R. A.; Casellato, A.; Castellano, E. E.; Herrald, P.; Riley, M. J.; Schenk, G. *J. Am. Chem. Soc.* **2007**, *129* (24), 7486–7487.

(69) Villar-Acevedo, G.; Nam, E.; Fitch, S.; Benedict, J.; Freudenthal, J.; Kaminsky, W.; Kovacs, J. A. *J. Am. Chem. Soc.* **2011**, *133* (5), 1419–1427.

(70) Kennepohl, P.; Neese, F.; Schweltzer, D.; Jackson, H. L.; Kovacs, J. A.; Solomon, E. I. *Inorg. Chem.* **2005**, *44* (6), 1826–1836.

(71) Jayatilaka, D. *J. Chem. Phys.* **1998**, *108* (18), 7587–7594.

(72) Neese, F. *J. Chem. Phys.* **2001**, *115* (24), 11080–11096.

Chapter 4. Formation of an O–O Bond by a Non-Heme Thiolate-Ligated Iron Complex

4.1 Introduction

Formation of an O–O bond is a crucial step in the biological oxidation of water to produce molecular O_2. Its microscopic reverse, namely the activation of an O–O bond, is an essential step in key oxidative transformations during metabolism. Both of the reactions are employed by Nature to garner energy, synthesize and degrade biomolecules in order to sustain life. A common feature of these two seemingly opposite, yet intimately interlinked, reactions in biological systems is that they are catalyzed by first-row transition metals such as manganese, iron, and copper. The ability to support different oxidation states, which aids the formation of high-valent metal-oxo species, is perhaps the most critical aspect of iron and manganese to enable an O–O bond activation or formation. The activation of an O–O bond by heme and non-heme iron enzymes such cytochrome P450[1,2], CPO[3], IPNS[4], and MMO[5,6] has been investigated over the past several decades and is now well understood. An O–O bond formation step, on the other hand, takes place in the oxo-bridged Mn cluster Mn_4CaO_5, which is referred to as the oxygen-evolving complex (OEC).[7] However, the mechanism of an O–O bond formation step in the OEC is not well understood as it follows the rate determining step.[8]

Examples of enzymatic iron-mediated O–O bond formation are exceedingly rare. Chlorite dismutase (Cld) is perhaps the only well-known example of an heme-ligated iron enzyme which converts toxic chlorite (ClO_2^-) to Cl^-, and in the process evolves O_2 as a byproduct.[9] Intriguingly, evidence for a reversible O–O bond formation has been put forward for horseradish peroxidase (HRP).[10] HRP is a heme-ligated iron metalloenzyme that catalyzes the oxidation of various organic

substrates by H_2O_2. A generally accepted mechanism for HRP-mediated H_2O_2 activation involves the O–O bond heterolysis in an Fe^{III}–OOH intermediate, which leads to the formation of the Fe^{IV}=O species with a π-cation porphyrin radical, $(Por^{\bullet+})Fe^{IV}$=O compound I, and H_2O. The reaction is facilitated by H^+ transfer to the distal oxygen from a nearby His42 residue. In the absence of proton donors, an Fe^{III}–OOH species undergoes an O–O bond homolysis to afford compound II, $(Por)Fe^{IV}$=O, and an ·OH radical. ^{18}O scrambling from labeled H_2O into H_2O_2 was detected, indicating that reversible O–O bond heterolysis might be taking place.[10] This first precedent for a reversible O–O bond formation at a heme-iron center may be indicative of a divergent mechanism in O_2-activating reactions that may be more common than previously thought.[11]

Biomimetic studies have been instrumental in gaining a deeper understanding of the metal-oxo mediated O–O bond formation chemistry. A number of Ru-,[12–17] Mn-,[18–20] and Co-based[21,22] catalysts have been shown to form an O–O bond in recent years. However, examples of synthetic iron-mediated O–O bond formation are rare. The first example of an iron complex capable of reversible O–O bond cleavage and formation was provided by Suzuki and Kodera in 2005.[23] The reported mononuclear peroxo-carbonate complex, $[Fe^{III}(qn)_2(O_2C(O)O)]^-$ (qn = quinoline-2-carboxylate),[24] was shown to reversibly cleave and form a peroxo bond, possibly via a radical coupling mechanism involving the carbonate radical or carbonate and the proximal Fe^{IV}=O or Fe^{V}=O species.[23] In the same year, Kodera et al. have also reported a structural and functional model of MMO, a dinuclear $[Fe^{III}_2(\mu\text{-}O)(6\text{-HPA})(OH_2)_2]^{4+}$ (6-HPA = 1,2-bis[2-{bis(2-pyridylmethyl)amino-methyl}-6-pyridyl]ethane) complex that was capable of stabilizing high-valent diiron core in solution.[25] However, it was not until 2012 that it was shown that $[Fe^{III}_2(\mu\text{-}O)(6\text{-HPA})(OH_2)_2]^{4+}$ reacted with H_2O_2 in the presence of a base (Et_3N) to afford a mixture of μ-

oxo-μ-peroxodiiron(III) and μ-oxodioxoiron(IV) existing in dynamic equilibrium as a result of reversible O–O bond homolytic cleavage.[26] Another example of a mononuclear non-heme N_5-coordinate iron complex features an O–O bond formation and O_2 liberation in the coupling reaction between a high-valent $[Fe^{IV}(O)(Bn\text{-}TPEN)]^{2+}$ (Bn-TPEN = *N*-benzyl-*N,N',N'*-tris(2-pyridyl-methyl)ethane-1,2-diamine) complex and excess *m*CPBA.[27,28] Finally, the study of iron complexes as water oxidation catalysts has attracted much attention in recent years. Reports of iron complexes such as $[Fe^{II}(TAML)]^{1-}$,[29,30] $[Fe^{II}(BQEN)]^{2+}$ (BQEN = *N,N'*-dimethyl-*N,N'*-bis(8-quinolyl)-ethane-1,2-diamine),[31] and $[Fe^{II}(^{Me2}Pytacn)]^{2+}$ (^{Me2}Pytacn = 1-(2'-pyridylmethyl)-4,7-dimethyl-1,4,7-triazacyclononane)[32] that can act as homogenous water oxidation catalysts are but a few examples that emerged in the last decade.

This chapter provides evidence for the formation of an O–O bond by a *cis*-thiolate ligated $[Fe^{II}(S^{Me2}N_4(tren))](PF_6)$ (**1**). Once oxygen atom donors (OAD) such as isopropyl 2-iodoxybenzoate (IBX-ester), iodosobenzene (PhIO), or NaClO are added to the ferrous solution of **1** in a protic solvent, formation of an orange μ-peroxo **3** intermediate is instantaneous. The OAD-derived orange intermediate **3** is identical in chemical behavior to its O_2-derived counterpart, which is described in great detail in Chapter 2. Oxygen-isotope labeling experiments reveal formation of a mixed-labeled H_2O_2 upon protonation of the OAD-derived orange intermediate **3**. At the current stage, radical coupling (RC) mechanism between the two Fe^{IV}=O intermediates, formed as a result of two-electron oxidation of **1** by OADs, is put forward. Attempts to trap the unobserved high-valent Fe^{IV}=O **4** intermediate with redox-inactive $Sc(OTf)_3$ metal ion resulted in identification of two new intermediates. More kinetic, spectroscopic, and computational investigations are underway to elucidate this unprecedented thiolate-ligated iron-mediated O–O bond formation chemistry.

4.2 Experimental

General Methods. All manipulations were performed using standard Schlenk techniques or under an N_2 atmosphere in a glovebox. Reagents and solvents were purchased from chemical vendors, were of highest available purity, and were used without further purification unless otherwise specified. $CDCl_3$ was purchased from Cambridge Isotope Labs and used as received. Tetrahydrofuran (THF) and diethyl ether (Et_2O) were purchased from Sigma-Aldrich and purified using a solvent purification column housed in a custom stainless-steel cabinet and dispensed by a stainless steel Schlenk-line (GlassContour). Methanol (MeOH) and methanol-d_4 (CD_3OD) were distilled over magnesium turnings and sublimed iodine, and rigorously degassed prior to use. CD_3OD was purchased from Cambridge Isotope Labs.

^1H NMR spectra were obtained on a Bruker AV300, AV301, or AV500 spectrometers. Chemical shifts are listed in parts per million and were reported relative to TMS by referencing the residual solvent. Magnetic moments (solution state) were obtained using the Evans method as modified for superconducting solenoids.[33,34] Temperatures were obtained using Van Geet's method.[35] UV/Vis spectra were recorded on a Varian Cary 60 spectrophotometer equipped with a fiber optic cable connected to a "dip" ATR probe (C-technologies). A custom-built two neck solution sample holder equipped with a threaded glass connector was sized specifically to fit the "dip" probe. Electrospray-ionization mass spectra were obtained on a Bruker Esquire Liquid Chromatograph-Ion Trap mass spectrometer. Gas chromatography-mass spectrometry (GC/MS) data were obtained using a 6890 gas chromatograph equipped with a 7683 autosampler and interfaced with a 5973 mass spectrometer.

Synthesis of Isopropyl 2-Iodoxybenzoate (IBX-Ester). Adapted from Ref. ([36]). 2-iodobenzoyl chloride (2.8 g, 10 mmol) was added to a 50 mL round bottom flask equipped with a stir bar and 20 mL of isopropyl alcohol was added. The mixture was stirred under reflux for 30 minutes and concentrated under a rotary evaporator. Crude isopropyl 2-iodobenzoate was purified by filtration through silica gel/sand with DCM as eluent. Reaction afforded 2.5 g (86%) of pure isopropyl 2-iodobenzoate. To a rigorously stirred solution of isopropyl 2-iodobenzoate in 20 mL DCM, NaClO (5% bleach, 15 mL) was added. Then, excess dry ice was added to the reaction mixture over the course of 10 minutes and the reaction was stirred overnight. The organic layer was separated, and the aqueous layer was extracted with DCM (3 x 10 mL). The organic layer was dried over anhydrous $MgSO_4$ (30 minutes) and the solvent was evaporated in vacuum to afford a white powder of pure IBX-ester (1.8 g, 5.6 mmol, 56%). ^{1}H NMR ^{1}H NMR (300 MHz, $CDCl_3$): δ = 8.47 (d, J = 7.8 Hz, 1H), 8.08 (d, J = 7.6 Hz, 1H), 7.93 (t, J = 7.5 Hz, 1H), 7.66 (t, J = 7.4 Hz, 1H), 5.35 (m, 1H), 1.40 (d, J = 6.2 Hz, 6H).

Synthesis of Mixed-Labeled ^{16}O/^{18}O-IBX-Ester. Adapted and modified from Ref. ([37]). In the glovebox, IBX-ester (0.155 mmol, 1.0 equiv., 0.050 g) was dissolved in dry MeOH (1 mL). To that, 97 % $H_2{}^{18}O$ (~9 μL, 2.9 equiv., 0.5 mmol) was added and the reaction mixture was stirred overnight. Then, a crushed powder of 3Å molecular sieves (~0.5 g) was added to the methanolic solution and the reaction mixture was stirred for an additional 2 hours. The sieves' dust was filtered off and MeOH was evaporated in vacuum afforded a white powder of mixed-labeled IBX-ester (0.049 g, 0.152 mmol, 97%). The ^{18}O content was found to be 61 ± 3 %, on the basis of GC-MS analysis of triphenylphosphine oxide ($Ph_3P^{16}O$ m/z = 278.1 amu vs. $Ph_3P^{18}O$ m/z = 280.1 amu) prepared by reaction of the labeled IBX-ester with triphenylphosphine dissolved in DCM.

Synthesis of [$Fe^{II}(S^{Me2}N_4$(tren))](PF_6) (1). 3-mercapto-3-methyl-2-butanone (0.260 g, 2.2 mmol), was dissolved in 10 mL MeOH. To that, NaOMe (0.108 g, 2.0 mmol) was added and the mixture was stirring for 10 min, followed by the addition of *tris*(2-amonoethyl)amine (TREN) (0.234 g, 2.2 mmol). After stirring for an additional 20 min, the solution was cooled to –40 °C for an hour. In a separate vial, $FeCl_2$ (0.456 g, 2.0 mmol) was dissolved in MeOH (5 mL) and cooled to –40 °C for an hour as well. The ferrous solution was then added dropwise into the cooled solution containing thiolate and TREN ligand. The solution turned dark green immediately, was let stirring at room temperature for an hour, followed by addition of $NaPF_6$ (0.334 g, 2.0 mmol). The reaction solution was stirred at room temperature overnight and then filtered through a bed of celite. MeOH was evacuated and the resulting dark-green precipitate was redissolved in MeCN (10 mL). The solution was filtered through a bed of celite again, MeCN concentrated down to 3 mL. The concentrate was layered with Et_2O (17 mL) to crush out the complex over two nights at –40 °C. To attain highest purity, the resulting dark brown-red solid was redissolved in MeOH (3 mL), filtered through a fine frit, and recrystallized under layered Et_2O over two nights at –40°C. Final light-green solid (0.6 g, 70% yield) is 96% pure using quantitative UV/Vis of [($Fe^{III}(S^{Me2}N_4$(tren)))$_2$(μ-O)](PF_6)$_2$ (**6**) in MeCN with λ_{max} (ε): 480 nm (5270 M^{-1} cm^{-1}, 20 °C).

Formation of [($Fe^{III}(S^{Me2}N_4$(tren)))$_2$(μ-O_2)](PF_6)$_2$ (3) via the Addition of Oxygen Atom Donors (OAD) to 1. A 0.378 mM solution of **1** was prepared in MeOH under an inert atmosphere in a glovebox. The resulting solution was transferred via gastight syringe to a custom-made two-neck vial equipped with septum cap and threaded dip-probe feed-through adaptor that had been previously purged with argon gas through a septum cap for at least 20 minutes. The solution was

cooled in an acetone/dry ice bath to –73 °C. Addition of IBX-ester (100 μL, 0.5 equiv., 9.45 mM in MeOH), PhIO (100 μL in THF, 1.0 equiv., 18.9 mM), or NaClO (100 μL in MeOH/H_2O, 1.0 equiv., 18.9 mM) resulted in the formation of metastable **3**. The same procedure was used to prepare IBX-ester generated 0.4 mM samples of **3** in EPR tubes for EPR spectroscopy and 10 mM samples in NMR tubes for ^{1}H NMR spectroscopy. Electronic absorption of **3** in MeOH with λ_{max} (ε): 465 nm (3,000 M^{-1} cm^{-1}, –73 °C), EPR (MeOH/EtOH glass (9:1), 8.0 K): silent in $\perp$ and || modes.

Formation of [$Fe^{III}(S^{Me2}N_4$(tren))(OH)](PF$_6$) (5) via the Addition of IBX-Ester to 1. A 0.378 mM solution of **1** was prepared in MeOH under an inert atmosphere in a glovebox. The resulting solution was transferred via gastight syringe to a custom-made two-neck vial equipped with septum cap and threaded dip-probe feed-through adaptor that had been previously purged with argon gas through a septum cap for at least 20 minutes. The solution was cooled in an acetone/dry ice bath to –73 °C. Addition of IBX-ester (100 μL, 0.5 equiv., 9.45 mM in MeOH) resulted in the formation of peroxo-bridged **3**. After that, **3** was brought up to –40 °C by quickly switching to acetonitrile/dry ice bath. Over the course of 30 minutes, the orange peroxo-bridged **3** cleanly converted to magenta colored **5.** The same procedure was used to prepare 0.4 mM samples of **5** in EPR tubes for EPR spectroscopy and 10 mM samples in NMR tubes for ^{1}H NMR spectroscopy. Electronic absorption of **5** in MeOH with λ_{max} (ε): 540 nm (1750 M^{-1} cm^{-1}, –40 °C), EPR (MeOH/EtOH glass (9:1), 117 K): $g_\perp$ = 2.24, $g_\parallel$ = 1.96.

Formation of a Blue Intermediate, via the Addition of O_2 or OAD to 1 in the presence of Sc(OTf)$_3$. A 0.378 mM solution of **1** was prepared in MeOH under an inert atmosphere in a

glovebox. The resulting solution (5 mL) was transferred via gastight syringe to a custom-made two-neck vial equipped with septum cap and threaded dip-probe feed-through adaptor that had been previously purged with argon gas through a septum cap for at least 20 minutes. The solution was cooled in an acetone/dry ice bath to –73 °C. Then, $Sc(OTf)_3$ (50 μL, 1.2 – 10 equiv., 0.045 – 0.378 M) was injected via gastight syringe into the reaction vial containing **1**. After 2 minutes of additional stirring, dry O_2, or IBX-ester (100 μL, 0.5 equiv., 9.45 mM in MeOH), was added into the reaction cell, resulting in the formation of a metastable blue species. The same procedure was used to prepare 10 mM samples of the blue species in EPR tubes for EPR spectroscopy. Electronic absorption of blue species in MeOH with λ_{max} (ε) = 626 nm (~ 1700 M^{-1} cm^{-1}, –73 °C). EPR ($\perp$-mode) (MeOH/EtOH glass (9:1), 117 K): silent.

Formation of a Blue Intermediate, via the Addition of $Sc(OTf)_3$ to μ-Peroxo 3 or μ-Oxo 6. A 0.378 mM solution of **1** was prepared in MeOH under an inert atmosphere in a glovebox. The resulting solution (5 mL) was transferred via gastight syringe to a custom-made two-neck vial equipped with septum cap and threaded dip-probe feed-through adaptor that had been previously purged with argon gas through a septum cap for at least 20 minutes. The solution was cooled in an acetone/dry ice bath to –73 °C. Argon stream was removed from the vial and a stream of O_2 gas was bubbled through the solution over the course of 2 minutes, resulting in the formation of metastable **3**. Then, $Sc(OTf)_3$ (50 μL, 50 μL, 1.2 – 10 equiv., 0.045 – 0.378 M) was injected via gastight syringe into the reaction vial containing **3**, resulting in the formation of a metastable blue species at λ_{max} = 626 nm. Alternatively, the same blue species can be derived by adding $Sc(OTf)_3$ (50 μL, 1.2 equiv., 45.4 mM) into the methanolic solution of an authentically generated μ-oxo **6** (5 mL, 0.189 mM).

Formation of a Green Intermediate, via the Addition of O_2 to 1 in the presence of $Sc(OTf)_3$. A methanolic solution of **1** (5 mL, 0.1 mmol, 20 mM) in a vial sealed with a septum cap was cooled in an acetone/dry ice bath to –73 °C for 10 minutes. To that, $Sc(OTf)_3$ (200 μL, 2 equiv., 1 M) was injected via gastight syringe and the vial was open to atmospheric O_2. The concentrated solution of **1** and $Sc(OTf)_3$ turned dark-green immediately. The solution was diluted to ~ 1 mM with cold MeOH to obtain UV/Vis and EPR spectra. Electronic absorption of a green intermediate in MeOH with λ_{max} = 360, 435, 720 nm. EPR (MeOH/EtOH glass (9:1), 117 K): 2.20, 2.14, 2.01.

Hydrogen Peroxide Detection Using a Potassium Permanganate Assay. A concentrated methanolic solution of **1** (0.2 mL, 5.5 mM) was prepared under an inert atmosphere in a glovebox. After cooling the solution to –73 °C in a dry ice/acetone cold bath for 10 min, IBX-ester (100 μL, 0.5 equiv., 5.5 mM in MeOH) was injected into a solution using a gas-tight syringe and the reaction mixture was stirred for an additional 10 minutes. IBX-ester injection promoted a rapid color change of the solution to dark orange, indicating a formation of peroxo-bridged **3**. A single drop of concentrated H_2SO_4 was then added to the dark orange solution of **3**, causing a rapid color change to purple (λ_{max} = 565 nm, solvent bound $[Fe^{III}(S^{Me2}N_4(tren))(MeOH)]^{2+}$ (**7-MeOH**)).[38] The purple solution was then filtered through a small silica plug, collected, and added in a single aliquot to a stirring aqueous solution of $KMnO_4$ (6 mL, 1.23 x 10^{-4} M). The decrease in $KMnO_4$ absorption band was monitored spectroscopically in one-minute intervals until no further change was detected. The amount of hydrogen peroxide present was calculated based on the decrease in absorbance at λ_{max} (ε) = 550 nm (2455 M^{-1} cm^{-1}, 293 K) according to the following reaction:

$$2\ KMnO_4 + 5H_2O_2 + 6H^+ \rightarrow 2Mn^{2+} + 5O_2 + 8H_2O + 2K^+$$

Hydrogen Peroxide Detection by GC/MS. A concentrated methanolic solution of **1** (3 mL, 100 mM) was prepared under inert atmosphere in a glovebox. After the solution was cooled to –73 °C in a dry ice/acetone cold bath for 10 min, IBX-ester (50 μL, 0.5 equiv., 1.0 M in MeOH) was injected into a solution using a gas-tight syringe and the reaction mixture was stirred for an additional 10 minutes. IBX-ester injection promoted a rapid color change of the solution to dark orange, indicating a formation of peroxo-bridged **3**. Methanolic solution of H_2SO_4 (0.5 eq., 50 μL, 0.15 mmol) was injected into the dark-orange solution, causing a rapid color change to purple (λ_{max} = 565 nm, solvent bound **7-MeOH**).[38] The resulting solution mixture was filtered through a small silica plug. The methanolic filtrate (1.0 μL) was manually injected into a GC MS with modified parameters, followed by the second injection of pure methanol (1.0 μL) 2 min into the run. Second injection was used to subtract solvent and gas background. GC injection split ratio was set to 10.0:1, gas saver to 20.0 mL/min after 2.0 min. Starting temperature: 40 °C, run temperature: 90 °C; total run time: 5.0 min. MS scanning parameters were set 10 – 60 amu.

4.3 Results and Discussion

4.3.1 *Low-Temperature Reactivity of $[Fe^{II}(S^{Me2}N_4(tren))]^+$ (**1**) with Oxo-Atom Donors*

Oxo-atom donors (OAD) are often utilized to generate and study high-valent Fe^{IV}=O species, while avoiding a complicated and multi-step iron-O_2 chemistry.[39–43] Motivated by the discovery and crystallographic characterization of a *cis*-thiolate ligated high-valent $[Fe^{IV}(O)(S^{Me2}N_4(tren))]^+$ (**4**) species (Chapter 3), various OADs were used in this study in an attempt to generate and spectroscopically characterize an Fe^{IV}=O **4** species via the direct two-

electron oxidation of the starting ferrous complex **1**. When monitored by the UV/Vis, addition of 1 – 10 equiv. of OADs such as isopropyl 2-iodoxybenzoate (IBX-ester), iodosobenzene (PhIO), or sodium hypochlorite (NaClO) to **1** in MeOH at –73 °C affords an orange intermediate at λ_{max} = 465 nm, (Figure 4.1).

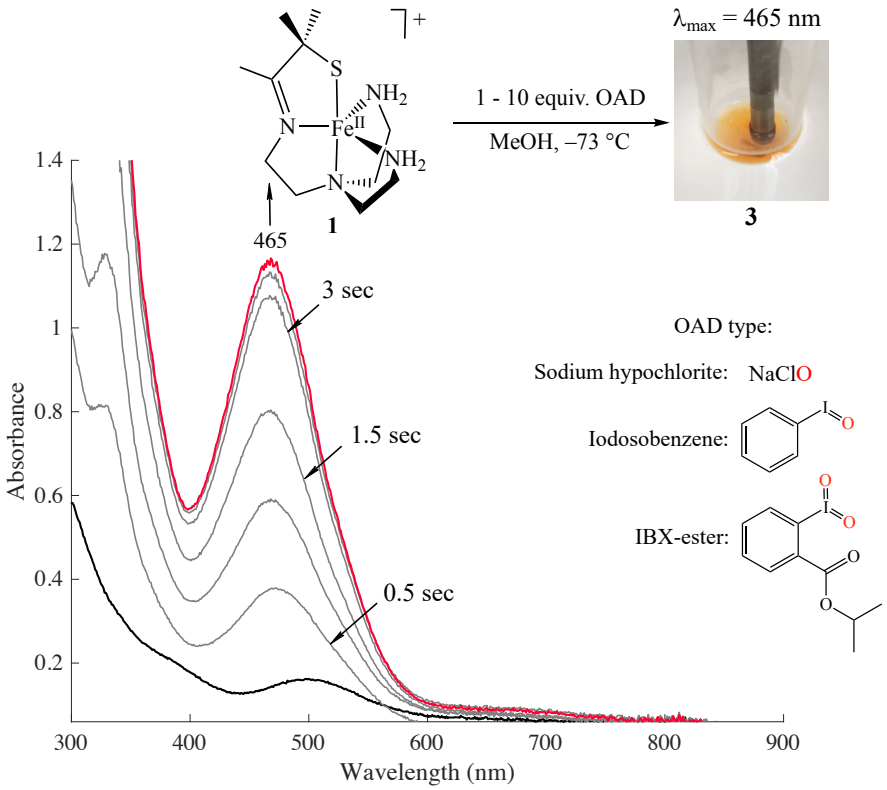

Figure 4.1. Electronic absorption spectrum showing that addition of stoichiometric or excess (1 – 10 equiv.) of oxo-atom donors such as IBX-ester, PhIO, or NaClO to $[Fe^{II}(S^{Me2}N_4(tren))]^+$ (**1**) in MeOH at –73 °C results in a fast formation an orange intermediate **3** at $\lambda_{max}(\varepsilon)$ = 465 nm (3,000 M^{-1} cm^{-1}).

The IBX-ester generated orange species at λ_{max} = 465 nm appears to have an identical electronic absorption spectrum as the O_2-derived intermediate **3**, best described as a μ-peroxo dimer, (Chapter 2). The orange intermediate was reproducibly generated by adding 1 equiv. IBX-ester to the methanolic solution of **1** (0.378 mM) in an O_2-free environment (O_2 ppm < 0.5 ppm) inside a glove box in an –34 °C freezer. And finally, the growth of the absorption band at 465 nm

was monitored under pseudo first order conditions between **1** (0.2 mM) and IBX-ester (4.3 mM) using a cryogenic stopped-flow instrument at –70 °C under anaerobic conditions. Again, the electronic absorption spectrum of IBX-generated orange intermediate is indistinguishable from the O_2-derived species **3**, (Figure 4.2).

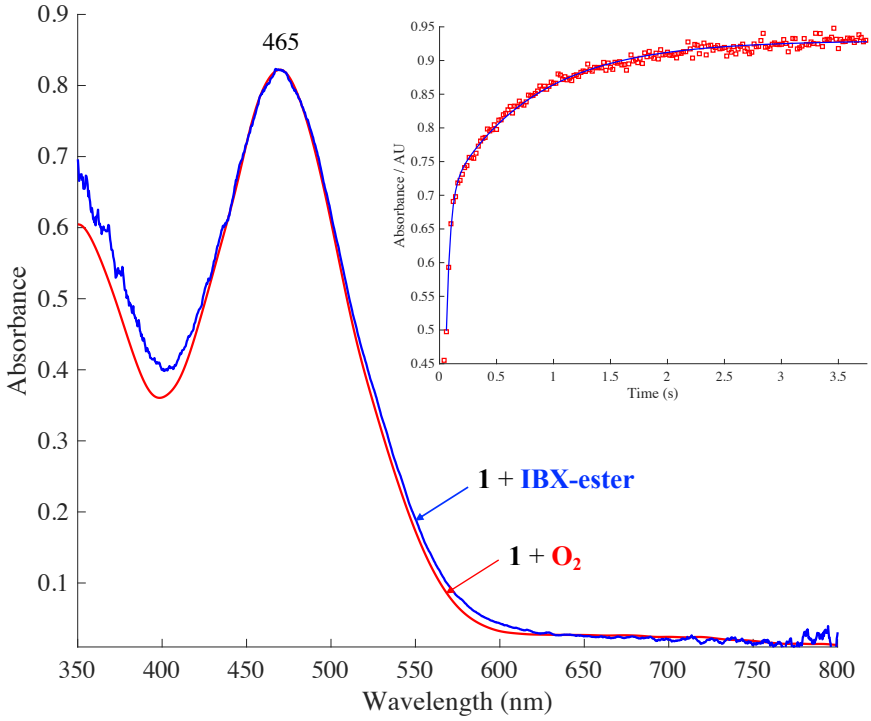

Figure 4.2. An overlay of stopped-flow spectra of O_2-generated (red) and IBX-ester generated (blue) orange species **3** at λ_{max} = 465 nm in MeOH at –70 °C. Inset: kinetic trace (λ = 465 nm) showing the formation of the orange intermediate **3** obtained upon mixing solutions of **1** (0.2 mM) and IBX-ester (4.3 mM) in MeOH at –70 °C.

Given that the current experimental evidence strongly supports the assignment of O_2-generated orange species as a μ-peroxo dimer (Chapter 2), then these results suggest that the IBX-ester generated orange species is also a μ-peroxo dimer, $[(Fe^{III}(S^{Me2}N_4(tren)))_2(\mu\text{-}O_2)]^{2+}$. In turn, this would imply that the high-valent Fe^{IV}=O **4**, generated as a result of addition of an oxo-atom donor to **1**, instantaneously couples to form an O–O bond and generate a μ-peroxo dimer **3**, (Figure 4.3), while eluding a direct spectroscopic observation at these conditions. Although the O_2- and

IBX-ester generated μ-peroxo **3** appear to have identical UV/Vis spectra, preliminary rapid-mixing experiments using a cryogenic stopped-flow instrument indicate that mechanism of formation from the two routes is different. Rapid mixing of solutions of **1** (0.2 mM) and O_2 (4.3 mM) in MeOH at –70 °C results in full conversion to the orange μ-peroxo **3** in 0.05 seconds. On the other hand, rapid mixing of solutions of **1** (0.2 mM) and IBX-ester (4.3 mM) takes at least 4 seconds (~ 80 times slower) to reach full conversion to μ-peroxo **3**, (Figure 4.2, inset). This indicates that the IBX-ester-generated **3** forms via an entirely different mechanistic pathway from O_2. At this point, it would be acceptable to presume that the orange intermediate **3** could be a high-valent Fe^{IV}=O **4** since this is the direct observable species obtained upon the addition of oxo-atom donors. If that were the case, then it would suggest that the O_2-activating pathway to **4** via a reversible formation of ferric-superoxo **2**, followed by binding of another equiv. of **1** to afford a μ-peroxo **3**, and lastly followed by an activation of an O–O bond to arrive at **4** is almost two orders of magnitude faster than a single-step oxo-atom transfer to **1**. Given prior experimental evidence, however, suggests that O_2-generated **3** is a fast and associative process of μ-peroxo dimer formation. Comparatively slow rate of formation of **3** via an addition of oxo-atom donors to **1** would be consistent with formation of **4**, followed by an O–O coupling step. Detailed kinetic studies for the formation of the μ-peroxo dimer **3** via oxo-atom donor addition to **1** are therefore required and have the potential to provide valuable insight and evidence for the involvement of high-valent Fe^{IV}=O **4** in an O–O bond coupling step.

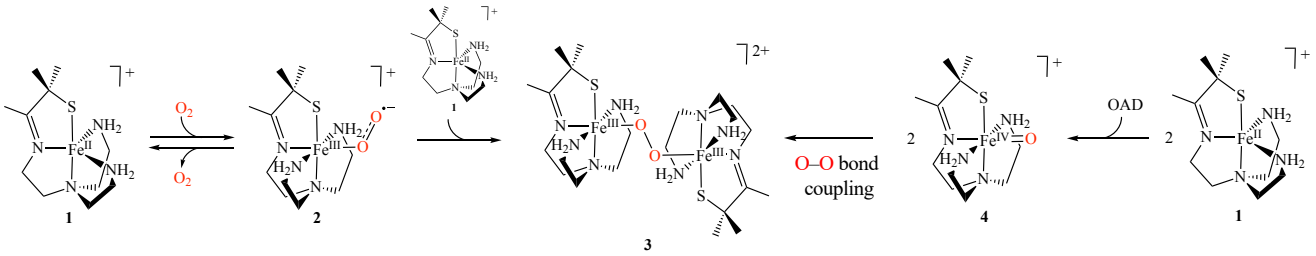

Figure 4.3. Proposed mechanism of formation of μ-peroxo dimeric **3** via O_2 binding to **1** route (left to center) and oxo-atom donor addition to **1** (right to center).

4.3.2 *Magnetic Characterization of IBX-Ester Derived μ-Peroxo **3** Intermediate*

In order to compare the IBX-generated orange intermediate **3** to its O_2-derived counterpart, it has been characterized with the same set of physical techniques. EPR measurements on the IBX-generated **3** shows no signal in the ⊥-mode in the range from 4.2 to 120 K. Additional EPR measurements, in collaboration with Professor David Britt at the University of California, Davis, corroborated that the IBX-generated orange species **3** was EPR silent in both the ⊥- and ||-modes over the temperature range from 4.2 to 120 K, thus excluding IBX-generated **3** from being an integer spin system as well ($S \neq 1, 2$). As a result, EPR measurements suggest that the orange intermediate **3** is an overall diamagnetic system, $S = 0$.

Both the O_2- and IBX-ester-derived **3** were studied with low temperature paramagnetic ^{1}H NMR spectroscopy. Measurements were taken in the +150 to –150 ppm range. The ^{1}H NMR spectrum of the parent compound **1** (10 mM) in CD_3OD at 193 K shows a single clearly resolved paramagnetically shifted peak at 117 ppm, (Figure 4.4, top). Moreover, the calculated magnetic moment of **1** is $\mu_{eff} = 4.64\ \mu_B$ in CD_3OD at 193 K, consistent with a $S = 2$ spin-state. The O_2-derived **3** was formed by bubbling dry O_2 gas into the NMR tube of **1** at –73 °C. The IBX-ester-derived **3** was formed by injecting a saturated solution of IBX-ester (100 μL, 30 mM) into the

NMR tube of **1** at –73 °C and the ^{1}H NMR spectra were taken again. The paramagnetically shifted peak of **1** at 117 ppm collapsed upon the formation of **3** from both routes, (Figure 4.4, middle and bottom). Both the O_2 and IBX-ester **3** show a sharp peak 8.97 ppm and at least two broadened peaks in 18 – 25 ppm region associated with solvent-exchangeable N–H protons, suggesting that the local ferric centers are paramagnetic at 193 K. Note that the IBX-ester derived **3** includes multiple aryl peaks from the IBX-ester reagent in 7 – 8 ppm region. The MeOH solvent peaks from the O_2 and IBX-ester **3** are identical, which indicates that they are characterized by the same local magnetic moment that arises from the iron center. The calculated magnetic moment of O_2 and IBX-ester **3** is $\mu_{eff} = 1.96\ \mu_B$ per iron, consistent with a $S = 1/2$ spin-state. The ^{1}H NMR results, therefore, also help to rule out that the orange intermediate **3**, formed via addition of oxo-atom donors, is a high valent Fe^{IV}=O species in an $S = 0$, 1, or 2 spin state at 193 K.

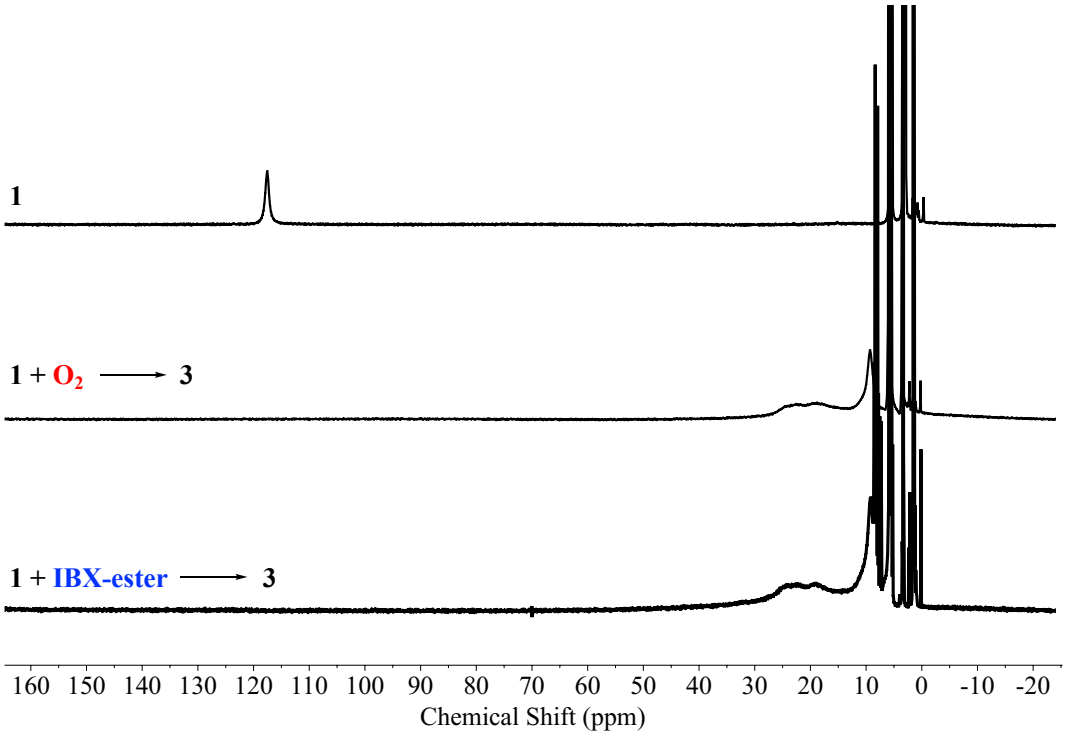

Figure 4.4. The paramagnetically shifted signal in the ^{1}H NMR spectra (500 MHz) of **1** (top) collapses to paramagnetically shifted signals upon the addition of O_2 and formation of the orange intermediate **3** (middle). The paramagnetically shifted peaks of IBX-ester generated orange intermediate **3** (bottom) are identical to O_2-formed **3**. Spectra were taken in CD_3OD at 193 K.

4.3.3 *Reactivity and Conversion of IBX-Ester Derived μ-Peroxo **3** to Hydroxo-Bound **5***

In order to compare to the reactivity studies that were explored with the O_2-generated orange intermediate **3** (Chapter 2), the reactivity of the IBX-ester generated **3** has been tested with the reduced ferrous **1**, HAT, and OAT reagents. If the IBX-ester generated **3** were a high-valent Fe^{IV}=O, it could potentially react with **1** to afford μ-oxo dimeric **6** with (λ_{max}= 500 nm). Thus, the reaction between the orange intermediate **3** and the starting ferrous complex **1** was monitored by the UV/Vis spectroscopy in MeOH at –73 °C in order to ascertain if the orange intermediate **3** would be susceptible to one-electron reduction from another equivalent of ferrous **1**. However, just as was observed with O_2-generated **3**, no reactivity between the IBX-ester derived intermediate and the ferrous complex **1** was observed. Similarly, the intermediate **3** appears to be unreactive towards HAT reagents such as DHA (BDE(C–H) = 78 kcal mol^{-1}),[44,45] CHD (BDE(C–H) = 76 kcal mol^{-1}),[45] and TEMPOH (BDE(O–H) = 69 kcal mol^{-1})[44,46] in MeOH at –73 °C when monitored by UV/Vis over the course of 2 as well as 24 hours. No reactivity between the IBX-ester (0.5 equiv. used) generated **3** and OAD reagents such as PPh_3, PMe_2Ph, PhSMe was detected in MeOH at –73 °C when monitored by UV/Vis over the course of 2 hours as well as 24 hours. Moreover, no phosphine oxide product (Ph_3P=O or Me_2PhP=O) or methylphenyl sulfoxide (MePhS=O) was detected by GC/MS chromatography relative to control.

The IBX-ester generated orange intermediate **3** is stable for hours in MeOH at –73 °C and exhibits the same reactivity as the O_2-derived **3** when warmed up. Upon warming from –73 °C to room temperature, stoichiometrically (0.5 molecular equiv.) IBX-ester-generated **3** fully converts, in less than 10 minutes, to an EPR silent (at 117 K ⊥-mode) μ-oxo dimer **6** at λ_{max}= 500 nm. However, if the orange intermediate **3** was generated from an addition of a slight excess of oxo-atom donors, then the reaction mixture completely bleaches out when warmed to room

temperature. This is likely the result of the thiolate-sulfur oxygenation reaction by the remaining unreacted oxo-atom donors in solution. However, when the stoichiometrically IBX-ester-generated **3** is warmed to –40 °C, as opposed to room temperature, it also converts to the same magenta species, characterized by an absorption band at λ_{max}= 540 nm, over the course of 30 minutes, (Figure 4.5, A). EPR measurements of the IBX-ester derived magenta species λ_{max}= 540 nm indicate that this is the same low spin S = 1/2 ferric-hydroxo $[Fe^{III}(S^{Me2}N_4(tren))(OH)]^+$ (**5**) intermediate characterized by an axial signal ($g_\perp$ = 2.24, $g_\parallel$ = 1.97), (Figure 4.5, B).

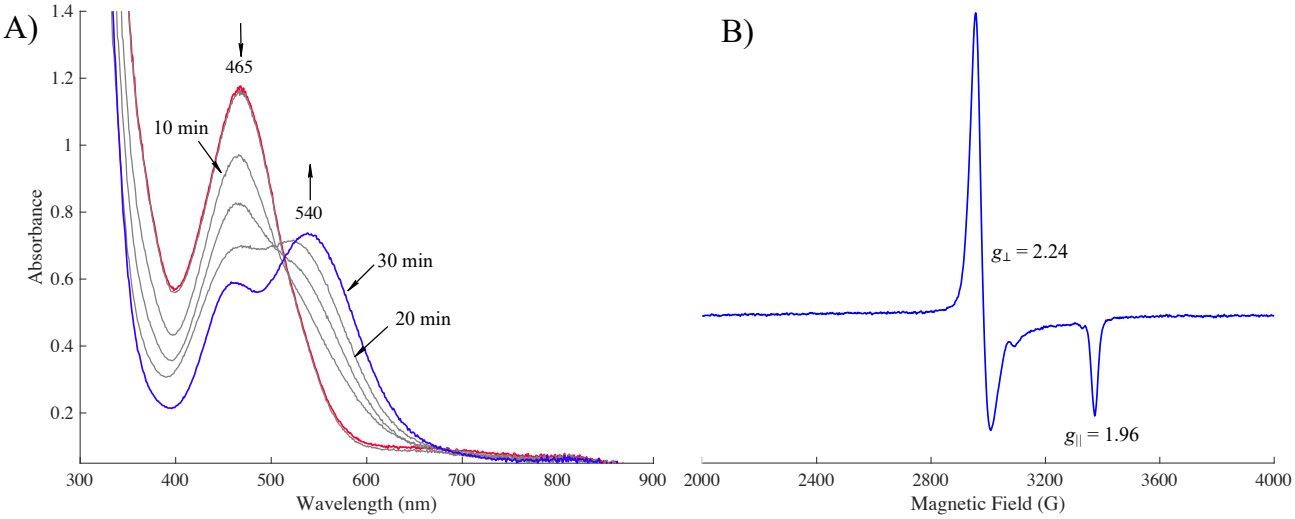

Figure 4.5. **A**) Electronic absorption spectrum of the conversion of the IBX-ester generated orange intermediate **3** (λ_{max} = 465 nm) to a hydroxo-bound $[Fe^{III}(S^{Me2}N_4(tren))(OH)]^+$ (**5**) (λ_{max} = 540 nm) intermediate over the course of 30 minutes in MeOH as a result of warming the reaction solution from –73 °C to –40 °C. **B**) 9.28 GHz CW X-band EPR (⊥-mode) of a hydroxo-bound **5** ($g_\perp$ = 2.24, $g_\parallel$ = 1.97) derived from the IBX-ester addition route. EPR measurements were taken at 117 K in MeOH/EtOH (9:1) glass.

4.3.4 *Hydrogen Peroxide Detection*

H_2O_2, released as a result of acid addition to IBX-ester-generated solution of **3**, was detected using $KMnO_4$ detection assay. Here, the orange intermediate **3** was generated by anaerobically injecting a concentrated solution of IBX-ester (50 μL, 0.5 equiv., 11.0 mM) to a

precooled methanolic solution of **1** (0.2 mL, 5.5 mM). A few drops of concentrated H_2SO_4 immediately afforded a solvent-bound **7-MeOH**. After the reaction mixture was passed through a plug of silica, the resulting filtered methanolic solution (0.2 mL) was added to the aqueous solution of $KMnO_4$ (6 mL, 1.23 x 10^{-4} M), (Figure 4.6). The amount of $KMnO_4$ consumed was calculated based on the change of absorbance at λ_{max} (ε) = 550 nm (2455 M^{-1} cm^{-1}, 293 K) according to the reaction shown in equation (10). According to the stoichiometry $KMnO_4$ consumed, 0.44 ± 0.03 equiv. H_2O_2 was produced per ~1 equiv. of **1** utilized. Detection of H_2O_2 released from the IBX-ester generated **3** suggests that IBX-ester addition to **1** result in an O–O bond formation.

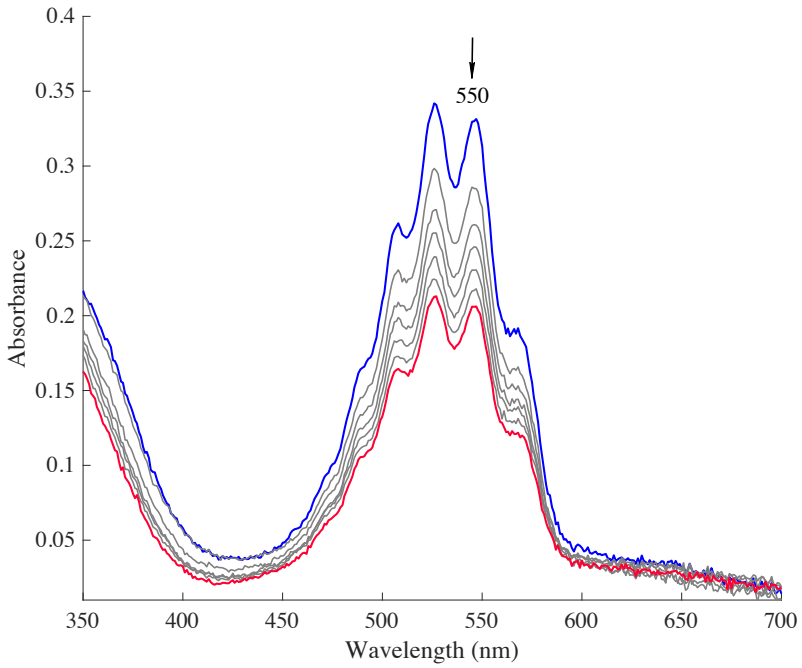

Figure 4.6. Electronic absorption spectrum showing the change in absorption of $KMnO_4$ (6 mL, 1.23 x 10^{-4} M aqueous solution, blue spectrum) which occurs upon the addition of H_2O_2 (red spectrum) that is released in the reaction between concentrated H_2SO_4 (2 drops) and IBX-ester generated **3** (0.2 mL, 5.5 mM in MeOH).

In order to unambiguously establish that oxo-atom donor addition to **1** resulted in an O–O bond coupling to afford a μ-peroxo dimeric **3**, isotope-labeling experiments with mixed-labeled $^{18}O/^{16}O$-IBX-ester were carried out and monitored by GC/MS. If IBX-ester indeed transferred oxo-

atoms to **1** to afford a high-valent Fe^{IV}=O en route to O–O bond coupling prior to acid-released H_2O_2, then ^{18}O-incorporation would result mixed-labeled H_2O_2 ($H_2{}^{16}O_2$ with *m/z* = 34 amu, $H^{16}O^{18}OH$ with *m/z* = 36 amu, $H_2{}^{18}O_2$ with *m/z* = 38 amu). To that purpose, mixed-labeled $^{18}O/^{16}O$-IBX-ester was prepared according to a modified procedure described for ^{18}O-labeled PhIO preparation.[37] The ^{18}O content was found to be 61 ± 3 %, on the basis of GC/MS analysis of triphenylphosphine oxide ($Ph_3P^{16}O$ *m/z* = 278.1 amu vs. $Ph_3P^{18}O$ *m/z* = 280.1 amu) prepared by reacting the mixed-labeled IBX-ester with Ph_3P in DCM. The preparation procedure of H_2O_2 released from the IBX-ester generated orange intermediate **3** is the same as outlined for the $KMnO_4$ detection assay. The base peak for $H_2{}^{16}O_2$ at *m/z* = 34, released from unlabeled ^{16}O-IBX-ester-generated intermediate **3**, was detected by the GC/MS, (Figure 4.7, A). More importantly, a distribution of mixed-labeled H_2O_2 ($H_2{}^{16}O_2$ with *m/z* = 34 amu, $H^{16}O^{18}OH$ with *m/z* = 36 amu, $H_2{}^{18}O_2$ with *m/z* = 38 amu) was detected in a roughly 1:2:1 ratio from the intermediate **3** prepared by the addition of mixed-labeled $^{16}O/^{18}O$-IBX-ester, consistent with the ^{18}O-isotope content (61 ± 3 %) (Figure 4.7, B). Background spectrum, also accounting for the natural abundance of $CH_3{}^{18}O^{+}H$ at *m/z* = 34 at 0.244(32) %,[47] was subtracted from the signal spectrum and the base peaks at *m/z* = 34 amu (for $H_2{}^{16}O_2$), 36 amu (for $H^{16}O^{18}OH$), and 38 amu (for $H_2{}^{18}O_2$) were normalized relative to O_2-derived H_2O_2 GC/MS spectrum, (Chapter 3). The lowered amount of H_2O_2 detected in both IBX-ester addition experiments relative to O_2 additions suggests that some decomposition, due to oxo-atom donor attack on the thiolate-sulfur, may be taking place.

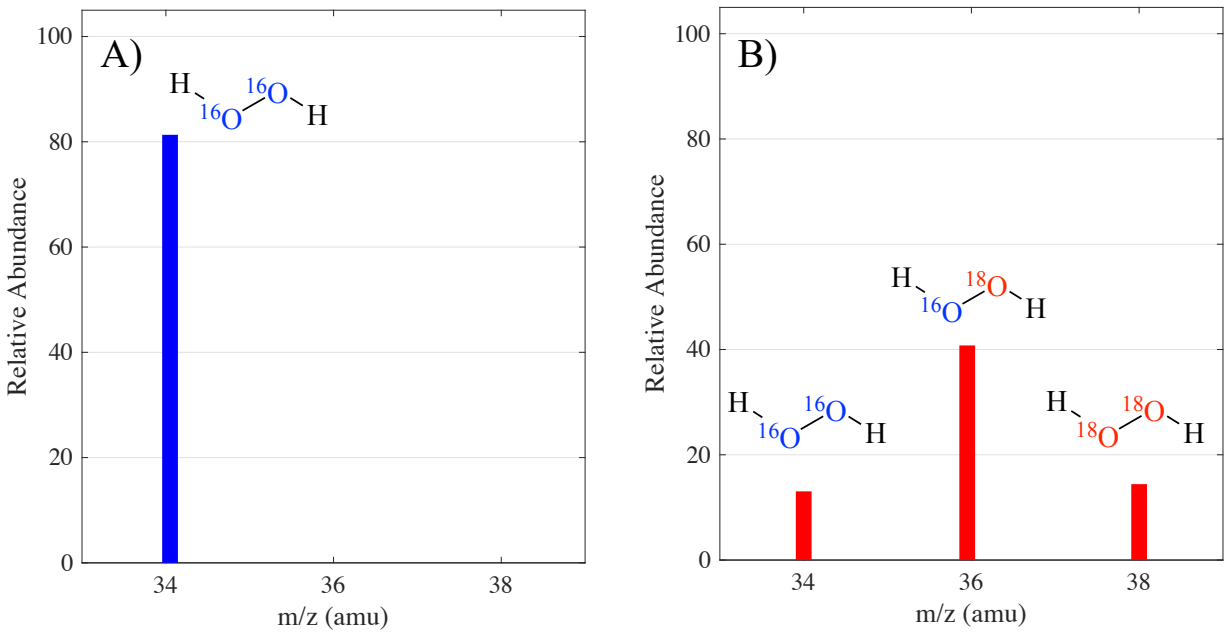

Figure 4.7. Mass spectra of cations produced by electron impact ionization for H_2O_2 generated from the addition of concentrated H_2SO_4 (1 drop) to the orange intermediate **3** formed from an addition of **A**) ^{16}O-labeled IBX-ester and **B**) mixed-labeled ^{16}O/^{18}O-IBX-ester to **1** (3 mL, 100 mM) in MeOH at –73 °C. Background spectrum was subtracted from the signal spectrum and the base peaks at *m/z* = 34 amu (for $H_2{}^{16}O_2$), 36 amu (for $H^{16}O^{18}OH$), and 38 amu (for $H_2{}^{18}O_2$) were normalized relative to O_2-derived H_2O_2 GC/MS spectrum, (Chapter 3).

4.3.5 *Attempts at Trapping High-Valent Thiolate-Ligated [Fe^{IV}(O)(S^{Me2}N$_4$(tren))]$^+$ (**4**)*

As discussed above, addition of typical OADs such as PhIO, IBX-ester, and NaClO resulted in the instantaneous formation of an orange intermediate at λ_{max} = 465 nm, best described as a μ-peroxo dimer. These results suggest that the O–O bond coupling step between 2 equiv. of high-valent Fe^{IV}=O **4**, that are hypothesized to form upon 2-electron oxidation of **1** by OADs, is energetically favorable and eludes spectroscopic characterization at –73 °C in MeOH. Therefore, a few strategies were attempted to trap the high-valent Fe^{IV}=O **4** species before the O–O bond forming reaction.

A generally considered pathway for the formation of an O–O bond between the two high-valent metal-oxos usually proceed via a radical coupling step, where the two metal-oxos possess

some radical character.[48] Formation of a binuclear μ-peroxo complex **3** as a result of addition of OADs suggests a direct coupling between the two Fe^{IV}=O **4** species, which may possess some radical character as well. Therefore, it may be possible to arrest an O–O bond coupling step between the two Fe^{IV}=O **4** species by trapping them with organic free radical present in solution in excess prior to addition of AODs. To that end, a stable organic radical TEMPO (2,2',6,6'-tetramethylpiperidin-1-oxyl) was used as a trapping reagent. Aerobic addition of 100 equiv. of TEMPO to a precooled solution of **1** (0.378 mM) in MeOH at –73 °C, prior to addition of 0.5 equiv. of IBX-ester, resulted in a slow growth of an absorption band at λ_{max} = 500 nm over the course of 12 minutes, likely a μ-oxo dimer **6**, (Figure 4.8). Air O_2 leak can be ruled out because it affords an orange μ-peroxo dimer **3** MeOH at –73 °C instantaneously. TEMPO appears to react with **1** to afford high-valent Fe^{IV}=O **4** species, which in turn reacts with another equiv. of **1** to afford a μ-oxo dimeric **6**. These results also suggest that the rate of formation of **4** is too slow to afford a critical concertation to initiate an O–O bond coupling step. Instead, the afforded Fe^{IV}=O **4** species instantaneously reacts with another equiv. of **1,** which is present in a relative excess to **4**. It has been previously shown that TEMPO can react with the iron(I) synthon $PhB(MesIm)_3Fe(COE)$ ($PhB(MesIm)_3$ = phenyltris(1-mesityli-midazol-2-ylidene)borate, COE = cis-cyclooctene) to afford an Fe^{III}–O intermediate capable of oxo-atom transfer to Me_2PhP and was trapped by the triphenylmethyl radical.[49]

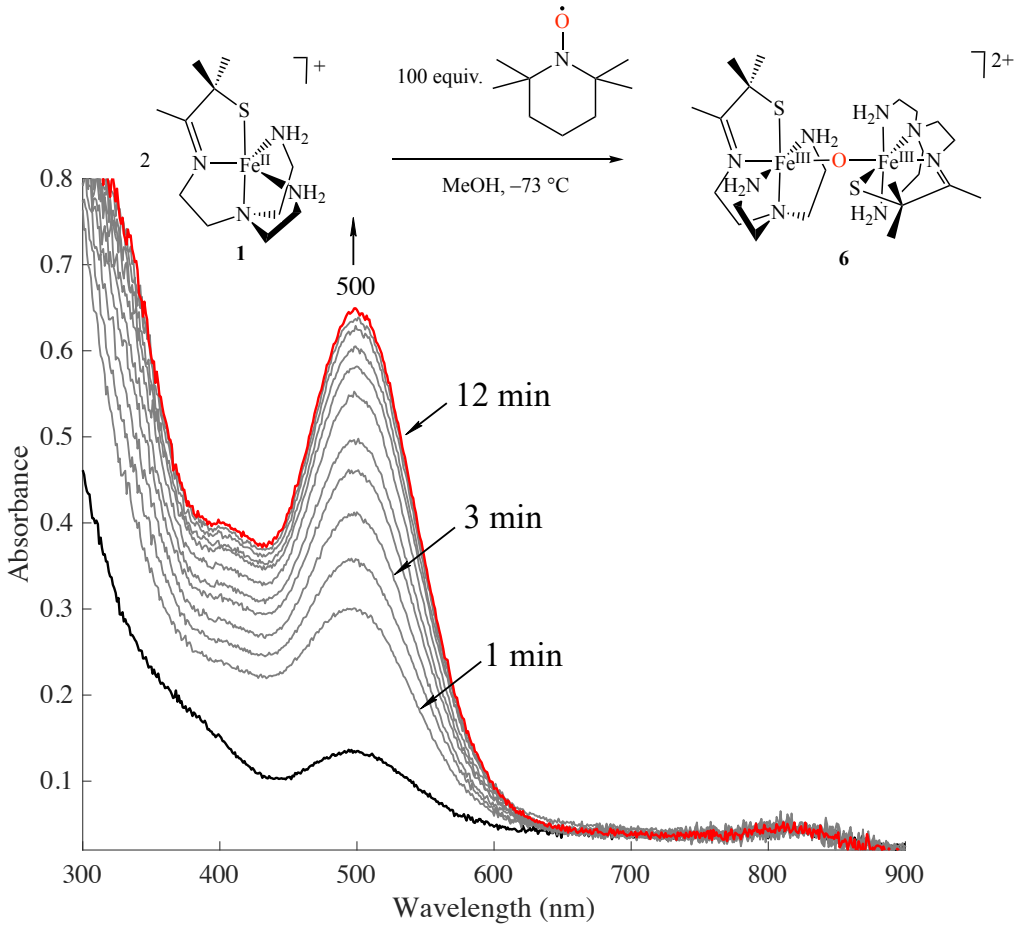

Figure 4.8. Electronic absorption spectrum showing a reaction between **1** (0.378 mM) and excess (100 equiv.) TEMPO results in growth of a μ-oxo dimer **6** at λ_{max}= 500 nm over the course of 12 minutes in MeOH at –73 °C.

Another strategy to trap a spectroscopically unobserved high-valent Fe^{IV}=O **4** species is by utilizing a redox-inactive metal ion such as $Sc(OTf)_3$ (OTf = trifluoromethanesulfonate). Redox-inactive metal ions (*e.g.* Ca^{II}, Zn^{II}, Sr^{II}, Sc^{III}, Lu^{III}, and Y^{III}) that function as Lewis acids have been shown to bind to high-valent metal-oxos and metal-peroxos, modulate their redox potential,[50,51] spin-state,[52] and reactivity.[50,53,54] Studying the effects of redox-inactive metal ions on high-valent metal-oxos and peroxos has attracted considerable attention due to their relevance in biological systems, such as the role of Ca^{II} or Sr^{II} in O_2 evolution during the photosynthesis.[55–57] Redox-inactive $Sc(OTf)_3$ metal became a particularly popular Lewis acid of choice as it has been shown

to facilitate trapping of high-valent Mn^{IV}– and Co^{IV}–oxos, as well as Cu^{II}–imido complexes,[58–61] as well as crystallographic characterization of [(TMC)Fe^{III}–O–$Sc^{III}(OTf)_4(OH_2)$] adduct.[53,62]

When monitored by the UV/Vis, addition of O_2 to **1** in the presence of excess (10 equiv.) $Sc(OTf)_3$ in MeOH at –73 °C affords a new intense blue intermediate at λ_{max} = 626, 525 (sh) nm over the course of 5 minutes, (Figure 4.9). Moreover, anaerobic addition of OADs (such as 0.5 equiv. of IBX-ester or 1 equiv. of PhIO) to the solution of **1** in the presence of 10 equiv. of $Sc(OTf)_3$ results in formation of the same intense blue species. The same blue intermediate has been observed in aprotic DMC solvent –73 °C. Warming the blue intermediate to room temperature results in the loss of spectral features, likely as a result of decomposition of the metal complex.

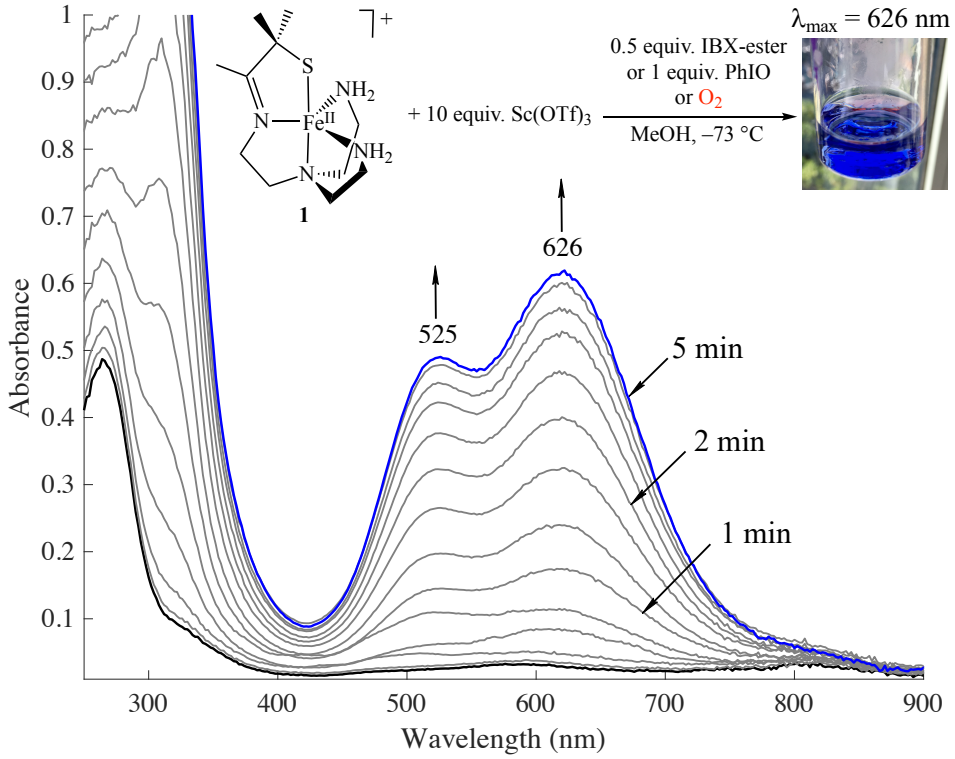

Figure 4.9. Electronic absorption spectrum showing a reaction between **1** (0.378 mM) and 10 equiv. $Sc(OTf)_3$ affords a new blue intermediate at λ_{max} = 626, 525 (sh) nm over the course of 5 minutes in MeOH at –73 °C.

In order to rule out that the new blue intermediate is simply an oxidized triflate-bound ferric intermediate, the starting ferrous complex **1** was oxidized in the presence of excess NaOTf

salt to generate authentic $[Fe^{III}(S^{Me2}N_4(tren))(OTf)]^+$ species. When monitored by UV/Vis, addition of 1 equiv. of $FeCp_2$ oxidant to **1** in the presence of 10 equiv. of NaOTf salt resulted in growth of an absorption band at λ_{max} = 523, 455 (sh) nm over the course of 15 minutes in MeOH at –73 °C, (Figure 4.10). The new intermediate at λ_{max} = 523 nm is district but falls in the usual spectral range of previously identified thiolate-ligated ferric derivatives of **1** but such as **7-OMe** (λ_{max} = 511 nm),[63] **7-MeOH** (λ_{max} = 565 nm),[38] **7-OAc** (λ_{max} = 537 nm),[64] and **7-Cl** (λ_{max} = 544 nm).[65] Therefore, the new intermediate at 523 nm would be consistent with a triflate-bound $[Fe^{III}(S^{Me2}N_4(tren))(OTf)]^+$ complex and new intermediate at 620 nm can be ruled out as a simple triflate-substituted product.

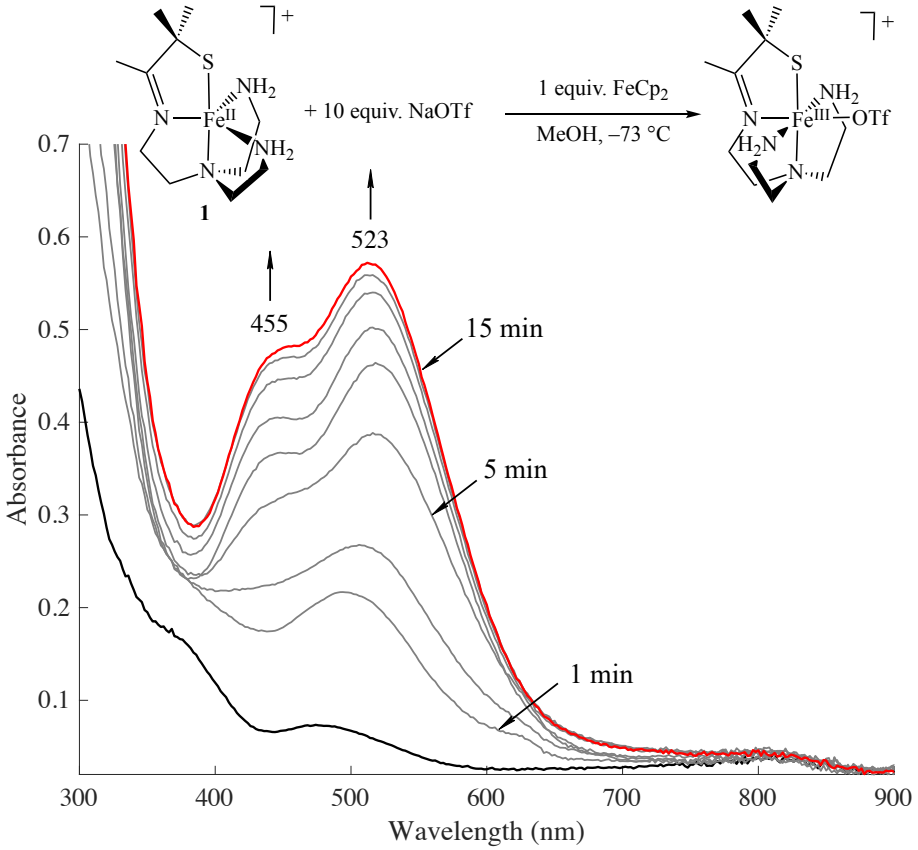

Figure 4.10. Electronic absorption spectrum showing oxidation of **1** (0.378 mM) with 1 equiv. $FeCp_2$ in the presence of 10 equiv. NaOTf to afford a metastable intermediate at λ_{max} = 523 nm, likely a triflate-bound $[Fe^{III}(S^{Me2}N_4(tren))(OTf)]^+$ species, in MeOH at –73 °C.

The same blue intermediate can be formed via addition of excess (10 equiv.) of $Sc(OTf)_3$ to O_2-generated μ-peroxo dimeric **3** in MeOH at –73 °C over the course of 30 minutes, (Figure 4.11, A). Since μ-peroxo dimeric **3** is stable at–73 °C over several days, $Sc(OTf)_3$ therefore appears to dramatically influence its reactivity and possibly accelerate an O–O bond activation. The blue intermediate is unlikely to be a peroxo-complex with an associated $Sc(OTf)_3$ ion because the same intermediate can be formed by adding excess (10 equiv.) $Sc(OTf)_3$ to an authentically generated μ-oxo dimer **6** in MeOH at –73 °C, (Figure 4.11, B). Taken together, these results suggest that the blue intermediate may be an oxo-, or hydroxo-bridged iron-scandium heterobimetallic dimer with $[(S^{Me2}N_4(tren))Fe^{III}–O–Sc^{III}(OTf)_3]^+$ or $[(S^{Me2}N_4(tren))Fe^{III}–O(H)–Sc^{III}(OTf)_3]^{2+}$ core. It is also important to note here that conversion from either **3** or **6** to the blue intermediate does not follow a conversion with a clean isosbestic point. This may indicate either the formation of multiple species *en route* to the blue intermediate or a presence of multiple final product species, such as $Fe^{III}–O–Sc^{III}$ and $Fe^{III}–O(H)–Sc^{III}$ type.

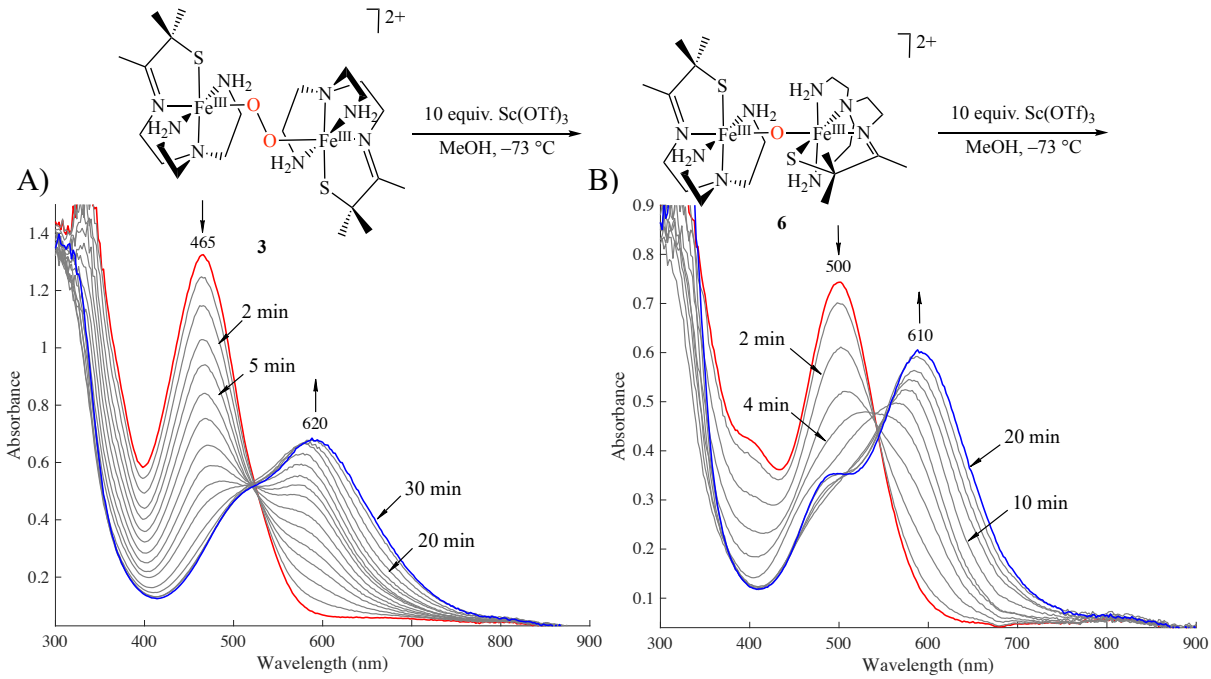

Figure 4.11. Electronic absorption spectrum showing: **A**) addition of 10 equiv. $Sc(OTf)_3$ to O_2-generated μ-peroxo **3** (λ_{max}= 465 nm) results in conversion to a blue intermediate at λ_{max}= 620 nm over the course of 30 minutes in MeOH at –74 °C. **B**) addition of 10 equiv. $Sc(OTf)_3$ to an authentically prepared μ-oxo dimer **6** (λ_{max}= 500 nm) results in conversion to a blue intermediate at λ_{max}= 610 nm over the course of 20 minutes in MeOH at –73 °C.

Finally, attempts to crystallize the blue intermediate at 620 nm has led to the discovery of yet another $Sc(OTf)_3$ dependent intermediate. During the crystallization set up, a concentrated methanolic solution of **1** (5 mL, 20 mM) was cooled at –80 °C for 15 minutes prior to the aerobic injection of 1.2 equiv. $Sc(OTf)_3$ (200 μL, 0.6 M). After cooling the iron-scandium mixture for another 10 minutes, the vial was opened to O_2, resulting in instantaneous formation of a dark-green solution. The reaction solution was diluted with precooled MeOH to ~ 1.0 mM and the absorption spectrum was taken by UV/Vis at –73 °C. The resulting spectrum of a reaction between a concentrated mixture of **1**and 1.2 equiv. $Sc(OTf)_3$ with O_2 afforded a new green intermediate at λ_{max} = 720, 435, 360 nm in MeOH at –73 °C, (Figure 4.12). The new intermediate was also characterized by an EPR, (Figure 4.13). CW X-band EPR ($\perp$-mode) indicates that a green

intermediate is a low spin (S = 1/2) ferric complex with a rhombic signal (g_x = 2.20, g_y = 2.14, g_z = 2.01), also atypical for the thiolate-ligated **1** chemistry. The green intermediate is stable at –80 °C for weeks but bleaches out in 10 minutes when warmed to room temperate. Moreover, warming the green intermediate to room temperature appeared to be accompanied by formation of bubbles in solution and pressurization of a closed reaction vial. Attempts to reproduce generation of the new green intermediate in dilute conditions (~0.4 mM) have proven to be so far unsuccessful.

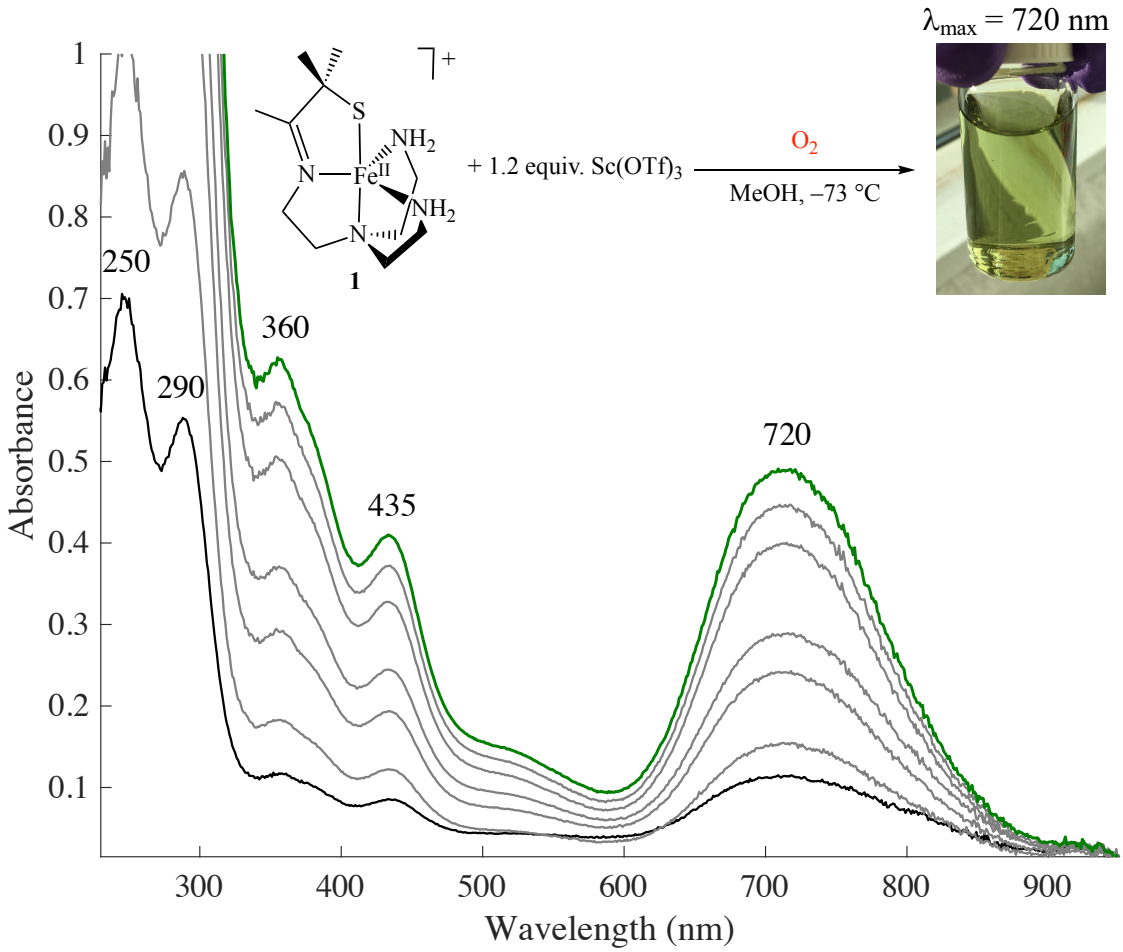

Figure 4.12. Electronic absorption spectrum showing a reaction between a concentrated mixture of **1** (~ 1.0 mM dilution) and 1.2 equiv. $Sc(OTf)_3$ with O_2 to afford a new green intermediate at λ_{max} = 720, 435, 360 nm in MeOH at –73 °C.

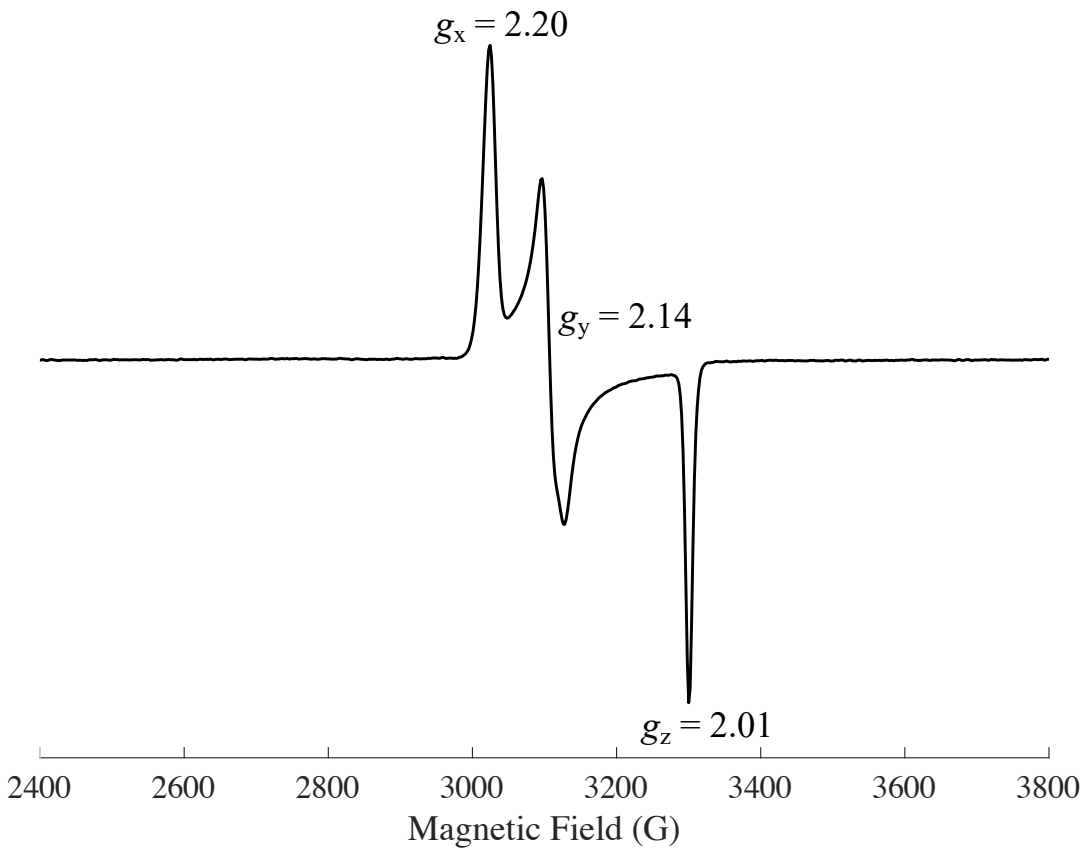

Figure 4.13. 9.28 GHz CW X-band EPR (⊥-mode) indicates that a green intermediate is a low spin (S = 1/2) ferric complex with a rhombic signal (g_x = 2.20, g_y = 2.14, g_z = 2.01). EPR measurements were taken at 117 K in MeOH/EtOH (9:1) glass.

4.4 Conclusions

This chapter provides evidence for the formation of an O–O bond by a *cis*-thiolate ligated $[Fe^{II}(S^{Me2}N_4(tren))](PF_6)$ (**1**). Addition of typical oxo-atom donors (OAD) such as isopropyl 2-iodoxybenzoate **(**IBX-ester), iodosobenzene (PhIO), or NaClO to the ferrous solution of **1** in a protic solvent, resulted in instantaneous formation of an orange μ-peroxo **3** intermediate. Comparison of the stopped-flow kinetic traces of the growth of O_2- and IBX-ester-derived μ-peroxo **3** reveals that the rate of formation of μ-peroxo **3** via oxo-atom donor addition is approximately two orders of magnitude slower. These results may be indicative of an O–O bond forming step. Detailed kinetic studies for the formation of the μ-peroxo dimer **3** via oxo-atom

donor addition to **1** are necessary and will provide more insight into the formation and involvement of high-valent Fe^{IV}=O **4** in an O–O bond coupling step. The IBX-ester-derived orange intermediate **3** is identical in chemical behavior to its O_2-derived counterpart. Similar to O_2-derived **3**, it is EPR silent over the temperature range from 4 K to 120 K and exhibits paramagnetically shifted ^{1}H NMR spectrum at 196 K. Moreover, the IBX-ester-derived **3** also converts to hydroxo-bound $[Fe^{III}(S^{Me2}N_4(tren))(OH)]^+$ intermediate upon slight warming to –40 °C. Oxygen-isotope labeling experiments reveal formation of a mixed-labeled H_2O_2 upon protonation of the mixed-labeled $^{16}O/^{18}O$-IBX-ester-derived orange intermediate **3**, suggesting a direct coupling step between the two Fe^{IV}=O. Computational studies will be required to shed more light on the plausible mechanism of this unprecedented thiolate-ligated iron-mediated O–O bond formation chemistry.

Attempts have been made to trap the spectroscopically unobserved high-valent Fe^{IV}=O **4** intermediate with TEMPO free radical and $Sc(OTf)_3$. Curiously, TEMPO free radical appears to react with the ferrous complex **1** to afford μ-oxo final product **6**, indicating that it too acts as an oxo-atom donor to, albeit less efficient. Attempts to trap the unobserved high-valent Fe^{IV}=O **4** intermediate with redox-inactive $Sc(OTf)_3$ metal ion resulted in identification of two new intermediates. An intense blue intermediate at λ_{max}= 620 nm forms upon the addition of O_2 or OADs in the presence of excess of $Sc(OTf)_3$. These results suggest that the blue intermediate may be an oxo-, or hydroxo-bridged iron-scandium heterobimetallic dimer with $[(S^{Me2}N_4(tren))Fe^{III}–O–Sc^{III}(OTf)_3]^+$ or $[(S^{Me2}N_4(tren))Fe^{III}–O(H)–Sc^{III}(OTf)_3]^{2+}$ core. On the other hand, reaction of concentrated **1**, in the presence of 1.2 equiv. $Sc(OTf)_3$, with O_2 afforded a new green intermediate at λ_{max}= 720 nm. Based on the rhombic EPR spectrum, the green intermediate appears to contain a low-spin (S = 1/2) state ferric core. $Sc(OTf)_3$ binding and reactivity studies provide a promising

lead to trap high-valent thiolate-ligated $[Fe^{IV}(O)(S^{Me2}N_4(tren))]^+$ (**4**) that has eluded spectroscopic characterization so far.

4.5 References

(1) Krest, C. M.; Silakov, A.; Rittle, J.; Yosca, T. H.; Onderko, E. L.; Calixto, J. C.; Green, M. T. *Nat. Chem.* **2015**, *7* (9), 696–702.

(2) Green, M. T.; Dawson, J. H.; Gray, H. B. *Science* **2004**, *304* (5677), 1653–1656.

(3) Stone, K. L.; Behan, R. K.; Green, M. T. *Proc. Natl. Acad. Sci. U. S. A.* **2005**, *102* (46), 16563–16565.

(4) Roach, P. L.; Clifton, I. J.; Hensgens, C. M. H.; Shibata, N.; Schofield, C. J.; Hajdu, J.; Baldwin, J. E. *Nature* **1997**, *387* (6635), 827–830.

(5) Shu, L. *Science* **1997**, *275* (5299), 515–518.

(6) Banerjee, R.; Proshlyakov, Y.; Lipscomb, J. D.; Proshlyakov, D. A. *Nature* **2015**, *518* (7539), 431–434.

(7) Cox, N.; Retegan, M.; Neese, F.; Pantazis, D. a.; Boussac, a.; Lubitz, W. *Science* **2014**, *345* (6198), 804–808.

(8) Vinyard, D. J.; Khan, S.; Brudvig, G. W. *Faraday Discuss.* **2015**, *185*, 37–50.

(9) Lee, A. Q.; Streit, B. R.; Zdilla, M. J.; Abu-Omar, M. M.; DuBois, J. L. *Proc. Natl. Acad. Sci.* **2008**, *105* (41), 15654–15659.

(10) Roth, J. P.; Cramer, C. J. *J. Am. Chem. Soc.* **2008**, *130* (25), 7802–7803.

(11) Gamba, I.; Codolà, Z.; Lloret-Fillol, J.; Costas, M. *Coord. Chem. Rev.* **2017**, *334*, 2–24.

(12) Gilbert, J. A.; Eggleston, D. S.; Murphy, W. R.; Geselowitz, D. A.; Gersten, S. W.; Hodgson, D. J.; Meyer, T. J. *J. Am. Chem. Soc.* **1985**, *107* (13), 3855–3864.

(13) Liu, F.; Concepcion, J. J.; Jurss, J. W.; Cardolaccia, T.; Templeton, J. L.; Meyer, T. J. *Inorg. Chem.* **2008**, *47* (6), 1727–1752.

(14) Concepcion, J. J.; Jurss, J. W.; Templeton, J. L.; Meyer, T. J. *J. Am. Chem. Soc.* **2008**, *130* (49), 16462–16463.

(15) Romain, S.; Bozoglian, F.; Sala, X.; Llobet, A. *J. Am. Chem. Soc.* **2009**, *131* (8), 2768–2769.

(16) Wada, T.; Tsuge, K.; Tanaka, K. *Angew. Chemie Int. Ed.* **2000**, *39* (8), 1479–1482.

(17) Binstead, R. A.; Chronister, C. W.; Ni, J.; Hartshorn, C. M.; Meyer, T. J. *J. Am. Chem. Soc.* **2000**, *122* (35), 8464–8473.

(18) Crandell, D. W.; Xu, S.; Smith, J. M.; Baik, M.-H. *Inorg. Chem.* **2017**, *56* (8), 4435–4445.

(19) Kim, S. H.; Park, H.; Seo, M. S.; Kubo, M.; Ogura, T.; Klajn, J.; Gryko, D. T.; Valentine, J. S.; Nam, W. *J. Am. Chem. Soc.* **2010**, *132* (40), 14030–14032.

(20) Guo, M.; Lee, Y. M.; Gupta, R.; Seo, M. S.; Ohta, T.; Wang, H. H.; Liu, H. Y.; Dhuri, S. N.; Sarangi, R.; Fukuzumi, S.; Nam, W. *J. Am. Chem. Soc.* **2017**, *139* (44), 15858–15867.

(21) Ishizuka, T.; Watanabe, A.; Kotani, H.; Hong, D.; Satonaka, K.; Wada, T.; Shiota, Y.; Yoshizawa, K.; Ohara, K.; Yamaguchi, K.; Kato, S.; Fukuzumi, S.; Kojima, T. *Inorg. Chem.* **2016**, *55* (3), 1154–1164.

(22) Brodsky, C. N.; Hadt, R. G.; Hayes, D.; Reinhart, B. J.; Li, N.; Chen, L. X.; Nocera, D. G. *Proc. Natl. Acad. Sci.* **2017**, *114* (15), 3855–3860.

(23) Furutachi, H.; Hashimoto, K.; Nagatomo, S.; Endo, T.; Fujinami, S.; Watanabe, Y.; Kitagawa, T.; Suzuki, M. *J. Am. Chem. Soc.* **2005**, *127* (13), 4550–4551.

(24) Hashimoto, K.; Nagatomo, S.; Fujinami, S.; Furutachi, H.; Ogo, S.; Suzuki, M.; Uehara, A.; Maeda, Y.; Watanabe, Y.; Kitagawa, T. *Angew. Chemie Int. Ed.* **2002**, *41* (7), 1202–

1205.

(25) Kodera, M.; Itoh, M.; Kano, K.; Funabiki, T.; Reglier, M. *Angew. Chemie Int. Ed.* **2005**, *44* (43), 7104–7106.

(26) Kodera, M.; Kawahara, Y.; Hitomi, Y.; Nomura, T.; Ogura, T.; Kobayashi, Y. *J. Am. Chem. Soc.* **2012**, *134* (32), 13236–13239.

(27) Martinho, M.; Banse, F.; Bartoli, J.-F.; Mattioli, T. A.; Battioni, P.; Horner, O.; Bourcier, S.; Girerd, J.-J. *Inorg. Chem.* **2005**, *44* (25), 9592–9596.

(28) Kroll, N.; Speckmann, I.; Schoknecht, M.; Gülzow, J.; Diekmann, M.; Pfrommer, J.; Stritt, A.; Schlangen, M.; Grohmann, A.; Hörner, G. *Angew. Chemie Int. Ed.* **2019**, *58* (38), 13472–13478.

(29) Ellis, W. C.; McDaniel, N. D.; Bernhard, S.; Collins, T. J. *J. Am. Chem. Soc.* **2010**, *132* (32), 10990–10991.

(30) Panda, C.; Debgupta, J.; Díaz Díaz, D.; Singh, K. K.; Sen Gupta, S.; Dhar, B. B. *J. Am. Chem. Soc.* **2014**, *136* (35), 12273–12282.

(31) Chambers, M. B.; Wang, X.; Elgrishi, N.; Hendon, C. H.; Walsh, A.; Bonnefoy, J.; Canivet, J.; Quadrelli, E. A.; Farrusseng, D.; Mellot-Draznieks, C.; Fontecave, M. *ChemSusChem* **2015**, *8* (4), 603–608.

(32) Fillol, J. L.; Codolà, Z.; Garcia-Bosch, I.; Gómez, L.; Pla, J. J.; Costas, M. *Nat. Chem.* **2011**, *3* (10), 807–813.

(33) Evans, D. F. *J. Chem. Soc.* **1959**, 2003.

(34) Live, D. H.; Chan, S. I. *Anal. Chem.* **1970**, *42* (7), 791–792.

(35) Van Geet, A. L. *Anal. Chem.* **1968**, *40* (14), 2227–2229.

(36) Zhdankin, V. V.; Koposov, A. Y.; Litvinov, D. N.; Ferguson, M. J.; McDonald, R.; Luu,

T.; Tykwinski, R. R. *J. Org. Chem.* **2005**, *70* (16), 6484–6491.

(37) Schardt, B. C.; Hill, C. L. *Inorg. Chem.* **1983**, *22* (10), 1563–1565.

(38) Theisen, R. M.; Kovacs, J. A. *Inorg. Chem.* **2005**, *44* (5), 1169–1171.

(39) Bukowski, M. R. *Science* **2005**, *310* (5750), 1000–1002.

(40) England, J.; Martinho, M.; Farquhar, E. R.; Frisch, J. R.; Bominaar, E. L.; Münck, E.; Que, L. *Angew. Chemie* **2009**, *121* (20), 3676–3680.

(41) Biswas, A. N.; Puri, M.; Meier, K. K.; Oloo, W. N.; Rohde, G. T.; Bominaar, E. L.; Münck, E.; Que, L. *J. Am. Chem. Soc.* **2015**, *137* (7), 2428–2431.

(42) Lim, M. H.; Rohde, J.-U.; Stubna, A.; Bukowski, M. R.; Costas, M.; Ho, R. Y. N.; Munck, E.; Nam, W.; Que, L. *Proc. Natl. Acad. Sci. U. S. A.* **2003**, *100* (7), 3665–3670.

(43) Zhou, A.; Kleespies, S. T.; Van Heuvelen, K. M.; Que, L. *Chem. Commun.* **2015**, *51* (76), 14326–14329.

(44) Warren, J. J.; Mayer, J. M. *Proc. Natl. Acad. Sci.* **2010**, *107* (12), 5282–5287.

(45) Xue, X. S.; Ji, P.; Zhou, B.; Cheng, J. P. *Chem. Rev.* **2017**, *117* (13), 8622–8648.

(46) Warren, J. J.; Tronic, T. a.; Mayer, J. M.; Bond, S. V. G. *Chem. Rev.* **2010**, *110* (12), 6961–7001.

(47) Tanko, J. M. *CRC Handbook of Chemistry and Physics: A Ready-Reference of Chemical and Physical Data*, 85th ed.; David R. Lide, Ed.; CRC Press LLC: Boca Raton, FL., 2004; Vol. 127.

(48) Kundu, S.; Schwalbe, M.; Ray, K. *Inorg. React. Mech.* **2012**, *8* (1–2), 41–57.

(49) Smith, J. M.; Mayberry, D. E.; Margarit, C. G.; Sutter, J.; Wang, H.; Meyer, K.; Bontchev, R. P. *J. Am. Chem. Soc.* **2012**, *134* (15), 6516–6519.

(50) Bang, S.; Lee, Y.-M.; Hong, S.; Cho, K.-B.; Nishida, Y.; Seo, M. S.; Sarangi, R.;

Fukuzumi, S.; Nam, W. *Nat. Chem.* **2014**, *6* (10), 934–940.

(51) Bae, S. H.; Lee, Y.; Fukuzumi, S.; Nam, W. *Angew. Chemie Int. Ed.* **2017**, *56* (3), 801–805.

(52) Swart, M.; Gruden, M. *Acc. Chem. Res.* **2016**, *49* (12), 2690–2697.

(53) Fukuzumi, S.; Morimoto, Y.; Kotani, H.; Naumov, P.; Lee, Y. M.; Nam, W. *Nat. Chem.* **2010**, *2* (9), 756–759.

(54) Nam, W.; Lee, Y. M.; Fukuzumi, S. *Acc. Chem. Res.* **2014**, *47* (4), 1146–1154.

(55) Lohmiller, T.; Shelby, M. L.; Long, X.; Yachandra, V. K.; Yano, J. *J. Phys. Chem. B* **2015**, *119* (43), 13742–13754.

(56) Boussac, A.; Rutherford, A. W. *Biochemistry* **1988**, *27* (9), 3476–3483.

(57) Renger, G. *J. Photochem. Photobiol. B Biol.* **2011**, *104* (1–2), 35–43.

(58) Chen, J.; Lee, Y.-M.; Davis, K. M.; Wu, X.; Seo, M. S.; Cho, K.-B.; Yoon, H.; Park, Y. J.; Fukuzumi, S.; Pushkar, Y. N.; Nam, W. *J. Am. Chem. Soc.* **2013**, *135* (17), 6388–6391.

(59) Pfaff, F. F.; Kundu, S.; Risch, M.; Pandian, S.; Heims, F.; Pryjomska-Ray, I.; Haack, P.; Metzinger, R.; Bill, E.; Dau, H.; Comba, P.; Ray, K. *Angew. Chemie Int. Ed.* **2011**, *50* (7), 1711–1715.

(60) Kundu, S.; Miceli, E.; Farquhar, E.; Pfaff, F. F.; Kuhlmann, U.; Hildebrandt, P.; Braun, B.; Greco, C.; Ray, K. *J. Am. Chem. Soc.* **2012**, *134* (36), 14710–14713.

(61) Hong, S.; Pfaff, F. F.; Kwon, E.; Wang, Y.; Seo, M.-S.; Bill, E.; Ray, K.; Nam, W. *Angew. Chemie Int. Ed.* **2014**, *53* (39), 10403–10407.

(62) Prakash, J.; Rohde, G. T.; Meier, K. K.; Jasniewski, A. J.; Van Heuvelen, K. M.; Münck, E.; Que, L. *J. Am. Chem. Soc.* **2015**, *137* (10), 3478–3481.

(63) Shearer, J.; Scarrow, R. C.; Kovacs, J. A. *J. Am. Chem. Soc.* **2002**, *124* (39), 11709–

11717.

(64) Theisen, R. M.; Shearer, J.; Kaminsky, W.; Kovacs, J. A. *Inorg. Chem.* **2004**, *43* (24), 7682–7690.

(65) Theisen, R. M. Synthetic Models and Reactivity of Sulfur-Ligated Iron Metalloenzymes, University of Washington, 2005.

Chapter 5. Geometric and Electronic Structure of a Crystallographically Characterized Thiolate-Ligated Binuclear Peroxo-Bridged Cobalt(III) Complex

Reprinted by permission from the Springer Nature Customer Service Centre GmbH: JBIC Journal of Biological Inorganic Chemistry, from Geometric and Electronic Structure of a Crystallographically Characterized Thiolate-Ligated Binuclear Peroxo-Bridged Cobalt(III) Complex, Maksym A. Dedushko, Dirk Schweitzer, Maike N. Blakely, Rodney D. Swartz, Werner Kaminsky, and Julie A. Kovacs *J. Biol. Inorg. Chem.* **2019**, 24, 919–926; Copyright © 2019, Society for Biological Inorganic Chemistry (SBIC).

5.1 Introduction

Photosynthesis is one of the most important biochemical processes for maintaining life on our planet.[1,2] This process involves capturing solar energy in chemical bonds via the catalytic oxidation of H_2O, in order to extract electrons, with O_2 as a by-product.[3–6] Nature had three billion years to refine this highly efficient Mn-containing catalyst, which is referred to as the oxygen evolving complex (OEC). The OEC consists of a $CaMn_3O_4$ cubane with a dangling Mn ion. Insights into the mechanism of water oxidation and O_2 evolution, as well as its microscopic reverse would contribute to the development of methods for the conversion of sunlight into storable fuels. The O–O bond formation step is not well understood[7] since it follows the rate-determining step in the mechanism.[8–12] An unobserved Mn-peroxo intermediate is proposed to form in this step,[9–11] followed by the rapid release of O_2.[13] Despite the fundamental importance of manganese-dioxygen

chemistry, it remains relatively unexplored.[14–16] Small molecules provide an advantage in that lower temperatures can be accessed by using organic solvents, thereby providing an opportunity to observe metastable intermediates. Mononuclear Mn-peroxo complexes include side-on η^2-bound peroxo $[Mn^{III}(O_2)(13\text{-TMC})]^+$,[17] and $[Mn^{III}(O_2)\kappa^4\text{-}N_4py]^+$.[18] There are fewer examples of binuclear Mn peroxo compounds, and no examples of Mn clusters containing a coordinated peroxo. Our group reported the first example of a spectroscopically and structurally characterized, metastable binuclear peroxo-bridged Mn(III) complex derived from dioxygen.[14,19] In addition, we have examined the effect of coordination environment on peroxo O–O bond lengths.[20]

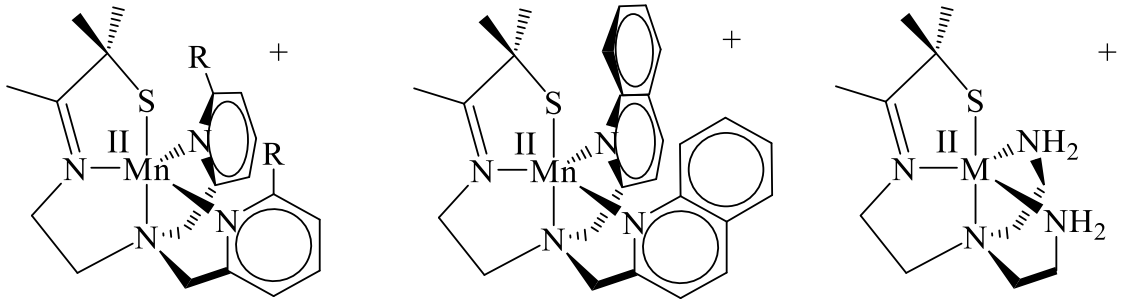

R = Me (**2**), H (**4**), MeO (**6**) **7** M = Mn (**5**), Co(**8**)

Figure 5.1. ChemDraw diagrams of $[Mn^{II}(S^{Me2}(6\text{-Me-DPEN}))]^+$ (**2**), $[Mn^{II}(S^{Me2}(6\text{-H-DPEN}))]^+$ (**4**), $[Mn^{II}(S^{Me2}(6\text{-MeO-DPEN}))]^+$ (**6**), $[Mn^{II}(S^{Me2}(\text{quinoEN}))]^+$ (**7**), $[Mn^{II}(S^{Me2}N_4(\text{tren}))](PF_6)$ (**5**), and $[Co^{II}(S^{Me2}N_4(\text{tren}))](PF_6)$ (**8**).

The inherent instability and reactive nature of dinuclear Mn(III)-peroxo complexes, both posited in nature and their synthetic analogues, renders the experimental investigation of their electronic and geometric structures difficult. Most of the reported complexes are mononuclear Mn(III)-peroxo compounds with a peroxo moiety bound in a side-on (η^2) binding mode.[15,21–24] There are very few examples of structurally characterized multi-nuclear Mn(III)-peroxo complexes.[19,25] We reported the first crystallographically characterized binuclear example, $\{[Mn^{III}(S^{Me2}(6\text{-Me-DPEN}))]_2(\mu\text{-}O_2)\}^{2+}$ (**1**) derived from O_2. $[Mn^{II}(S^{Me2}(6\text{-Me-DPEN}))]^+$ (**2**) binds dioxygen, the microscopic reverse of photosynthetic O_2 evolution by the OEC, on the millisecond

timescale to form a superoxo intermediate, which then converts to **1**, *en route* to a binuclear μ-oxo end-product, $\{[Mn^{III}(S^{Me2}(6\text{-Me-DPEN}))]_2(\mu\text{-O})\}^{2+}$ (**3**).[19] The isolation of peroxo complex **1** was possible because the rate-determining step was determined to be the O–O bond cleaving step.[19] The N-heterocycles (N^{Ar}) of $[Mn^{II}(S^{Me2}(6\text{-Me-DPEN}))]^+$ (**2**) can be derivatized providing a convenient method for determining how steric and electronic properties affect the stability of metastable dioxygen intermediates.[20] Manganese dioxygen intermediates are not observed in the absence of steric bulk, for example with a H-substituent in the 6-position, $[Mn^{II}(S^{Me2}(6\text{-H-DPEN}))]^+$ (**4**), or with primary amines in the ligand scaffold, $[Mn^{II}(S^{Me2}N_4(\text{tren}))]^+$ (**5**). Our group has shown that steric bulk increases metal ion Lewis acidity by lengthening metal-ligand bonds, resulting in a stronger peroxo O–O bond.[26]

More recent work by our group has led to the observation of two new metastable peroxo intermediates formed in the reaction between O_2 and thiolate-ligated Mn(II) derivatives (Figure 5.1) of **2**, $[Mn^{II}(S^{Me2}(6\text{-MeO-DPEN}))]^+$ (**6**) and $[Mn^{II}(S^{Me2}(\text{quinoEN}))]^+$ (**7**).[20] Changing the steric bulk and electron donor character of the ligand was shown to affect the barriers to O_2 binding and release, as well as O–O bond cleavage.[20] The less sterically encumbered 6-MeO-pyridine complex **6** binds O_2 more readily than the other derivatives, **2** and **7**, and O_2 release from the superoxo is more favored. In addition, the 6-MeO-pyridine complex forms a total of four metastable intermediates with dioxygen, two of which follow a peroxo, *en route* to a mono oxo-bridged dimer product.[20] Thiolate ligands (RS^-) were incorporated, because they have been shown to lower the activation barrier to O_2 binding,[27,28] as well as provide a convenient spectroscopic handle for observing reactive dioxygen intermediates.[29]

The photosynthetic OEC's dioxygen evolving properties can also be mimicked by cobalt complexes, the most notable example being Nocera's bioinspired artificial leaf.[5,30] Discrete

molecular Co_4O_4 cubane clusters, such as $[Co_4O_4(OAc)_4(py)_4]^+$, have also been shown to evolve O_2 upon the addition of OH^-.[31] A Co–peroxo is proposed to form as an intermediate, however, it was not observed. The mechanism is proposed to involve an oxidized trapped valence $Co^{III}_2Co^{IV}_2$ cubane cluster, and coupling between two oxyls on an adjacent Co^{IV}_2 pair ($O–Co^{IV}–Co^{IV}–O \rightarrow \bullet O–Co^{III}–Co^{III}–O\bullet$ to afford an unobserved $Co^{III}–O–O–Co^{III}$ peroxo.[30]

The mechanism for the O–O bond forming step is likely to be different for Co and Mn, given that the oxo wall separates them:[32] the former is almost certain to proceed via an oxyl coupling mechanism,[12] whereas the latter could proceed via a nucleophilic attack mechanism involving Mn(V)=O and M-OH (M = Ca(II) or Mn(III)) intermediates.[33] Developing a better understanding of the geometric and electronic structural differences between small molecule Mn(III) and Co(III) peroxo complexes, and the properties critical to O_2 release,[12] is likely to shed more light on these reactions, and provide insight into metal-dependent mechanisms. There are many examples of synthetic Co(II) complexes that readily react with molecular O_2 at room temperature to form isolable dinuclear μ-peroxo Co(III) complexes, including a crystallographically characterized pac-man Schiff-base calixpyrrole-ligated binuclear Co(III) peroxo,[34] and a crystallographically characterized fused pincer-ligated binuclear Co(III) peroxo complex.[35–40] However, there are few (if any) structurally analogous pairs of binuclear μ-peroxo-bridged Co(III) and Mn(III) complexes. Whereas Mn(III) peroxo complexes are metastable, the added stability of low-spin d^6 transition-metal complexes is likely to stabilize a small molecule Co(III) peroxo, making it easier to obtain a structure. Described herein, is a crystallographically characterized, O_2-derived thiolate-ligated Co(III)-μ-peroxo complex, which is structurally analogous to our previously reported series of O_2-derived Mn–peroxo complexes.[19]

5.2 Experimental

General Methods. All manipulations were performed using Schlenk line techniques or under a N_2 atmosphere in a glovebox. Reagents and solvents were purchased from commercial vendors were of highest available purity and were used without further purification unless otherwise noted. MeOH (Na) and MeCN (CaH_2) were dried and distilled prior to use. Acetonitrile, Diethyl ether, and THF were rigorously degassed and purified using solvent purification columns housed in a custom stainless-steel cabinet and dispensed by a stainless-steel Schlenk-line (GlassContour). $[Co^{II}(S^{Me2}N_4(tren))](PF_6)$ (**8**) was prepared according to literature procedures.[41] NMR spectra were recorded on a Bruker DPX 500 FTNMR spectrometer and referenced to the residual protio solvent. Electrospray-ionization mass spectra were obtained on a Bruker Esquire Liquid Chromatograph-Ion Trap mass spectrometer. Cyclic voltammograms were recorded in MeCN solutions with $Bu_4N(PF_6)$ (0.100 M) as the supporting electrolyte, using an EG&G Princeton Applied Research potentiostat with a glassy carbon working electrode, an SCE reference electrode, and a platinum auxiliary electrode. Electronic absorption spectra were recorded using a Hewlett-Packard 8453 diode array spectrometer. Elemental analyses were performed by Atlantic Microlab, Inc. (Norcross, GA).

Synthesis of $[Co^{III}(S^{Me2}N_4(tren))]_2$(*trans*-$\mu$-1,2-$O_2$)$(PF_6)_2$•MeCN (9). Reduced $[Co^{II}(S^{Me2}N_4(tren))](PF_6)$ (**8**) (317 mg, 0.71 mmol) was dissolved in 100 mL of acetonitrile. The solution was exposed to air at room temperature and left to stir overnight. The dark red solution was evaporated to dryness, and the resulting red powder was washed with diethyl ether over a frit. The remaining solid was dissolved in 10 mL acetonitrile and layered with 30 mL of diethyl ether. The two layers were allowed to diffuse overnight at –40 °C to afford red crystals of **9**. ESI-MS:

Calculated *m/z* for $[C_{22}H_{50}Co_2N_8O_2S_2]^{2+}$ = 320.1 found *m/z* = 320.4. Electronic Absorption Spectrum (MeCN): λ_{max} (nm) ($\varepsilon(M^{-1}cm^{-1})$): 270(6500). ^{1}H NMR (500 MHz, CD_3CN) δ ppm 1.45 (s, 6H), 2.05 (s, 3H), 2.44 (s, 2H), 2.72 (dd, *J* = 11.07, 4.37 Hz, 2H), 2.78 (q, *J* = 6.38 Hz, 2H), 3.00 (s, 2H), 3.33 (dd, *J* = 12.00, 5.44 Hz, 2H), 3.40 (t, *J* = 8.50, 8.50 Hz, 2H), 3.66 (t, *J* = 7.22, 7.22 Hz, 2H). Reduction Potential (MeCN, vs. SCE): +220 mV (reversible). Elemental Analysis for $C_{22}H_{50}Co_2F_{12}N_8O_2P_2S_2$ Calcd: C, 28.39; H, 5.42; N, 12.04. Found: C, 28.86; H, 5.41; N, 12.92.

X-Ray Crystallographic Structure Determination. A 0.19 x 0.17 x 0.14 a black prism of $[Co^{III}(S^{Me2}N_4(tren))]_2$(*trans*-$\mu$-1,2-$O_2$)]$(PF_6)\cdot$MeCN (**9**) was mounted on a glass capillary with oil. Data was collected at –143 °C on a Nonius Kappa CCD single crystal X-ray diffractometer, Mo Kα-radiation. Crystal-to-detector distance was 30 mm and exposure time was 15 seconds per degree for all sets. The scan width was 2°. Data collection was 94.5% complete to 29.61° in θ and 96.9% complete to 25° in θ. A total of 18,295 partial and complete reflections were collected covering the indices, h = –9 to 8, k = –13 to 14, l = –15 to 14. 6,556 reflections were symmetry independent and the R_{int} = 0.0408 indicated that the data was above average quality (0.07). Indexing and unit cell refinement indicated a triclinic P lattice. The space group was found to be P-1 (No.2). The data for **9** was integrated and scaled using hkl-SCALEPACK.[42,43] Solution by direct methods (SHELXS, SIR97) produced a complete heavy atom phasing model consistent with the proposed structure.[44,45] The structure was completed by difference Fourier synthesis with SHELXL.[46,47] Scattering factors are from Waasmair and Kirfel.[11] Hydrogen atoms were placed in geometrically idealized positions and constrained to ride on their parent atoms with C---H distances in the range 0.95-1.00 Angstrom. Isotropic thermal parameters Ueq were fixed such that they were 1.2 Ueq of their parent atom Ueq for CH's and 1.5 Ueq of their parent atom Ueq in case

of methyl groups. All non-hydrogen atoms were refined anisotropically by full-matrix least-squares. Final solution plotted using ORTEP and POV-Ray programs.[48,49]

Table 5.1. Crystal data and structure refinement parameters for $[Co^{III}(S^{Me2}N_4(tren))]_2(trans\text{-}\mu\text{-}1,2\text{-}O_2)](PF_6)_2\cdot MeCN$ (**9**).

	9
Formula	$C_{13}H_{28}CoF_6N_5OPS$
Molecular Weight (g mol^{-1})	506.36
Temperature (K)	130(2)
Crystal System	Triclinic
Space Group	P -1
a, (Å)	7.9820(7)
b, (Å)	11.2500(10)
c, (Å)	12.0810(13)
α, (°)	98.554(5)
β, (°)	90.311(7)
γ, (°)	108.434(7)
V (Å^3)	1016.14(17)
Z	2
R_1	0.0733
R_w	0.0979
GOF	0.970

Computational Details. Calculations were performed using the ORCA v.4.0.0 quantum chemistry package developed by Neese and coworkers.[50] Geometry optimizations employed the B3LYP hybrid functional and 6-311G basis set for all complexes. Tight convergence criteria were required for self-consistent field (SCF) solutions. The Grid4 (GridX4) integration grid size, and the conductor-like polarizable continuum model (CPCM), were used for geometry optimizations.[51]

Crystallographic coordinates were used as a starting point for geometry optimizations of peroxo $\{[Co^{III}(S^{Me2}N_4(tren))]_2(\textit{trans}\text{-}\mu\text{-}1,2\text{-}O_2)\}^{2+}$ (**9**) using the B3LYP/6-311G functional/basis set. Details regarding the theoretical calculations for peroxo-bridged $[Mn^{III}(S^{Me2}N_4(quinoEN)]_2(\mu\text{–}O_2)(BPh_4)_2$ (**10**) and $\{[Mn^{III}(S^{Me2}N_4(6\text{-}MeO\text{-}DPEN)]_2\text{-}(\mu\text{-}O_2)\}^{2+}$ (**11**) reported elsewhere.[20] Canonical molecular orbital isosurfaces were visualized at an isovalue of 0.03 a_0^3 using UCSF Chimera software.[52]

5.3 Results and Discussion

5.3.1 *Spectroscopic and Crystallographic Characterization of $\{[Co^{III}(S^{Me2}N_4(tren))]_2(trans\text{-}\mu\text{-}1,2\text{-}O_2)\}^{2+}$ (**9**)*

The reaction between $[Co^{II}(S^{Me2}N_4(tren))](PF_6)$ (**8**) and dioxygen (O_2) in MeCN at ambient temperature results in a color change from pale yellow to red, with the concomitant growth of peaks at $\lambda_{max}(\varepsilon(M^{-1}cm^{-1}))$ = 280(11350), 385(3085), and 485(1250) nm (Figure 5.2). The ^{1}H NMR of this dioxygen product, **9**, (Figure 5.3) only contains peaks in the diamagnetic region of the spectrum, consistent with oxidation of the S = 3/2 Co(II) precursor[41] to low-spin (L.S.) S = 0 Co(III).

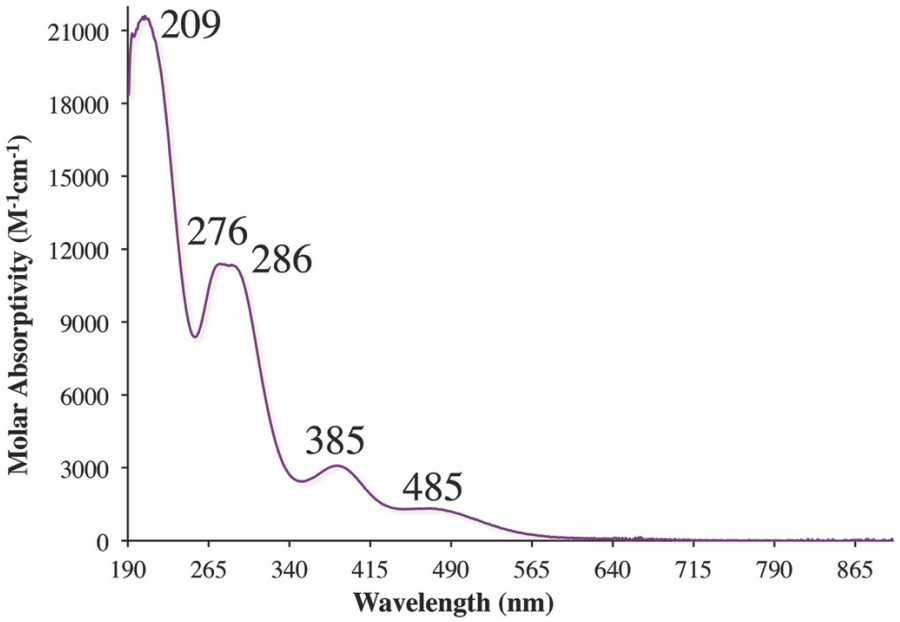

Figure 5.2. Quantitative electronic absorption spectrum of peroxo-bridged **9.**

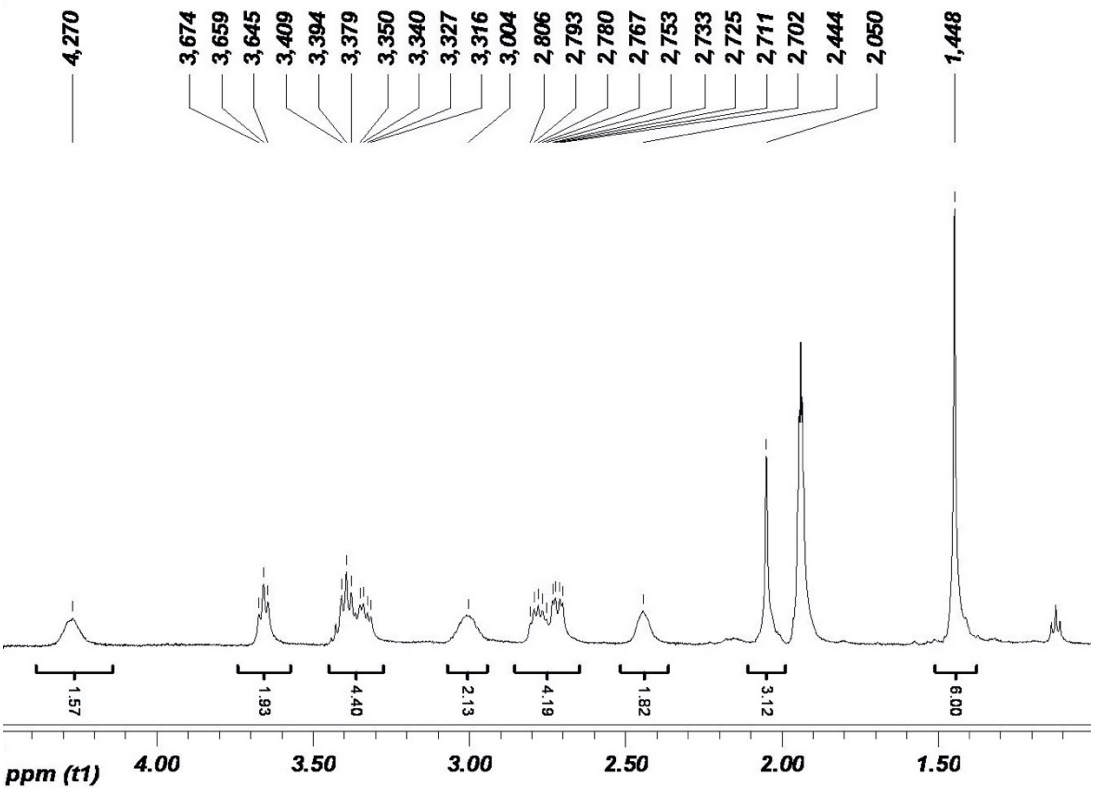

Figure 5.3. ^{1}H NMR spectrum of low-spin (S = 0) $[Co^{III}(S^{Me2}N_4(tren))]_2$(*trans*-$\mu$-1,2-$O_2$)$(PF_6)_2$•MeCN (**9**) in CD_3CN.

The ESI-MS of **9** (Figure 5.4) displays peak at *m/z* = 320.0, consistent with the addition of two oxygen atoms to a dicationic dimer (M + 32, where M= 608.2, *z* = 2), or the addition a single oxygen atom to a monocationic monomer (M + 16, where M= 304.1. *z* = 1). These two would be distinguishable based on their isotope distribution pattern. As shown in the simulated spectrum of Figure S1, peaks would be separated by 1/2 mass unit for a dicationic dimer, versus one mass unit for a monocationic monomer. The experimental data would therefore be consistent with the former. This was consistently the case across a wide range of applied skim voltages (4 – 10 V to 30 – 70 V), implying that we are looking at either a Co-peroxo with a remarkably weak O–O bond, or a Co–oxo. The reaction of **8** with isotopically labeled $^{18}O_2$ results in a peak shift to *m/z* to 322.0 (M + 18), consistent with incorporation of a one oxygen atom, derived from dioxygen.

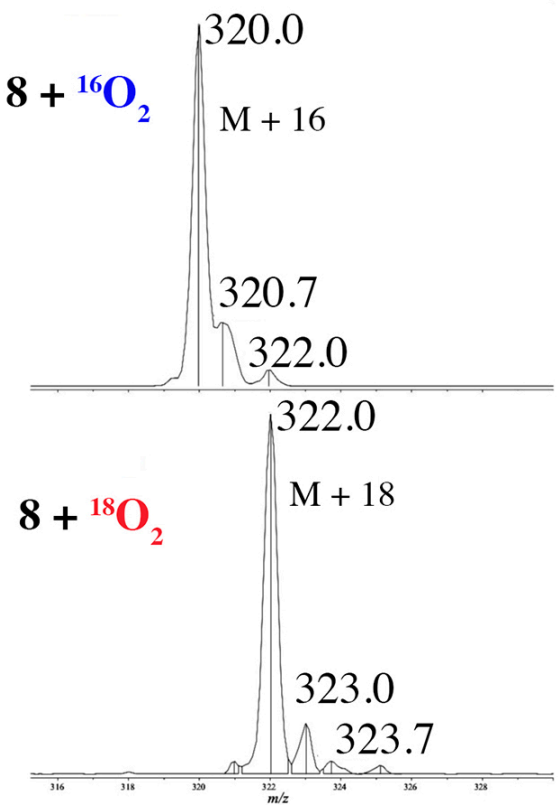

Figure 5.4. ESI-MS of peroxo-bridged **9** derived from $^{16}O_2$ (top) and $^{18}O_2$ (bottom).

Crystallization from MeCN/Et_2O afforded single crystals of **9** suitable for X-ray crystallography. As shown in the ORTEP diagram of Figure 3, $\{[Co^{III}(S^{Me2}N_4(tren))]_2(\textit{trans}\text{-}\mu\text{-}1,2\text{-}O_2)\}^{2+}$ (**9**), is binuclear and contains an O_2 moiety bridging between two Co ions in a *trans*-μ-1,2- configuration. The Co–S bond length of **9** (2.2180(9) Å) is 0.083 Å shorter than the reduced precursor **8** (Co–S = 2.3006(7) Å), and the average Co–N bond length distance is 0.173 Å shorter than the corresponding distance in **8**. More importantly, the Co–S, average Co-N, and Co-O bond lengths in **9** are comparable (Table 1) to the previously characterized hydroxo complex $[Co^{III}(S^{Me2}N_4(tren))(OH)]^+$ (**12**),[53] consistent with the oxidation of the high-spin Co(II) (S = 3/2) ion in **8** to a low-spin Co(III) (S = 0) ion in **9**. The Co–O bond length in **9** (1.899(2) Å) is comparable to that of **12**, as well as other previously reported Co(III) peroxo compounds.[35,54,55] The O–O bond length of dicationic **9** (1.482(4) Å) is consistent with a peroxo, but is 0.054 Å longer than that of neutral $(B_2pz_4Py)Co^{III}$–O–O–$Co^{III}(B_2pz_4Py)$, which contains two dianionic ligands.[51] This indicates that the peroxo in **9** is highly activated. The two halves of the dimer are twisted relative to each other with a dihedral angle of 180°, and the plane containing the Co(III)–O–O–Co(III) core is approximately perpendicular to the plane containing two Co–S bonds. The and Co-O-O bond angle (114°) is more obtuse than the corresponding Mn–O–O angle of **1** (Table 5.2), but is comparable to most Co^{III}–peroxo compounds.[35,54–61]

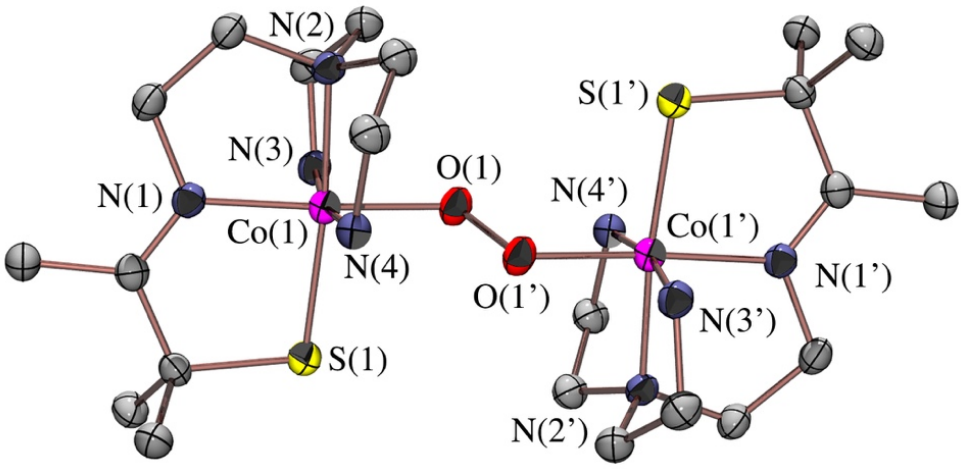

Figure 5.5. ORTEP of peroxo-bridged $\{[Co^{III}(S^{Me2}N_4(tren))]_2(trans\text{-}\mu\text{-}1,2\text{-}O_2)\}^{2+}$ (**9**) showing 50% probability ellipsoids and the atom labeling scheme. Hydrogens are omitted for clarity.

5.3.2 *Structural and Electronic Comparison Between $\{[Co^{III}(S^{Me2}N_4(tren))]_2(trans\text{-}\mu\text{-}1,2\text{-}O_2)\}^{2+}$ (**9**) and $\{[Mn^{III}(S^{Me2}N_4(6\text{-}Me\text{-}DPEN)]_2(trans\text{-}\mu\text{-}1,2\text{-}O_2)\}^{2+}$ (**1**)*

Structure **9** is analogous to our previously reported crystallographically characterized *trans*-μ-1,2-peroxo bridged Mn(III) complex, $\{[Mn^{III}(S^{Me2}N_4(6\text{-}Me\text{-}DPEN)]_2(trans\text{-}\mu\text{-}1,2\text{-}O_2)\}^{2+}$ (**1**),[19] as well as two additional spectroscopically characterized Mn(III)-peroxo compounds, $[Mn^{III}(S^{Me2}N_4(quinoEN)]_2(\mu\text{-}O_2)(BPh_4)_2$ (**10**) and $\{[Mn^{III}(S^{Me2}N_4(6\text{-}MeO\text{-}DPEN))]_2\text{-}(\mu\text{-}O_2)\}^{2+}$ (**11**), for which spectroscopically calibrated DFT calculated structures are available (Figure 5.6).[19] Relative to **1** (1.452(5)), the peroxo O–O bond of bimetallic Co(III)-peroxo **9** is 0.03 Å longer, and closer to that of O_2^{2-} (1.49 Å),[62] indicating that the peroxo is more activated in **9**.

Table 5.2. Selected bond distances (Å) and bond angles (deg) for $[Co^{II}(S^{Me2}N_4(tren))](PF_6)$ (**8**), peroxo-bridged $[Co^{III}(S^{Me2}N_4(tren))]_2(trans\text{-}\mu\text{-}1,2\text{-}O_2)(PF_6)_2$•MeCN (**9**), peroxo-bridged $[Mn^{III}(S^{Me2}N_4(6\text{-Me-DPEN}))]_2(trans\text{-}\mu\text{-}1,2\text{-}O_2)(BPh_4)_2$•$2CH_3CH_2CN$ (**1**), and hydroxo bound $[Co^{III}(S^{Me2}N_4(tren))(OH)](PF_6)$ (**12**).[53]

	8 (d^7, S = 3/2; H.S.)	**9** (d^6, S = 0; L.S.)	**1** (d^4, S = 2; H.S.)	**12**
M(1)–S(1)	2.3006(7)	2.2180(9)	2.275(11)	2.217(3)
M(1)–N(1)	2.050(2)	1.900(2)	2.040(3)	1.892(8)
M(1)–N(2)	2.223(2)	1.978(3)	2.203(3)	1.971(8)
M(1)–N(3)	2.107(2)	1.935(2)	2.410(3)	1.935(6)
M(1)–N(4)	2.086(2)	1.963(2)	2.492(3)	1.935(6)[a]
M(1)–O(1)	N/A	1.899(2)	1.832(3)	1.869(6)
O(1)–O(1')	N/A	1.482(4)	1.452(5)	N/A
M(1)•••O(1')	N/A	2.845	2.481	N/A
M(1)–O(1)–O(1')	N/A	114.0(2)	97.5(6)	N/A
O(1)–M(1)–S(1)	N/A	94.88(7)	85.12(9)	95.8(2)
O(1)–M(1)–N(3)	N/A	90.9(1)	92.4(1)	87.7(2)
O(1)–M(1)–N(1)	N/A	174.24(9)	165.5(1)	178.0(3)
O(1)–M(1)–N(2)	N/A	90.61(9)	111.1(1)	90.0(3)
S(1)–M–N(2)	163.96(6)	174.24(7)	163.3(1)	174.3(2)
S(1)–M–N(3)	112.25(6)	94.10(8)	109.0(1)	94.23(17)
S(1)–M–N(4)	106.90(6)	94.05(8)	105.6(1)	94.23(17)[a]
N(1)–M–N(4)	125.14(8)	92.0(1)	101.7(1)	92.17(17)[a]

[a]N(4) = N(3') for this structure, since a crystallographic mirror plane relates the two atoms (N(3) and N(3')).

An activated O–O bond should be susceptible to cleavage, consistent with our inability to observe the intact dimer by mass spectrometry (*vide supra*). An activated O–O bond should be susceptible to cleavage, consistent with our inability to observe the intact dimer by mass spectrometry. Only half of the dimer, consisting of a monocationic cobalt-oxo, is detected in ESI-MS, even at the lowest applied skim voltage (4 – 10 V), (Figure 5.4). Peroxos are π-donors that can be stabilized via the removal of antibonding electron density from the peroxo π* orbitals via π-back-donation into a metal ion t_{2g} d-orbital. With low-spin d^6 Co(III), the π-symmetry t_{2g} orbitals are filled, whereas they are half-filled with a high-spin d^4 Mn(III) ion. If the t_{2g} orbitals are filled, then this

pathway for O–O bond stabilization is not available. In addition, with the cobalt peroxo **9** there are two short H-bonds (N(2)–H(2E)••••O(1') = 2.051 Å) to the bridging peroxo oxygens (Figure 5.7), which are absent in the Mn(III) compound. It is possible that these H-bonds also contribute to O–O bond activation in **9**. However, there are other examples of bridging Co peroxo compounds lacking H-bonds with similar distances.[35,63]

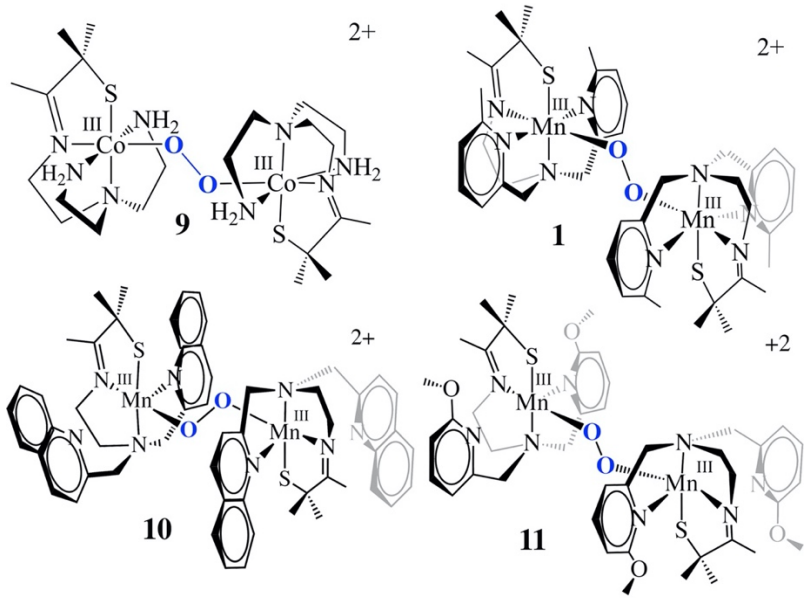

Figure 5.6. ChemDraw sketches of $\{[Co^{III}(S^{Me2}N_4(tren))]_2(\textit{trans}\text{-}\mu\text{-}1,2\text{-}O_2)\}^{2+}$ (**9**), $\{[Mn^{III}(S^{Me2}(6\text{-}Me\text{-}DPEN))]_2(\textit{trans}\text{-}\mu\text{-}1,2\text{-}O_2)\}^{2+}$ (**1**), $\{[Mn^{III}(S^{Me2}N_4(quinoEN)]_2\text{-}(\mu\text{-}O_2)\}^{2+}$ (**10**),[19] and $\{[Mn^{III}(S^{Me2}N_4(6\text{-}MeO\text{-}DPEN)]_2\text{-}(\mu\text{-}O_2)\}^{2+}$ (**11**).[19]

We recently showed that metal ion Lewis acidity can influence peroxo O–O bond lengths by facilitating π-back-donation of electron density from the peroxo π^* orbital.[16,17] Metal ion Lewis acidity was found to depend on the steric properties of the ligand scaffold. Ligands with sterically demanding substituents on the aryl ring (e.g., **2**, **5**, and **7**, Figure 5.1) were found to possess unusually long M•••N^{Ar} distances in the corresponding M(III) derivatives.[64] Elongation of the Mn•••N^{Ar} distances was shown to increase metal ion Lewis acidity and create a virtual coordinatively unsaturated metal ion.[16,17] This facilitates π-back donation from the filled peroxo

π*(O–O) orbital to the metal ion, resulting in a shorter peroxo O–O bond.[16] With less sterically demanding primary amines (e.g., **5** and **8**, Figure 5.1), on the other hand, M–N (M = Mn or Co) distances in the corresponding M(III) derivatives were found to be significantly shorter.

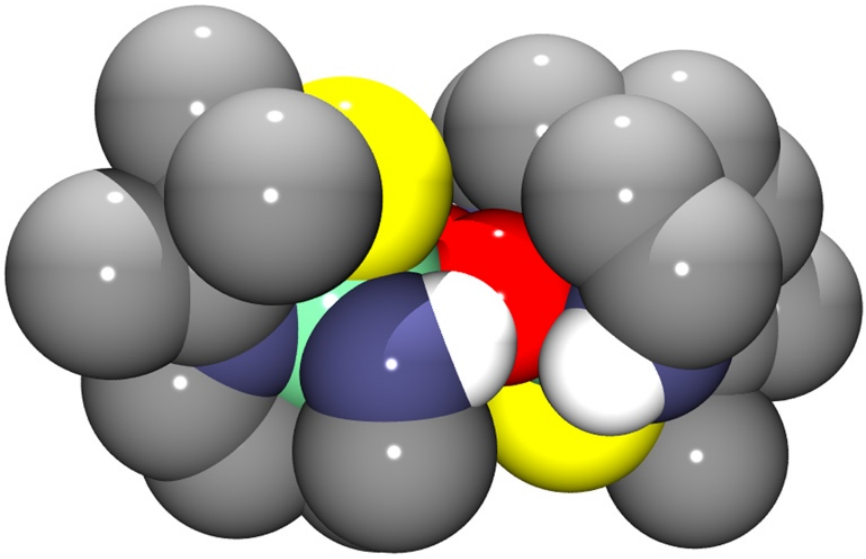

Figure 5.7. Space-filling diagram of peroxo-bridged $\{[Co^{III}(S^{Me2}N_4(tren))]_2(\textit{trans}\text{-}\mu\text{-}1,2\text{-}O_2)\}^{2+}$ (**9**) showing N–H hydrogen bonding to the peroxo (red).

5.3.3 *Theoretical Comparison of $\{[Co^{III}(S^{Me2}N_4(tren))]_2(trans\text{-}\mu\text{-}1,2\text{-}O_2)\}^{2+}$ (**9**), $\{[Mn^{III}(S^{Me2}N_4(quinoEN)]_2\text{-}(\mu\text{-}O_2)\}^{2+}$ (**10**), and $\{[Mn^{III}(S^{Me2}N_4(6\text{-}MeO\text{-}DPEN)]_2\text{-}(\mu\text{-}O_2)\}^{2+}$ (**11**)*

To gain more insight into the electronic structure differences governing peroxo O–O bond activation, DFT calculations were performed on Co–peroxo **9** and compared to the Broken Symmetry (BS) DFT-calculated structures for our previously reported Mn peroxo compounds $\{[Mn^{III}(S^{Me2}N_4(quinoEN))]_2\text{-}(\mu\text{-}O_2)\}^{2+}$ (**10**) and $\{[Mn^{III}(S^{Me2}N_4(6\text{-}MeO\text{-}DPEN))]_2\text{-}(\mu\text{-}O_2)\}^{2+}$ (**11**) of Scheme 1.[20] Complex **9** was geometry optimized using the B3LYP hybrid functional and the 6-

311G basis set, yielding metal-ligand and peroxo O–O bond lengths that are in reasonable agreement with crystallographic parameters (maximum bond length deviation of 3.7%). Notably, the calculated O–O bond length of 1.521 Å supports a more activated peroxo moiety in **9**.

The DFT calculated Mulliken charge of the metal ions in **9** (+1.45), **11** (+1.59), and **10** (+1.60) indicate that metal ion metal ion Lewis acidity does not necessarily follow the expected periodic trends Co > Mn. Steric constraints imposed by the ligand elongate two of the Mn•••N^{Ar} distances[20] for the Mn-peroxo complexes $\{[Mn^{III}(S^{Me2}N_4(quinoEN))]_2\text{-}(\mu\text{–}O_2)\}^{2+}$ (**10**, Figure 5.6) and $\{[Mn^{III}(S^{Me2}N_4(6\text{-}MeO\text{-}DPEN))]_2\text{-}(\mu\text{–}O_2)\}^{2+}$ (**11**, Scheme 5.1), and this is reproduced by the calculations. Conversely, the calculated electron density localized on the bridging peroxo oxygens is higher with Co-containing **9** (–0.56), relative to Mn-containing **11** (–0.48) and **10** (–0.49). This trend reflects the fact that the π*(O–O) orbital that cannot π-back-donate into the filled t_{2g} orbitals of a L.S. d^6 Co(III) ion, resulting in a the localization of electron density on the peroxo oxygens and destabilization of the peroxo O–O bond. An analysis of the frontier orbital of both the Co and Mn-peroxo complexes, **9** and **11** (Figure 5.8), corroborates the strong dependence of the extent of O–O bond activation on the electronic properties of the metal ion. The highest occupied molecular orbital (HOMO) contains significant π*(O–O) character for both Co-peroxo **9** and Mn-peroxo **11**. However, the HOMO of Mn-peroxo $\{[Mn^{III}(S^{Me2}N_4(6\text{-}MeO\text{-}DPEN))]_2\text{-}(\mu\text{–}O_2)\}^{2+}$ (**11**) is fairly delocalized, extending over both the O–O π* and singly occupied t_{2g} Mn d-orbitals (Figure 5.8, right). This would be consistent with higher calculated Lewis acidity of the Mn ions as well as the observed stabilization of the peroxo O–O bond. The HOMO of Co-peroxo **9** (Figure 5.8, left), however, is dominated by the π*(O–O) orbital and predominantly peroxo in character, consistent with lack of π-back-donation into the fully occupied Co t_{2g} d-orbitals (Figure 5.8). The LUMO of both **9** and **11** is antibonding with respect to the M–O(peroxo) bond.

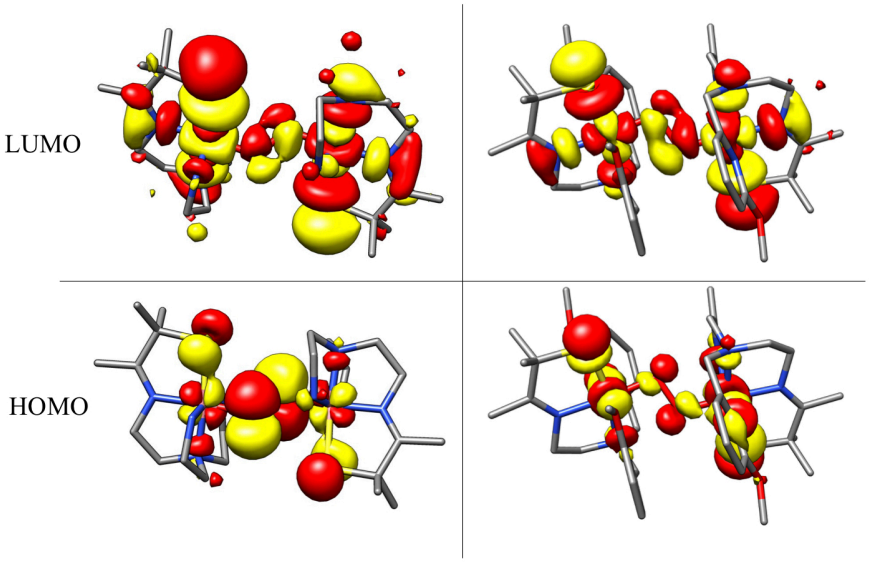

Figure 5.8. Frontier orbitals of $Co^{III}(S^{Me2}N_4(tren))]_2(\textit{trans}\text{-}\mu\text{-}1,2\text{-}O_2)\}^{2+}$(**9**) (left) and $\{[Mn^{III}(S^{Me2}N_4(6\text{-MeO-DPEN})]_2(\textit{trans}\text{-}\mu\text{-}1,2\text{-}O_2)\}^{2+}$ (**11**) visualized at an isovalue of 0.03 a_0^3.

5.4 Conclusions

This work describes the structure and properties of a O_2-derived thiolate-ligated, peroxo-bridged Co(III) dimer and provides a comparison with structurally analogous peroxo-bridged Mn(III) dimers. It also provides a rationale for the effects of both electronic structural differences and the ligand scaffold can have on peroxo O–O bond activation. The electronic structure of the metal ion, as well as the metal ion Lewis acidity, are shown to have a profound impact on peroxo O–O bond activation and stability. The lack of steric bulk in the Co peroxo compound is shown to decrease metal center Lewis acidity relative to the Mn peroxo compounds, resulting in a more activated peroxo O–O bond. In addition, with its completely filled π-symmetry t_{2g} set of orbitals, the L.S. d^6 Co(III) ion is incapable of providing stability to the peroxo O–O bond through π-back-donation from the π^*(O–O). DFT calculations support this by showing that, with Co(III), the HOMO contains more electron density localized in the peroxo π^*(O–O) orbital, relative to the HOMO of the structurally analogous Mn(III) peroxo complex, resulting in a more activated peroxo

O–O bond. The substitution-inert character of the Co(III) ion facilitates the isolation of a significantly more activated peroxo, however. Insight into some of the key factors governing O–O bond activation can serve as a benchmark for future small-molecule design.

5.5 References

(1) Leslie, M. *Science* **2009**, *323* (5919), 1286–1287.

(2) Barber, J. *Chem. Soc. Rev.* **2009**, *38* (1), 185–196.

(3) Askerka, M.; Brudvig, G. W.; Batista, V. S. *Acc. Chem. Res.* **2017**, *50* (1), 41–48.

(4) Yano, J.; Yachandra, V. *Chem. Rev.* **2014**, *114* (8), 4175–4205.

(5) Nocera, D. G. *Acc. Chem. Res.* **2012**, *45* (5), 767–776.

(6) Cox, N.; Pantazis, D. A.; Neese, F.; Lubitz, W. *Acc. Chem. Res.* **2013**, *46* (7), 1588–1596.

(7) Renger, G. *J. Photochem. Photobiol. B Biol.* **2011**, *104* (1–2), 35–43.

(8) Retegan, M.; Krewald, V.; Mamedov, F.; Neese, F.; Lubitz, W.; Cox, N.; Pantazis, D. A. *Chem. Sci.* **2015**, *7* (1), 72–84.

(9) Cox, N.; Retegan, M.; Neese, F.; Pantazis, D. A.; Boussac, A.; Lubitz, W. *Science* **2014**, *345* (6198), 804–808.

(10) Brudvig, G. W. *Philos. Trans. R. Soc. B Biol. Sci.* **2008**, *363* (1494), 1211–1218.

(11) Dismukes, G. C.; Brimblecombe, R.; Felton, G. A. N.; Pryadun, R. S.; Sheats, J. E.; Spiccia, L.; Swiegers, G. F. *Acc. Chem. Res.* **2009**, *42* (12), 1935–1943.

(12) Betley, T. A.; Wu, Q.; Van Voorhis, T.; Nocera, D. G. *Inorg. Chem.* **2008**, *47* (6), 1849–1861.

(13) Armstrong, F. A. *Philos. Trans. R. Soc. B Biol. Sci.* **2008**, *363* (1494), 1263–1270.

(14) Coggins, M. K.; Brines, L. M.; Kovacs, J. A. *Inorg. Chem.* **2013**, *52* (21), 12383–12393.

(15) Shook, R. L.; Gunderson, W. A.; Greaves, J.; Ziller, J. W.; Hendrich, M. P.; Borovik, A. S. *J. Am. Chem. Soc.* **2008**, *130* (28), 8888–8889.

(16) Rees, J. A.; Martin-Diaconescu, V.; Kovacs, J. A.; DeBeer, S. *Inorg. Chem.* **2015**, *54* (13), 6410–6422.

(17) Annaraj, J.; Cho, J.; Lee, Y. M.; Kim, S. Y.; Latifi, R.; De Visser, S. P.; Nam, W. *Angew. Chemie - Int. Ed.* **2009**, *48* (23), 4150–4153.

(18) Geiger, R. A.; Leto, D. F.; Chattopadhyay, S.; Dorlet, P.; Anxolabéhère-Mallart, E.; Jackson, T. A. *Inorg. Chem.* **2011**, *50* (20), 10190–10203.

(19) Coggins, M. K.; Sun, X.; Kwak, Y.; Solomon, E. I.; Rybak-Akimova, E.; Kovacs, J. A. *J. Am. Chem. Soc.* **2013**, *135* (15), 5631–5640.

(20) Poon, P. C. Y.; Dedushko, M.; Sun, X.; Yang, G.; Toledo, S.; Hayes, E. C.; Johansen, A.; Rees, J. A.; Stoll, S.; Rybak-Akimova, E.; Kovacs, J. A. *J. Am. Chem. Soc.* **2019**, *141* (38), 15046–15057.

(21) Seo, M. S.; Kim, J. Y.; Annaraj, J.; Kim, Y.; Lee, Y. M.; Kim, S. J.; Kim, J.; Nam, W. *Angew. Chemie - Int. Ed.* **2007**, *46* (3), 377–380.

(22) Vanatta, R. B.; Strouse, C. E.; Hanson, L. K.; Valentine, J. S. *J. Am. Chem. Soc.* **1987**, *109* (5), 1425–1434.

(23) Kitajima, N.; Komatsuzaki, H.; Hikichi, S.; Osawa, M.; Moro-oka, Y. *J. Am. Chem. Soc.* **1994**, *116* (25), 11596–11597.

(24) Singh, U. P.; Sharma, A. K.; Hikichi, S.; Komatsuzaki, H.; Moro-oka, Y.; Akita, M. *Inorganica Chim. Acta* **2006**, *359* (13), 4407–4411.

(25) Bossek, U.; Weyhermiiller, T.; Wieghardt, K.; Nuber, B.; Weiss, J. *J. Am. Chem. Soc.* **1990**, *112* (17), 6387–6388.

(26) Coggins, M. K.; Martin-Diaconescu, V.; Debeer, S.; Kovacs, J. A. *J. Am. Chem. Soc.* **2013**, *135* (11), 4260–4272.

(27) Brown, C. D.; Neidig, M. L.; Neibergall, M. B.; Lipscomb, J. D.; Solomon, E. I. *J. Am. Chem. Soc.* **2007**, *129* (23), 7427–7438.

(28) Kovacs, J. A.; Brines, L. M. *Acc. Chem. Res.* **2007**, *40* (7), 501–509.

(29) Kovacs, J. A. *Acc. Chem. Res.* **2015**, *48* (10), 2744–2753.

(30) Brodsky, C. N.; Hadt, R. G.; Hayes, D.; Reinhart, B. J.; Li, N.; Chen, L. X.; Nocera, D. G. *Proc. Natl. Acad. Sci.* **2017**, *114* (15), 201701816.

(31) Smith, P. F.; Hunt, L.; Laursen, A. B.; Sagar, V.; Kaushik, S.; Calvinho, K. U. D.; Marotta, G.; Mosconi, E.; De Angelis, F.; Dismukes, G. C. *J. Am. Chem. Soc.* **2015**, *137* (49), 15460–15468.

(32) Holm, R. H. *Chem. Rev.* **1987**, *87* (6), 1401–1449.

(33) Gao, Y.; Åkermark, T.; Liu, J.; Sun, L.; Åkermark, B. *J. Am. Chem. Soc.* **2009**, *131* (25), 8726–8727.

(34) Volpe, M.; Hartnett, H.; Leeland, J. W.; Wills, K.; Ogunshun, M.; Duncombe, B. J.; Wilson, C.; Blake, A. J.; McMaster, J.; Love, J. B. *Inorg. Chem.* **2009**, *48* (12), 5195–5207.

(35) Schaefer, W. P.; Marsh, R. E. *J. Am. Chem. Soc.* **1966**, *88* (1), 178–179.

(36) Sykes, A. G.; Weil, J. A. In *Progress in Inorganic Chemistry*; 1970; Vol. 13, pp 1–106.

(37) Kotani, H.; Hong, D.; Satonaka, K.; Ishizuka, T.; Kojima, T. *Inorg. Chem.* **2019**, *58* (6), 3676–3682.

(38) Jin Seog Seo; Hynes, R. C.; Williams, D.; Chin, J. *J. Am. Chem. Soc.* **1998**, *120* (38), 9943–9944.

(39) Givaja, G.; Volpe, M.; Edwards, M. A.; Blake, A. J.; Wilson, C.; Schröder, M.; Love, J. B. *Angew. Chemie - Int. Ed.* **2007**, *46* (4), 584–586.

(40) Wang, D.; Lindeman, S. V.; Fiedler, A. T. *Inorg. Chem.* **2015**, *54* (17), 8744–8754.

(41) Brines, L. M.; Shearer, J.; Fender, J. K.; Schweitzer, D.; Shoner, S. C.; Barnhart, D.; Kaminsky, W.; Lovell, S.; Kovacs, J. a. *Inorg. Chem.* **2007**, *46* (22), 9267–9277.

(42) Otwinowski, Z.; Minor, W. *Macromolecular Crystallography*, 1st ed.; Sweet, R. M., Carter, C. W., Eds.; Acadmic Press: New York, 1997.

(43) Mackay, S.; Edwards, C.; Henderson, A.; Gilmore, C.; Stewart, N.; Shankland, K.; Donald, A. University of Glasgow 1997.

(44) Altomare, A.; Cascarano, G.; Giacovazzo, C.; Guagliardi, A.; Burla, M. C.; Polidori, G.; Camalli, M. *J. Appl. Crystallogr.* **1994**, *27* (3), 435.

(45) Altomare, A.; Burla, M. C.; Camalli, M.; Cascarano, G. L.; Giacovazzo, C.; Guagliardi, A.; Moliterni, A. G. G.; Polidori, G.; Spagna, R. *J. Appl. Crystallogr.* **1999**, *32* (1), 115–119.

(46) Sheldrick, G. M. University of Göttingen, Germany. 1997.

(47) Sheldrick, G. M. *Acta Crystallogr. Sect. C Struct. Chem.* **2015**, *71* (1), 3–8.

(48) Burnett, M. N.; Johnson, C. K. Oak Ridge National Laboratory Report ORNL-6895 1996.

(49) Persistence of Vision Pty. Ltd.: Williamstown, Victoria, Australia 2013.

(50) Neese, F. *Interdiscipl. Rev. Comput. Mol. Sci.* **2012**, *2*, 73–78.

(51) Barone, V.; Cossi, M. *J. Phys. Chem. A* **1998**, *102* (11), 1995–2001.

(52) Pettersen, E. F.; Goddard, T. D.; Huang, C. C.; Couch, G. S.; Greenblatt, D. M.; Meng, E. C.; Ferrin, T. E. *J. Comput. Chem.* **2004**, *25*, 1605–1612.

(53) Swartz, R. D.; Coggins, M. K.; Kaminsky, W.; Kovacs, J. A. *J. Am. Chem. Soc.* **2011**, *133*

(11), 3954–3963.

(54) Nurdin, L.; Spasyuk, D. M.; Fairburn, L.; Piers, W. E.; Maron, L. *J. Am. Chem. Soc.* **2018**, *140* (47), 16094–16105.

(55) Ramprasad, D.; Gilicinski, A. G.; Markley, T. J.; Pez, G. P. *Inorg. Chem.* **1994**, *33* (13), 2841–2847.

(56) Rigsby, M. L.; Mandal, S.; Nam, W.; Spencer, L. C.; Llobet, A.; Stahl, S. S. *Chem. Sci.* **2012**, *3* (10), 3058–3062.

(57) Ludovici, C.; Fröhlich, R.; Vogtt, K.; Mamat, B.; Lübben, M. *Eur. J. Biochem.* **2003**, *269* (10), 2630–2637.

(58) Howard-Jones, A. R.; Adam, V.; Cowley, A.; Baldwin, J. E.; Bourgeois, D. *Photochem. Photobiol. Sci.* **2009**, *8* (8), 1150–1156.

(59) Fukuzumi, S.; Mandal, S.; Mase, K.; Ohkubo, K.; Park, H.; Benet-Buchholz, J.; Nam, W.; Llobet, A. *J. Am. Chem. Soc.* **2012**, *134* (24), 9906–9909.

(60) Cho, Y. I.; Joseph, D. M.; Rose, M. J. *Inorg. Chem.* **2013**, *52* (23), 13298–13300.

(61) Wang, H. Y.; Mijangos, E.; Ott, S.; Thapper, A. *Angew. Chemie - Int. Ed.* **2014**, *53* (52), 14499–14502.

(62) Vaska, L. *Acc. Chem. Res.* **1976**, *9* (5), 175–183.

(63) Fritch, J. R.; Christoph, G. G.; Schaefer, W. P. *Inorg. Chem.* **1973**, *12* (9), 2170–2175.

(64) Coggins, M. K.; Toledo, S.; Shaffer, E.; Kaminsky, W.; Shearer, J.; Kovacs, J. A. *Inorg. Chem.* **2012**, *51* (12), 6633–6644.

Chapter 6. Ligand Design and Synthesis to Support Heterobimetallic Mn-Ca Complexes

6.1 Introduction

Clean and renewable energy development is necessary for transition to a more sustainable future.[1,2] Continual technological and industrial development to support growing world population is maintained with the steady increase of global energy consumption. At present, the global energy consumption reaches almost 18 terawatts (TW) of power from all energy sources.[3] Based on current projections, the global annual energy consumption rate will double by 2050, and triple by the end of the century.[4,5] The unlimited energy demand has been met mostly with burning fossil fuels such as oil, gas, and coal – a limited global resource. Moreover, in the process, fossil fuel combustion has been adversely affecting global climate by increasing atmospheric and oceanic CO_2 levels, polluting air, deteriorating marine and land ecosystems.[4,6] Without drastic intervention, this trend will eventually result in severe disruptions to economic activity, food security, and ecological degradation.[2,7,8] Transition to renewable and carbon-neutral energy sources is required to address issues of both the growing energy demand and climate change.

Solar energy is the most promising renewable energy alternative. The sun provides our planet with 100,000 TW of solar power on an annual basis.[9] This means that the energy from one hour of sunlight is equivalent to all the energy humanity is consuming in a year. Existing technologies to capture solar energy and convert it to electricity are developing rapidly.[10–12] However, its high capital costs, energy storage infrastructure, and material instability creates a bottleneck to large scale application.[13] Therefore, fundamental research is needed in order to

improve efficiency of solar energy capture and conversion into storable fuels. Current photovoltaic materials based on photosynthetic principles of water splitting overcome the thermodynamic barrier to H_2O oxidation by absorbing photons to create an oxidizing hole.[11] Although H_2O electrolysis occurs at 1.23 V (vs. NHE, standard conditions), commercial electrolyzers operate with high overpotentials of at least 1.6 – 2.0 V due to system inefficiencies such as electron-hole recombination and band gap mismatch.[11,14,15] Additionality, slow kinetics of H_2O oxidation is a major barrier to improved efficiency for existing fuel cells.[16] Understanding how Nature overcomes the kinetics of H_2O oxidation and accomplishes the uphill O–O bond forming step is may be valuable to design more efficient solar fuel cells. A deeper look into Nature's own process of capturing solar energy – photosynthesis – may provide insights for a long-term solution.

Photosynthesis is a process that converts light energy into chemical bond energy.[17–19] It accomplishes that by splitting water in a highly endothermic (ΔG = + 359 kJ mol^{-1}) reaction to produce O_2, four protons, and four electrons that are used for the reductive fixing of CO_2 into sugars.[20] The metal complex involved in the photosynthesis, Oxygen Evolving Complex (OEC), is embedded in membrane-protein complex called photosystem II (PS II).[21] The OEC catalyst is a heterometallic cubane cluster that contains three Mn ions, a Ca^{2+} ion, and a dangling Mn (Mn_{dang}) bridged by oxo atoms (Figure 6.1).[22] The OEC cycles through a series of five-intermediate states (S_i, i = 0 – 4) which represent the number of oxidizing equivalents stored on the OEC as a result of four consecutive photons absorbed by the PS II.[23] Here, the OEC acts as a redox capacitor and after all four oxidizing equivalents have been accumulated (the S_4 state), a spontaneous reaction of O–O bond formation and O_2 release occurs. During the reaction, the OEC cluster provides a high degree of redox flexibility, while the protein residues modulate the redox potential and provide pathways for electrons, protons, H_2O and O_2 channels.[24–26] Thus, the OEC catalyst within

the PS II coordinates a catalytic H_2O splitting reaction at close to the thermodynamic potential while also avoiding the release of detrimental reactive intermediates.[27]

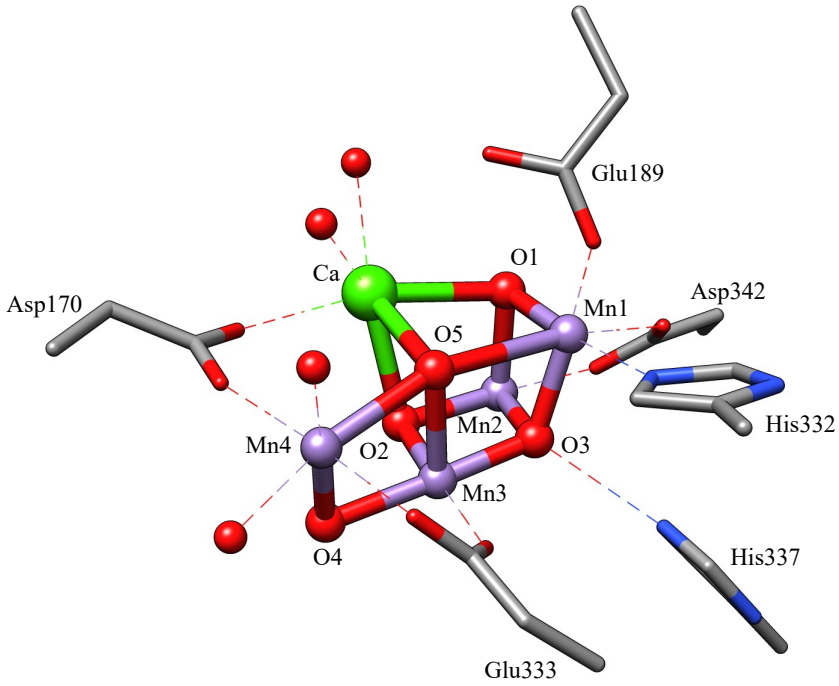

Figure 6.1. Crystal structure of active site of the OEC of photosystem II at the resolution of 1.9 Å from *Thermosynechococcus vulcanus*, PDB 3WU2.[22]

Spectroscopic and reactivity studies suggest that both Mn_{dang} and Ca^{II} ions in the OEC perform essential roles in the O–O forming step.[17,20,28] Little is known about the mechanism of O–O bond formation because it follows a rate-determining step.[29,30] Nonetheless, molecular-level understanding this step is critical to the development of efficient solar fuel cells. Two mechanisms of the O–O bond formation have been proposed: radical coupling (**RC**) and acid-base (**AB**) reaction. **RC** mechanism involves coupling of two Mn^{IV}-oxyl radicals (Figure 6.2, left) and **AB** mechanism involves nucleophilic attack of electrophilic $Mn^{V}{\equiv}O$ by $Ca^{II}–OH_2$ (Figure 6.2, right).[31–34] Ca^{II} ion likely acts as a Lewis acid, lowers the pK_a of coordinated water to promote formation of bound OH^- in close proximity to $Mn^{V}{\equiv}O$.[28] The importance of Lewis acidic Ca^{II} has

been shown by recent experiments where replacement of Ca^{II} by a less Lewis acidic Sr^{II} resulted in significant decrease of O_2 production.[18] Both the **RC** and **AB** mechanisms stipulate the formation of a peroxo intermediate prior to O_2 release via reductive elimination.

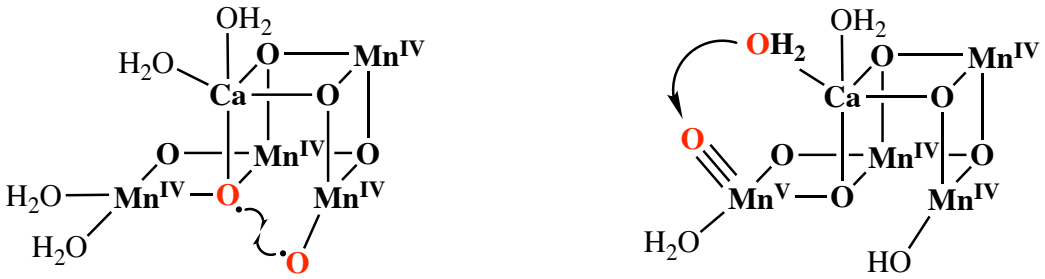

Figure 6.2. Proposed mechanisms of O–O bond formation step involving either Mn^{IV}-oxyl radical coupling (left) Ca^{II}–OH_2 nucleophilic attack on Mn^{V}≡O (right).

This project aims to test existing proposed mechanisms for O–O bond formation and provide insights into the electronic structure of the reactive intermediates involved in this process. The biomimetic approach to this problem envisages designing and characterizing functional complexes capable of forming reactive metal-oxygen intermediates that form an O–O bond. As mentioned earlier, this step is proposed to involve either coupling between two Mn^{IV}-oxyl radicals or the nucleophilic attack of Ca^{II}–OH_2 on high-valent Mn^{V}≡O. Therefore, ligand design is centered on synthesizing binucleating systems that resemble these two OEC fragments. This can be achieved through synthesizing *sterically encumbered*, *site-differentiated* ligands to pre-organize either two Mn^{II} ions, or a Mn^{II} with an adjacent Ca^{II} ion.

These requirements can be met with a modified Robson-type ligand. In 1970s, Richard Robson reported the first example of a macrocyclic ligand capable of chelating two metal ions in close proximity. He sought to design synthetic bimetallic complex capable of binding, in a bridging manner, and activating molecular dinitrogen (N_2).[35] The bimetallic macrocyclic complex was formed through Schiff-based condensation of 2-hydroxy-5-methyl-1,3-benzenedicarboxaldehyde

with 1,3-diaminopropane in the presence of various metal acetate salts (Figure 6.3).[36,37] After Robson's report, the field of macrocyclic and non-macrocyclic bimetallic complexes has seen extensive growth with an application to areas of homogeneous catalysis, metalloenzyme biochemistry, magnetic exchange, and electrical conductivity processes, to name a few. To that end, multiple homo- (Mn^{II}–Mn^{II}, Fe^{II}–Fe^{II}, Co^{II}–Co^{II}, Ni^{II}–Ni^{II}, Cu^{II}–Cu^{II}, and Zn^{II}–Zn^{II})[37,38] and heterobimetallic (Cu^{II}–Mn^{II}, Cu^{II}–Fe^{II}, Cu^{II}–Co^{II})[39,40] complexes have been synthesized and characterized.

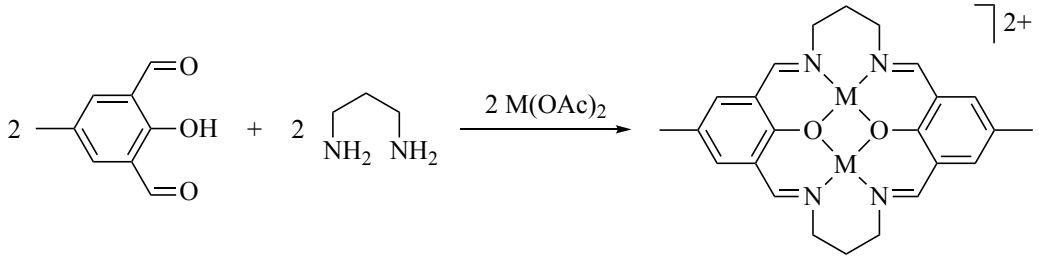

Figure 6.3. A generalized depiction of the binucleating macrocyclic ligand first reported by Robson.[36,37]

Conceptually, Robson-type ligand is a convenient jumping-off point. First, it allows for a rational approach to designing a binucleating complex with two chelating pockets (N_2O_2 type) comprised of tertiary amines and shared phenoxy bridge. Second, bridging phenoxy ligands are likely to facilitate electronic communication between the two metals. And lastly, the two metals are positioned in close enough proximity as to trap or share a small diatomic molecule such as O_2. However, this concept needs to be modified and extended to meet the criteria of this research. Namely, acyclic and asymmetric ligand framework may be required to ensure controlled and site-directed incorporation of Mn and Ca ions. Schiff-base precursors must include modifiable functional groups to tune steric and electronic properties of the ligand backbone. The plane of the

dinuclear complex needs to have enough structural flexibility to be able to bend during an O–O bond formation step. Described herein is the synthesis of compartmental binucleating ligands and progress towards mettalation.

6.2 Experimental

General Methods. All manipulations were performed using standard Schlenk techniques or under an N_2 atmosphere in a glovebox. Reagents and solvents were purchased from chemical vendors, were of highest available purity, and were used without further purification unless otherwise specified. $CDCl_3$ was purchased from Cambridge Isotope Labs and used as received. Tetrahydrofuran (THF) and diethyl ether (Et_2O) were purchased from Sigma-Aldrich and purified using a solvent purification column housed in a custom stainless-steel cabinet and dispensed by a stainless steel Schlenk-line (GlassContour). Methanol (MeOH) was distilled over calcium hydride (CaH_2) and rigorously degassed prior to use.

^{1}H NMR spectra were obtained on a Bruker AV300, AV301, or AV500 spectrometers. Chemical shifts are listed in parts per million and were reported relative to TMS by referencing the residual solvent. UV/Vis spectra were recorded on a Varian Cary 60 spectrophotometer equipped with a fiber optic cable connected to a “dip” ATR probe (C-technologies). A custom-built two neck solution sample holder equipped with a threaded glass connector was sized specifically to fit the “dip” probe. Electrospray-ionization mass spectra were obtained on a Bruker Esquire Liquid Chromatograph-Ion Trap mass spectrometer. Gas chromatography-mass spectrometry (GC/MS) data were obtained using a 6890 gas chromatograph equipped with a 7683 autosampler and interfaced with a 5973 mass spectrometer. FT-IR spectra were recorded on a Perkin-Elmer Frontier FT-IR spectrometer as nujol mulls on NaCl salt plates. X-ray

crystallography data were recorded on a Bruker APEX II single crystal X-ray diffractometer with Mo Kα radiation.

Synthesis of 1-(3,5-di-*Tert*-Butyl-2-Hydroxyphenyl) Ethanone (1). Adapted from Ref. ([41]). $TiCl_4$ (M.W. = 189.679 g mol^{-1}, ρ = 1.726 g mL^{-1}, 1.21 mL, 11.0 mmol) was slowly injected aerobically to finely crushed 2,4-di-*tert*-butylphenol (M.W. = 206.32 g mol^{-1}, 2.06 g, 10.0 mmol) in a 250 mL Schlenk flask flushed with N_2 at room temperature. The resulting dark-red mixture was stirred at r.t. for 15 minutes until gas evolution has stopped. Then, excess acetyl chloride (M.W. = 78.50 g mol^{-1}, ρ = 1.104 g mL^{-1}, 2.84 mL, 40.0 mmol) was added to the solid. The resulting dark-red think slurry was stirred at r.t. for 15 minutes, then slowly brought up to 120 °C and left to stir at this temperature overnight. The reaction mixture was then cooled to r.t., diluted with CH_2Cl_2 (30 mL) and quenched with DI H_2O (30 mL). A cloudy dark-orange solution was obtained, which was extracted with CH_2Cl_2 (3 x 30 mL). The organic layer was washed with DI H_2O (2 x 30 mL), dried with Na_2SO_4 for 30 minutes, filtered, and concentrated under reduced pressure. The crude material was purified by silica gel column chromatography using a mixture of hexanes-EtOAc (9:1). The desired product was obtained as light-yellow powder in 48% yield (1.20 g). IR (Nujol): *v* 1636, 1330, 1276, 1241 1204, 1187, 1105, 1024, 972, 877, 820, 663, 660 cm^{-1}. ^1H NMR (300 MHz, $CDCl_3$): δ = 1.32 (s, 9H, ^{t}Bu), 1.43 (s, 9H, ^{t}Bu), 2.65 (s, 3H, CH_3), 7.56 (m, 2H, ArH), 12.99 (s, 1H, OH). ESI-MS: expected *m/z*(+) for $[C_{16}H_{24}O_2 + H^+]$ = 249.18, found *m/z*(+) = 249.0 (M + 1).

Synthesis of 2-Acetyl-4,6-di-*Tert*-Butylphenyl Acetate (2-Me). In a glovebox, a solution of **1** (M.W. = 248.0 g mol^{-1}, 2.48 g, 10.0 mmol) in anhydrous THF (20 mL) was added dropwise to a rigorously stirred solution of insoluble NaH (M.W. = 23.998 g mol^{-1}, 0.264 g, 11.0 mmol) in THF (60 mL) in a 250 mL round-bottom Schlenk flask. The resulting neon-yellow mixture was stirred at r.t. for 15 minutes until H_2 gas evolution has stopped and no trace of unreacted NaH solid was observed. Then, acetyl chloride (M.W. = 78.50 g mol^{-1}, ρ = 1.104 g mL^{-1}, 0.71 mL, 10.0 mmol) was added to the reaction mixture and left stirring for overnight. The reaction mixture was quenched with a mixture of ice (9 g) and 1N HCl (15 mL). The organic phase was extracted with ethyl acetate (3 x 20 mL), washed with brine (2 x 20 mL) and DI H_2O (2 x 20 mL). The organic layer was dried with $NaSO_4$ for 30 minutes, filtered, and concentrated under reduced pressure. The desired product was obtained as a white powder in 74% yield (2.22 g). IR (Nujol): *v* 1757, 1692, 1594, 1582, 1246, 1208, 1097, 1009, 651, 626 cm^{-1}. ^1H NMR (300 MHz, $CDCl_3$): δ = 1.34 (s, 9H, ^{t}Bu), 1.37 (s, 9H, ^{t}Bu), 2.34 (s, 3H, CH_3), 2.53 (s, 3H, CH_3), 7.57 (d, *J* = 2.4 Hz, 1H, ArH), 7.59 (d, *J* = 2.4 Hz 1H, ArH). ESI-MS**:** expected *m/z*(–) for $[C_{18}H_{26}O_3^-]$ = 290.40, found *m/z*(–) = 290.2 (M^-).

Synthesis of 2-Acetyl-4,6-di-*Tert*-Butylphenyl Benzoate (2-Ph). Following the procedure outlined for the synthesis of **2-Me**, a solution of **1** (M.W. = 248.0 g mol^{-1}, 2.48 g, 10.0 mmol) in anhydrous THF (20 mL) was added dropwise to a rigorously stirred solution of insoluble NaH (M.W. = 23.998 g mol^{-1}, 0.264 g, 11.0 mmol) in THF (60 mL) in a 250 mL round-bottom Schlenk flask. The resulting neon-yellow mixture was stirred at r.t. for 15 minutes until H_2 gas evolution has stopped and no trace of unreacted NaH was observed. Then, acetyl chloride (M.W. = 78.50 g mol^{-1}, ρ = 1.104 g mL^{-1}, 0.71 mL, 10.0 mmol) was added to the reaction mixture and left stirring

for overnight. The reaction mixture was quenched with a mixture of ice (9 g) and 1N HCl (15 mL). The organic phase was extracted with ethyl acetate (3 x 20 mL), washed with brine (2 x 20 mL) and DI H_2O (2 x 20 mL). The organic layer was dried with $NaSO_4$ for 30 minutes, filtered, and concentrated under reduced pressure. The desired product was obtained as a white powder in 65% yield (1.95 g). IR (Nujol): *v* 1743, 1695, 1600, 1587, 1263, 1210, 1098, 1066, 1060, 1024 cm^{-1}. ^1H NMR (300 MHz, $CDCl_3$): δ = 1.37 (s, 9H, ^{t}Bu), 1.39 (s, 9H, ^{t}Bu), 2.51 (s, 3H, CH_3), 7.52 (t, *J* = 7.7 Hz, 2H, Ar(2)H), 7.61 (d, *J* = 2.5 Hz, 1H, Ar(1)H), 7.64 (d, *J* = 2.5 Hz, 1H, Ar(1)H), 7.65 (tt, *J* = 7.4 Hz, 1H, Ar(2)H), 8.22 (dd, *J* = 7.0 Hz, 2H, Ar(2)H). ESI-MS: expected *m/z*(+) for [$C_{23}H_{28}O_3 + Na^+$] = 375.47, found *m/z*(+) = 375.2 ($M + Na^+$).

Synthesis of 1-(3,5-di-*Tert*-Butyl-2-Hydroxyphenyl)Butane-1,3-Dione (3-Me). Adapted from Ref. ([42]). In a glovebox, to a stirring solution of **2-Me** (M.W. = 290.0 g mol^{-1}, 1.00 g, 3.45 mmol) in anhydrous THF (80 mL), a solution of KO^{t}Bu (M.W. = 112.21 g mol^{-1}, 0.387 g, 3.45 mmol) in THF (20 mL) was added. The reaction was stirred at r.t. overnight. The pH was adjusted to 3 using 3 HCl aqueous solution. The resulting mixture was concentrated on rotary evaporator to give a brown oil that was extracted with CH_2Cl_2 (100 mL). The organic layer was isolated and extracted with 5% $NaHCO_3$ (2 x 100 mL), DI H_2O (2 x 100 mL), and brine (2 x 100 mL). The organic layer was dried over Na_2SO_4, filtered, and concentrated on a rotary evaporator. The resulting oily residue was recrystallized and washed with cold hexanes to give a white powder in 47% yield (0.47 g). IR (Nujol): ν 1682, 1604, 1161, 1052, 897 cm^{-1}. ^1H NMR (300 MHz, $CDCl_3$): δ = 1.31 (s, 9H, ^{t}Bu), 1.43 (s, 9H, ^{t}Bu), 1.79 (s, 3H, CH_3), 2.91 (s, 2H, CH_2), 7.57 (d, *J* = 2.6 Hz, 1H, ArH), 7.81 (d, *J* = 2.6 Hz, 1H, ArH), 12,65 (s, 1H, ArOH). ESI-MS: expected *m/z*(–) for [$C_{18}H_{26}O_3 - H^+$] = 290.40, found *m/z*(–) = 290.0 ($M - H^+$).

Synthesis of 1-(3,5-di-*Tert*-Butylphenyl) Benzyl Enol (3-Ph). Adapted from Ref. ([42]). In a glovebox, to a stirring solution of **2-Me** (M.W. = 290.0 g mol^{-1}, 1.00 g, 3.45 mmol) in anhydrous THF (80 mL), a solution of KO^{t}Bu (M.W. = 112.21 g mol^{-1}, 0.387 g, 3.45 mmol) in THF (20 mL) was added. The reaction was stirred at r.t. overnight. The pH was adjusted to 3 using 3 HCl aqueous solution. The resulting mixture was concentrated on rotary evaporator to give a brown oil that was extracted with CH_2Cl_2 (100 mL). The organic layer was isolated and extracted with 5% $NaHCO_3$ (2 x 100 mL), DI H_2O (2 x 100 mL), and brine (2 x 100 mL). The organic layer was dried over Na_2SO_4, filtered, and concentrated on a rotary evaporator. The resulting oily residue was recrystallized and washed with cold hexanes to give a white powder in 47% yield (0.47 g). IR (Nujol): ν 1612, 1573, 1180, 1071, 813 cm^{-1}.^{1}H NMR (300 MHz, $CDCl_3$): δ = 1.35 (s, 9H, ^{t}Bu), 1.45 (s, 9H, ^{t}Bu), 4.65 (s, 1H, OH), 6.83 (s, 1H, C=C(H)-C), 7.52 (t, *J* = 7.6 Hz, 2H, Ar(2)H), 7.53 (tt, *J* = 7.4 Hz, 1H, Ar(2)H), 7.56 (d, *J* = 2.4 Hz, 1H, Ar(1)H), 7.59 (d, *J* = 2.4 Hz, 1H, Ar(1)H), 7.93 (dd, *J* = 6.7 Hz, 2H, Ar(2)H). 12.66 (s, 1H, ArOH). ESI-MS: expected *m/z*(–) for [$C_{18}H_{26}O_3$ – H^+] = 351.40, found *m/z*(–) = 351.4 (M – H^+).

Synthesis of [(en)NaMn$_3$O$_4$(L$_3$)(OMe)] (4). Ethylene diamine (4 equiv., 1.37 mmol 91 μL, ρ = 0.899 mg μL^{-1},) was added to **3-Me** (3 equiv., 0.300 g, 1.03 mmol) in 10 mL of anhydrous THF resulting in an immediate color change to bright yellow. After stirring for 1 hour, NaOMe (3 equiv., 0.054 g, 1.03 mmol) was added, and the reaction mixture was allowed to stir for additional 15 minutes, after which time, $MnSO_4 \cdot H_2O$ (3 equiv., 1.03 mmol, 0.169 g) was added, and the reaction mixture was allowed to stir overnight. The resulting orange-red reaction mixture was filtered through a bed of celite, the solvent was pumped off under vacuum, and the resulting red powder was redissolved in a minimal amount of toluene. X-ray quality crystals of **4** were grown by layering

CH_2Cl_2 on a toluene solution.

X-Ray Crystallographic Data Determination. A yellow piece, 1-(3,5-di-*tert*-butylphenyl) benzyl enol **(3-Ph),** measuring 0.23 x 0.17 x 0.06 mm^3 was mounted on a loop with oil. Data was collected at -173 °C on a Bruker APEX II single crystal X-ray diffractometer, Mo-radiation. Crystal-to-detector distance was 40 mm and exposure time was 10 seconds per frame for all sets. The scan width was 0.5°. Data collection was 99.6% complete to 25° in θ. A total of 8935 reflections were collected covering the indices, –13<=h<=13, –13<=k<=13, –13<=l<=13. 4753 reflections were symmetry independent and the R_{int} = 0.0334 indicated that the data was of better than average quality (0.07). Indexing and unit cell refinement indicated a triclinic lattice. The space group was found to be P $\bar{1}$ (No. 2).

A yellow prism, [(en)$NaMn_3O_4(L_3)$(OMe)] (**4**), measuring 0.09 x 0.06 x 0.05 mm^3 was mounted on a loop with oil. Data was collected at -173 °C on a Bruker APEX II single crystal X-ray diffractometer, Mo-radiation. Crystal-to-detector distance was 40 mm and exposure time was 30 seconds per frame for all sets. The scan width was 0.5°. Data collection was 100% complete to 25° in θ. A total of 89545 reflections were collected covering the indices, -18<=h<=18, -20<=k<=20, -22<=l<=22. 18011 reflections were symmetry independent and the R_{int} = 0.1139 indicated that the data was of somewhat worse than average quality (0.07). Indexing and unit cell refinement indicated a triclinic lattice. The space group was found to be P $\bar{1}$ (No. 2).

Data was integrated and scaled using SAINT, SADABS within the APEX2 software package by Bruker.[43] Solution by direct methods (SHELXT[44] or SIR97[45]) produced a complete heavy atom phasing model consistent with the proposed structure. The structure was completed by difference Fourier synthesis with SHELXL.[46,47] Scattering factors are from Waasmair and Kirfel.[48]

Hydrogen atoms were placed in geometrically idealized positions and constrained to ride on their parent atoms with C---H distances in the range 0.95-1.00 Angstrom. Isotropic thermal parameters U_{eq} were fixed such that they were 1.2 U_{eq} of their parent atom Ueq for CH's and 1.5 U_{eq} of their parent atom U_{eq} in case of methyl groups. All non-hydrogen atoms were refined anisotropically by full-matrix least-squares. Final solutions were plotted using ORTEP and POV-Ray programs.[49,50]

Table 6.1. Crystal data, intensity collections [a] and structure refinement parameters for 1-(3,5-di-*tert*-butylphenyl) benzyl enol (**3-Ph**) and [(en)$NaMn_3O_4(L_3)(OMe)$] (**4**).

	3-Ph	**4**
Formula	$C_{23}H_{28}O_3$	$C_{70}H_{109}Mn_3N_8NaO_7$
Molecular Weight (g mol^{-1})	352.45	1362.46
Temperature (K)	100(2)	100(2)
Crystal System	Triclinic	Triclinic
Space Group	P $\bar{1}$	P $\bar{1}$
a, (Å)	10.3282(5)	14.0391(16)
b, (Å)	10.4401(5)	15.6116(18)
c, (Å)	10.4891(6)	17.2259(18)
α, (°)	75.699(3)	80.111(3)
β, (°)	62.677(3)	80.350(3)
γ, (°)	78.381(3)	81.918(4)
V ($Å^3$)	968.59(9)	3642.4(7)
Z	2	2
R_1	0.0492[b]	0.0547[b]
R_w	0.1191[c]	0.1029[c]
GOF	1.031	1.002

[a] Mo Ko(α,-) (λ = 0.71070 Å) radiation; graphite monochromator; -90 °C. [b] $R = \Sigma ||F_o| - |F_c|| / \Sigma |F_o|$. [c] $R_w = [\Sigma w(|Fo| - |Fc|)^2/\Sigma wF_o^2$, where $w^{-1} = [\sigma^2_{count} + (0.05\ F^2)^2]/4F^2$.

6.3 Results and Discussion

6.3.1 *Compartmental ligand design: rationale and strategy*

In order to attempt to synthesize a binucleating complex that resembles either a Mn-Mn or Mn-Ca fragment of the OEC cubane during the critical O–O bond formation step, certain design criteria must be taken into consideration. First, the overall ligand scaffold needs to contain differentiated compartments that can bind for two metal ions in close proximity. Second, ligand scaffold must have a flexible backbone around the two metal ion sites to allow for some degree of bending during the O–O bond forming step. Third, ligand precursors need to be asymmetric to ensure controlled Schiff-based condensation at one end. And lastly, synthetic route to these Schiff-based precursors needs to include a facile ability to synthesize a variety of structurally related ligands in order to tune its steric and electronic properties. Ligand complex that satisfies the above-mentioned criteria is depicted in Figure 6.4.

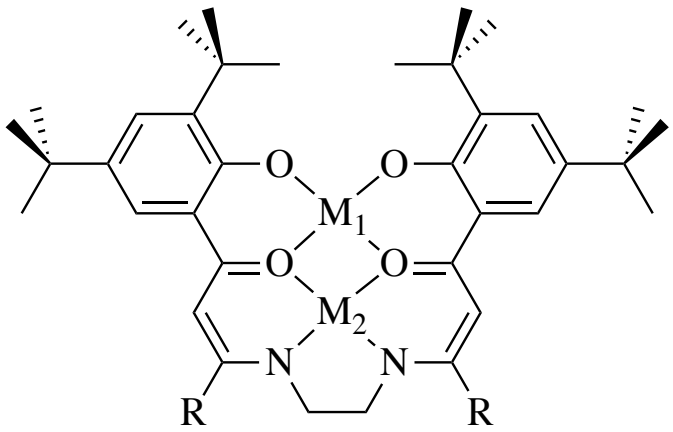

Figure 6.4. Target asymmetric binucleating ligand to support homo- (M_1 = M_2 = Mn^{II}) and heteronuclear (M_1 = Ca^{II} or Sr^{II}, M_2 = Mn^{II}) complexes. R = -CH_3, -C_6H_5.

Metal-templated Schiff-based condensation will ensure an insertion of the desired metal ion (e.g. Mn^{II}) in the N_2O_2 pocket, leaving the second O_2O_2 cite for the second metal (Mn^{II} for homometallic complex; Ca^{II} or Sr^{II} for heterometallic complex). *Tert*-butyl groups on the phenoxide moiety are intended to provide steric bulk to prevent diamine condensation at phenoxide end, intramolecular dimerization, and stacking. Successful, high-yield synthetic route to the final product used in the Schiff condensation has been developed and consists of three main steps, as shown in Figure 6.5. Step one and step three have been adopted with modifications from Zaveri *et. al* and Benisvy *et. al*, respectively.[41,42] Following sections describe detailed synthetic procedures as well as physical characterization of each step products.

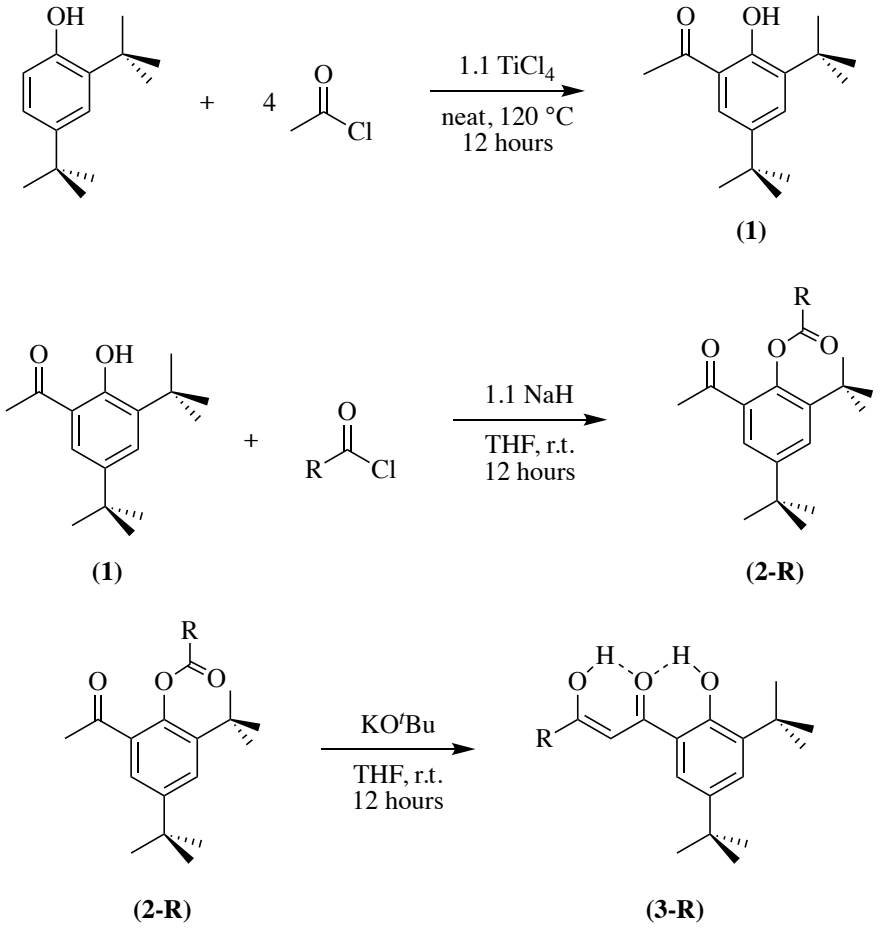

Figure 6.5. Overall synthetic route to the structurally related Schiff-base precursors **3-R**. R = $-CH_3$ or $-C_6H_5$.

6.3.2 *Step 1) Synthesis of 1-(3,5-di-Tert-Butyl-2-Hydroxyphenyl) Ethanone (**1**)*

A common route to forming the hydroxyphenyl butanone is via methylation of commercially available 3,5-di-*tert*-butyl-2-hydroxybenzaldehyde using MeMgBr Grignard reagent..[51] Obvious advantage of this synthetic route is high yield (96% reported) of 1-(3,5-di-tert-butyl-2-hydroxyphenyl) ethanone formed. However, MeMgBr is reactive with air and moisture, highly flammable, and forms explosive mixtures. Moreover, the reaction takes place in two parts over 16 hours.

Alternatively, hydroxyphenyl ethanone is also accessible via an efficient $TiCl_4$ mediated phenol acetylation. $TiCl_4$ acts as a Lewis acid for direct of *ortho*-acylation of 2,4-di-*tert*-butylphenol, following previously reported procedure.[41] $TiCl_4$ (M.W. = 189.679 g mol^{-1}, ρ = 1.726 g mL^{-1}, 482 μL, 4.4 mmol) was slowly added to 2,4-di-*tert*-butylphenol (M.W. = 206.32 g mol^{-1}, 0.826 g, 4 mmol) in a Schlenk flask flushed with N_2 at room temperature. The resulting dark cherry-red mixture was stirred at r.t. for 15 minutes until gas evolution has stopped. Then, acetyl chloride (M.W. = 78.50 g mol^{-1}, ρ = 1.104 g mL^{-1}, 213 μL, 3 mmol) was added to the solid and the resulting thick dark-red solution was stirred at r.t. for 15 minutes. The dark solution was then brought up to 120 °C and left to stir at this temperature for an additional hour. The reaction mixture was then cooled to r.t., diluted with CH_2Cl_2 (15 mL) and quenched with DI H_2O (15 mL). A cloudy dark-orange solution was obtained which was extracted with CH_2Cl_2 (3 x 10 mL). The organic layer was washed with DI H_2O (2 x 30 mL), dried (Na_2SO_4) for 30 minutes, and concentrated under reduced pressure. The procedure calls for additional purification of the crude material by silica gel column using a mixture of hexanes-EtOAc (1:1). ^{1}H NMR of the product before and after the column purification, however, shows no appreciable difference in the product's purity except for presence of hexane and ethyl acetate solvents present.

Formation of a thick slush was a point of concern since it mixes poorly. Therefore, instead, 2,4-di-*tert*-butylphenol was first dissolved in a minimal amount of CH_2Cl_2 (15 mL), degassed-pumped three times, concentrated to about 5 mL, and proceeded with the addition of $TiCl_4$ and acetyl chloride as described above. The resulting orange oil contained a few unknown side products when checked with ^{1}H NMR. Moreover, the orange oil turned green after two days in air at r.t. Therefore, performing a neat reaction as reported is most optimal.

^{1}H NMR proves to be the most convenient and telling way to monitor the success of the reaction. 1-(3,5-di-tert-butyl-2-hydroxyphenyl) ethanone, has an ^{1}H NMR spectrum that reflects the structural change within the 2,4-di-*tert*-butylphenol upon its acetylation, (Figure 6.6). Two *tert*-butyl groups show up slightly upfield at δ = 1.32 (s, 9H), 1.53 (s, 9H). Since *ortho*-hydrogen has been replaced with the acetyl group, we expect to see loss of its doublet signal at 6.63 ppm and addition of a singlet from acetyl's methyl group at 2.65 ppm (s, 3H). Acetyl's methyl singlet moves upfield from free acetyl chloride 2.69 to 2.58 ppm as a consequence of losing of electronegative chloride for an aryl group. Furthermore, H_A and H_B become more equivalent and show up at 7.56 ppm (m, 2ArH). Lastly, they hydroxy proton at 4.61 ppm moves downfield to 12.99 ppm as a consequence of hydrogen bonding to the acetyl group *ortho* to the hydroxyl group.

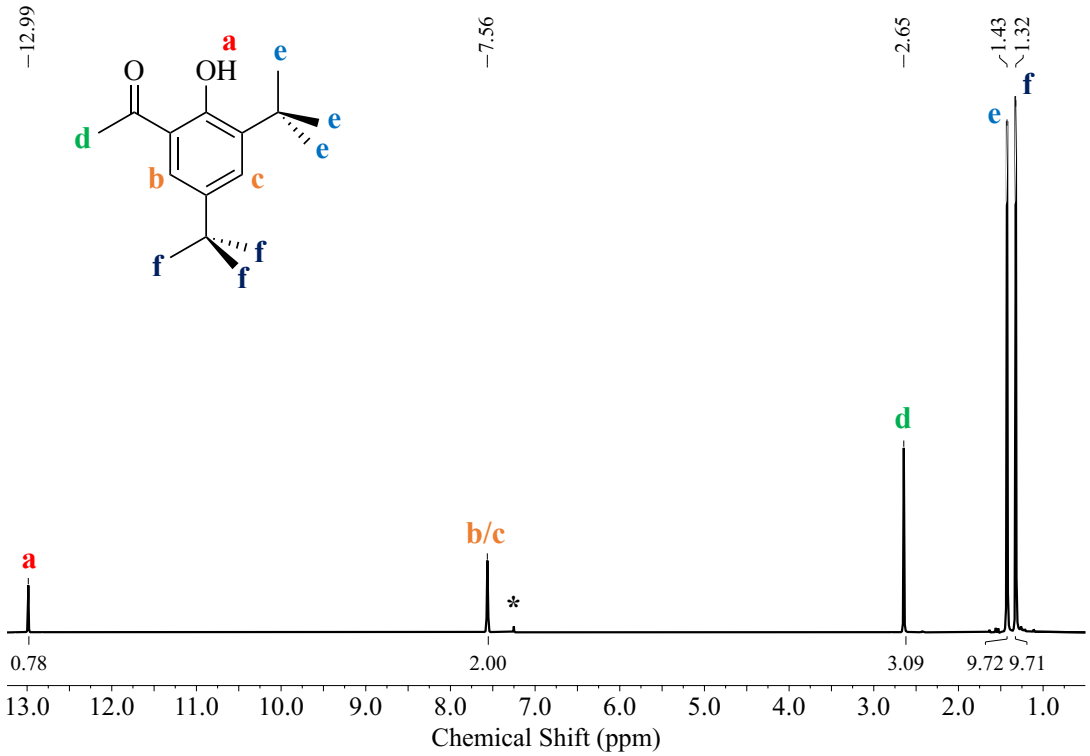

Figure 6.6. ^{1}H NMR (300 MHz, $CDCl_3$) spectrum of 1-(3,5-di-*tert*-butyl-2-hydroxyphenyl) ethanone (**1**). * denotes solvent peak.

The IR spectrum exhibits typical ring C–C stretching frequencies in the region of 1100-600 cm^{-1} region, the C–O vibrations in the 1250-1200 cm^{-1} region, and the ring C=C 1350-1250 cm^{-1}. The hydroxyl group OH^- group of phenols is expected to absorb strongly in 3700-3584 cm^{-1} region. Intramolecular hydrogen bonding of the –OH to the *ortho* acyl group is expected to reduce the stretching band and has been indeed reported at 2959 cm^{-1}.[41] The OH band is not observed here due to masking from the dominant stretches of Nujol in the 3000 cm^{-1} region. However, the most characteristic band observed at 1636 cm^{-1} is assigned to ketonic C=O stretch, (Figure 6.7, right). The ESI-MS spectrum shows **1** (expected *m/z*(+) = 249.18) as the major product, (Figure 6.7, left).

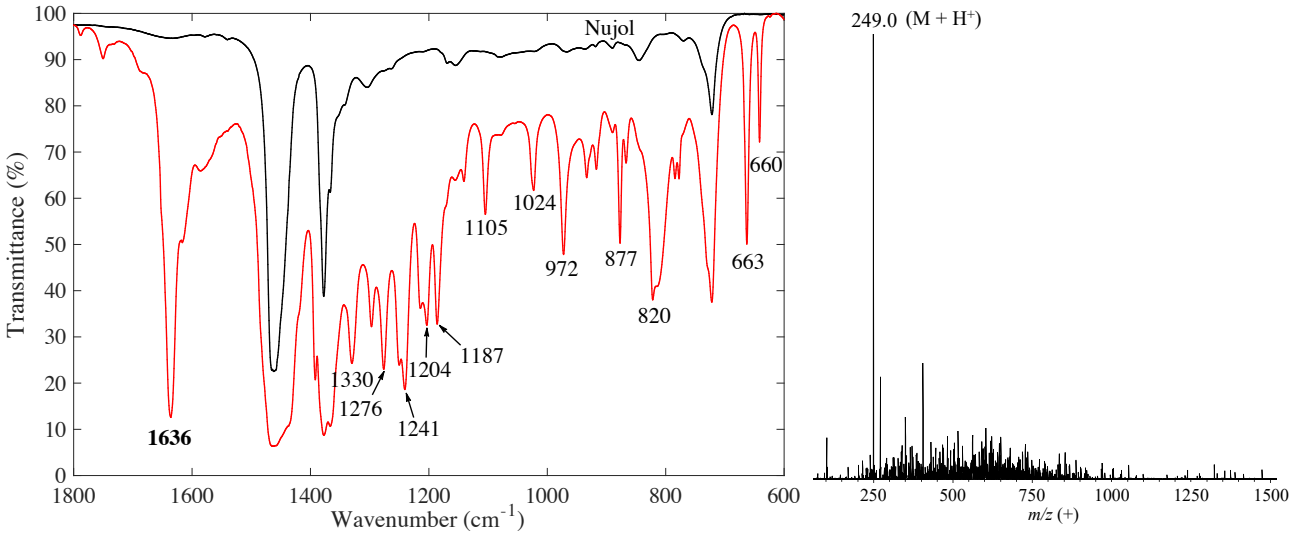

Figure 6.7. The FT-IR (right) and ESI-MS (left) spectra of 1-(3,5-di-*tert*-butyl-2-hydroxyphenyl) ethanone (**1**).

6.3.3 *Step 2) Synthesis of 2-Acetyl-4,6-di-Tert-Butylphenyl Acetate (**2-Me**) and 2-Acetyl-4,6-di-Tert-Butylphenyl Benzoate (**2-Ph**)*

A versatile and high-yielding synthetic procedure has been developed for the second step. At this point, esterification of **1** with various acyl chlorides ensures the desired asymmetric product in the final step. Acetyl chloride and benzoyl chloride were used for the esterification step to prepare 2-acetyl-4,6-di-*tert*-butylphenyl acetate (**2-Me**) and 2-acetyl-4,6-di-*tert*-butylphenyl benzoate (**2-Ph**). Anaerobic addition of 1.1 equiv. of insoluble strong base NaH (pK_a = 35.0) to an THF solution of **1** afforded a neon-yellow solution. An instantaneous H_2 gas evolution, as a result of phenol deprotonation, allowed the deprotonation reaction to go to completion. The, stoichiometric addition of acyl chloride (acetyl or benzoyl chloride) afforded desired **2-Me** or **2-Ph** products, respectively, after stirring under inert atmosphere overnight.

^{1}H NMR spectra of **2-Me** and **2-Ph** indicate that the reaction proceeds to completion without leftover starting complex **1,** as indicated by the complete disappearance of the phenolic

proton at 12.99 ppm. ^{1}H NMR spectrum of **2-Me** features an addition of a singlet from ester's methyl group at 2.53 ppm (s, 3H), (Figure 6.8), while **2-Ph** exhibits aryl ester's aromatic protons at 7.52 ppm (t, 2H), 7.65 ppm (tt, 1H,), and 8.22 ppm (dd, 2H), (Figure 6.9).

The IR spectrum of **2-Me** exhibits new ester characteristic stretches at 1757 and 1692 cm^{-1}, (Figure 6.10, right). The ESI-MS spectrum shows **2-Me** (expected *m/z*(–) = 290.20) as the major product, (Figure 6.10, left). Likewise, the IR spectrum of **2-Ph** exhibits ester characteristic stretches at 1743 and 1695 cm^{-1}, (Figure 6.11, right). As the result of presence of an aryl ester, the ESI-MS detects one or two **2-Ph** associated with cationic Na^{+} and K^{+} (Figure 6.11, left).

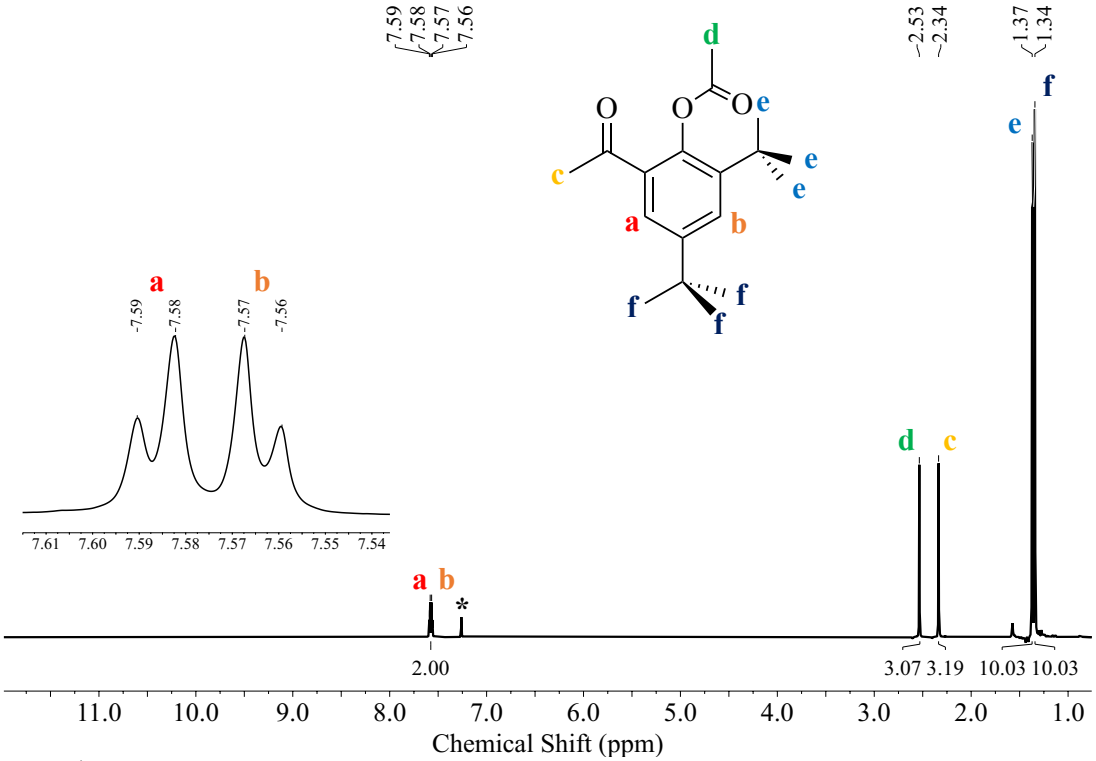

Figure 6.8. ^{1}H NMR ($CDCl_3$, 300 MHz) spectrum of 2-acetyl-4,6-di-*tert*-butylphenyl acetate (**2-Me**). Aryl proton multiplet is enlarged for clarity. * denotes solvent peak.

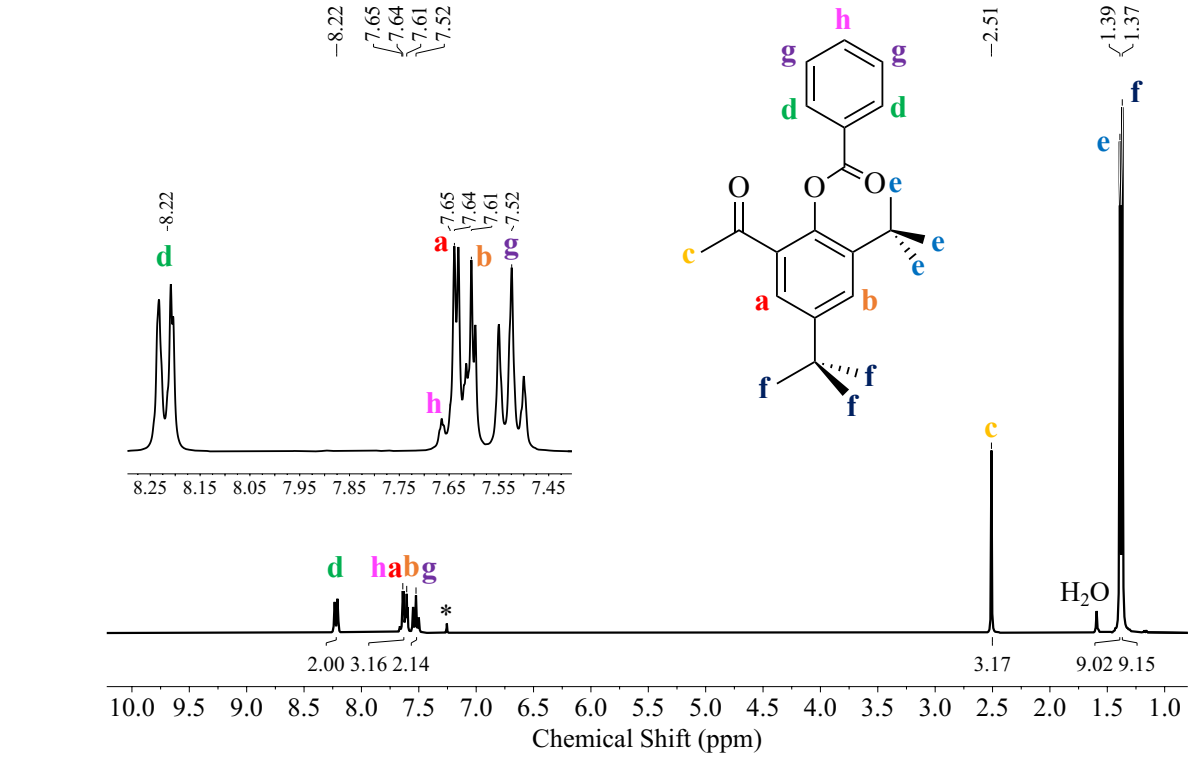

Figure 6.9. ^{1}H NMR ($CDCl_3$, 300 MHz) spectrum of 2-acetyl-4,6-di-*tert*-butylphenyl benzoate (**2-Ph**). Aryl proton multiplet is enlarged for clarity. * denotes solvent peak.

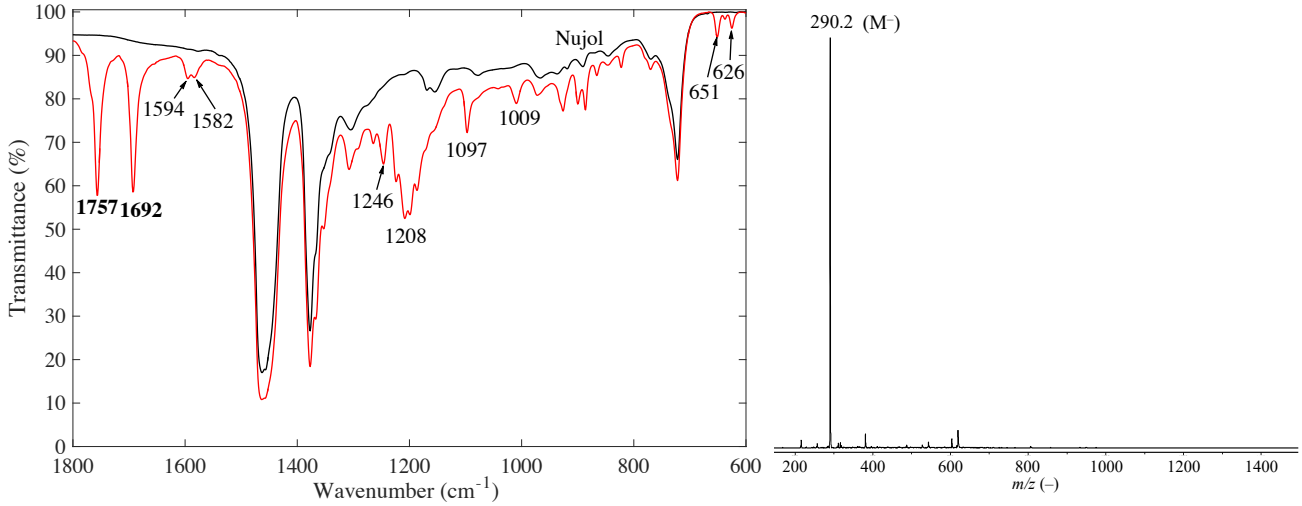

Figure 6.10. The FT-IR (right) and ESI-MS (left) spectra of 2-acetyl-4,6-di-*tert*-butylphenyl acetate (**2-Me**).

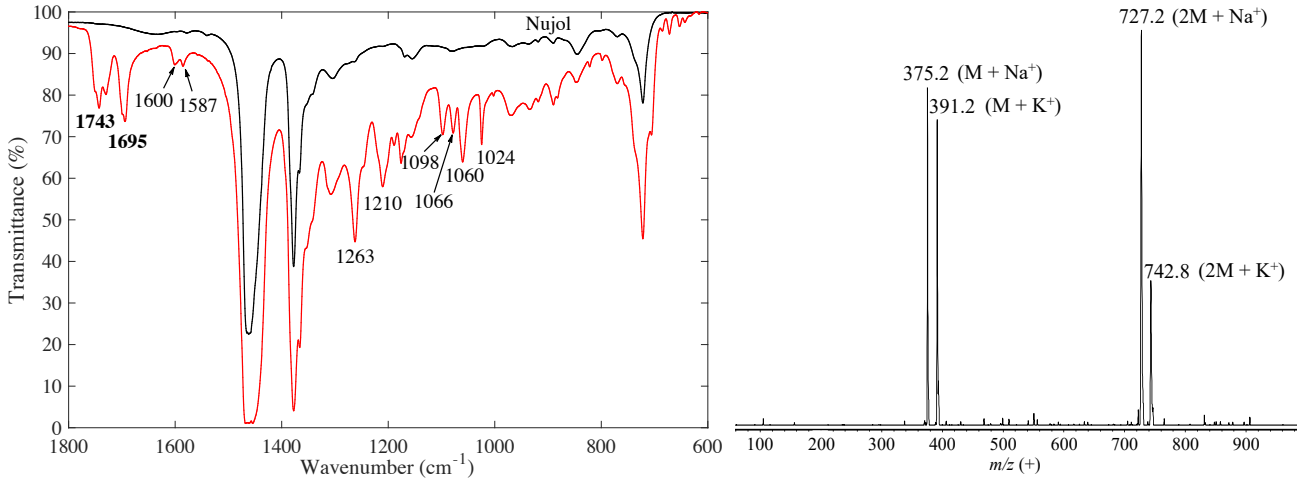

Figure 6.11. The FT-IR (right) and ESI-MS (left) spectra of 2-acetyl-4,6-di-*tert*-butylphenyl benzoate (**2-Ph**).

6.3.4 *Step 3) Synthesis of 1-(3,5-di-tert-butyl-2-hyroxypphenyl) butane-1,3-dione (**3-Me**) and 1-(3,5-di-tert-butylphenyl) benzyl enol (**3-Ph**)*

Finally, the corresponding **3-Me** dione and **3-Ph** enol were achieved by Baker-Venkataraman rearrangement reaction. KO^{t}Bu base (pK_a = 17.0) was added stoichiometrically to a stirring solution of **3-Me** or **3-Ph** in anhydrous THF and was allowed to stir overnight at room temperature. While the reported procedure for the synthesis of **3-Me** called for a 12-hour reflux in THF under inert atmosphere,[42] heating the reaction mixture usually resulted in formation of dione and enolic final products. On the other hand, stirring overnight at room temperature afforded a single form of **3-Me** or **3-Ph** in about 50% yield.

^{1}H NMR spectra of **3-Me** and **3-Ph** indicate that the rearrangement reaction proceeds to completion in both cases. ^{1}H NMR spectrum of **3-Me** features an addition of a singlet from the methyl group moving upfield to 1.79 ppm (s, 3H), (Figure 6.12), ^{1}H NMR spectrum of **3-Ph** exhibits aryl ester's aromatic protons at 7.52 ppm (t, 2H), 7.53 ppm (tt, 1H), and 7.93 ppm (dd, 2H), (Figure 6.13). The phenolic proton in **3-Me** at 12.65 ppm and in **3-Ph** at 12.66 ppm can be

resolved as well. However, the enolic -OH group in both products is likely broadened as a result of fast solvent proton exchange.

The IR spectrum of **3-Me** exhibits enol characteristic stretches at 1682 and 1604 cm^{-1}, (Figure 6.14, right). The ESI-MS spectrum shows **3-Me** (expected *m/z*(–) = 290.40) as the major product, (Figure 6.14, left). Likewise, the IR spectrum of **3-Ph** exhibits enol characteristic stretches at 1612 and 1573 cm^{-1}, (Figure 6.15, right). The ESI-MS spectrum shows **3-Ph** (expected *m/z*(–) = 351.40) as the major product, (Figure 6.15, left). Lastly, single yellow crystal of **3-Ph** suitable for X-ray diffraction, were in THF at r.t., as shown in the ORTEP diagram, (Figure 6.16). The structure features extensive hydrogen bonding between the phenolic and enolic hydroxo groups.

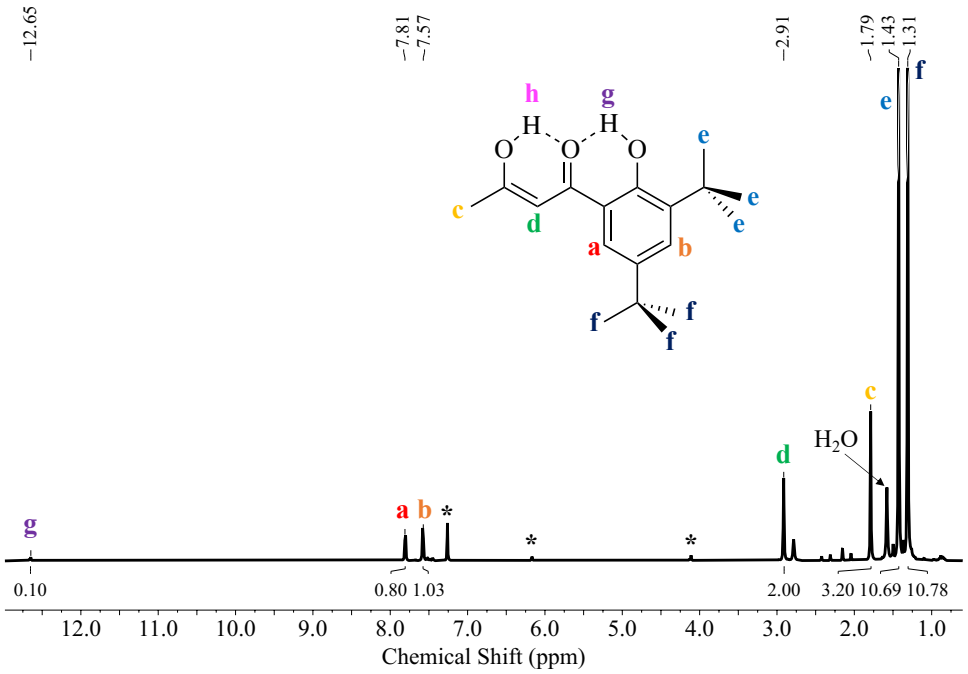

Figure 6.12. ^1H NMR ($CDCl_3$, 300 MHz) spectrum of 1-(3,5-di-*tert*-butyl-2-hydroxyphenyl)butane-1,3-dione (**3-Me**). Aryl proton multiplet is enlarged for clarity. * denotes solvent peak.

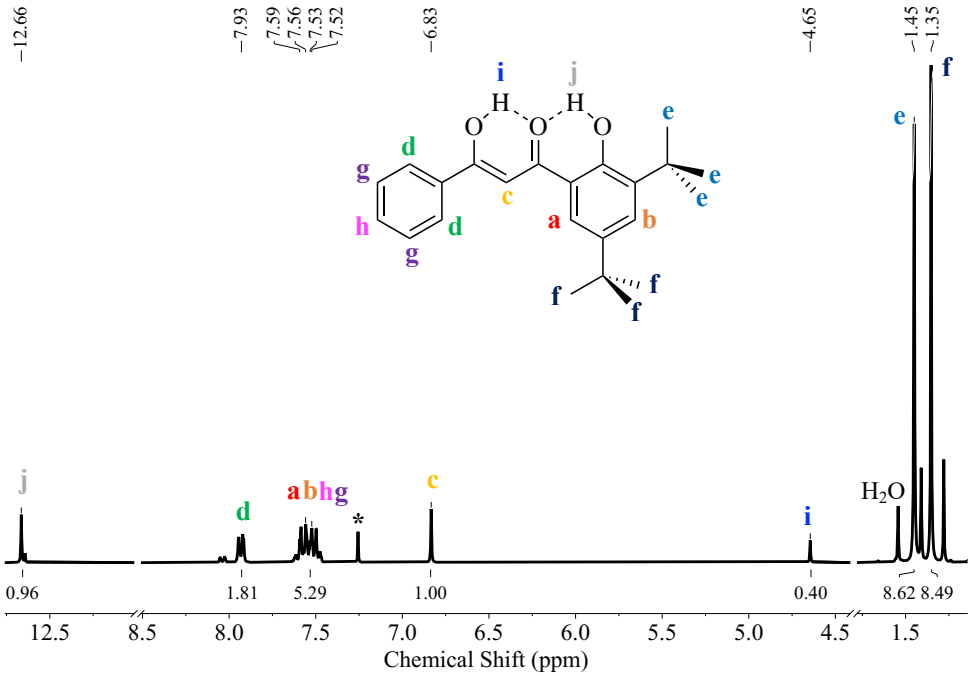

Figure 6.13. ^{1}H NMR ($CDCl_3$, 300 MHz) spectrum of 1-(3,5-di-*tert*-butylphenyl) benzyl enol (**3-Ph**) Aryl proton multiplet is enlarged for clarity. * denotes solvent peak.

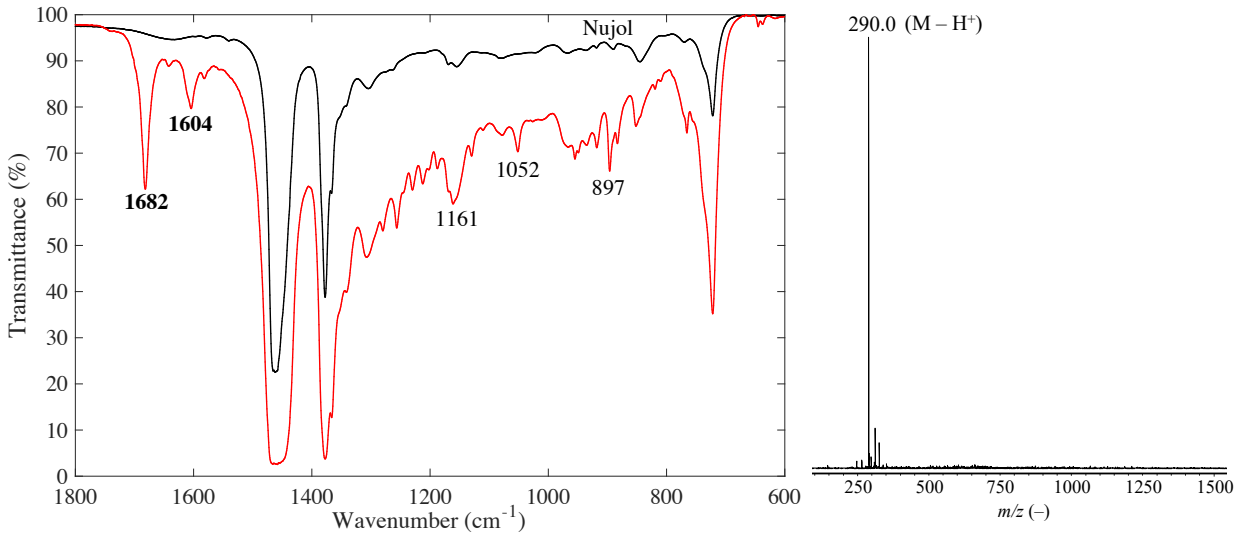

Figure 6.14. The FT-IR (right) and ESI-MS (left) spectra of 1-(3,5-di-*tert*-butyl-2-hydroxyphenyl)butane-1,3-dione (**3-Me**).

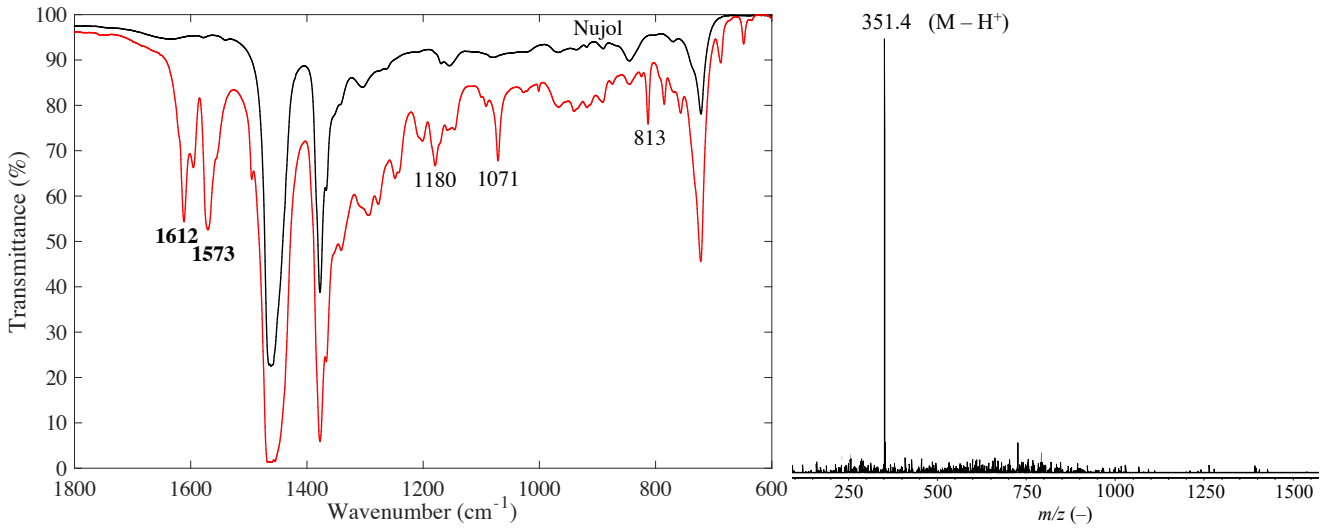

Figure 6.15. The FT-IR (right) and ESI-MS (left) spectra of 1-(3,5-di-*tert*-butylphenyl) benzyl enol (**3-Ph**).

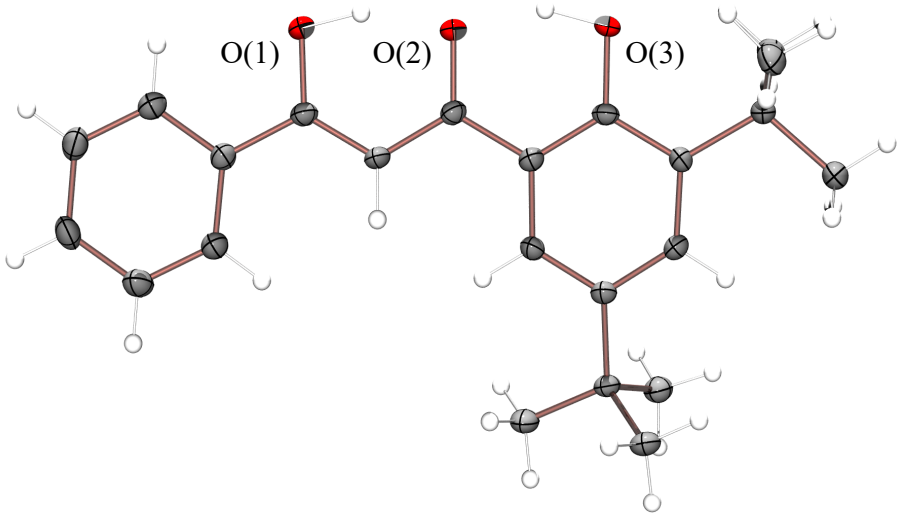

Figure 6.16. ORTEP diagram of 1-(3,5-di-*tert*-butylphenyl) benzyl enol (**3-Ph**) displaying 50% probability ellipsoids and atom-labeling scheme.

6.3.5 *Synthesis of [(en)NaMn$_3$O$_4$(L$_3$)(OMe)] (**4**) Cubane Complex*

Schiff-based mettalation attempts using the enolic **3-Me** and **3-Ph** precursors did not yield the desired binucleating Robson-type complex, (Figure 6.4). Multiple mettalation attempts

resulted in formation of insoluble yellow solids using both **3-Me** and **3-Ph** ligand precursors, which immediately turn dark green when opened to O_2, suggesting oxidation of bound Mn ions. Open air metallation, as well as metallation by overnight reflux yielded intractable dark green reaction mixtures, which are difficult to purify. Instantaneous color change to green may indicate that mettalation does take place. However, more trials are required in order to establish an efficient procedure to achieve the desired binucleating complexes. Nonetheless, stoichiometric addition of ethylene diamine to **3-Me**, followed by the addition of NaOMe, and finally $MnSO_4 \cdot H_2O$, afforded a heterobimetallic cubane complex, $[(en)NaMn_3O_4(L_3)(OMe)]$ (**4**), (Figure 6.17).

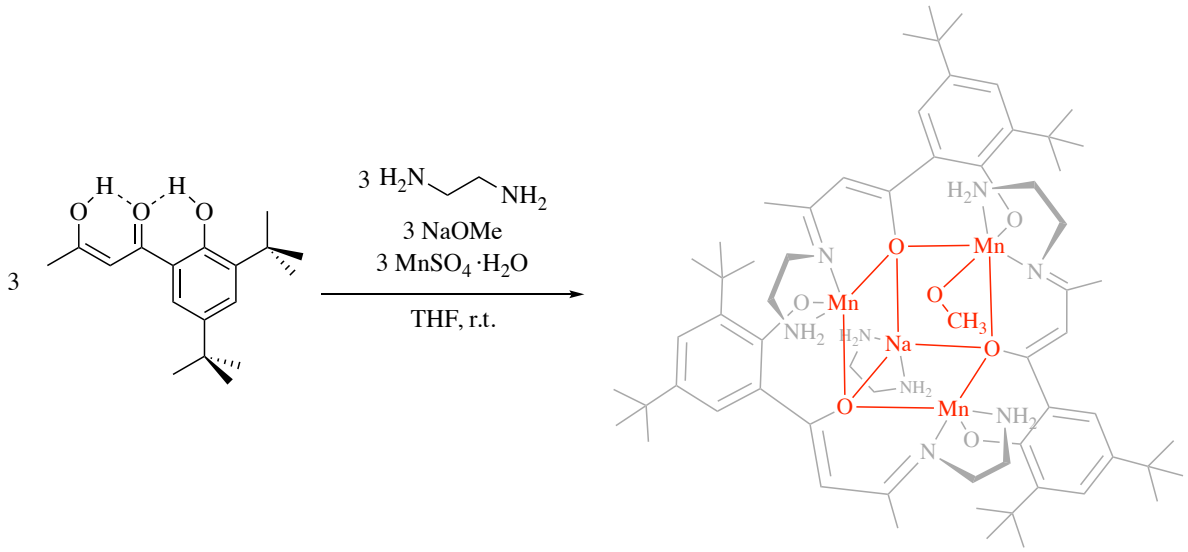

Figure 6.17. Synthetic route to $[(en)NaMn_3O_4(L_3)(OMe)]$ (**4**).

The $NaMn_3O_4$ cubane complex **4** has been characterized by X-ray crystallography, (Figure 6.18). The cubane is composed of flexible **3-Me** ligand that supports an "open" cubane core. Moreover, it contains a sodium, rather than calcium, ion diagonally opposite from the exogenous methoxide ligand, which is positioned above a triangular arrangement of three Mn ions. Mn(1) and Mn(2) ions are five-coordinate (N_2O_3), while a Mn(3) ion is in a or six-coordinate (N_2O_4) environment, (Figure 6.15, right). The average Mn–Mn distance of 3.43(5) Å within the cubane core is longer than "open" radiation-damage-free OEC complex in the S_1 state (2.9(3) Å),[52]

suggesting the lower average oxidation state on Mn ions in **4**. Each Mn ion is ligated by one primary amine (N(1), N(3), or N(5)), one imine nitrogen (N(2), N(4), or N(6)), a phenoxide oxygen (O(2), O(4), or O(6)), and an enolate oxygen (O(1), O(3), or O(5)) all derived from the same **3-Me** ligand. A Na ion is coordinated to O(1), O(3) and O(5) atoms of the cubane core and capped by a molecule of ethylene diamine. The phenoxide oxygens of **3-Me** are terminal, while its enolate oxygens form vertices of the cubane and bridge Mn and Na ions. The Mn(1)–O(7) = 2.2515(19) Å, Mn(2)–O(7) = 2.2450(19) Å, and Mn(3)–O(7) = 2.219(2) Å bond lengths indicate that O(7) of the methoxide ligand is singly bridging in **4**, indicating that this $NaMn_3O_4$ cluster in an "open" form. The "open" cubane core appears to be supported by a flexible ligand framework as well as lower oxidation states of Mn ions and not Jahn-Teller distortions, which would not arise in high-spin d^5 Mn^{II} ions.

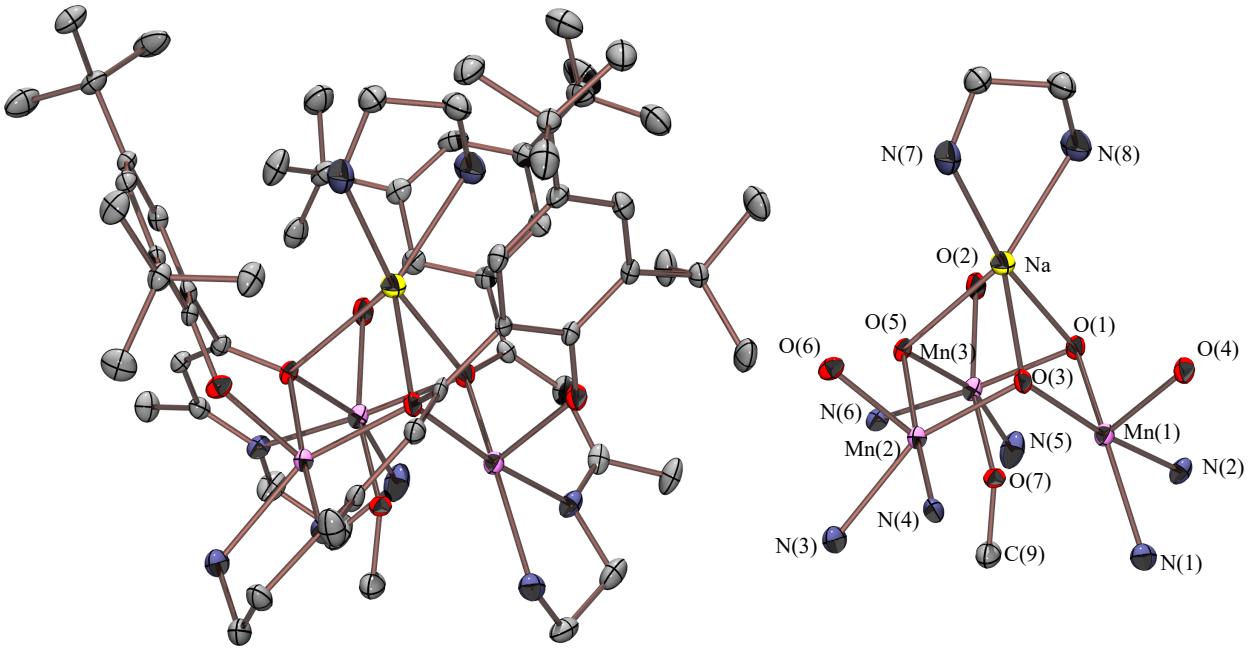

Figure 6.18. ORTEP diagram of $[(en)NaMn_3O_4(L_3)(OMe)]$ (**4**) (full complex – right; cubane core only – left) displaying 50% probability ellipsoids and atom-labeling scheme. All hydrogen atoms, counterions, and solvents of crystallization have been removed for clarity. Selected bond lengths for **4**: Mn(1)–O(7), 2.2515(19) Å; Mn(2)–O(7), 2.2450(19) Å; Mn(3)–O(7), 2.219(2) Å; Mn(1)–O(1), 2.1544(18) Å; Mn(2)–O(3), 2.1306(18) Å; Mn(3)–O(5), 2.1512(19) Å; Mn(1)–O(3), 2.2048(19) Å; Mn(2)–O(5), 2.2191(19) Å; Mn(3)–O(1), 2.2250(19) Å.

6.4 Conclusions

The biomimetic modeling approach relies on the design and synthesis of new ligand systems. The ability to envision a small inorganic complex that can encapsulate key geometric and chemical properties of a biological system is at the heart of this truly creative field. Moreover, it provides an opportunity to isolate and spectroscopically characterize previously unobserved reactive intermediates and to probe the influence of the coordination environment on its chemistry. This chapter provides a detailed description of a successfully developed, versatile, and high-yielding synthetic route to the Schiff-based precursors on modified literature methods.[41,42] The design criteria, namely differentiated compartmental scaffolding, flexible backbone, and availability of modifiable groups, allows for a synthesis of a wide variety of structurally-related ligands with tunable steric and electronic properties. Gram quantities of R = -CH_3 and -Ph of precursor ligands can be obtained in near quantitative yield, which can then be converted to their corresponding **3-Me** and **3-Ph** enol forms, as shown by ^{1}H NMR, FT-IR, ESI-MS, and X-ray crystallography.

Presently, mettalation attempts to afford the desired heterobimetallic Robson-type complexes have been unsuccessful. However, these mettalation attempts have also resulted in synthesis and crystallographic characterization of a heterobimetallic cubane [(en)$NaMn_3O_4(L_3)$(OMe)] (**4**) structure. The cubane contains three Mn^{II} ions bridged by three O atoms to a Na^+ ion. An exogenous methoxide ligand is positioned diagonally opposite from the Na^+ ion and is ligated to Mn(3) only, forming an "open" core. An "open" heterometallic $NaMn_3O_4$ cubane cluster core appears to be also supported by a flexible **3-Me** ligand framework. Presently, there are no examples of synthetic cubane structures in an "open" form that are relevant to the OEC. Therefore, this complex, together with a few other examples developed in the Kovacs group,

provide an exciting opportunity to gain more insight into the nature of structural changes that the OEC undergoes during the Kok cycle.[53,54] Synthesizing the same cubane structure, but with a Ca^{II} ion, is perhaps the most relevant next step. Structural comparison of Na- vs. Ca-bound cubane cores will provide a clearer picture for the influence of these redox-inactive metals on the cubane distortion and metrical parameters.

6.5 References

(1) Armstrong, R. C.; Wolfram, C.; de Jong, K. P.; Gross, R.; Lewis, N. S.; Boardman, B.; Ragauskas, A. J.; Ehrhardt-Martinez, K.; Crabtree, G.; Ramana, M. V. *Nat. Energy* **2016**, *1* (1), 1–8.

(2) IPCC. In *Climate Change and Land: an IPCC special report on climate change, desertification, land degradation, sustainable land management, food security, and greenhouse gas fluxes in terrestrial ecosystems*; 2020; pp 1–36.

(3) *Annual Energy Outlook*; U.S. Energy Information Administration, 2020.

(4) Lewis, N. S.; Nocera, D. G. *Proc. Natl. Acad. Sci.* **2006**, *103* (43), 15729–15735.

(5) Terreson, D.; Richardson, S.; West, J.; Terreson, D.; Richardson, S.; West, J.; March, W. *Resour. Futur.* **2020**.

(6) Davis, S. J.; Caldeira, K.; Matthews, H. D. *Science* **2010**, *329* (5997), 1330–1333.

(7) Olsson, L.; Barbosa, H.; Bhadwal, S.; Cowie, A.; Delusca, K.; Flores-Renteria, D.; Hermans, K.; Jobbagy, E.; Kurz, W.; Li, D.; Jean Sonwa, D.; Stringer, L. In *Land degradation. Climate Change and Land: an IPCC special report on climate change, desertification, land degradation, sustainable land management, food security, and greenhouse gas fluxes in terrestrial ecosystems*; 2019; pp 345–436.

(8) Mbow, C.; Rosenzweig, C.; G. Barioni, L.; G. Benton, Ti.; Herrero, M.; Krishnapillai, M.; Liwenga, E.; Pradhan, P.; G. Rivera-Ferre, M.; Sapkota, T.; N. Tubiello, F.; Xu, Y. In *Food Securiy. Climate Change and Land: an IPCC special report on climate change, desertification, land degradation, sustainable land management, food security, and greenhouse gas fluxes in terrestrial ecosystems*; 2019; pp 437–550.

(9) Lewis, N. S.; Crabtree, G. *Basic Research Needs for Solar Energy Utilization*; U.S. Department of Energy: Washington, DC, 2005.

(10) Hagberg, D. P.; Yum, J.-H.; Lee, H.; De Angelis, F.; Marinado, T.; Karlsson, K. M.; Humphry-Baker, R.; Sun, L.; Hagfeldt, A.; Grätzel, M.; Nazeeruddin, M. K. *J. Am. Chem. Soc.* **2008**, *130* (19), 6259–6266.

(11) Walter, M. G.; Warren, E. L.; McKone, J. R.; Boettcher, S. W.; Mi, Q.; Santori, E. A.; Lewis, N. S. *Chem. Rev.* **2010**, *110* (11), 6446–6473.

(12) Wang, Y.; Suzuki, H.; Xie, J.; Tomita, O.; Martin, D. J.; Higashi, M.; Kong, D.; Abe, R.; Tang, J. *Chem. Rev.* **2018**, *118* (10), 5201–5241.

(13) McCrory, C. C. L.; Jung, S.; Peters, J. C.; Jaramillo, T. F. *J. Am. Chem. Soc.* **2013**, *135* (45), 16977–16987.

(14) Herron, J. A.; Kim, J.; Upadhye, A. A.; Huber, G. W.; Maravelias, C. T. *Energy Environ. Sci.* **2015**, *8* (1), 126–157.

(15) Holladay, J. D.; Hu, J.; King, D. L.; Wang, Y. *Catal. Today* **2009**, *139* (4), 244–260.

(16) Park, S.; Shao, Y.; Liu, J.; Wang, Y. *Energy Environ. Sci.* **2012**, *5* (11), 9331.

(17) Yano, J.; Yachandra, V. *Chem. Rev.* **2014**, *114* (8), 4175–4205.

(18) Renger, G. *J. Photochem. Photobiol. B Biol.* **2011**, *104* (1–2), 35–43.

(19) Nocera, D. G. *Acc. Chem. Res.* **2012**, *45* (5), 767–776.

(20) Cox, N.; Retegan, M.; Neese, F.; Pantazis, D. A.; Boussac, A.; Lubitz, W. *Science* **2014**, *345* (6198), 804–808.

(21) Deisenhofer, J.; Epp, O.; Miki, K.; Huber, R.; Michel, H. *Nature* **1985**, *318* (6047), 618–624.

(22) Umena, Y.; Kawakami, K.; Shen, J.-R.; Kamiya, N. *Nature* **2011**, *473* (7345), 55–60.

(23) Kok, B.; Forbush, B.; McGloin, M. *Photochem. Photobiol.* **1970**, *11* (6), 457–475.

(24) DEBUS, R. *Coord. Chem. Rev.* **2008**, *252* (3–4), 244–258.

(25) Debus, R. J. *Biochim. Biophys. Acta - Bioenerg.* **2001**, *1503* (1–2), 164–186.

(26) Ho, F. M.; Styring, S. *Biochim. Biophys. Acta - Bioenerg.* **2008**, *1777* (2), 140–153.

(27) Rutherford, A. W.; Osyczka, A.; Rappaport, F. *FEBS Lett.* **2012**, *586* (5), 603–616.

(28) Lohmiller, T.; Shelby, M. L.; Long, X.; Yachandra, V. K.; Yano, J. *J. Phys. Chem. B* **2015**, *119* (43), 13742–13754.

(29) Retegan, M.; Krewald, V.; Mamedov, F.; Neese, F.; Lubitz, W.; Cox, N.; Pantazis, D. A. *Chem. Sci.* **2016**, *7* (1), 72–84.

(30) Vinyard, D. J.; Khan, S.; Brudvig, G. W. *Faraday Discuss.* **2015**, *185*, 37–50.

(31) Cox, N.; Retegan, M.; Neese, F.; Pantazis, D. a.; Boussac, a.; Lubitz, W. *Science* **2014**, *345* (6198), 804–808.

(32) Brudvig, G. W. *Philos. Trans. R. Soc. B Biol. Sci.* **2008**, *363* (1494), 1211–1219.

(33) Dismukes, G. C.; Brimblecombe, R.; Felton, G. A. N.; Pryadun, R. S.; Sheats, J. E.; Spiccia, L.; Swiegers, G. F. *Acc. Chem. Res.* **2009**, *42* (12), 1935–1943.

(34) Betley, T. A.; Wu, Q.; Van Voorhis, T.; Nocera, D. G. *Inorg. Chem.* **2008**, *47* (6), 1849–1861.

(35) Robson, R. *Aust. J. Chem.* **1970**, *23* (11), 2217.

(36) Pilkington, N.; Robson, R. *Aust. J. Chem.* **1970**, *23* (11), 2225.

(37) Hoskins, B. F.; Robson, R.; Williams, G. A. *Inorganica Chim. Acta* **1976**, *16* (C), 121–133.

(38) Groh, S. E. *Isr. J. Chem.* **1976**, *15* (3–4), 277–307.

(39) Casellato, U.; Vigato, P. A.; Fenton, D. E.; Vidali, M. *Chem. Soc. Rev.* **1979**, *8* (2), 199.

(40) Guerriero, P.; Tarnburini, S.; Vigato, P. A. *Coord. Chem. Rev.* **1995**, *139* (C), 17–243.

(41) Bensari, A.; Zaveri, N. T. *Synthesis (Stuttg).* **2003**, No. 2, 0267–0271.

(42) Zats, G. M.; Arora, H.; Lavi, R.; Yufit, D.; Benisvy, L. *Dalt. Trans.* **2011**, *40* (41), 10889.

(43) Bruker. APEX2 (Version 2.1-4), SAINT (Version 7.34A), SADABS (Version 2007/4). BrukerAXS Inc: Madison 2007.

(44) Altomare, A.; Cascarano, G.; Giacovazzo, C.; Guagliardi, A.; Burla, M. C.; Polidori, G.; Camalli, M. *J. Appl. Crystallogr.* **1994**, *27* (3), 435.

(45) Altomare, A.; Burla, M. C.; Camalli, M.; Cascarano, G. L.; Giacovazzo, C.; Guagliardi, A.; Moliterni, A. G. G.; Polidori, G.; Spagna, R. *J. Appl. Crystallogr.* **1999**, *32* (1), 115–119.

(46) Sheldrick, G. M. SHELXL-97, Program for the Refinement of Crystal Structures, University of Göttingen, Germany 1997.

(47) Sheldrick, G. M. *Acta Crystallogr. Sect. C Struct. Chem.* **2015**, *71* (1), 3–8.

(48) Waasmaier, D.; Kirfel, A. *Acta Crystallogr. Sect. A Found. Crystallogr.* **1995**, *51* (3), 416–431.

(49) Burnett, M. N.; Johnson, C. K. ORTEP-III: Oak Ridge Thermal Ellipsoid Plot Program for Crystal Structure Illustration. Oak Ridge National Laboratory Report ORNL-6895, 1996.

(50) Persistence of Vision Raytracer. Persistence of Vision Pty. Ltd.: Williamstown, Victoria, Australia, 2004.

(51) Kündig, E. P.; Botuha, C.; Lemercier, G.; Romanens, P.; Saudan, L.; Thibault, S. *Helv. Chim. Acta* **2004**, *87* (3), 561–579.

(52) Suga, M.; Akita, F.; Hirata, K.; Ueno, G.; Murakami, H.; Nakajima, Y.; Shimizu, T.; Yamashita, K.; Yamamoto, M.; Ago, H.; Shen, J.-R. *Nature* **2015**, *517* (7532), 99–103.

(53) Cox, N.; Retegan, M.; Neese, F.; Pantazis, D. A.; Boussac, A.; Lubitz, W. *Science* **2014**, *345* (6198), 804–808.

(54) Capone, M.; Bovi, D.; Narzi, D.; Guidoni, L. *Biochemistry* **2015**, *54* (42), 6439–6442.